Investigations of materials hosting exotic magnetism with spin-density functional theory

HAWKHEAD, ZACHARY

HAWKHEAD, ZACHARY (2022) *Investigations of materials hosting exotic magnetism with spin-density functional theory* , Durham theses, Durham University. Available at Durham E-Theses Online: http://etheses.dur.ac.uk/14737/

Investigations of materials hosting exotic magnetism with spin-density functional theory

Zachary Hawkhead

St Chad's College

A thesis presented for the degree of

Doctor of Philosophy

Centre for Materials Physics
University of Durham
United Kingdom

August 2022

Investigations of materials hosting exotic magnetism with spin-density functional theory

Zachary Hawkhead

Abstract

Spin-density functional theory (spin-DFT) has long been used to study materials exhibiting collinear spin textures. Recently it has become more common to apply non-collinear spin-DFT to tackle systems with more exotic magnetism.

In this thesis, we use spin-DFT both as a predictive tool and as a means of explaining phenomena uncovered by experiment. We use calculations to complement muon-spin spectroscopy (μSR) studies of two skyrmion hosting materials, Cu_2OSeO_3 and $GaV_4S_{8-y}Se_y$, as well as crystallography and magnetometry measurements of $[Cu(pyz)_{0.5}(gly)]ClO_4$. For Cu_2OSeO_3 we use structural relaxation to find likely stopping sites for an implanted muon. Our predicted muon sites lead to good agreement with the measured μSR spectra. For the $GaV_4S_{8-y}Se_y$ series, we are able to see how the spin density changes upon substitution, consistent with observations of a spin-glass at high substitution. In a pressure study of $[Cu(pyz)_{0.5}(gly)]ClO_4$, we find that calculated changes to the structure well match X-ray crystallography measurements, capturing the relevant changes to the Cu separation. We see dramatic change in the secondary exchange mechanism consistent with structural distortions at high pressure.

Next, in $Cr_{1/3}MS_2$ (M = Nb or Ta), we predict a gap-like feature in the density of states (DoS) which is then confirmed through magnetometry measurements. This gap explains the low temperature transport and magnetism in these materials. Extending the study to $N_{1/3}NbS_2$, for N in the first period transition metals, we show that only Cr intercalation results in this gap. We predict the magnetic properties of the series through a band filling mechanism.

Finally, we make use of a recently developed exchange and correlation (xc) functional and implement it in CASTEP. This functional improves the treatment of non-collinear spin which allows us to realise a spin-ice state in $Dy_2Ti_2O_7$.

Contents

Abbreviations

μSR	muon-spin spectroscopy 3, 20, 67, 69, 70, 72, 75, 77, 82, 85, 119, 122, 158, 160
ARPES	angle-resolved photoemission spectroscopy 67
bcc	body centred cubic 60, 61, 133, 142
BO	Born-Oppenheimer 25, 70
BZ	Brillouin zone 49, 51, 59, 60, 107, 169, 171–174
CDW	charge density waves 113, 162
CM	collinear magnetism 18, 35, 37, 61, 128
CSL	chiral soliton lattice 103, 105, 126, 159
DFPT	density functional perturbation theory 55, 57
DFT	density functional theory 16–20, 26, 27, 32, 34, 40, 41, 44, 55, 58, 59, 62–65, 67–72, 75, 79, 85, 86, 89, 91, 93, 96, 97, 100, 101, 103, 104, 106–108, 116, 119, 126–129, 150, 157–161, 163, 172
DFT+μ	density functional theory + μ 70, 73, 77, 85, 158, 160, 161
DM	density mixing 56–58, 65, 92, 109, 134, 146, 150, 163
DMI	Dzyaloshinskii–Moriya interaction 19, 43, 71, 92, 104, 105, 126, 161
DoF	degrees of freedom 26
DoS	density of states 3, 20, 59, 60, 69, 103, 106–108, 110–113, 116, 118, 123–126, 159, 169, 171, 172
EDFT	ensemble density functional theory 56–58, 65, 107, 134, 136, 137, 150, 155, 163
FFT	fast Fourier transform 50, 167
FT	Fourier transform 50, 132
GGA	generalised gradient approximation 44–46, 89, 93, 107
hcp	hexagonal close packed 140

HEG	homogeneous electron gas 44
HK	Hohenberg-Kohn 20, 27, 32, 40, 41, 56
HK I	first Hohenberg-Kohn theorem 27, 40
HK II	second Hohenberg-Kohn theorem 27, 30
KS	Kohn-Sham 20, 27, 30–33, 35–37, 40, 41, 43, 46–50, 52, 55, 59, 60, 66, 136, 154, 164
LCAO	linear combination of atomic orbitals 62, 63, 107
LDA	local density approximation 44
LSDA	local spin-density approximation 21, 44–46, 60, 61, 64, 79, 127, 130, 131, 133, 135, 136, 138–141, 144, 146, 147, 150–156, 159, 160
MP	Monkhorst and Pack 51, 59, 60, 72, 73, 89, 107, 109, 133, 150
NCM	non-collinear magnetism 18, 19, 35, 37, 39, 58, 61, 64, 128
PBC	periodic boundary conditions 47, 70, 140
PBE	Perdew, Burke and Ernzerhof 45, 59, 60, 64, 73, 79, 80, 89, 96, 97, 100, 107, 109, 129, 130
PDoS	projected density of states 107, 110, 111, 113, 125, 170, 174
QCP	quantum critical point 88, 99, 101
SCF	self-consistent field 56, 59, 64, 92, 107, 134–136, 146, 150, 155
SOC	spin-orbit coupling 18, 43, 54, 55, 64, 105, 108, 111, 112, 126, 134, 142
spin-DFT	spin-density functional theory 3, 17–21, 34, 35, 37, 38, 40, 41, 58, 60, 61, 64, 65, 67, 69, 81, 84, 85, 89, 92, 97, 107, 128, 135, 137, 146, 147, 149, 150, 153, 157–162
TMDC	transition-metal dichalcogenide 20, 21, 103, 104, 106, 107, 113, 120–123, 125, 126, 159, 160
VDW	Van der Waals 93, 106, 107, 109
xc	exchange and correlation 3, 32, 36, 38, 39, 44, 46, 64, 73, 89, 107, 109, 128, 129, 131, 133, 134, 138–141, 146, 149, 150, 155, 156, 159, 163

Declaration

The work in this thesis is based on research carried out in the Department of Physics, University of Durham, England. No part of this thesis has been submitted elsewhere for any other degree or qualification, and it is the sole work of the author unless referenced to the contrary in the text.

Zachary Hawkhead
Durham, 11 August, 2022

List of publications

T. J. Hicken, S. J. R. Holt, K. J. A. Franke, **Z. Hawkhead**, A. Štefančič, M. N. Wilson, M. Gomilšek, B. M. Huddart, S. J. Clark, M. R. Lees, F. L. Pratt, S. J. Blundell, G. Balakrishnan, T. Lancaster. "Magnetism and Néel skyrmion dynamics in $\mathrm{GaV_4S_{8-y}Se_y}$". Physical Review Research **2**, 032001(R), 2020.

T. J. Hicken, M. N. Wilson, K. J. A. Franke, B. M. Huddart, **Z. Hawkhead**, M. Gomilšek, S. J. Clark, F. L. Pratt, A. Štefančič, A. E. Hall, M. Ciomaga Hatnean, G. Balakrishnan, and T. Lancaster. "Megahertz dynamics in skyrmion systems probed with muon-spin relaxation". Physical Review B **103**, 024428, 2021.

T. J. Hicken, **Z. Hawkhead**, M. N. Wilson, B. M. Huddart, A. E. Hall, G. Balakrishnan, C. Wang, F. L. Pratt, S. J. Clark, T. Lancaster. "Energy-gap driven low-temperature magnetic and transport properties in $\mathrm{Cr_{1/3}}M\mathrm{S_2}$ (M=Nb, Ta)". Physical Review B **105**, L060407, 2022.

B. M. Huddart, A. Hernández-Melián, T. J. Hicken, M. Gomilšek, **Z. Hawkhead**, S. J. Clark, F. Pratt, and T. Lancaster. "MuFinder: A program to determine and analyse muon stopping sites", Computer Physics Communications **280**, 108488, 2022.

M. J. Coak, S. P. M. Curley, J. P. Tidey, D. Graf, **Z. Hawkhead**, S. J. Clark, T. Lancaster, Z. E. Manson, J. L. Manson, and P. A. Goddard. "Pressure-induced magnetic ordering in a molecule-based dimer", *in preparation.*

Z. Hawkhead, T. J. Hicken, B. M. Huddart, S. J. Clark and T. Lancaster. "Band-filling-induced magnetism in $N_{1/3}\mathrm{NbS}_2$", *in preparation.*

Z. Hawkhead, N. Gidopoulos, S. J. Blundell, S. J. Clark and T. Lancaster. "First-principles calculations of magnetic states in pyrochlores using source-corrected exchange and correlation", *in preparation.*

S. J. Clark and **Z. Hawkhead**. "Non-collinear spin density functional theory", *in preparation.*

Acknowledgements

Firstly, I would like to thank my supervisors Tom Lancaster and Stewart Clark. I am incredibly lucky to have worked with two of the most brilliant professors in the department. Tom is exactly the kind of supervisor any PhD student would wish for. Thank you for all of your support and dedication throughout. Developing new software has been such an integral and enjoyable part of my PhD. Without Stewart's guidance, I would not be the programmer I am today, so I would like to thank him for his many tips and tricks about parallel programming, Fortran, emacs, as well as for everything I now know about supercomputers. Together, you make a formidable supervisory team.

A particular thanks must also go to Nikitas Gidopoulos for many invaluable discussions about DFT and quantum mechanics. Not only is he a genius, he is also the kindest and most patient person you are likely to meet.

My thanks go to Durham University and the UK Skyrmion Project for funding my studentship, and to Durham Hamilton HPC, ARCHER2, and the UK Materials and Molecular Modelling Hub for computing resources.

A PhD is by no means a solo endeavour and many people in the Centre for Materials Physics have made the experience so enjoyable. My thanks go to the other members of the Durham Skyrmion project and wider *magnet men*: Thomas Hicken, Luke Turnbull, Sam Moody, Murray Wilson, Matt Littlehales, Ben Huddart and Ben Nicholson. Particular mention must go to Thomas Hicken for working with me on so many projects. I have also been extremely fortunate to share my office with an incredible bunch of people over the last four years, thank you to the original occupants of PH305, Tim Callow, Tom Pitts,

Ben Pearce and Matjaž Gomilšek, and more recently Michael Hertaeg, Alberto Hernández-Melián and Alistair Brewin. Thank you all so much, it was a pleasure sharing this experience with you.

My friends have provided a much needed distraction from physics, I thank Sam White and Henrie Hall for putting up with my complaints and for entertaining me with many (often infuriating) discussions about politics, the monarchy and so much more. Alongside physics, my time in Durham has been dominated by music – everyone at DUPO has enriched my university experience and I'm fortunate to have been surrounded by such fantastic musicians.

My family have always been my greatest champions. None of this would have been possible without their support, particularly Grandma Kath, Grandad Derek and of course my wonderful Mother, Yannina. While wandering past a levitating Malteser at a secondary school open day, my Mum pointed at it and told me, "That's physics, it's really boring!". Hopefully I haven't bored you too much talking about it in the years since. Thank you for everything.

Finally, I would like to thank Ikki Shafiq for his love and support throughout the entire process of doing my PhD and beyond. You have been amazing from day one and I do not have the words to express my gratitude for everything you do for me.

Zachary Hawkhead
London, 7 December, 2022

For Grandma Jean and Grandad Frank,
they always pushed me to be my best.

Chapter 1

Introduction

> *If I have seen further it is by standing on the shoulders of giants.*
>
> —Sir Isaac Newton

The quote that opens this chapter is perhaps one of the most succinct and accurate descriptions of physics. The work presented in this thesis, in small part, builds on over 100 years of research that started with the development of quantum mechanics. In the simplest terms, in condensed matter physics, we wish to understand the properties of materials. What causes them to behave how they do? Quantum mechanics allows us to describe materials in terms of the interactions between the electrons and nuclei which are the building blocks of everything we see around us. We must throw away the old ideas of Newton, of point particles with well defined positions and momenta, and embrace the wavefunction and wave-mechanics [1]. While brilliant, quantum mechanics loses some of the intuitive nature of classical mechanics which does not help its reputation outside of the physics community. From a practical point of view, solving quantum mechanical equations to describe realistic systems is non-trivial. Finding ways to solve quantum systems is of such importance that the 1998 Nobel prize in Chemistry was shared by Walter Kohn for his involvement in the development of density functional theory (DFT), the method of choice for quantum calculations in this thesis. We will use DFT to probe materials which display another counter-intuitive property, magnetism.

One could hand a fridge magnet to almost anyone and they would likely tell you that it sticks to metal. A smaller group of people may recognise that this fridge magnet will stick to metals which contain iron. However, for something so common, a full explanation of *how* it sticks to a fridge seems almost impossible. Even Richard Feynman could not do it justice [2]. Magnetism is a purely quantum phenomenon; Niels Bohr and Hendrika van Leeuwen independently showed in their respective theses that, using classical physics, there can be no net magnetisation in a solid [3, 4, 5]. In this thesis we will show how DFT calculations can be an invaluable tool in describing magnetism and magnetic interactions in condensed matter systems. We will also implement cutting edge methods in a DFT code which allow us to realise magnetic states which were previously unattainable in spin-density functional theory (spin-DFT).

DFT has become a front-runner amongst methods for calculating properties of materials from quantum mechanics. The Thomas-Fermi model, developed not long after Schrödinger introduced his famous equation, framed the quantum problem in terms of the electron density [6, 7, 1]. This paved the way for Hohenberg and Kohn to lay out the mathematical foundation of DFT in 1964 [8] and for Kohn and Sham to devise an efficient scheme for calculations of electronic properties in 1965 [9]. With the addition of spin-DFT [10, 11], we are now in a position to calculate the electronic properties of materials that exhibit magnetic ordering.

The term magnetism encompasses a whole range of configurations of electron spins in a material, the most simple being ferromagnetism (the fridge magnet mentioned above) and antiferromagetism. Ferromagnets have been a source of intrigue for thousands of years [12], while antiferromagnets were discovered more recently by Néel in 1948 [13]. More exotic magnetic states have been the focus of consistent research for decades, an example being the search for *spin ices* in the pyrochlores, culminating in the discovery of such a state in $Ho_2Ti_2O_7$ in 1998 [14, 15]. Spin-DFT is a common tool for studying systems displaying collinear magnetism (CM), that is ferromagnetism or antiferromagnetism where the electron spins are parallel or antiparallel [16, 17, 18]. More recently, with the improvements in computing power and new computational methods, it is becoming increasingly possible to apply spin-DFT to systems displaying non-collinear magnetism (NCM). While calculations of materials hosting NCM are not yet common, it is certainly possible to use spin-DFT to examine their properties and magnetic states. An early example of the successes of non-collinear spin-DFT is the understanding of the Invar effect in Fe-Ni alloys [19]. By calculating the magnetic moments of the ions at a range of densities, van Schilfgaarde *et al.* [19] were able to show that Fe-Ni undergoes a continuous transition to a non-collinear state. They were then able to conclude that this magnetisation is the cause of the high thermal expansion coefficient of this alloy. Despite successes, relativistic effects in the form of spin-orbit coupling (SOC) were still missing from computations of electronic structures. Known to cause a number of magnetic phenomena such as the De Haas-Van-Alphen effect and magnetic anisotropy [20], SOC was first included in calculations of band structures in the 1970s [21, 22, 23]. SOC is now a common consideration when performing calculations using non-collinear spin-DFT. Implementation of non-collinear spin-DFT in popular codes, such as CASTEP [24], FLEUR [25] and VASP [26], has allowed the wider physics community to investigate NCM in a first principles approach. Non-collinear spin-DFT is now available in many codes with a large diversity of implementations, which allows users to choose the code best suited to their objectives. With the inclusion of constrained minimisation techniques in some of the major DFT codes [27, 28], more advanced NCM structures can be realised with spin-DFT. In general these methods add a Lagrange multiplier into a Hamiltonian which acts as an energy penalty, biasing the electronic minimisation to find a state with a particular spin configuration. An example study using such constraints can be found in Ref. [29], whereby constraints are used to realise a series of NCM states around a curved crystal. From these states, the authors are able to use the total energy to extract anisotropy constants as a function of curvature. Spin-DFT has also proven useful at comparing the relative stability of NCM states and from that, calculating Dzyaloshinskii–Moriya interaction (DMI) constants [30]. Recent work by Mankovsky and Ebert [31], using a Green's function approach, applies the Liechtenstein method [32, 33] to calculate parameters which can then be used in a micromagnetic simulation [34] using the Landau–Lifshitz–Gilbert equation. Alternative methods for calculating properties of non-collinear magnets, including the spin-spiral stiffness, are based on methods for calculating the magnetic susceptibility [35]. Previous studies using this technique have yielded promising results [36, 37].

This thesis will introduce the many electron problem and motivate the need for DFT, as well as describing how DFT calculations actually work. We will use DFT and spin-DFT to investigate the properties of a range of materials that host exotic magnetic states, touching on some important themes. We will study the effects of impurities in magnetic crystals and how they contribute to the magnetic order. Also, we will investigate the underlying interactions that cause magnetism and how electronic structure impacts upon the spin structures found in a material. Finally, by leveraging cutting edge developments in the theory of DFT, we shall implement new methods for better capturing complex configurations of non-collinear spins using spin-DFT. We aim to demonstrate the current state of research in the field of DFT and how it can be used in conjunction with experimental techniques to further our understanding of magnetism in the solid state.

1.1 Layout of thesis

The layout of this thesis is as follows:

Chapter 2: We derive the Hohenberg-Kohn (HK) theorems and the Kohn-Sham (KS) scheme which forms the basis for the DFT calculations we will present in later chapters. We introduce spin and motivate the use of spin-DFT to perform calculations of magnetic properties. We finish by describing the implementation of DFT in a plane-wave code.

Chapter 3: We look at the uses of DFT for calculating properties of materials hosting magnetic skyrmions relevant to experimental physicists. We introduce the muon-spin spectroscopy (μSR) technique and discuss how DFT can be used to solve the muon-site problem by calculating where an implanted muon would stop. We report muon stopping sites in the skyrmion hosting material, Cu_2OSeO_3 calculated from DFT. We also look at the applications of spin-DFT to examine chemical substitution in the skyrmion hosts GaV_4S_8 and GaV_4Se_8. We provide an explanation for observed magnetic properties in the high substitution limit by examining the spin density around the magnetic ions.

Chapter 4: We report a pressure study of the magnetic exchange couplings in a quantum magnet, $[Cu(pyz)_{0.5}(gly)]ClO_4$. We show that it undergoes structural distortions that correspond to a change in the ratio between the main magnetic exchange constants. This change suggests that the ground state magnetic structure changes from a disordered state to one that exhibits long range magnetic order.

Chapter 5: We report a theoretical and experimental study of the electronic structure of a selection of intercalated transition-metal dichalcogenide (TMDC) materials. We examine the density of states (DoS) and band structures of $Cr_{1/3}MS_2$ (M = Nb or Ta) and find that there is a gap-like feature at the

Fermi level. We present experimental evidence for this gap and measure its size. We calculate from first principles the transport properties of $\mathrm{Cr}_{1/3}M\mathrm{S}_2$ (M = Nb or Ta) and compare to experiment finding good agreement. We also report electronic structure calculations of TMDCs intercalated with transition metals from the first period. We show that the magnetism across the series can be well described by electron band filling in the electronic shells of the transition metal intercalant.

Chapter 6: We provide an overview of method for improving the non-collinear results of the local spin-density approximation (LSDA), as well as details of how we implemented this method in CASTEP. By applying the new functional to calculations of a set of simple magnetic materials, we test the implementation and explore the effects it has on the internal magnetic fields. After demonstrating that the implementation is successful, we use it to calculate the magnetic structure of the spin-ice material, $\mathrm{Dy_2Ti_2O_7}$. Along with comparison to the LSDA, we show that the corrected functional improves the ability of a spin-DFT calculation to capture complex magnetic structures.

Chapter 7: In this chapter we conclude the thesis by summarising the main results presented throughout. Having presented our results, we place the work in context by briefly revisiting the state of the field and discuss potential avenues for further development.

Apppendix A: We provide a mathematical explanation of the process involved in finding a ground state using the variational principle. This form of energy minimisation is used in every calculation presented in this thesis to determine the ground state electronic structure.

Apppendix B: We present a derivation of the reciprocal representation of the Hartree potential used to approximate electron–electron interactions. We discuss the implications for the efficiency of a calculation by calculating the Hartree potential in reciprocal space.

Apppendix C: We provide links and documentation for useful programs developed by the author during the completion of this thesis. This includes code used to plot all band structures and Fermi surfaces presented in this thesis.

Chapter 2

Many electrons and density functional theory

> *Protons give an atom its identity, electrons its personality.*
>
> —Bill Bryson,
>
> *A Short History of Nearly Everything*

2.1 Many electron systems

In quantum mechanics, the behaviour of a collection of quantum particles can be determined from the many particle wavefunction, Ψ. With knowledge of Ψ one can extract the probability distribution of all of the particles and associated physical properties. In condensed matter, Ψ is a function of all the electrons and the nuclei that form a material. The wavefunction is the solution to the Schrödinger equation [1],

$$\begin{split} i\hbar\frac{\partial}{\partial t}\Psi(\boldsymbol{r}_1,\ldots,\boldsymbol{r}_N;\boldsymbol{R}_1,\ldots,\boldsymbol{R}_M,t) = \\ \hat{\mathcal{H}}(\boldsymbol{r}_1,\ldots,\boldsymbol{r}_N;\boldsymbol{R}_1,\ldots,\boldsymbol{R}_M)\Psi(\boldsymbol{r}_1,\ldots,\boldsymbol{r}_N;\boldsymbol{R}_1,\ldots,\boldsymbol{R}_M,t), \end{split} \tag{2.1}$$

where $\hat{\mathcal{H}}(\boldsymbol{r}_1,\ldots,\boldsymbol{r}_N;\boldsymbol{R}_1,\ldots,\boldsymbol{R}_M)$ is the many body Hamiltonian operator, and $\boldsymbol{r}$ and $\boldsymbol{R}$ are the positions of the electrons and the nuclei respectively. We note that the Schrödinger equation has no explicit spin dependence, unlike the Dirac equation [38], and has to be added in by hand. In this thesis we will consider only the time independent Schrödinger equation,

$$\hat{\mathcal{H}}(\boldsymbol{r})\Psi(\boldsymbol{r}_1,\ldots,\boldsymbol{r}_N;\boldsymbol{R}_1,\ldots,\boldsymbol{R}_M) = E\Psi(\boldsymbol{r}_1,\ldots,\boldsymbol{r}_N;\boldsymbol{R}_1,\ldots,\boldsymbol{R}_M), \tag{2.2}$$

where E is the total ground state energy. Throughout this thesis the atomic unit system will be used, unless otherwise required for clarity, whereby the electron charge, e, reduced Planck's constant, $\hbar$, Bohr atomic radius, a_0, and the electron mass, m_e, are equal to one.

The Hamiltonian consists of a kinetic energy operator and a potential energy operator,

$$\hat{\mathcal{H}} = \hat{T} + \hat{V}, \tag{2.3}$$

$$\hat{T} = -\frac{1}{2}\sum_{N,M}\{\boldsymbol{\nabla}_N^2 + \boldsymbol{\nabla}_M^2\}, \tag{2.4}$$

where $\boldsymbol{\nabla}^2_{N,M}$ is the Laplacian operator for electrons and nuclei respectively. Without considering additional external potentials, the potential energy operator is given by:

$$\hat{V} = \sum_{i,I}\frac{Z_I}{|\boldsymbol{r}_i - \boldsymbol{R}_I|} + \frac{1}{2}\sum_{i,j,i\neq j}\frac{1}{|\boldsymbol{r}_i - \boldsymbol{r}_j|} + \frac{1}{2}\sum_{I,J,I\neq J}\frac{Z_I Z_J}{|\boldsymbol{R}_I - \boldsymbol{R}_J|}, \tag{2.5}$$

where $\boldsymbol{r}$ and $\boldsymbol{R}$ are the positions of the electrons and nuclei. The three terms in Eq. 2.5 are the electron-nuclear interaction, the electron-electron interaction and the nuclear-nuclear interaction respectively, and Z_I is the nuclear charge of the I^{th} nucleus. The indexing of the two sums is such that it avoids self interaction and the factors of a half fix the double counting of electron-electron and nuclear-nuclear interactions.

2.1.1 Born-Oppenheimer approximation

In Eq. 2.2 the Schrödinger equation is impossible to solve exactly for any system of interest to condensed matter due to the large number of electrons ($\sim 10^{24}$), and the interactions between them. Over the previous century many approximations and reformulations have been taken to make this problem more tractable. The Born-Oppenheimer (BO) approximation [39] is one such way of simplifying the Schrödinger equation. We note that the difference in mass scales of electrons and nuclei is significant ($m_{\mathrm{p}} \approx 1800 m_{\mathrm{e}}$), and therefore the motion of each responds on different timescales. The electrons respond quickly to any nuclear motion and will remain in their instantaneous ground state.

Using the BO approximation one can then separate the electronic and nuclear wavefunctions into product states,

$$\Psi(\boldsymbol{r}_1, \ldots, \boldsymbol{r}_N; \boldsymbol{R}_1, \ldots, \boldsymbol{R}_M) = \Psi^{\mathrm{elec}}_{\boldsymbol{R}_1, \ldots, \boldsymbol{R}_M}(\boldsymbol{r}_1, \ldots, \boldsymbol{r}_N)\chi(\boldsymbol{R}_1, \ldots, \boldsymbol{R}_M), \tag{2.6}$$

where χ is the nuclear part of the wavefunction and the nuclear positions are treated as parameters of the electronic state. The electronic Hamiltonian is then,

$$\hat{\mathcal{H}}_{\mathrm{elec}} = \hat{T}_{\mathrm{elec}} + \hat{V}_e = -\frac{1}{2}\sum_i \boldsymbol{\nabla}_i^2 + \sum_{i,I} \frac{Z_I}{|\boldsymbol{r}_i - \boldsymbol{R}_I|} + \frac{1}{2}\sum_{i,j,i \neq j} \frac{1}{|\boldsymbol{r}_i - \boldsymbol{r}_j|}. \tag{2.7}$$

The BO approximation is valid for a wide range of condensed matter systems, however it has limitations such as when considering nuclear motion in metals or small band-gap semiconductors. For instance, it may be inappropriate in the discussion of electron-phonon couplings in superconducting materials [40]. In this thesis it is reasonable to assume that the BO approximation is valid for the systems considered.

2.2 Density functional theory

As stated above, the Schrödinger equation is impossible to solve exactly for any condensed matter system, which has meant that research into approximate methods has been of continued interest over the past 100 years. Density functional theory (DFT) has emerged as one of the favourite methods for condensed matter physicists to calculate properties of a wide range of solid state materials from first principles [41]. While DFT is often less accurate than other methods such as coupled cluster theory [42], its speed allows one to compute systems with many hundreds of electrons with relative ease. Rather than approximating the wavefunction like many other approaches such as Hartree-Fock theory [43] and coupled cluster theory [42], DFT seeks to find approximations to the electronic density. Once the density is found, observables can be obtained in much the same way as from the wavefunction, with the added benefit that the density is much simpler than the wavefunction, as discussed below.

It is worth exploring briefly the scale of the gain which is achieved by centring our computation around the density, which is given by:

$$n(\boldsymbol{r}) = N \int \mathrm{d}\boldsymbol{r}_2 \ldots \int \mathrm{d}\boldsymbol{r}_N \Psi^*(\boldsymbol{r}_1, \ldots, \boldsymbol{r}_N)\Psi(\boldsymbol{r}_1, \ldots, \boldsymbol{r}_N), \tag{2.8}$$

where $n(\boldsymbol{r})$ is the electronic density, the parametric dependence of the wavefunction on nuclear positions has been omitted for clarity. We see that the density has many fewer degrees of freedom (DoF) than the many particle wavefunction with three DoF compared to $3N$ DoF for the wavefunction; this reduction in dimensionality means that it is easier to store than the wavefunction and allows for DFT to handle much larger systems than any wavefunction approach. To estimate the real world benefit, consider a wavefunction and density stored on a very coarse $10 \times 10 \times 10$ grid, we can then estimate the storage requirements of each. For only four electrons, the density would require approximately 10 kB of storage. Whereas the wavefunction, for the same very small system, would require 10 TB of storage; one would only have to consider seven electrons before we exceeded the total storage capacity currently on Earth.

This section will show that it is indeed possible to simplify the many electron problem by using the electronic density, and introduce the Kohn-Sham (KS) formalism which is the basis of all the calculations presented in this thesis.

2.2.1 Hohenberg-Kohn theorems

Having motivated the use of the electronic density in calculations of quantum properties, the Hohenberg-Kohn (HK) theorems provide a sound theoretical basis for making such a change. Hohenberg and Kohn demonstrated that the density is sufficient to describe a system of electrons through two theorems [8]. The first Hohenberg-Kohn theorem (HK I) shows that there is a one-to-one mapping between the external potential and the density; since the potential defines the Hamiltonian, the external potential also uniquely defines the wavefunction. Since the density is uniquely defined and equivalent to the wavefunction, it is sufficient to describe the groundstate properties of the system. We use this density to describe properties of a system. The language of DFT is that of *functionals*, that is a mapping of a function onto a number, in a similar way that a *function* is a mapping of one number onto another. A common example from DFT is an energy functional, $E[n(\boldsymbol{r})]$, which maps the density, $n(\boldsymbol{r})$ onto an energy. The second Hohenberg-Kohn theorem (HK II) shows that the groundstate density is such that it minimises the HK energy functional and can be obtained variationally. The proof of the first theorem is in two parts.

HK I.1 *Two potentials differing by more than a constant yield different wave-functions.*

Proof. We present a proof using *reductio ad absurdum.* Consider two potentials $\hat{V}_1$ and $\hat{V}_2$ which differ by more than a constant such as the electron-nuclear potential from two different materials; both potentials lead to the same wavefunction Ψ. For simplicity, we assume without loss of generality that $\Psi = \Psi(\boldsymbol{r})$ is a single particle wavefunction. The ground state energy of each potential is given by

$$(\hat{T} + \hat{V}_1)\Psi(\boldsymbol{r}) = E_1\Psi(\boldsymbol{r}), \tag{2.9}$$

$$(\hat{T} + \hat{V}_2)\Psi(\boldsymbol{r}) = E_2\Psi(\boldsymbol{r}). \tag{2.10}$$

Taking the difference of Eq. 2.9 and Eq. 2.10 leads to

$$(\hat{V}_1 - \hat{V}_2)\Psi(\boldsymbol{r}) = (E_1 - E_2)\Psi(\boldsymbol{r}), \tag{2.11}$$

and since the potentials $\hat{V}_1$ and $\hat{V}_2$ are multiplicative operators, and assuming that $\Psi(\boldsymbol{r}) \neq 0$,

$$\hat{V}_1 - \hat{V}_2 = E_1 - E_2 = \text{const.} \tag{2.12}$$

Therefore one finds a contradiction as the difference of the potentials is simply the difference of their energies, which is a constant. This proves that two different potentials must lead to different wavefunctions.

HK I.2 *Two different groundstate wavefunctions lead to two different densities.*

Proof. As above we employ *reductio ad absurdum* to show that the wavefunction uniquely defines the density. Consider two wavefunctions Ψ_1 and Ψ_2 which are necessarily related to two unique potentials, $\hat{V}_1$ and $\hat{V}_2$. From the variational principle,

$$E_1 = \langle\Psi_1|\,\hat{\mathcal{H}}_1\,|\Psi_1\rangle < \langle\Psi_2|\,\hat{\mathcal{H}}_1\,|\Psi_2\rangle\,, \tag{2.13}$$

and

$$E_2 = \langle\Psi_2|\,\hat{\mathcal{H}}_2\,|\Psi_2\rangle < \langle\Psi_1|\,\hat{\mathcal{H}}_2\,|\Psi_1\rangle\,. \tag{2.14}$$

Adding Eq. 2.14 to Eq. 2.13,

$$\langle\Psi_1|\,\hat{\mathcal{H}}_1\,|\Psi_1\rangle + \langle\Psi_2|\,\hat{\mathcal{H}}_2\,|\Psi_2\rangle < \langle\Psi_2|\,\hat{\mathcal{H}}_1\,|\Psi_2\rangle + \langle\Psi_1|\,\hat{\mathcal{H}}_2\,|\Psi_1\rangle\,, \tag{2.15}$$

$$\begin{aligned}&\left\langle \Psi_1(\boldsymbol{r}) \middle| -\frac{1}{2}\nabla^2 + V_1(\boldsymbol{r}) \middle| \Psi_1(\boldsymbol{r}) \right\rangle + \left\langle \Psi_2(\boldsymbol{r}) \middle| -\frac{1}{2}\nabla^2 + V_2(\boldsymbol{r}) \middle| \Psi_2(\boldsymbol{r}) \right\rangle \\ < &\left\langle \Psi_2(\boldsymbol{r}) \middle| -\frac{1}{2}\nabla^2 + V_1(\boldsymbol{r}) \middle| \Psi_2(\boldsymbol{r}) \right\rangle + \left\langle \Psi_1(\boldsymbol{r}) \middle| -\frac{1}{2}\nabla^2 + V_2(\boldsymbol{r}) \middle| \Psi_1(\boldsymbol{r}) \right\rangle,\end{aligned} \tag{2.16}$$

cancelling kinetic energy terms and switching to integral notation,

$$\begin{aligned}&\int \mathrm{d}\boldsymbol{r} \Big\{ \Psi_1^*(\boldsymbol{r}) V_1(\boldsymbol{r}) \Psi_1(\boldsymbol{r}) + \Psi_2^*(\boldsymbol{r}) V_2(\boldsymbol{r}) \Psi_2(\boldsymbol{r}) \Big\} \\ < &\int \mathrm{d}\boldsymbol{r} \Big\{ \Psi_2^*(\boldsymbol{r}) V_1(\boldsymbol{r}) \Psi_2(\boldsymbol{r}) + \Psi_1^*(\boldsymbol{r}) V_2(\boldsymbol{r}) \Psi_1(\boldsymbol{r}) \Big\},\end{aligned} \tag{2.17}$$

using that for a single particle wavefunction, $\Psi_i^*(\boldsymbol{r})\Psi_i(\boldsymbol{r}) = n_i(\boldsymbol{r})$, and that potentials commute with the wavefunction,

$$\begin{aligned}&\int \mathrm{d}\boldsymbol{r} \Big\{ V_1(\boldsymbol{r}) n_1(\boldsymbol{r}) + V_2(\boldsymbol{r}) n_2(\boldsymbol{r}) \Big\} \\ < &\int \mathrm{d}\boldsymbol{r} \Big\{ V_1(\boldsymbol{r}) n_2(\boldsymbol{r}) + V_2(\boldsymbol{r}) n_1(\boldsymbol{r}) \Big\},\end{aligned} \tag{2.18}$$

finally we arrive at,

$$\int \mathrm{d}\boldsymbol{r}\ [V_1(\boldsymbol{r}) - V_2(\boldsymbol{r})][n_1(\boldsymbol{r}) - n_2(\boldsymbol{r})] < 0. \tag{2.19}$$

If we assume that two potentials can correspond to the same density, *i.e.* $n_1 = n_2$, Eq. 2.19 is a contradiction. Therefore the proof is complete.

Having shown that the electron density is sufficient to describe a system of electrons, we now need a way to guarantee that a density is the groundstate solution for an ensemble of electrons. It is possible to describe the energy as a functional of the density,

$$E[n] = \int \mathrm{d}\boldsymbol{r}\ n(\boldsymbol{r}) V_{\mathrm{en}} + F_{\mathrm{HK}}[n(\boldsymbol{r})], \tag{2.20}$$

with

$$F_{\mathrm{HK}}[n] = T[n] + E_{\mathrm{ee}}[n(\boldsymbol{r})]. \tag{2.21}$$

The universal functional, F_{HK}, comprises the kinetic energy functional and the electron-electron interaction. There is not an exact form of this functional. However, F_{HK} is equivalent to the full electronic Schrödinger equation as we have made no approximation. The key point to note about Eq. 2.21 is that there is no dependence on the wavefunction and it provides a way of extracting the total energy of a system directly from the density.

HK II solves the problem of finding the ground state density given the universal functional. Consider a trial density $\tilde{n}$ with associated wavefunction $\tilde{\Psi}$,

$$\langle\tilde{\Psi}|\,\hat{\mathcal{H}}\,|\tilde{\Psi}\rangle = E[\tilde{n}] \tag{2.22}$$

and

$$\langle\Psi_0|\,\hat{\mathcal{H}}\,|\Psi_0\rangle = E[n_0], \tag{2.23}$$

where n_0 and Ψ_0 respectively are the groundstate density and wavefunction of $\hat{\mathcal{H}}$. From the variational principle we get the condition that,

$$E[n_0] < E[\tilde{n}], \tag{2.24}$$

thus proving that the groundstate density can be determined uniquely by varying the density and finding the energy minimum.

2.2.2 Kohn-Sham formalism

The HK theorems are an important step towards being able to solve systems of electrons *ab initio*, however it does not solve the fundamental problem of interacting electrons. KS theory reimagines the system of *interacting* electrons as an auxiliary system of *non-interacting* electrons. Crucially this auxiliary system has the same density as the fully-interacting electrons [9]. Kohn and Sham solved two problems. First, the problem of interacting electrons. Secondly, eradicating the need for complex approximations to the kinetic energy functional. The wavefuntion in a KS picture is described by a Slater determinant [44] constructed of KS orbitals, Φ. The significance of the KS orbitals is not a simple matter and much discussion has been had in the literature [45, 46, 47]. How-

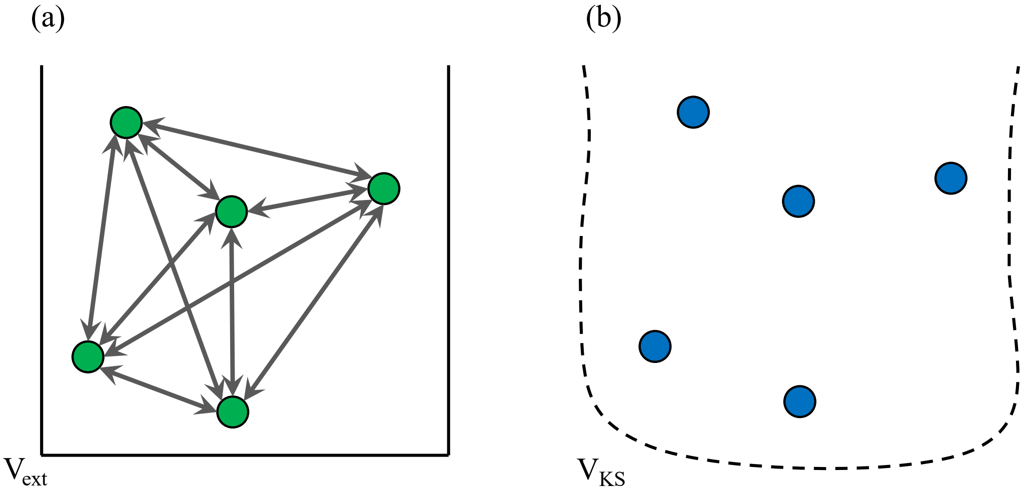

Figure 2.1: Schematic of the KS formalism, (a) shows a system of electrons (green) and their interaction sitting in an external potential, V_{ext}. (b) shows the KS system with non-interacting electrons (blue) sitting in a KS effective potential. The effective potential includes all of the effects of the external potential and the electron-electron interactions. In principle the KS system is exact. However, in practice approximations are made in constructing the KS potential.

ever, the interpretation taken in this thesis is that each KS orbital represents a non-interaction electron state.

From the Slater determinant description of the wavefunction, the density is given by

$$n(\boldsymbol{r}) = \sum_i f_i |\phi_i(\boldsymbol{r})|^2, \tag{2.25}$$

where ϕ_i is the i^{th} orbital of Φ, equivalent to a single particle wavefunction and f_i is the occupancy of ϕ_i, and is a number in the range 0 to 1. The kinetic energy functional for the KS system in terms of the orbitals is approximated by,

$$T_{\text{s}}[n(\boldsymbol{r})] = -\frac{1}{2}\sum_i f_i \int \mathrm{d}\boldsymbol{r}\ \phi_i^*(\boldsymbol{r})\boldsymbol{\nabla}^2\phi_i(\boldsymbol{r}), \tag{2.26}$$

whereby the single-particle kinetic energy functional, $T_{\text{s}}[n(\boldsymbol{r})]$, is given by a sum over orbitals of the non-interacting single-particle kinetic energy. The electron-nuclear energy is defined by,

$$E_{\text{en}}[n(\boldsymbol{r})] = \int \mathrm{d}\boldsymbol{r}\ n(\boldsymbol{r})V_{\text{en}}(\boldsymbol{r}), \tag{2.27}$$

and the electron-electron interaction energy is approximated by the Hartree energy,

$$E_{\text{H}}[n(\boldsymbol{r})] = \frac{1}{2}\int \mathrm{d}\boldsymbol{r}\int \mathrm{d}\boldsymbol{r}'\ \frac{n(\boldsymbol{r})n(\boldsymbol{r}')}{|\boldsymbol{r}-\boldsymbol{r}'|}. \tag{2.28}$$

So far we have not considered the indistinguishability of electrons. The electron wavefunction must be anti-symmetric under exchange as they are Fermions [$\psi(\boldsymbol{r}_1, \boldsymbol{r}_2) = -\psi(\boldsymbol{r}_2, \boldsymbol{r}_1)$]. Also, electrons are correlated, meaning that changes in the electron density in one part of space are dependent on the electron density in a separate part of space. In the context of DFT, correlation is defined as all of the effects not captured thus far in the total energy functional. The remaining effects are encompassed in the exchange and correlation (xc) functional,

$$E_{\text{xc}}[n(\boldsymbol{r})] = T[n(\boldsymbol{r})] - T_{\text{s}}[n(\boldsymbol{r})] + E_{\text{ee}}[n(\boldsymbol{r})] - E_{\text{H}}[n(\boldsymbol{r})], \tag{2.29}$$

where $T[n(\boldsymbol{r})]$ and $E_{\text{ee}}[n(\boldsymbol{r})]$ are as defined in the universal functional (Eq. 2.21).

Given these definitions, the KS functional is expressed,

$$\begin{aligned} E_{\text{KS}}[n(\boldsymbol{r})] = &-\frac{1}{2}\sum_i f_i \int \mathrm{d}\boldsymbol{r}\ \phi_i^*(\boldsymbol{r})\boldsymbol{\nabla}^2\phi_i(\boldsymbol{r}) + \frac{1}{2}\int \mathrm{d}\boldsymbol{r}\int \mathrm{d}\boldsymbol{r}'\ \frac{n(\boldsymbol{r})n(\boldsymbol{r}')}{|\boldsymbol{r}-\boldsymbol{r}'|} \\ &+ \int \mathrm{d}\boldsymbol{r}\ [n(\boldsymbol{r})V_{\text{en}}(\boldsymbol{r})] + E_{\text{xc}}[n(\boldsymbol{r})]. \end{aligned} \tag{2.30}$$

By including the xc term (Eq. 2.29) in Eq. 2.30 we can see that the KS formulation of DFT is exactly equivalent to the universal HK functional (Eq. 2.21). A consequence of this is that the exact xc functional, if it were known, would be as difficult to solve as the fully interaction Schrödinger equation as one must reintroduce the full electron-electron interactions. Many approximations exist for the xc functional, some of which are discussed in Sec. 2.4.

From the definitions presented above one can construct the KS potential which bounds our fictitious system of non-interacting electrons,

$$V_{\mathrm{KS}}(\boldsymbol{r}) = V_{\mathrm{en}}(\boldsymbol{r}) + \int \mathrm{d}\boldsymbol{r}' \, \frac{n(\boldsymbol{r}')}{|\boldsymbol{r} - \boldsymbol{r}'|} + \frac{\delta E_{\mathrm{xc}}[n(\boldsymbol{r})]}{\delta n(\boldsymbol{r})}. \tag{2.31}$$

The final term in Eq. 2.31 describes a *functional derivative*, much the same as the derivative of a function, it outputs the change in a functional with respect to some change in a function. Having derived the KS potential we arrive at the KS equations which allows for computation of all groundstate properties,

$$\left\{ -\frac{1}{2}\boldsymbol{\nabla}^2 + V_{\mathrm{KS}}(\boldsymbol{r}) \right\} \phi_i(\boldsymbol{r}) = \epsilon_i \phi_i(\boldsymbol{r}). \tag{2.32}$$

The KS equations are a set of N coupled single-particle Schrödinger equations in an effective KS potential. This reduction of complexity means that it is now possible to obtain a solution. The solution must be obtained self-consistently by improving the set of orbitals iteratively until the input orbitals are equal to the resulting orbitals [48]. Details of numerical implementations are discussed in Sec. 2.5.

2.2.3 Total energy from Kohn-Sham orbitals

The KS energy functional given in Eq. 2.30 is only one way of calculating the total energy of a system. It is often preferable to calculate the total energy using the eigenenergies of the KS orbitals. We can write the KS functional in terms of the constituent functionals,

$$E_{\mathrm{KS}} = T_{\mathrm{s}}[n(\boldsymbol{r})] + E_{\mathrm{en}}[n(\boldsymbol{r})] + E_{\mathrm{H}}[n(\boldsymbol{r})] + E_{\mathrm{xc}}[n(\boldsymbol{r})]. \tag{2.33}$$

Given the groundstate orbitals, ϕ_i, we can construct the energy of a single orbital,

$$\epsilon_i = \langle \phi_i | \, \hat{T}_{\mathrm{s}} + \hat{V}_{\mathrm{en}} + \hat{V}_{\mathrm{H}} + \hat{V}_{\mathrm{xc}} \, | \phi_i \rangle \, . \tag{2.34}$$

If we now define a new energy, $\tilde{E}$, which is the energy of the orbitals,

$$\begin{aligned}\tilde{E}[n(\boldsymbol{r})] &= \sum_i f_i \epsilon_i, \\ &= \sum_i [f_i \langle \phi_i | \hat{T}_\mathrm{s} | \phi_i \rangle] + \int \mathrm{d}\boldsymbol{r}\ [V_\mathrm{en}(\boldsymbol{r})n(\boldsymbol{r}) + V_\mathrm{H}(\boldsymbol{r})n(\boldsymbol{r}) + V_\mathrm{xc}(\boldsymbol{r})n(\boldsymbol{r})],\end{aligned} \tag{2.35}$$

where f_i is the occupancy of each orbital, we can redefine the total energy,

$$E_\mathrm{KS} = \tilde{E}[n(\boldsymbol{r})] + E_\mathrm{H}[n(\boldsymbol{r})] + E_\mathrm{xc}[n(\boldsymbol{r})] - \int \mathrm{d}\boldsymbol{r}\ [V_\mathrm{H}(\boldsymbol{r})n(\boldsymbol{r}) + V_\mathrm{xc}(\boldsymbol{r})n(\boldsymbol{r})]. \tag{2.36}$$

The main benefit of reformulating the total energy in this way is that the Laplacian terms relating to the kinetic energy are contained inside $\tilde{E}$, and therefore do not need to be recomputed.

2.3 Spin-density functional theory

DFT as discussed in Sec. 2.2 is only concerned with the locations of the electrons through the electron density. We have made no reference to the fact that electrons carry angular momentum, both orbital and spin. Spin-density functional theory (spin-DFT) [10, 11] is a logical extension to DFT which introduces electron interactions with static magnetic fields. (The magnetic fields are included in the Hamiltonian as a Zeeman-like term, and therefore is applicable to fields which interact with electron spins only rather than orbital momentum.)

Spin-DFT was developed with the intention of calculating the effects of external magnetic fields on the electronic structure, although many spin-DFT calculations are performed on materials in zero-field. While, in principle, DFT is able to handle open-shell systems (systems with unpaired electrons), spin-DFT is often the default choice when dealing with such systems. Spin-DFT is able to handle such things as spontaneous magnetisation arising in ferromagnetic materials, as it allows for the number of spin-up and spin-down electrons to differ by more than one.

There are two types of systems we can treat with spin-DFT: systems displaying collinear magnetism (CM), where spins are constrained to be parallel or antiparallel, and systems with non-collinear magnetism (NCM), where no such constraint is applied. NCM has been of particular interest in the last few decades, for example, the prediction and later discovery of magnetic skyrmions [49, 50, 51].

2.3.1 Collinear spin-density functional theory

We will start by defining some terms. As well as the electron charge density, spin-DFT is also concerned with the spin density. In a CM treatment the spins are treated as either spin up or spin down, typically aligned in the z direction, although this choice is arbitrary. We can define a density associated with each of the spin-up and spin-down electrons, $n^{\uparrow}(\boldsymbol{r})$, $n^{\downarrow}(\boldsymbol{r})$, and the relation to the total density,

$$n(\boldsymbol{r}) = n^{\uparrow}(\boldsymbol{r}) + n^{\downarrow}(\boldsymbol{r}). \tag{2.37}$$

The total number of electrons in the system is fixed, although the number of spin-up and spin-down electrons is free to vary. We can also define the overall spin density,

$$s(\boldsymbol{r}) = n^{\uparrow}(\boldsymbol{r}) - n^{\downarrow}(\boldsymbol{r}). \tag{2.38}$$

By convention the magnetisation density is given by,

$$m_z(\boldsymbol{r}) = -\mu_{\mathrm{B}} s(\boldsymbol{r}), \tag{2.39}$$

where μ_{B} is the Bohr magneton [52].

Since we now include spin, each of the KS orbitals and the KS energy functional (Eq. 2.30) gain a spin dependence. The KS orbitals become,

$$\phi_i(\boldsymbol{r}) \rightarrow \phi_i^{\sigma}(\boldsymbol{r}),\ \ \sigma = \uparrow, \downarrow \tag{2.40}$$

and the KS functional becomes,

$$\begin{aligned} E_{\mathrm{KS}}[n(\boldsymbol{r})] &\rightarrow E_{\mathrm{KS}}[n^{\uparrow}(\boldsymbol{r}), n^{\downarrow}(\boldsymbol{r})] \\ &= -\frac{1}{2}\sum_{i} f_i \sum_{\sigma=\uparrow,\downarrow} \int \mathrm{d}\boldsymbol{r}\ \phi_i^{\sigma *}(\boldsymbol{r}) \boldsymbol{\nabla}^2 \phi_i^{\sigma}(\boldsymbol{r}) \\ &+\frac{1}{2}\int \mathrm{d}\boldsymbol{r} \int \mathrm{d}\boldsymbol{r}'\ \frac{n(\boldsymbol{r})n(\boldsymbol{r}')}{|\boldsymbol{r}-\boldsymbol{r}'|} + \int \mathrm{d}\boldsymbol{r}\ n(\boldsymbol{r}) V_{\mathrm{ext}}(\boldsymbol{r}) + E_{\mathrm{xc}}[n^{\uparrow}, n^{\downarrow}], \end{aligned} \tag{2.41}$$

where the xc functional depends explicitly on the spin-up and spin-down densities, and the kinetic energy now includes a sum over spin for the spin dependent KS orbitals. The electron-nuclear potential has been replaced by two more general external potentials,

$$\begin{aligned} V_{\mathrm{ext}}^{\uparrow}(\boldsymbol{r}) &= V_{\mathrm{en}}(\boldsymbol{r}) + \mu_{\mathrm{B}} B_z(\boldsymbol{r}) \\ V_{\mathrm{ext}}^{\downarrow}(\boldsymbol{r}) &= V_{\mathrm{en}}(\boldsymbol{r}) - \mu_{\mathrm{B}} B_z(\boldsymbol{r}), \end{aligned} \tag{2.42}$$

where $B_z(\boldsymbol{r})$ is an external magnetic field in the z direction. In atomic units, $\mu_{\mathrm{B}} = 1/2$, however for clarity we will use the symbol rather than the numerical value. The magnetic field acts differently on the spin-up and the spin-down electrons leading to a different expression for each.

We arrive now at a new set of KS equations taking into account spin,

$$\left\{ -\frac{1}{2}\nabla^2 + V_{\mathrm{H}} + V_{\mathrm{ext}} + \frac{\delta E_{\mathrm{xc}}[n^{\uparrow}, n^{\downarrow}]}{\delta n^{\sigma}(\boldsymbol{r})} \right\} \phi_i^{\sigma}(\boldsymbol{r}) = \epsilon_i^{\sigma} \phi_i^{\sigma}(\boldsymbol{r}). \tag{2.43}$$

These equations are known as the *spin-unrestricted* KS equations [52]. While the Hartree and external potentials depend only on the total electronic density, the xc potential depends explicitly on the spin densities. Any xc functionals must be constructed to account for both densities. Equations 2.43 must be solved self-consistently in the same way as the non-spin or *spin-restricted* KS equations. There is an added complication in the solving of the unrestricted equations in that the total number of each spin-up and spin-down electrons is not fixed. This means that when calculating occupancies one must also vary the number of electrons in each spin channel to find the minimum in energy.

One common consequence of this is that a calculation will often not find the global minimum in energy if multiple possible magnetic states can exist in the material. An example of such an effect can be found in Fe which may be either non-magnetic, ferromagnetic or antiferromagnetic [53, 54]. Which state is realised will depend on the initialization of the trial orbitals.

2.3.2 Non-collinear spin-density functional theory

In the case of non-collinear spin-DFT there is no longer a restriction on the spin being aligned with a particular axis. At every point in space the electron spin is able to point in any local spin direction. The treatment of NCM is more complicated than CM as the KS orbitals now becomes two-component spinors,

$$\phi_i(\boldsymbol{r}) = \begin{pmatrix} \varphi_i^{\uparrow}(\boldsymbol{r}) \\ \varphi_i^{\downarrow}(\boldsymbol{r}) \end{pmatrix} . \tag{2.44}$$

We can define a density matrix that is generated from the spinor-wavefunction,

$$\begin{aligned} \hat{n}(\boldsymbol{r}) &= \sum_i f_i \left|\phi_i(\boldsymbol{r})\right\rangle \left\langle\phi_i(\boldsymbol{r})\right| \\ &= \sum_i f_i \left(\varphi_i^{\uparrow *}(\boldsymbol{r}), \varphi_i^{\downarrow *}(\boldsymbol{r})\right) \begin{pmatrix} \varphi_i^{\uparrow}(\boldsymbol{r}) \\ \varphi_i^{\downarrow}(\boldsymbol{r}) \end{pmatrix} = \begin{pmatrix} n_{\uparrow\uparrow}(\boldsymbol{r}) & n_{\uparrow\downarrow}(\boldsymbol{r}) \\ n_{\downarrow\uparrow}(\boldsymbol{r}) & n_{\downarrow\downarrow}(\boldsymbol{r}). \end{pmatrix} \end{aligned} \tag{2.45}$$

It is more useful to describe the non-collinear density in terms of the charge density and the spin density/magnetisation [55],

$$\begin{aligned} \hat{n}(\boldsymbol{r}) &= \frac{1}{2}\big(n(\boldsymbol{r})\mathrm{I}_{2\times 2} + \boldsymbol{\sigma}\cdot\boldsymbol{s}(\boldsymbol{r})\big) \\ &= \frac{1}{2}\left(n(\boldsymbol{r})\mathrm{I}_{2\times 2} - \frac{1}{\mu_{\mathrm{B}}}\boldsymbol{\sigma}\cdot\boldsymbol{m}(\boldsymbol{r})\right), \end{aligned} \tag{2.46}$$

where $\boldsymbol{s}(\boldsymbol{r})$ is the vector spin density, $\boldsymbol{m}(\boldsymbol{r})$ is the vector magnetisation density, $\mathrm{I}_{2\times 2}$ is the identity matrix and $\boldsymbol{\sigma}$ is the vector of Pauli spin matrices given by [5],

$$\sigma_x = \begin{pmatrix} 0 & 1 \\ 1 & 0 \end{pmatrix}, \ \sigma_y = \begin{pmatrix} 0 & -\mathrm{i} \\ \mathrm{i} & 0 \end{pmatrix}, \ \sigma_x = \begin{pmatrix} 1 & 0 \\ 0 & -1 \end{pmatrix}. \tag{2.47}$$

As the eigenvalues of the density matrix represent observable properties it is necessarily Hermitian, therefore $n_{\uparrow\downarrow} = n^{*}_{\downarrow\uparrow}$.

There are also a number of ways of expressing a non-collinear potential. In matrix form we have a spin potential given by,

$$\hat{\mathcal{V}}(\boldsymbol{r}) = \begin{pmatrix} V_{\uparrow\uparrow}(\boldsymbol{r}) & V_{\uparrow\downarrow}(\boldsymbol{r}) \\ V_{\downarrow\uparrow}(\boldsymbol{r}) & V_{\downarrow\downarrow}(\boldsymbol{r}) \end{pmatrix}. \tag{2.48}$$

This matrix is also Hermitian. Using this new matrix form for the spin potential, we can express the Hartree and electron-nuclear terms,

$$\hat{\mathcal{V}}_{\mathrm{H}}(\boldsymbol{r}) = \frac{1}{2}\begin{pmatrix} V_{\mathrm{H}}(\boldsymbol{r}) & 0 \\ 0 & V_{\mathrm{H}}(\boldsymbol{r}) \end{pmatrix}, \tag{2.49}$$

$$\hat{\mathcal{V}}_{\mathrm{en}}(\boldsymbol{r}) = \frac{1}{2}\begin{pmatrix} V_{\mathrm{en}}(\boldsymbol{r}) & 0 \\ 0 & V_{\mathrm{en}}(\boldsymbol{r}) \end{pmatrix}. \tag{2.50}$$

Note that the spin potentials in Eq. 2.49 and Eq. 2.50 are diagonal in spin space as there is no spin dependence on either potential.

We can also give spin potentials in terms of the contributions from a scalar potential $V(\boldsymbol{r})$ and a vector magnetic field $\boldsymbol{B}(\boldsymbol{r})$ [55],

$$\hat{\mathcal{V}}(\boldsymbol{r}) = V(\boldsymbol{r})\mathrm{I}_{2\times 2} + \mu_{\mathrm{B}}\boldsymbol{\sigma}\cdot\boldsymbol{B}(\boldsymbol{r}). \tag{2.51}$$

If we constrain the $\boldsymbol{B}$-field to be along the z-axis, and take the trace of $\hat{\mathcal{V}}(\boldsymbol{r})$ then we recover the expression for a collinear potential in Eq. 2.42.

When we consider xc in non-collinear spin-DFT it becomes more complicated. At present there are no widely used xc-functionals specifically designed for NCM [56]. Therefore we must make use of spin-dependent xc-functionals designed for the collinear case. As these functionals are functionals of the spin-up and spin-down densities, we perform a local rotation of the NCM density (Eq. 2.45) in spin space such that the density is locally collinear (diagonal) [11, 55],

$$\hat{n}(\boldsymbol{r}) \Rightarrow \begin{pmatrix} \tilde{n}_{\uparrow\uparrow}(\boldsymbol{r}) & 0 \\ 0 & \tilde{n}_{\downarrow\downarrow}(\boldsymbol{r}) \end{pmatrix}. \tag{2.52}$$

After this local rotation we are then able to calculate the xc-energy from the standard collinear functionals,

$$E_{\mathrm{xc}} = E_{\mathrm{xc}}[\tilde{n}_{\uparrow\uparrow}, \tilde{n}_{\downarrow\downarrow}]. \tag{2.53}$$

From the collinear xc-energy we can calculate the matrix elements of the locally collinear spin potential as in Eq. 2.43,

$$\tilde{\mathcal{V}}_{\mathrm{xc}}(\boldsymbol{r}) = \begin{pmatrix} V_{\mathrm{xc}}^{\uparrow\uparrow}(\boldsymbol{r}) & 0 \\ 0 & V_{\mathrm{xc}}^{\downarrow\downarrow}(\boldsymbol{r}), \end{pmatrix} \tag{2.54}$$

where the matrix elements are given by,

$$\tilde{V}_{\mathrm{xc}}^{\tau}(\boldsymbol{r}) = \frac{\delta E_{\mathrm{xc}}[\tilde{n}_{\uparrow\uparrow}, \tilde{n}_{\downarrow\downarrow}]}{\delta \tilde{n}_{\tau}(\boldsymbol{r})}, \ \tau = \uparrow\uparrow, \downarrow\downarrow . \tag{2.55}$$

Both $\tilde{n}$ and $\tilde{\mathcal{V}}_{\mathrm{xc}}$ must be transformed back into the locally unrotated frame by performing the inverse transform of Eq. 2.52. It is not possible in general to perform a global transformation, therefore it must be performed piece-wise at each point in space.

A consequence of the potentials being 2×2 matrices is that the total energy for a non-collinear state is calculated in a different manner than the non-spin-polarised case (Eq. 2.36),

$$
\begin{aligned}
E_{\mathrm{KS}} = \sum_i f_i \epsilon_i + E_{\mathrm{H}}[n(\boldsymbol{r})] + E_{\mathrm{xc}}[\tilde{n}] \\
- \int \mathrm{d}\boldsymbol{r}\ [\mathrm{Tr}\{\mathcal{V}_{\mathrm{H}}(\boldsymbol{r})\} n(\boldsymbol{r}) + \mathrm{Tr}\{\mathcal{V}_{\mathrm{xc}}(\boldsymbol{r})\} n(\boldsymbol{r})].
\end{aligned}
\tag{2.56}
$$

Strictly it is not necessary to perform the rotation of $\mathcal{V}_{\mathrm{xc}}$ if one is only using it to calculate the total energy since the trace is invariant with respect to the choice of basis [57].

2.3.3 Hohenberg-Kohn theorems including spin

Collinear spin

In Sec. 2.3.1 and Sec. 2.3.2 we have formulated the KS equations for a fictitious set of non-interacting electrons in an effective spin potential. However the KS formalism requires that the HK theorems hold true, this is not obviously true for spin potentials. Since the development of spin-DFT by von Barth and Hedin in 1972 [10], there has been much discussion of the validity of the HK theorems. In the case of collinear spin-DFT, Von Barth and Hedin themselves show that for a single electron orbital, the spin potential is not uniquely defined, and conclude that in general the HK theorems cannot hold. This breakdown of the HK theorems was then extended to many-electron wavefunctions by Capelle and Vignale [58]. They show that in the case of full polarisation (i.e. $n^{\uparrow} = n$, $n^{\downarrow} = 0$), there are an infinity of potentials which map to the spin-down density. It is assumed in Eq. 2.12 that for HK I to be valid, the wavefunction and therefore the density, must be non-zero. The case discussed by Capelle and Vignale is a direct extension to this. It is obvious that for a system with no density, the potential cannot be unique, however this is of little consequence in practice as it is very uncommon to consider a such a polarised system. This breakdown of HK I is often call a *trivial non-uniqueness.*

In a collinear system there is another type of non-uniqueness which is termed a *systematic non-uniqueness* by Capelle and Vignale. In DFT it is possible to determine the potential from the density, with the freedom of a constant. This constant shift in the potential leads to an overall shift in the total energies obtained by the KS equations. As a result, only the differences in energy can be extracted with confidence from a DFT calculation, which is rarely a problem as this is often aligned most closely with experimental observables. In the case of collinear DFT there is also a freedom of a second constant. As the potential is formed from an electronic part and a magnetic part, $V = V_{\text{elec}} + \mu_{\text{B}} B_z$, we find that there is an extra freedom in the B-field. This second constant results in a non-uniqueness in the magnetisation potential. We can overcome this systematic non-uniqueness by placing a constraint on the number of spin-up and spin-down electrons (i.e. fixing the magnetisation density) [55]. Calculations, in practice, can be performed either with or without this constraint. By omitting the constraint on magnetisation we allow the system to fall into different magnetic minima, each of which is a true magnetic configuration of the system.

Non-collinear spin

To describe the HK theorems in the context of non-collinear spin-DFT, we must briefly stray away from the usual language used to describe DFT. Using second quanisation, we can define a set of number operators, related to the number of electrons. Firstly we define the total number operator,

$$\hat{N} = \hat{N}^{\uparrow} + \hat{N}^{\downarrow}, \tag{2.57}$$

and the magnetisation operator,

$$\hat{m} = \hat{N}^{\uparrow} - \hat{N}^{\downarrow}, \tag{2.58}$$

where $\hat{N}^{\uparrow}$ and $\hat{N}^{\downarrow}$ are the number operators for spin-up and spin-down electrons respectively. A non-uniqueness of the spin potential arises when these operators commute with the Hamiltonian [55, 59]. As the total number of electrons is fixed, $[\hat{\mathcal{H}}, \hat{N}] = 0$; this is also true for standard DFT. In collinear systems we also have a definite number of spin-up and spin-down electrons, therefore $[\hat{\mathcal{H}}, \hat{N}^{\uparrow}] = [\hat{\mathcal{H}}, \hat{N}^{\downarrow}] = 0$. Consequently the magnetisation operator also commutes with the Hamiltonian, this leads to the systematic non-uniqueness discussed above. It was suggested by Eschrig and Pickett [59] that one could find a system with a non-collinear arrangement of spins where the spin-up and spin-down number operators commute with the Hamiltonian. This would result in the same systematic non-uniqueness described by Capelle and Vignale for the collinear case. However, it was shown by Gidopoulos [55] that the only way for this to occur is for the magnetisation to be globally collinear. We can conclude therefore that for a spin potential which is in general non-collinear, there is a direct one-to-one mapping of the spin potential and the spin density.

2.3.4 Spin-orbit interaction

To discuss more complex magnetic phenomena, we first cover some preliminaries about angular momentum. Electrons interacting with an atomic nucleus have orbital angular momentum as well as spin angular momentum which is an intrinsic property. In the non-relativistic limit, the quantum numbers related with these angular momenta are *good quantum numbers*, meaning that angular momentum operators commute with the electronic Hamiltonian. For the orbital angular momentum we have two operators, total angular momentum, $\hat{L}^2$, and by convention the z-component of the orbital angular momentum, $\hat{L}_z$ [5]. Acting on an electron wavefunction we have,

$$\hat{L}^2 \left|\psi\right\rangle = l(l+1)\hbar^2 \left|\psi\right\rangle , \tag{2.59}$$

and

$$\hat{L}_z \left|\psi\right\rangle = m_l \hbar \left|\psi\right\rangle , \tag{2.60}$$

where l is the angular momentum quantum number and m_l is the magnetic quantum number and can take values of $-l, -l+1, \ldots, l-1, l$. We have explicitly included $\hbar$ as the fundamental quantum mechanical unit of momentum.

Similarly for spin angular momentum we consider two operators, $\hat{S}^2$ and $\hat{S}_z$ with quantum numbers s and m_s respectively. The eigenequations for these operators are thus,

$$\hat{S}^2 \left|\psi\right\rangle = s(s+1)\hbar^2 \left|\psi\right\rangle , \tag{2.61}$$

and

$$\hat{S}_z \left|\psi\right\rangle = m_s\hbar \left|\psi\right\rangle . \tag{2.62}$$

For electrons, s takes the value of 1/2. In the same way as orbital angular momentum, m_s can take the values $-s, \ldots, s$. Therefore the eigenvalues of $\hat{S}_z$ are $\hbar/2$ and $-\hbar/2$, known as spin up and spin down respectively.

A complication occurs when electrons are moving at relativistic speeds. At these speeds, spin and orbital angular momentum are not necessarily conserved and can transfer from one to the other, this is known as spin-orbit coupling (SOC). In this case we define the total angular momentum, $\boldsymbol{J} = \boldsymbol{L} + \boldsymbol{S}$, which is always conserved. We can define a correction to the KS Hamiltonian which encompasses this effect known as the Thomas interaction, $\hat{\mathcal{H}}_{\text{SO}} = \lambda \hat{\boldsymbol{S}} \cdot \hat{\boldsymbol{L}}$, where λ is a material parameter [5, 60]. We can see that this effect is a function of the total vector spin, and therefore we must consider this in a non-collinear treatment as we require all components.

In a crystal system, SOC can become important as it links the electron spin to the underlying lattice. Where there is a preferential spin direction with respect to the lattice, known as magnetocrystaline anisotropy, SOC provides that link. Of particular importance to long-range magnetic ordering in a material is the so-called Dzyaloshinskii–Moriya interaction (DMI), or anti-symmetric exchange interaction [61, 62]. The form of DMI can be derived by applying second order perturbation theory to the SOC interaction [60]. This interaction causes canting of spins and as a result, SOC is essential for the investigation of such magnetic states.

2.4 Exchange and correlation functionals

In this section we shall discuss the most common functionals used for calculations in condensed matter. From the introduction of the xc functional by Kohn and Sham there has been active research into developing improved functionals resulting in huge choice for DFT users [63, 64]. The local density approximation (LDA) and generalised gradient approximation (GGA) are the most common functionals and have proved to be instrumental in the success of DFT. Despite their apparent simplicity, they can be used to model accurately a wide range of materials while remaining computationally inexpensive.

2.4.1 Local spin-density approximation

The LDA was originally proposed by Kohn and Sham in Ref. [9] and is the oldest xc functional. It uses the xc-energy from the homogeneous electron gas (HEG) to model that of whatever system is being studied, it is typical for the LDA to be generalised to include spin, known as the local spin-density approximation (LSDA). The functional takes the form,

$$E_{\text{xc}}^{\text{LSDA}} = \sum_{\sigma=\uparrow,\downarrow} \int \mathrm{d}\boldsymbol{r}\ \epsilon_{\text{xc}}^{\text{HEG}}[n^{\uparrow}, n^{\downarrow}] n^{\sigma}(\boldsymbol{r}), \tag{2.63}$$

where $\epsilon_{\text{xc}}^{\text{HEG}}$ is the xc-kernel of the HEG, defined as the xc energy per unit volume at a given spin density, and σ is the spin. The exchange part of the xc-kernel is known exactly while the correlation part must be parametrised from quantum Monte Carlo calculations, the particular parematrisation used in this thesis that of Perdew and Zunger [65].

Despite the LSDA being a coarse approximation, it has a number of benefits. In the case of covalent, ionic and metallic systems, the LSDA will reproduce experimental geometries within approximately 10% [66]. The LSDA works best when applied to systems with smoothly varying densities which best approximate the HEG. Importantly for computation the LSDA is local, meaning one only needs to have knowledge of the HEG at the density in question, this means it is fast to compute. There are a series of known limitations to the LSDA, primarily that LSDA tends to produce densities that are overly homogeneous [66]. As a result of this homogeneity the binding energies obtained by LSDA tend to be overpredicted in molecules, this has consequences for structural calculations which often underpredict bond lengths compared with experiment [67, 66]. For magnetic systems, the LSDA has been shown to produce magnetic moments with a large variation in the accuracy [56].

2.4.2 Generalised gradient approximation

As an extension to the LSDA, GGA uses the gradient of the density in addition to density itself, with the aim of capturing some of the effects of variations in the density. The general form for GGAs is,

$$E_{\mathrm{xc}}^{\mathrm{GGA}} = \sum_{\sigma=\uparrow,\downarrow} \int \mathrm{d}\boldsymbol{r}\ \epsilon_{\mathrm{xc}}^{\mathrm{GGA}}[n^{\uparrow}, n^{\downarrow}, \boldsymbol{\nabla} n^{\uparrow}, \boldsymbol{\nabla} n^{\downarrow}] n^{\sigma}(\boldsymbol{r}). \tag{2.64}$$

There is no unique way to define the GGA, and many different parametrisations exist. GGAs typically fall into two distinct groups, (i) empirical functionals that have been parametrised using experimental data from a class of materials, and (ii) functionals that have been parametrised to preserve exact quantities. The most common functional in group (i) is BLYP [68] which has proved to be accurate for molecular systems, however in physics where crystalline solids are king, the functional of choice is often that of Perdew, Burke and Ernzerhof (PBE) [69] or PBEsol [70] from group (ii), both allow for improved accuracy when calculating properties of solids compared to LSDA, the latter of which is known to be still more accurate for the prediction of lattice parameters.

As with the LSDA, GGAs are not perfect, it is well known that LSDA and GGA underestimate electronic band gaps in most materials [71, 72], occasionally predicting semiconductors to be metallic, for example La_2CuO_4 [73]. With regards to structural parameters, GGAs have the opposite problem to the LSDA whereby the binding energy is underpredicted, leading to larger lattice parameters than found experimentally [67]. In terms of performance, GGAs have the added complexity of the gradient of the density. This means that the functional is no longer purely local and this incurs a small penalty in terms of computation speed.

2.4.3 Jacob's ladder and beyond

The so called *Jacob's ladder* of xc functionals [74] starts with Hartree theory and steps up the ladder, reaching for the lofty heights of *chemical accuracy* with the exact xc functional. The LSDA and GGAs are the first two rungs of the ladder, the next rung belongs to meta-GGAs [75, 76] which build on the success of GGAs by including the electron kinetic energy as well as the gradient of the density. Meta-GGAs incur a further computational cost compared to GGAs and as such are not as popular for general use.

It is worth mentioning *hybrid functionals* which do not form part of the *Jacob's ladder*. Hybrids can be found throughout the literature [77, 78, 79] and are most often used when a particular physical quantity is poorly approximated by standard xc functionals since they can by tuned to produce the desired result; as such hybrid functionals may not be strictly *ab initio*.

When choosing an xc functional, one is faced with dozens of options, many of which promise excellent agreement with some particular experimental parameter, but are computationally expensive [80]. Extreme caution must be taken in choosing an xc functional, as one might find poorer results from a more expensive computation.

2.5 Implementation

In order to find solutions to quantum mechanical problems using the theory outlined above we need to be able to take the continuous parameters of the KS equations and use discrete analogues. It is important to do this so that accuracy can be maintained and uncertainties quantified, ideally in such a way that numerical errors can be made arbitrarily small.

For all calculations in this thesis, we will use the *plane wave pseudopotential* approach whereby KS orbitals are represented by a plane-wave basis set and atom cores are represented by pseudopotentials. There are a range of benefits to this approach. For instance, the plane-wave basis set can be arbitrarily large leading to a systematic improvement in total energy. Other approaches exist, such as Gaussian basis sets, but these basis sets are not complete and sample space inconsistently as they differentiate between atoms and vacuum [81, 82, 83].

2.5.1 Periodic boundary conditions

As we are interested in material properties in the solid state, we model the materials as infinite crystals. The biggest advantage of crystals is that they are formed of infinitely repeating units known as *unit cells* and this allows us to calculate macroscopic numbers of electrons using just the electrons in the unit cell. A requirement of periodic boundary conditions (PBC) is that the external potential, and therefore density, is also periodic,

$$V_{\text{ext}}(\boldsymbol{r}+\boldsymbol{R}) = V_{\text{ext}}(\boldsymbol{r}), \tag{2.65}$$

and

$$n(\boldsymbol{r}+\boldsymbol{R}) = n(\boldsymbol{r}), \tag{2.66}$$

where $\boldsymbol{R}$ is a *real space lattice vector* given by

$$\boldsymbol{R} = n_1\boldsymbol{a} + n_2\boldsymbol{b} + n_3\boldsymbol{c}, \text{ with } n_1, n_2, n_3 \in \mathbb{Z}, \tag{2.67}$$

where $\boldsymbol{a}$, $\boldsymbol{b}$, $\boldsymbol{c}$ are the *lattice vectors* that span the parallelopiped which defines the unit cell.

From the real lattice vectors we can define the *reciprocal lattice vectors*,

$$\boldsymbol{G} = h\boldsymbol{a}^* + k\boldsymbol{b}^* + l\boldsymbol{c}^*, \text{ with } h, k, l \in \mathbb{Z}, \tag{2.68}$$

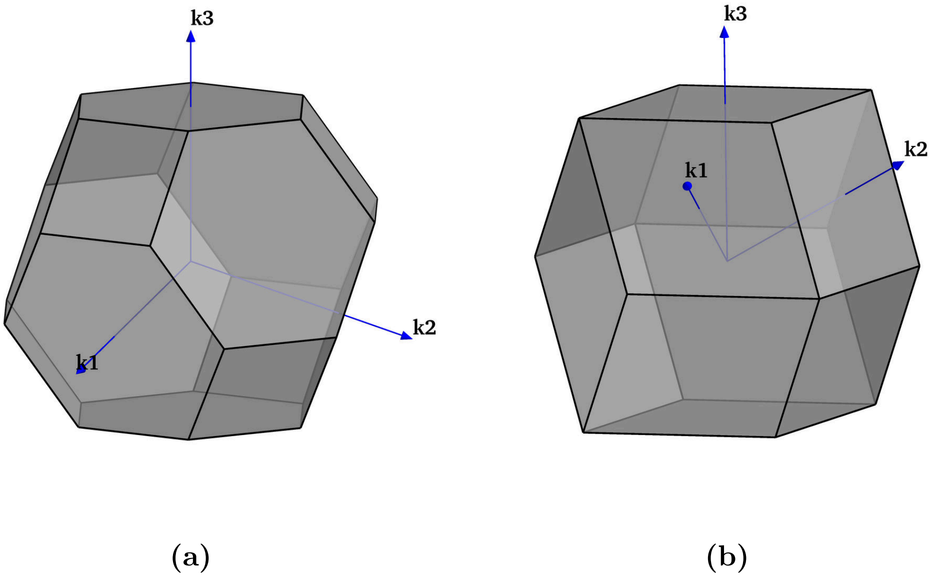

Figure 2.2: The first Brillouin zones of the (a) fcc and (b) bcc cubic lattices. Each BZ is centred at the point $k = (0, 0, 0)$.

where $\boldsymbol{a}^*, \boldsymbol{b}^*, \boldsymbol{c}^*$ are given by

$$\boldsymbol{a}^* = \frac{2\pi}{\Omega}\boldsymbol{b} \times \boldsymbol{c}, \tag{2.69}$$

$$\boldsymbol{b}^* = \frac{2\pi}{\Omega}\boldsymbol{c} \times \boldsymbol{a}, \tag{2.70}$$

$$\boldsymbol{c}^* = \frac{2\pi}{\Omega}\boldsymbol{a} \times \boldsymbol{b}, \tag{2.71}$$

with Ω the unit cell volume given by the scalar triple product of the lattice vectors.

2.5.2 Bloch functions

By requiring that the potential and density are periodic, this does not necessarily constrain the KS orbitals to be periodic. However, from the definition of the density we know that the magnitude of the KS orbitals must have the lattice periodicity, therefore

$$\phi_i^{\boldsymbol{k}}(\boldsymbol{r} + \boldsymbol{R}) = \phi_i^{\boldsymbol{k}}(\boldsymbol{r})e^{i\boldsymbol{k}\cdot\boldsymbol{R}}, \tag{2.72}$$

where $\boldsymbol{k}$ is a constant vector, i indicates the orbital, and $\boldsymbol{R}$ is a real lattice vector. From here we arrive at the Bloch theorem [84], which states that an orbital can be expressed as a lattice periodic function and a plane wave,

$$\phi_i^{\boldsymbol{k}}(\boldsymbol{r}) = u_i^{\boldsymbol{k}}(\boldsymbol{r})e^{i\boldsymbol{k}\cdot\boldsymbol{r}}, \text{ with} \tag{2.73}$$

$$u_i^{\boldsymbol{k}}(\boldsymbol{r}+\boldsymbol{R}) = u_i^{\boldsymbol{k}}(\boldsymbol{r}). \tag{2.74}$$

The vector $\boldsymbol{k}$ is a vector in reciprocal space and is therefore also periodic. However, this time the periodicity is that of the reciprocal lattice, therefore the KS orbitals are constant under the tranformation $\boldsymbol{k} \to \boldsymbol{k}+\boldsymbol{G}$. This periodicity in reciprocal space allows us to define a reciprocal analogue to the unit cell, whereby all $\boldsymbol{k}$-vectors exist uniquely inside this reciprocal unit cell,

$$\boldsymbol{k} = k_1\boldsymbol{a}^* + k_2\boldsymbol{b}^* + k_3\boldsymbol{c}^*, \text{ with } -\frac{1}{2} \leq k_i \leq \frac{1}{2},\ i = 1,2,3. \tag{2.75}$$

This set of $\boldsymbol{k}$-points is known as the first Brillouin zone (BZ), and is uniquely defined for a particular lattice. There are a number of ways to describe the Brilloun zone, but simply it is the locus of points in reciprocal space which are closer to the origin than any other lattice point, i.e. the Wigner-Seitz cell of the reciprocal lattice [5].

Neglecting symmetry, there exists a unique set of KS orbitals for any choice of $\boldsymbol{k}$ in the BZ, $\boldsymbol{k}$ is therefore another continuous variable which we must sensibly discretise (see 2.5.4). Each set of orbitals at every $\boldsymbol{k}$-point represents N electrons, and each orbital is normalised such that

$$\int \mathrm{d}\boldsymbol{r}\ \phi_i^{\boldsymbol{k}*}(\boldsymbol{r})\phi_i^{\boldsymbol{k}}(\boldsymbol{r}) = 1. \tag{2.76}$$

When the orbitals are constructed from Bloch waves, the density becomes

$$n(\boldsymbol{r}) = \sum_{\boldsymbol{k}}\sum_i f_i^{\boldsymbol{k}} w_{\boldsymbol{k}} |\phi_i^{\boldsymbol{k}}(\boldsymbol{r})|^2 \tag{2.77}$$

with

$$\sum_{\boldsymbol{k}} w_{\boldsymbol{k}} = N, \tag{2.78}$$

where $w_{\boldsymbol{k}}$ is the weighting of the $\boldsymbol{k}$-vectors such that the total number of electrons is conserved, and $f_i^{\boldsymbol{k}}$ is the occupancy of the i^{th} band at $\boldsymbol{k}$. As we can use the symmetry of the crystal to reduce the number of $\boldsymbol{k}$-points we include, the weighting is modified to account for the symmetry equivalent $\boldsymbol{k}$-points represented by each $\boldsymbol{k}$-point.

2.5.3 Plane waves and reciprocal space

Knowing that the orbitals contain a lattice periodic part aids us in choosing basis functions. In this thesis the basis functions used are plane waves. Using a plane-wave basis, any KS orbital can be written as,

$$\phi^{\sigma}_{i,\boldsymbol{k}}(\boldsymbol{r}) = \frac{1}{\sqrt{\Omega}} \sum_{\boldsymbol{G}} c^{\sigma}_{i,\boldsymbol{k}}(\boldsymbol{G}) e^{i(\boldsymbol{G}+\boldsymbol{k})\cdot\boldsymbol{r}}, \tag{2.79}$$

where $\boldsymbol{G}$ is a reciprocal lattice vector and $c^{\sigma}_{i,\boldsymbol{k}}(\boldsymbol{G})$ are complex wavefunction coefficients in reciprocal space and can be computed through a Fourier transform (FT),

$$c^{\sigma}_{i,\boldsymbol{k}}(\boldsymbol{G}) = \frac{1}{\sqrt{\Omega}} \int_{\Omega} \mathrm{d}\boldsymbol{r}\ \phi^{\sigma}_{i,\boldsymbol{k}}(\boldsymbol{r}) e^{-i(\boldsymbol{G}+\boldsymbol{k})\cdot\boldsymbol{r}}. \tag{2.80}$$

A consequence of using a plane-wave basis is that it becomes convenient to define many of the objects in reciprocal space, which in some cases leads to significant efficiency savings. These savings are only possible because of an algorithm known as a fast Fourier transform (FFT), which reduces the scaling of the FT from $\mathcal{O}(N^2)$ to $\mathcal{O}(N\log(N))$. Firstly, for the non-interacting kinetic energy operator in Eq. 2.32, we can make use of the properties of exponentials to simplify the derivatives,

$$\begin{aligned}\frac{1}{2}\boldsymbol{\nabla}^2\phi^{\sigma}_{i,\boldsymbol{k}}(\boldsymbol{r}) &= \frac{1}{\sqrt{2\Omega}}\boldsymbol{\nabla}^2\left(\sum_{\boldsymbol{G}} c^{\sigma}_{i,\boldsymbol{k}}(\boldsymbol{G})e^{i(\boldsymbol{G}+\boldsymbol{k})\cdot\boldsymbol{r}}\right)\\ &= \frac{-1}{\sqrt{2\Omega}}\left(\sum_{\boldsymbol{G}}(\boldsymbol{G}+\boldsymbol{k})^2 c^{\sigma}_{i,\boldsymbol{k}}(\boldsymbol{G})e^{i(\boldsymbol{G}+\boldsymbol{k})\cdot\boldsymbol{r}}\right),\end{aligned} \tag{2.81}$$

which simply involves multiplying the orbital coefficients by a prefactor. Not only is this easy to implement, it also avoids including unnecessary uncertainty through numerical differentiation techniques. Next we consider the Hartree term in Eq. 2.31, which when expressed in real space involves an integral which is both slow and numerically challenging. However, by employing reciprocal space the Hartree potential is given by

$$V_{\mathrm{H}}(\boldsymbol{G}) = \frac{n(\boldsymbol{G})}{\boldsymbol{G}^2}. \tag{2.82}$$

For more details see App. B.

2.5.4 Brillouin-zone sampling and plane-wave cut-off energies

We introduced above the idea of Bloch wavevectors, $\boldsymbol{k}$, and the BZ. Of course we must limit ourselves to a finite number of $\boldsymbol{k}$-points to describe the wavefunction, noting that as long as the orbitals are smoothly varying in reciprocal space this is a valid approximation. One common method of generating a $\boldsymbol{k}$-point set is that of Monkhorst and Pack (MP) [85] whereby in fractional coordinates the $\boldsymbol{k}$-points lie on a $N_x \times N_y \times N_z$ grid centred around (0,0,0). A MP grid is particularly useful as it samples the BZ evenly and without bias and the number of $\boldsymbol{k}$-points can be increased to improve the sampling by increasing the dimensions of the grid. It is often the case in calculations of crystals that one would want to make use of the crystal symmetry to improve upon calculation times, this can easily be handled by a MP grid because it is unbiased. By applying crystal symmetry, that is identifying all translations, rotations, inversions and mirrors, one can *fold* the $\boldsymbol{k}$-point set down to an *irreducible wedge*, the weighting of each $\boldsymbol{k}$-point is then adjusted by the number of symmetry equivalent points each $\boldsymbol{k}$-point in the irreducible wedge accounts for. This allows us to reduce the number of $\boldsymbol{k}$-points in the calculation without any loss of accuracy.

Each plane wave included in the basis has a corresponding $\boldsymbol{G}$-vector and in principle we would require an infinite set of $\boldsymbol{G}$-vectors to describe the system properly. However we note that in the regions of interest, the KS orbitals tend to be smoothly varying and therefore largely independent of high frequency plane waves in the basis. We can then define a maximum $\boldsymbol{G}$-vector, excluding all $\boldsymbol{G}$-vectors larger than this value, this leads to a $\boldsymbol{G}$-sphere in reciprocal space. This maximum $\boldsymbol{G}$-vector, $\boldsymbol{G}_{\text{cut}}$, is typically defined in terms of a kinetic energy E_{cut},

$$|\boldsymbol{G}_{\text{cut}}| = \sqrt{2E_{\text{cut}}}, \tag{2.83}$$

this is why it is common in the literature for basis cut-offs in plane-wave codes to be quoted in units of energy. From the definition of the density being the square of the KS orbitals, for the density to be known to the same level of accuracy one must technically use twice the number of plane waves. However, it is often worth using fewer for the computational gain. Being able to set the accuracy of the basis set simply with an energy is one of the biggest advantages of using a plane-wave basis. In the case of local basis functions it is not always possible to systematically improve upon convergence in such a controlled way.

When considering a new system it is always important to determine the best choice of $\boldsymbol{k}$-point set and energy cut-off as they are both highly system dependent. In most cases $\boldsymbol{k}$-point convergence and plane wave convergence are largely independent, with $\boldsymbol{k}$-points depending mostly on the cell geometry and the basis set depending mostly on the species. However, care must always be taken to ensure the convergence is robust.

2.5.5 Pseudopotentials

Having mentioned many advantages of plane-wave basis sets, there is one particular inconvenience that arises from their use. The choice of a plane-wave basis has no *a priori* assumption of the shape of the orbitals: plane waves can be used to build up any periodic function. However, this means that one must use a much larger set of basis functions compared to a basis set which presupposes the shape of the orbitals. Pseudopotentials are therefore crucial to the use of a plane-wave basis set as they allow us to use far fewer basis functions [86, 87]. To motivate the use of pseudopotentials we first recognise that not all electrons in our system contribute equally to the properties of interest and can broadly be separated into *core* and *valence* electrons. The core electrons are close to the nucleus, and occupy low energy states, being so low in energy they contribute little to the physical properties of the system. We use the *frozen core approximation* to treat all core electrons up to some cut-off radius r_c along with the nucleus as a non-polarisable core which is pre-computed. A pseudopotential is an effective potential for the valence electrons which incorporates the core effects, and is such that the behaviour of the valence electrons outside the cut-off radius is the same as one would obtain in an all-electron treatment. The orbitals in a full electron treatment inside the core region typically oscillate with high frequencies, this means that many more precious basis functions are required to capture these oscillations. Under a pseudopotential approximation most of this oscillatory behaviour is smoothed out and requires fewer plane waves, see Fig. 2.3.

Broadly there are two types of pseudopotentials used in solid state calculations: *norm-conserving* [88] and *ultrasoft* [89]. Norm-conserving pseudopotentials are generated such that the pseudo-wavefunction outside of the core region leads to the same density as the all electron wavefunctions. However, this contraint sometimes means the resulting potential leads to a pseudo-wavefunction which is not significanly smoother. By relaxing this charge constraint of norm-conserving pseudopotentials, ultrasoft pseudopotentials are able to have much

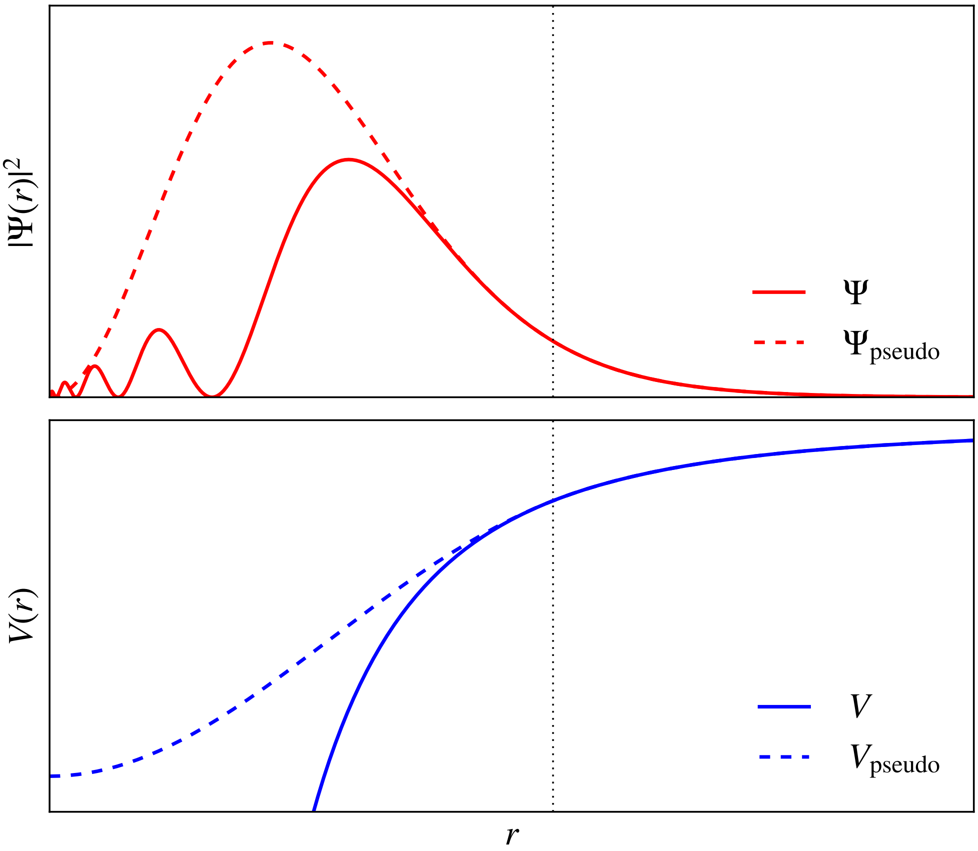

Figure 2.3: Schematic of a pseudopotential and resulting wavefunction. The divergence of the Coulomb potential (blue solid line) results in fast oscillations in the wavefunction below the cut-off radius (red solid line), the pseudopotential (blue dashed line) removes these oscillations in the new approximate wavefunction (red dashed line). The cut-off radius is shown by the vertical dotted line.

larger cut-off radii resulting in fewer plane waves needed for same level of accuracy. Due to the smaller basis set, calculations using ultrasofts are generally slightly faster than if a norm-conserving pseudopotential were used.

The pseudopotentials are also where SOC is included if desired. The orbital contribution of the electron angular momentum comes from their interaction with atomic orbitals. Rather than directly including SOC in the Hamiltonian, it is more convenient to alter the pseudopotentials to include the effects. Instead of solving the Schrödinger equation for each atom, the Dirac equation is used to account for relativistic effects of the electrons [90, 91]. For each atomic orbital, instead of simply storing the l quantum numbers, we store the j quantum numbers which include spin. Unlike the Schrödinger equation, the Dirac equation includes both spin and SOC [92].

2.6 Calculating properties

We have built up a catalogue of theory and numerical approaches to define all of the interesting physical *objects* required to build up the KS orbitals and Hamiltonian in a computer. From what now is essentially bytes of data stored in memory (often in a large parallel machine), we need to be able to obtain meaningful physical properties. There is a wide selection of available codes one could use to calculate material properties from DFT, each with slightly different approaches to suit their intended audience. For all calculations in this thesis the plane-wave pseudopotential code CASTEP is used [24]. Through its use of plane waves it is designed to be system agnostic and gives uniformly accurate results regardless of the chemistry of the material [93].

DFT allows us to calculate a large number of properties including structural, spectral and optical properties [94], and using extensions to standard DFT one can obtain effects that on the surface would be surprising from a static zero temperature theory, such as phonons using density functional perturbation theory (DFPT) [95, 96].

2.6.1 Energy minimisation

The first step in any electronic structure calculation is calculating the total energy, this can be done in one of two ways: either by direct diagonalisation or by gradient descent methods. Diagonalisation of the Hamiltonian is mathematically the most obvious route. When all terms in the Hamiltonian are expressed in reciprocal space,

$$\hat{\mathcal{H}}_{\mathrm{KS}}(\boldsymbol{G})c^{\sigma}_{i,\boldsymbol{k}}(\boldsymbol{G}) = \epsilon^{\sigma}_{i,\boldsymbol{k}}c^{\sigma}_{i,\boldsymbol{k}}(\boldsymbol{G}), \tag{2.84}$$

the single-particle KS equation is an eigenvalue equation with $c^{\sigma}_{i,\boldsymbol{k}}(\boldsymbol{G})$ as the eigenfunctions. However, when using a plane-wave basis set this diagonalisation is extremely slow due the the number of basis functions used.

Instead we use an iterative approach using gradient descent methods known as the self-consistent field (SCF) calculation. Below we present an outline of an iterative minimisation to show the principles involved, for a more detailed discussion see App. A. In this case we need to find the downhill direction of the total energy with respect to the orbitals, this can be achieved through a functional derivative of the total energy with respect to the orbitals,

$$\begin{aligned}\frac{\delta E_{\text{tot}}}{\delta \langle \phi^{\sigma}_{i\boldsymbol{k}}(\boldsymbol{r})|} &= \frac{\delta}{\delta \langle \phi^{\sigma}_{i\boldsymbol{k}}(\boldsymbol{r})|} \langle \phi^{\sigma}_{i\boldsymbol{k}}(\boldsymbol{r})| \hat{\mathcal{H}}_{\text{KS}} |\phi^{\sigma}_{i\boldsymbol{k}}(\boldsymbol{r})\rangle \\ &= \hat{\mathcal{H}}_{\text{KS}} |\phi^{\sigma}_{i\boldsymbol{k}}(\boldsymbol{r})\rangle .\end{aligned} \tag{2.85}$$

A functional derivative, or variational derivative, is much the same as a standard derivative, however instead of investigating the change of a function, $f(x)$, with respect to a variable, $\mathrm{d}x$, we look at the change of a functional, $F[f(x)]$, with respect to a small change in a function, $\epsilon g(x)$ [38]. From Eq. 2.85 we can see that the gradient of the total energy is obtained by applying the Hamiltonian to the orbitals. This means that for any set of orbitals and their corresponding Hamiltonian we can find the downhill direction, using this gradient we can update the orbitals by stepping down hill and recalculate the density and Hamiltonian for the new orbitals,

$$\phi(\boldsymbol{r}) \rightarrow n(\boldsymbol{r}) \rightarrow \hat{\mathcal{H}}(\boldsymbol{r}), \tag{2.86}$$

where the arrows indicate a mapping from the density to the Hamiltonian as described by the HK theorems. The above method is known as ensemble density functional theory (EDFT) [97], and is a robust method which is guaranteed to find a stable minimum. At all points in an EDFT minimisation the approximate orbitals correspond exactly to the density and the Hamiltonian, it is therefore a fully self-consistent method.

While robust, EDFT is often slow, which is where a different method can be employed: density mixing (DM) [98, 99]. In a DM minimisation the density does not strictly correspond to the trial orbitals, as at each iteration a new

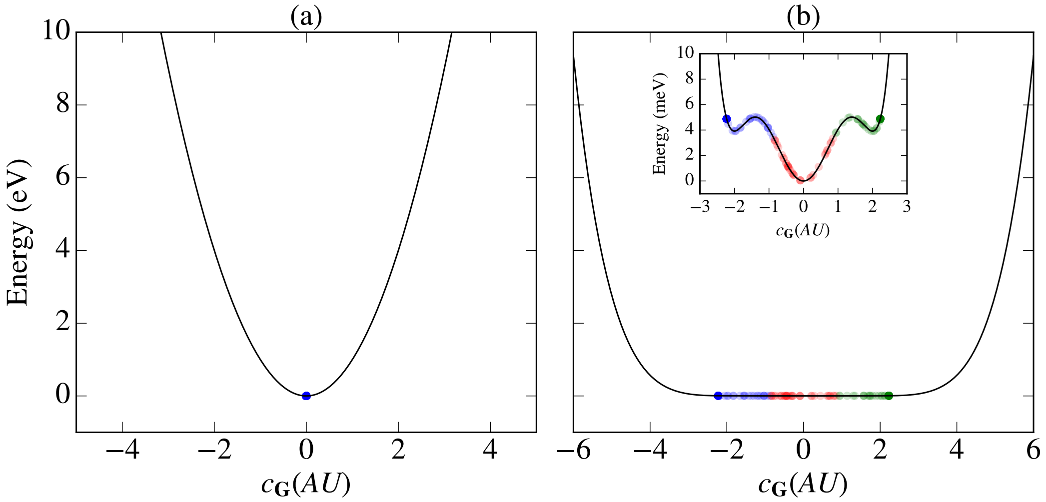

Figure 2.4: Example of simple one-dimensional gradient descent algorithm applied to (a) a simple one-minimum system and (b) a more complex system with multiple shallow minima. Each scatter point indicated the result of a single run of the gradient descent algorithm starting from an initial random value of $c_{\boldsymbol{G}}$. In (b) the colour of the points indicates which minimum the result is closest, from left to right: blue, red, green. Inset plot shows a zoomed in version of the energy landscape.

guess of the density is formed by *mixing* some fraction of the previous density into the new density. Due to the mixing, the density and orbitals are never self-consistent until the orbitals reach convergence. DM is typically faster than EDFT, however it is not guaranteed to monotonically decrease the energy and this can lead to numerical issues often known as *charge/spin sloshing* where the energy *bounces* back and forth around a minimum. This often occurs in materials with complex energy landscapes.

In practice the convergence criteria is set by the user and once the changes in energy from each iteration falls below this level the calculation terminates. The level of convergence depends on the type of calculation, typically 10^{-6} eV/atom is sufficiently accurate for the calculating most electronic properties, while a finer tolerance of 10^{-8} eV/atom may be needed for calculations using DFPT which are more sensitive to the ground state orbitals.

Minimisation in non-collinear systems

Minimising the energy is often the least problematic part of a DFT study. One may encounter the issues described above with DM, but it is usually possible to optimise the mixing parameters to avoid spin sloshing. If that fails, switching to an EDFT minimisation will almost always lead to a ground state, just not as quickly. There is a more fundamental issue in the minimisation when considering calculations involving non-collinear spins. Firstly, for a system which can host NCM, there are typically multiple stable spin configurations, meaning that there are multiple minima in the energy landscape. On top of this, the energy difference between non-collinear states is often very small. In the work of Edström *et al.* [29], they show energies calculated by varying the magnetic structure of a curved magnet. The difference in the energy of these states is of the order 0.5 meV/atom. These represent very difficult energy scales for minimisation algorithms as the minima are shallow. Example calculations of a one-dimensional gradient descent algorithm comparing the performance between a simple one-minimum system and a system with multiple shallow minima is shown in Fig. 2.4. For each of the deep potential well, Fig. 2.4a, and the shallow well, Fig. 2.4b, we have performed multiple calculations from randomly initialised positions with the same energy tolerance and step size. In the case of the single deep well, the results are closely clustered around the analytical minimum within the convergence tolerance set in the calculation. This most closely approximates the minimisation of a DFT calculation without considering spin. For the multiple shallow minimum case, the results are spread out around the analytic minima. The initial position determines which minimum the calculation falls into which is why spin initialisation is often required for spin-DFT calculations. The spread of the results is a consequence of the shallow minima replicating the effects of non-collinear spins. It is often difficult to guarantee that the calculation will find the desired non-collinear state. This is the reason why, in many cases, energy penalties which favour a particular spin configuration are often included in the Hamiltonian [27, 28].

2.6.2 Spectral calculations

Some of the most important ways of gaining insight into a materials is by investigating their band structure and density of states (DoS) [100, 101, 102]. A band structure describes the dispersion relation, $E(\boldsymbol{k})$, where $\boldsymbol{k}$ is the set of $\boldsymbol{k}$-points in the first BZ that forms a path through the high symmetry points. From a self-consistent groundstate calculation in DFT, so long as the density is well converged with respect to $\boldsymbol{k}$-points and basis set, the orbitals can be evaluated at any $\boldsymbol{k}$-point. An example of a DFT band structure is shown in Fig. 2.5 where the $\boldsymbol{k}$ axis is path through the BZ, Greek letters represent points inside the BZ and Latin letters represent points on the surface of the BZ. Strictly, a band structure in the KS scheme is an approximation to the fully interacting band structure as each band represents a non-interaction KS orbital rather than an interacting electron. For example, from Fig. 2.5 we see that Si has am indirect band-gap which is known from experiment and that PBE captures the s-orbital shape of the bands at the Γ-point. However, this highlights the band-gap problem in DFT as the PBE gap is approximately 0.57 eV compared to ~1.1 eV found experimentally [103].

The procedure for calculating the DoS in DFT is essentially the same as a band structure, instead of sampling the BZ along a high symmetry path one chooses a set of $\boldsymbol{k}$-points which uniformly sample the BZ. As with choosing SCF $\boldsymbol{k}$-points, the obvious choice is a MP grid. In principle the same grid could be used as for the electronic minimisation. However, this would usually produce a very coarse DoS. Because the $\boldsymbol{k}$-point set is finite the resulting DoS would be a series of δ-functions rather than a smooth curve, to better approximate a continuous DoS various broadening schemes are applied such as Gaussian or Lorentzian. More recently, adaptive broadening techniques such as introduced by Yates *et al.* [105] have been used to increase resolution. Instead of using a fixed-width Gaussian to broaden each peak (which may exaggerate effects of flatter bands) the Gaussian width is varied based on the gradient of the each band. Even broadening the peaks, we can see in Fig. 2.5 that we are left with

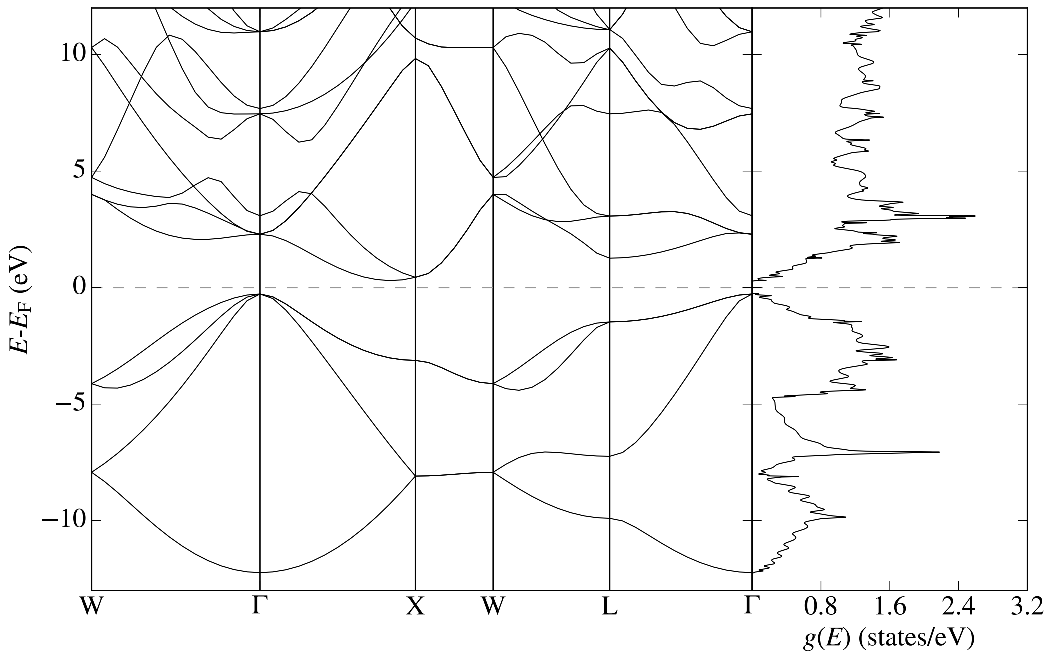

Figure 2.5: Band structure (left) and DoS (right) of Si calculated under PBE, two atoms of Si were included in the unit cell. The Fermi level is shown by the dotted line. For the band structure the path through the BZ is given in terms of high symmetry points for the cubic crystal system. Plots produced using dispersion.py [104] (See App. C)

a function which is not entirely smooth, this can be improved by increasing the $\boldsymbol{k}$-point-grid. The MP grid used for the DoS in Fig. 2.5 is 25×25×25 compared with a 9×9×9 for the minimisation.

2.6.3 Band structures with spin

It is possible to calculate the band structure of a material using spin-DFT [106, 107]. For a collinear magnetic material, a band structure is a useful tool for identifying magnetic states. In a collinear treatment, we treat the spin-up and spin-down electrons separately through the coupled KS equations (Eq. 2.43), therefore we have two sets of eigenenergies, $\epsilon_i^{\uparrow,\downarrow}$, associated with each spin. This allows us to effectively plot two band structures, one for each of the spins. Figure 2.6 shows a band structure of body centred cubic (bcc) Fe calculated using the LSDA. Just from the band structure we can see that bcc Fe has an overall magnetic moment, either ferromagnetic or ferrimagnetic, as the spin up

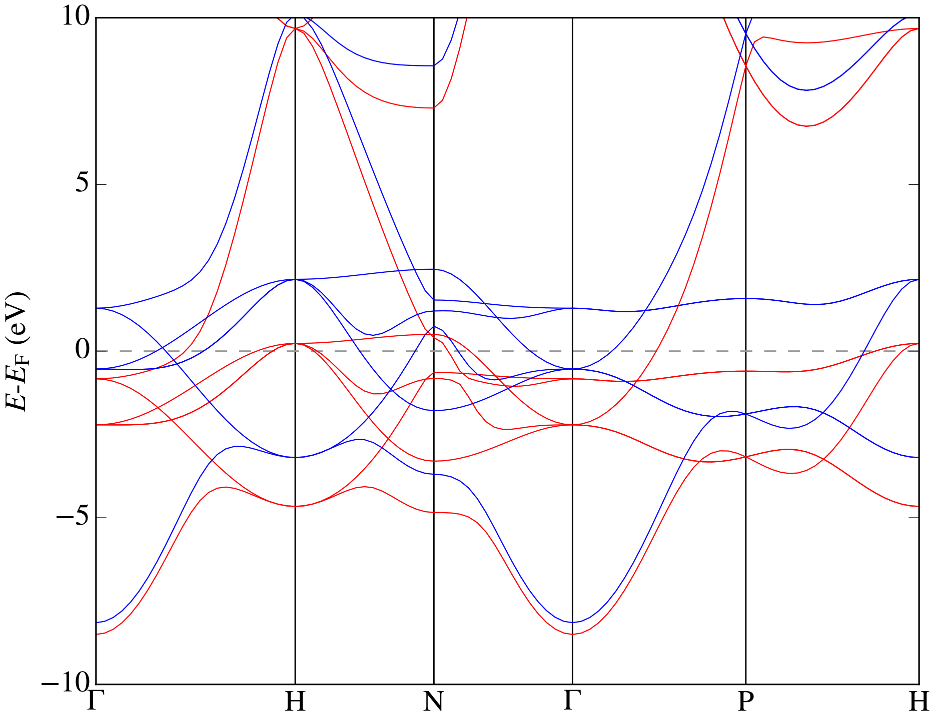

Figure 2.6: Spin polarised band structure of bcc Fe calculated under the LSDA. Spin up and spin down bands are shown in red and blue respectively. The splitting of the spin up and spin down bands shows there is a ferromagnetic moment. The Fermi level is shown by the dotted line. Plots produced using dispersion.py [104] (See App. C)

and spin down bands are non-degenerate. If, for example, a material had no overall magnetic moment, such as a paramagnet or an antiferromagnet, these bands would be degenerate. Therefore it is possible to get a quick understanding of the magnetism of a material from its spin-polarised band structure.

In calculations where the spin is treated as non-collinear, the band structures are not as immediately illuminating as a collinear band structure. We are not able to categorise the electrons into purely spin up and spin down, and we only have one eigenenergy related to each spinor wavefunction. CM is a special case of NCM, so it is possible to find a collinear solution. However as this state would still be described by spinor orbitals, special effort would be required to project the spin onto a global quantisation axis, in which case one could plot spin up and spin down bands. In general this is not the case and only one set of bands is presented from a non-collinear spin-DFT calculation.

2.6.4 Forces and geometry optimisation

It is often the case that a crystal structure is known from some experimental technique and electronic structure calculations are needed on the material, it is unlikely that the experimental structure is the equilibrium structure according the whichever approximation in DFT is being employed. At zero temperature one would expect there to be no forces acting upon a unit cell and its atoms, and that the atomic positions would be such that the total energy is minimised. We can calculate atomic forces by brute force, calculating finite differences by moving each atom a little and calculating the resulting Hessian matrix. This method would be extremely inefficient. Fortunately there is a simple way to calculate forces from first principles through the Hellmann-Feynman theorem [108, 109], which states that for the forces on the I^{th} nucleus is given by

$$\boldsymbol{F}_I = -\frac{\partial E}{\partial \boldsymbol{R}_I} = \left\langle \Phi_{\boldsymbol{R}} \left| \frac{\partial \hat{\mathcal{H}}}{\partial \boldsymbol{R}_I} \right| \Phi_{\boldsymbol{R}} \right\rangle , \tag{2.87}$$

where $\boldsymbol{R}_I$ is the position of the I^{th} nucleus and $|\Phi_{\boldsymbol{R}}\rangle$ is a general electronic wavefunction which depends parametrically on the nuclear positions. The benefit of this approach is that we can calculate the downhill direction for each of the nuclei without having to vary the orbitals. Instead we only need to compute the derivative of the Hamiltonian, many terms of which can be calculated in reciprocal space, which we have previously shown to be quick and efficient.

2.6.5 Mulliken population analysis

Knowing the overall electron density is indeed very helpful, however we may often want to reduce the complexity even further. From the language of chemistry, we may wish to know about local atomic charges and spins, or perhaps bond occupancies. Given a plane-wave basis set, this is not something that is immediately achievable since the basis set is delocalised. The most common way of calculating atomic charges is Mulliken population analysis [110], which derives the charges from the occupancies of a linear combination of atomic orbitals

(LCAO). We must then project our orbitals calculated on a plane-wave basis set onto a new LCAO basis. The procedure for this projection was provided by Sanchez-Portal *et al.* [111] and implemented in CASTEP using the procedure by Segall *et al.* [112, 113].

A plane-wave basis and an LCAO basis differ in a few key ways. Firstly a plane-wave basis set is orthonormal whereas LCAO basis functions are not. Secondly, plane-wave bases form a complete set, an LCAO does not. This is not to say that an LCAO basis is inherently worse than plane waves, just suitable for different systems such as molecules.

Given that the plane-wave basis set is complete, we are projecting eigenstates onto a smaller Hilbert space spanned by the LCAO functions. The ability of the atomic basis to represent the eigenstates is given by a spilling factor, which quantifies the degree of orthogonality between the plane-wave and the LCAO bases.

2.7 Practicalities

We have now outlined the underlying theory and implementation of a plane-wave, pseudopotential DFT code. Here, we will briefly discuss the process involved in performing DFT calculations using CASTEP. A more detailed description of performing these calculations may be found in the CASTEP documentation [114]. Starting from defining the material parameters, we will outline how one chooses the type of calculation to perform along with the level of theory. We will go on to cover details specific to the sort of magnetic calculations presented in this thesis. Finally, we will discuss the running of a CASTEP calculation on large distributed computers.

2.7.1 Crystal structure

Before one can do anything with a DFT code, one must define the locations of the atoms, and in the case of a periodic system, the unit cell. In CASTEP, the way to define a structure is by using a `.cell` file, this contains information about the atoms, the lattice, the $\boldsymbol{k}$-points and the symmetry. One can build a `.cell` file by hand, or use tools to do it automatically, typically from a `.cif` which is one of many crystallographic standard file formats. Care must be taken in converting from a `.cif`, as if they are generated by experimental structure refinement, they may have fractional occupancies of some atomic sites. Where possible one should seek to use a primitive unit cell, which can significantly decrease compute time. Symmetry is also a consideration, we mentioned above that the crystal symmetry can be used to reduce the $\boldsymbol{k}$-point set and speed up the calculation. However, symmetry is not always advisable, particularly in the case of NCM calculations, where one desires to find a magnetic structure which is not consistent with the crystal symmetry.

2.7.2 Level of theory

The purpose of a calculation informs what level of theory one may wish to include. A decision must be made about the choice of xc functional, we have only highlighted a small number of functionals available and some of their attributes. All calculations in this thesis, with the exception of calculations performed in Chap. 6, use either the LSDA or PBE functionals.

The treatment of spin is also an important consideration, one which is not always obvious. At a basic level, one should use the level of theory best suited to the expected magnetism. For example, if a material is expected to be non-magnetic, use non-spin-polarised DFT; if the material in question contains exotic non-collinear spin structures, use a NCM spin-DFT treatment. However, it is rarely that straightforward. If one wishes to perform a structural relaxation of a magnetic material, using spin-DFT is likely a poor choice. Each time a geometry optimisation step is taken, it is possible that the next SCF calculation may result in a slightly different magnetic structure, meaning comparisons between iterations may fail. Equally, if the aim of the calculation is to examine the effects of SOC, a NCM treatment will be required, even if the material is non-magnetic.

2.7.3 Initialisation

If a calculation is done using spin-DFT, it is likely because the desired outcome includes some sort of magnetic state. As many possible magnetic states exist in magnetic materials, it is unlikely that the desired spin structure will be realised without clever initialisation. Instead of using a fully random initial density to seed the calculation, we can impose some spin projected onto some or all of the atoms in the cell. This initial spin can either be collinear or non-collinear. This does not in any way mean that the results are less valid as the solution is still self-consistent. If the initialised spin configuration is not physical, it will not be present in the solution. One consideration when using spin initialisation is the choice of minimisation algorithm. If we choose DM, the initial density including the spin will be mixed into successive minimisation steps, increasing the likelihood of finding the minimum associated with that particular magnetic configuration. On the other hand, as EDFT is fully self consistent at each step in the minimisation, the initial density is replaced after a single step. That is not to say that using EDFT renders spin initialisation pointless, as the first step may be enough to start the minimisation from a region in phase space close to the desired solution.

2.7.4 Parallelisation

We have mentioned that DFT is highly favoured amongst first principles approaches mostly due to its speed. That is not to say that DFT calculations are not computationally expensive. While the smallest calculations comprising a few atoms (~ 10) will comfortably run on a mid-range laptop, many calculations require the use of supercomputers. CASTEP is a parallel code written to take advantage of the many computer cores available on large supercomputers. As a user, the parallelism of a calculation is worth considering to achieve the best efficiency, both of time and resources. The two main forms of parallelism in CASTEP are $\boldsymbol{k}$-point and $\boldsymbol{G}$-vector, with $\boldsymbol{k}$-point parallelism being preferable. The aim is to reduce the amount of communication occurring between processes on the supercomputer. The orbitals defined in Eq. 2.79 shows the dependence on $\boldsymbol{k}$-point and $\boldsymbol{G}$-vector. By distributing fully over $\boldsymbol{k}$-points, there are a full set of orbitals on each parallel process, therefore we are able to solve the KS equations at the same time for different $\boldsymbol{k}$-points. In this case communication overhead is low as each process has its own set of orbitals, only the total density must be shared across the nodes. We gain extra time savings if we further distribute the orbitals by $\boldsymbol{G}$-vector. More of the calculations can be performed in parallel if we share out the plane wave coefficients of the orbitals. However, as we no longer have full orbitals stored on each process, some additional communication overhead is required to recombine the orbitals. A poor parallelisation scheme can be detrimental to a calculation, possibly resulting in wasted resources or in the worse case the calculation may take too long to fit within any time limits imposed on the machine. Over parallelisation is also a possibility. In this case, there may not be enough $\boldsymbol{G}$-vectors. If one uses more processes than the product of $\boldsymbol{k}$-points and $\boldsymbol{G}$-vectors, some processes may be without any data.

Chapter 3

DFT in practice: Understanding skyrmion hosting materials

> *The antidote for a blended poison will be equal to more than the sum of the antidotes for each of the separate components.*
>
> —J. K. Rowling,
>
> *Harry Potter and the Half Blood Prince*

In this chapter we shall explore how density functional theory (DFT) can be used to add insight to experimental measurements, with a particular focus on skyrmion hosting materials. There are some experimental techniques such as angle-resolved photoemission spectroscopy (ARPES) [115] and resonant x-ray scattering [116] that allow us to directly probe the electronic structure of a material. However, no technique allows one to extract the level of detail available from a DFT calculation. We will start by presenting calculations of the muon stopping sites in Cu_2OSeO_3, applicable to muon-spin spectroscopy (μSR) experiments. Next, we will demonstrate the use of spin-density functional theory (spin-DFT) to probe the effects of chemical substitution in $GaV_4S_{8-y}Se_y$. We use our calculations to show that upon substitution, the S rich crystals and Se rich crystals display distinctly different distributions of spin density that affect the stability of magnetic states. The aim of this chapter is to showcase many

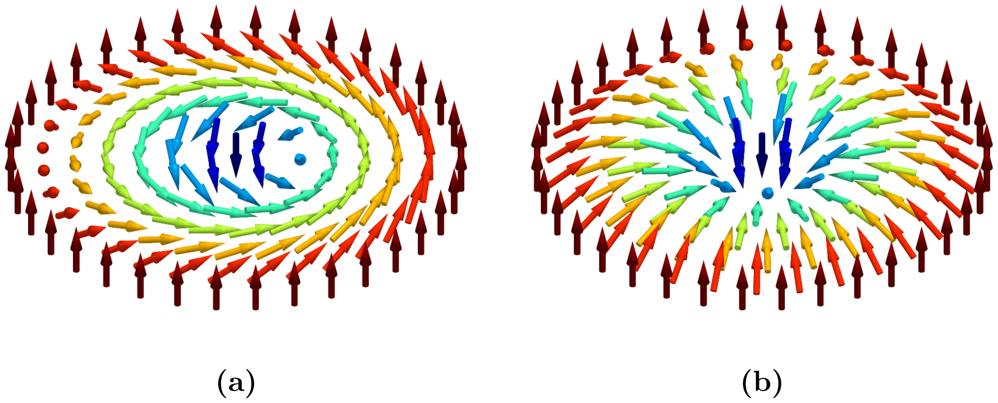

Figure 3.1: Illustrations of isolated magnetic skyrmions. Skyrmions are named by the type of domain wall created by a cut through the centre, the two types are (a) Bloch skyrmion and (b) a Néel skyrmion.

of the techniques outlined in Chap. 2, and how they can be used to probe a number of material properties.

The work in this chapter is based on published works in Ref. [117] and Ref. [118]. The DFT calculations were performed by myself and the data analysed alongside collaborators at the University of Durham. Muon site calculations were performed first by hand by myself and then as part of the testing of the MuFinder program [119].

3.1 Introduction

Skyrmions in condensed matter systems are magnetic topological objects that exhibit *vortex-like* spin configurations [50, 51]. A skyrmion is a spin texture characterised by a winding of magnetic moments around a central point. We can assign a numerical value to this winding by counting the number of times the spins wrap around a sphere. In the case of a skyrmion, the absolute value of this topological winding number must be greater than or equal to 1, and is a fundamental property of the skyrmion. Due to this topological feature, skyrmions cannot undergo any continuous transformation which results in a spin texture with trivial winding. In physical terms this relates to an energy barrier for the creation and destruction of magnetic skyrmions. Magnetic skyrmions have been the subject of much research as they promise to offer solutions in low energy data storage. Figure 3.1 shows examples of skyrmions found in condensed matter. Skyrmions are in general incommensurate with the unit cell of a material, with sizes ranging up to approximately 100 nm [120]. Even though the size of skyrmions means that direct calculation of the skyrmion state in spin-DFT is often impossible with current computers, spin-DFT can still be a useful tool in providing insight into the magnetic properties of these materials. DFT is invaluable as an aid to the experimental physicist as it can provide information about a material which is otherwise inaccessible by experimental techniques, such as density of states (DoS) and band structures of bulk materials. We can treat spin at three different levels in DFT: fully non-collinear with spinor wavefunctions, spin polarised with spin-up and spin-down densities, or finally we can assume all spins are paired using standard DFT.

3.1.1 Muon spin-spectroscopy

Experimental techniques for studying magnetic phenomena can be broadly put into two groups: first we have methods that look at the bulk magnetism such as neutron scattering [121], and we have methods that look at local magnetic effects such as μSR [122, 123]. In μSR, spin-polarised positive muons (μ^+) are fired at a sample where they come to a rest at some unknown location in the crystal. Being spin-half fermions, the muons precess in the local magnetic field of the sample, the frequency of this precession is proportional to the field strength. The muons have a short average lifespan, 2.19 μs [124], and eventually decay into a positron (e^+) and two neutrinos. The positron is emitted on average along the direction of the muon spin, and its decay direction is detected by an array of detectors placed around the sample. A typical experimental setup is shown in Fig. 3.2. By counting the proportion of positrons hitting the front and back detectors as a function of time, one can use the positron distribution to infer the spin direction of the implanted muons and use this to determine the magnetic field at the muon stopping site.

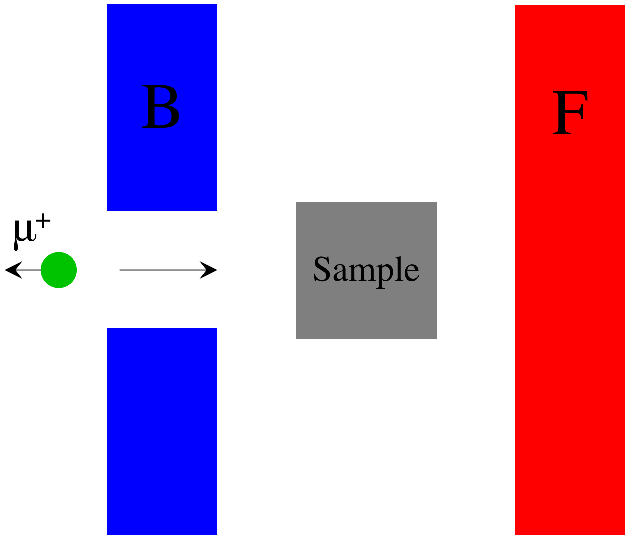

Figure 3.2: Schematic of a typical μSR experimental set up with a positive muon travelling from left to right. A positive muon enters a sample with its spin anti-aligned with its momentum. Front and back positron detectors are labelled F and B respectively.

3.1.2 DFT+μ

DFT has become the preeminent tool for seeking the muon stopping site in a technique dubbed density functional theory + μ (DFT+μ). Early work was carried out in the 1990s [125, 126, 127] before a new concerted effort in 2013 [128, 129, 130]. In a DFT+μ calculation, the muon is treated as a light H ion, i.e. a single proton. Muons are much heavier than electrons ($m_\mu \approx 200 m_e$) yet still not as heavy as a proton, this calls into question the use of the Born-Oppenheimer (BO) approximation since the muon may exhibit some quantum behaviour which we neglect. There have been some attempts to quantify this quantum nature [131, 128], however for the materials presented here we can assume these effects are small and proceed with the BO approximation. Since positive muons are used in μSR rather than negative muons, using a H ion models the muon as a proton impurity; these impurities have been long studied with DFT [132]. Implanted muons in μSR are ultra-dilute, therefore there is a vanishing probability that muons will interact with each other. Using periodic boundary conditions (PBC) means that if the calculation cell is too small, the muon will interact with its periodic image. It if often necessary to build a supercell if the unit cell is not sufficiently large to prevent self-interaction, this is common practice in impurity studies using DFT [133]. We can perform a series of geometry optimisation calculations (see Sec 2.6.4) with one μ^+ per cell initially placed at random in the unit cell. When all the forces have been resolved, the resultant μ^+ position is a candidate muon stopping site. By using the crystal symmetry, one can reduce the number of initial random positions by eliminating symmetry equivalent starting positions. Since a geometry optimisation is not a dynamical process, we gain no information about the stopping mechanism or the path taken to the site. Careful analysis of the resulting sites is important as many of the sites may not be realised experimentally, for example there may be a large energy barrier for a muon to enter a particular region of the crystal which is not reflected in the energy of the site. The final μ^+ positions will typically correspond to only a small number of muon stopping sites. However, we will have a set of distinct coordinates for each initial position. By looking at a combination of the symmetry of the sites and the total energy, it is possible to group the sites together and conclude which clusters are likely to represent the true physically muon stopping sites.

3.2 Muon sites in Cu_2OSeO_3

Skyrmions were discovered in the insulating, multiferroic material, Cu_2OSeO_3 in 2012 [134], sparking a cascade of new research [135, 136, 137]. Cu_2OSeO_3 is a cubic non-centrosymmetric material with the space group $P2_13$, it comprises tertrahedra of Cu^{2+} ions [138]. There are two inequivalent Cu ions which exist with a 3:1 ratio, the spins on each inequivalent Cu ion point in opposite directions forming a ferrimagnetic state [139]. The lack of inversion centre in Cu_2OSeO_3 leads to non-zero Dzyaloshinskii–Moriya interaction (DMI). Competition between the DMI and Heisenberg exchange is what leads to the stabilisation of Bloch skyrmions (Fig. 3.1a) in Cu_2OSeO_3 [136].

For skyrmion-hosting materials to have useful applications, it is important to understand the spin dynamics of skyrmions. There have been reports of skyrmion dynamics in Cu_2OSeO_3 in the GHz regime: counterclockwise, breathing, and clockwise modes [140]. There have also been reports in Cu_2OSeO_3 of THz excitations in high-energy magnon bands [141, 142, 143, 144]. To investigate potential dynamics which occur in the MHz regime one can employ longitudinal-field μSR, where the sample is placed into a magnetic field aligned along the muon beam direction. To fully understand these results one must know the magnetic field distribution at the muon site in these materials. As such, knowing where the muon stops, and the number of potential stopping sites can allow us to probe this distribution; if the magnetic structure of a material is known, we can use the muon stopping site coordinates to simulate the expected spectra and compare to experiment [145].

3.2.1 Computational methods

To ensure the calculations of the muon stopping sites are accurate, we performed convergence testing on Cu_2OSeO_3. The two parameters which contribute to the overall convergence are the plane-wave cut-off radius and the Monkhorst and Pack (MP) $\boldsymbol{k}$-point sampling, discussed in Sec. 2.5.4. The energy dependence of cut-off energy and $\boldsymbol{k}$-point grid size is mostly independent. Therefore while testing one parameter, the other may be held fixed. For $\boldsymbol{k}$-point convergence, it is sensible to use a moderate value for the cut-off energy as this typically leads to more accurate convergence. For the plane-wave cut off we performed non-spin polarised DFT calculations to obtain the total energy for a range of cut-off radii (energies) from 100 eV to 2900 eV. The final cut-off energy is chosen to be large enough to assume that the calculation is converged and we can compare the resultant total energies of the lower cut-off calculations to the final energy. The MP grid was held fixed at 3×3×3. When converging the MP grid, the cut-off energy was fixed at 600 eV and we calculated the total energy for all the odd cubic grids from 1×1×1 to 15×15×15. For the calculations of Cu_2OSeO_3 we have chosen an acceptable convergence tolerance of 10 meV/atom which allows us to resolve the energy differences of each muon site. Looking at Fig. 3.3,

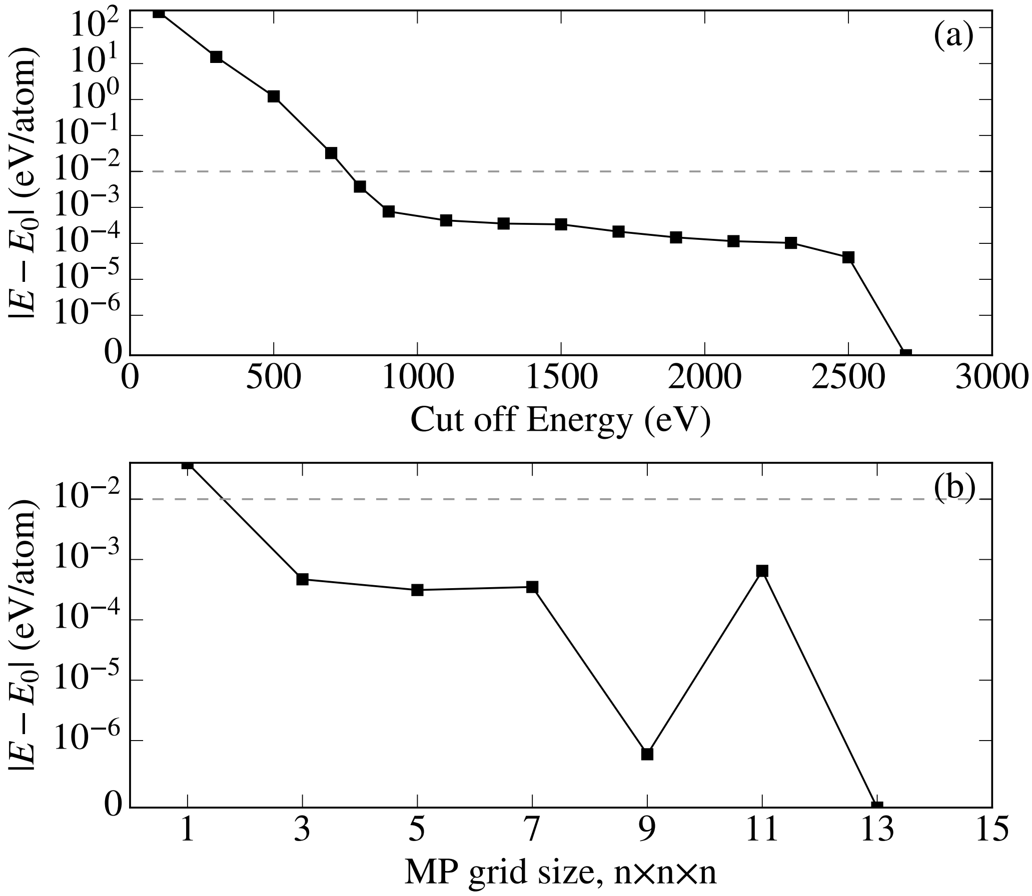

Figure 3.3: Convergence testing of (a) plane-wave basis set and (b) $\boldsymbol{k}$-point set for Cu_2OSeO_3. The grey dotted line shows a convergence criteria of 10 meV/atom. The energy E_0 is assumed to be the value obtained by using the highest convergence parameter in each case. Absolute values are used to enable the use of a log scale.

we see our convergence tolerance requires a plane-wave cut off of 800 eV and a 3×3×3 MP grid. As a useful rule of thumb, the larger the direct space unit cell, the smaller the MP grid required for good convergence. The change in energy as one increases the size of the MP grid is not monotonic, for Cu_2OSeO_3 this can be seen clearly in Fig. 3.3b.

To calculate the muon stopping sites in Cu_2OSeO_3, we performed DFT+μ calculations under the Perdew, Burke and Ernzerhof (PBE) exchange and correlation (xc) functional. We randomly generated 52 initial positions which sampled a symmetry-reduced region of the unit cell. These initial coordinates were generated using MuFinder [119]. To model the muon, we used an ultrasoft

H pseudopotential and included a charge of $+1e$ to account for the surplus electron. We experimentally determined lattice parameters of $a = b = c = 8.925$ Å [146] which we held fixed throughout the geometry optimisation calculations. This unit cell is large enough to limit self interaction between the muon and its periodic images, therefore we performed all calculations on the primitive cell. Due to the large size and the number of calculations required, using a supercell would be prohibitively computationally expensive.

3.2.2 Results and discussion

In Cu_2OSeO_3 we find that the positions of the muons are clustered into three distinct sites shown in Fig. 3.5, with coordinates given in Table 3.1. The sites we find are different from those previously reported in Ref. [147], which were found by locating the minima of the electrostatic potential in the crystal with no muon present. The energy distribution of the candidate sites is shown in Fig. 3.4. We can see that energy alone is not a sufficient metric for grouping together the sites. Although it is possible to see plateaus in the energy, they do not always correspond to a single site. By including the symmetry of the site, we are able to more effectively group the sites into meaningful clusters. From Fig. 3.4, we can see that only 27 of the 52 positions calculated make up the three sites, the remaining positions do not fit into these clusters, often having no symmetry relation with any other site. In addition, the remaining geometries are much higher in energy.

Sites 1 (Fig. 3.5b) and 2 (Fig. 3.5c) are each located approximately 1 Å from the nearest O ion, which is common for muon stopping sites due to the electronegativity of O [149]. All three sites have low relative energy differences, suggesting that they could all be occupied. However, site 3 is notable in that it sits along the Cu–O bond inside the tetragonal cage of Cu ions and causes significant distortion of the crystal, with the nearest Cu ion being displaced by approximately 0.7 Å, or 35% of the undistorted bond length. The initial muon positions that relax to this final site are mostly initialized inside the Cu cage.

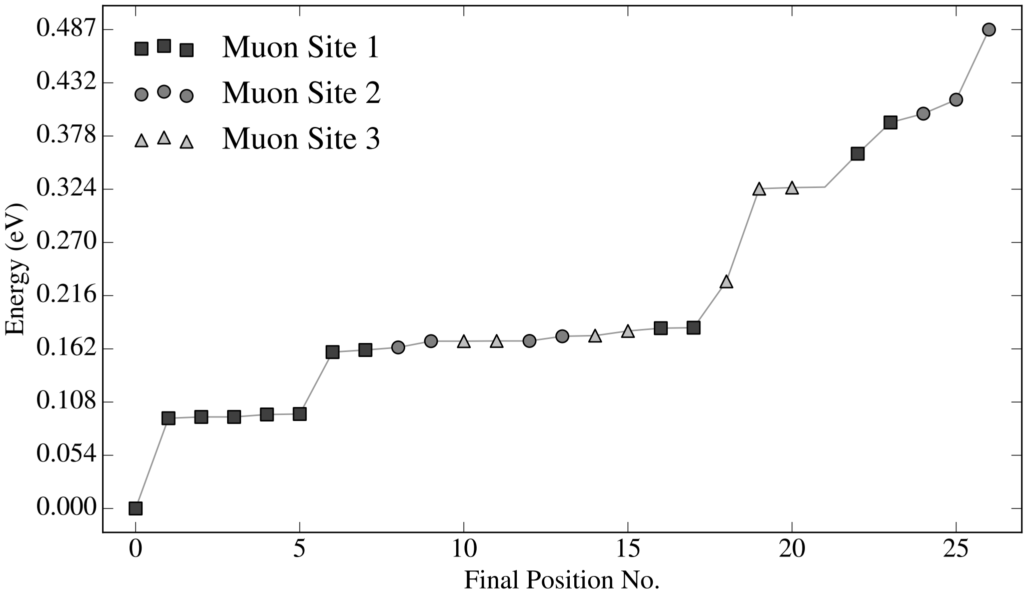

Figure 3.4: Energies of final muon position in Cu_2OSeO_3 grouped by muon site. Energy is a good, but not sufficient, predictor of the muon site clustering.

Due to the large local distortions of the crystal, it is unlikely a muon relaxing outside this tetrahedron would have sufficient energy to occupy this site due to the significant energy barrier to entering the cage. We therefore conclude that site 3 is unoccupied, leaving two sites which matches the experimental observations with zero-field μSR of two magnetic sites [147]. Muon sites 1 and 2 show no significant distortion of the Cu or Se ions. However, the O ions local to the muon are commonly shifted so as to be closer to the muon, sometimes by up to 1 Å.

Muon site	Fractional coordinates	Energy (eV)
1	(0.906, 0.590, 0.100)	0.0
2	(0.172, 0.365, 0.319)	0.09
3	(0.224, 0.670, 0.289)	0.15

Table 3.1: Fractional positions of the muon stopping sites in Cu_2OSeO_3. Energies are given relative to the lowest energy muon site.

Knowing the positions of the muon stopping sites from DFT allows for simulation of the magnetic field distributions of a known magnetic structure, hence allowing for comparison to experimental data [150]. There have been a

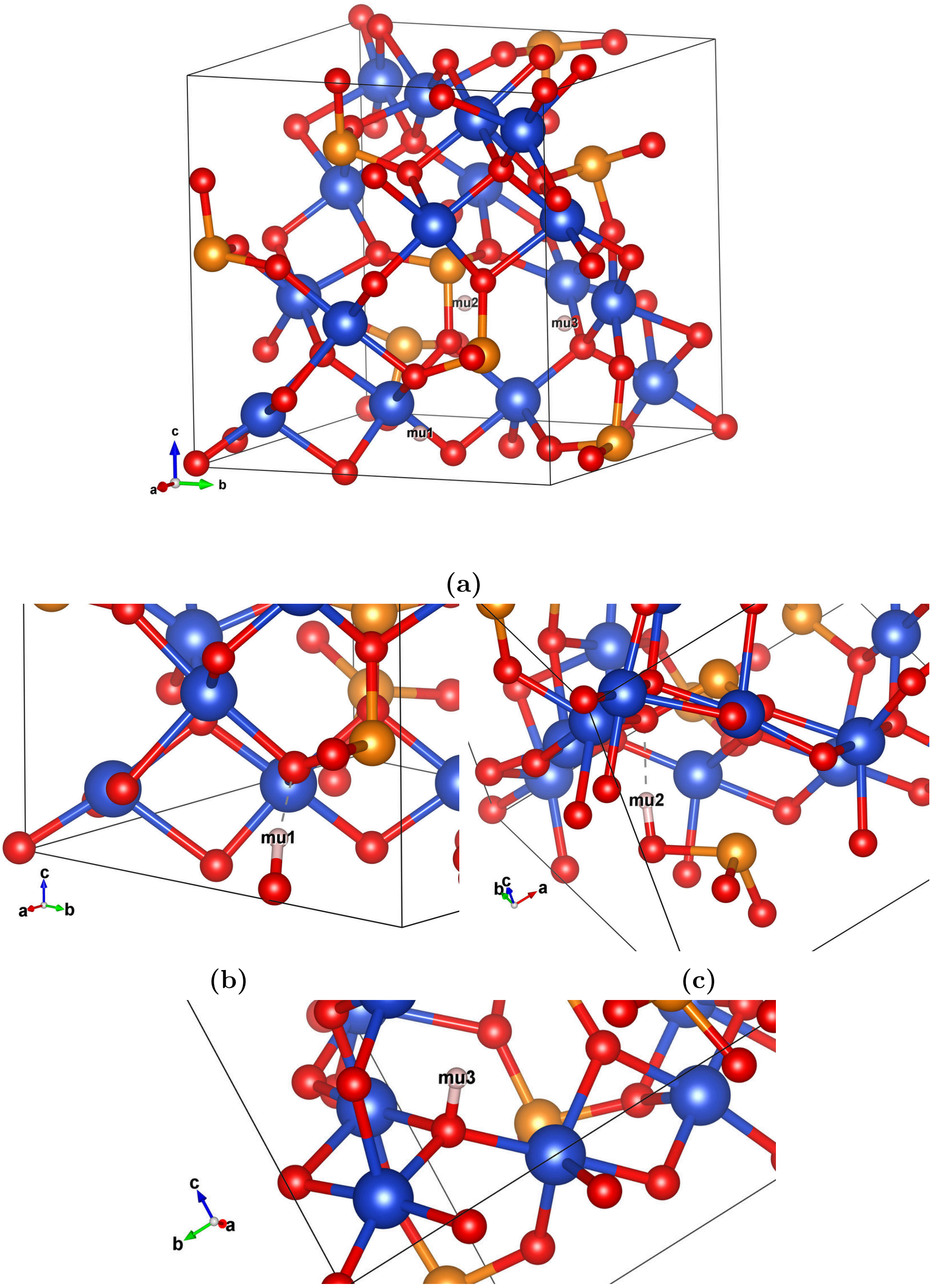

(a)

(b)

(c)

(d)

Figure 3.5: (a) Example positions of the three lowest energy stopping sites in Cu_2OSeO_3. Close up views of the local environment for (b) the lowest energy, (c) the second lowest energy and (d) the highest energy site which sits inside the Cu tetrahedron. Cu, O and Se atoms are shown in blue, red and orange respectively. Images produced with VESTA [148].

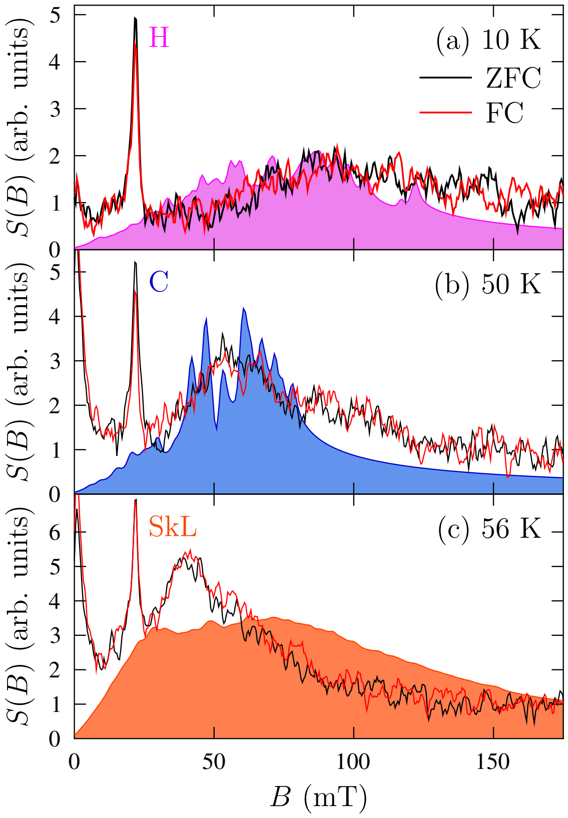

Figure 3.6: Spectral intensities as a function of magnetic field for three magnetic structures. (a) Helical, (b) conical and (c) skyrmion lattice. Black and red lines show distributions from μSR experiments for zero-field cooling and field cooling protocols respectively. Field distributions calculated from muon stopping sites in Table 3.1 shown in solid colour. Image reproduced from Ref. [118].

number of examples in the literature where calculating the field distributions from DFT+μ can aid in the interpretation of μSR data [117, 118, 151]. The muon stopping sites calculated above are used to produce field distributions for Cu_2OSeO_3, shown in Fig. 3.6. Simulated fields agree well with the experimental data for the conical and helical phases, and less well for the skyrmion phase. This suggests that there are dynamic processes on the muon timescale which are not captured in the simulation, which is calculated from a static magnetic state. We are able to make inferences about the dynamics of the skyrmion lattice as a result of first principles calculations, independently of analysing the μSR data.

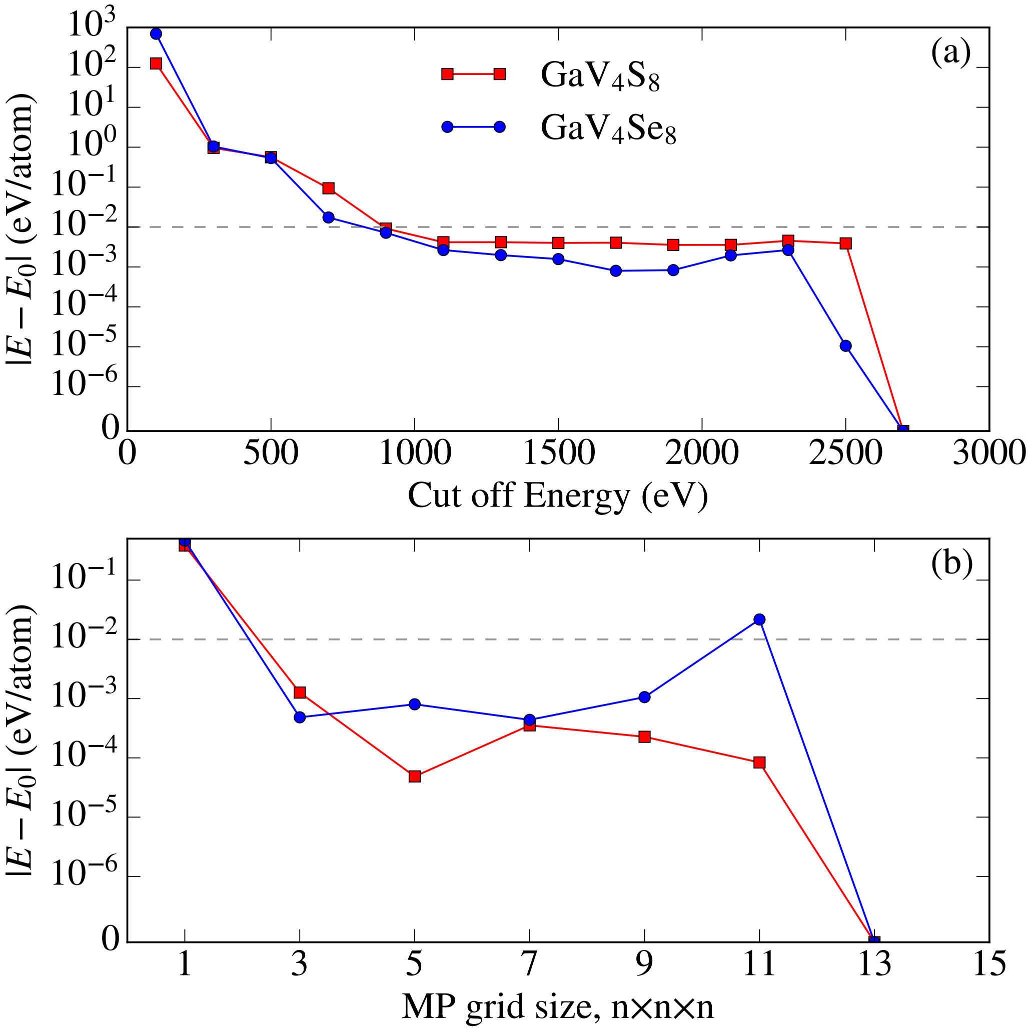

Figure 3.7: Convergence testing of (a) plane-wave basis set and (b) $\boldsymbol{k}$-point set for GaV_4S_8 (red) and GaV_4Se_8 (blue). The grey dotted line shows a convergence criteria of 10 meV/atom. The energy E_0 is assumed to be the value obtained by using the highest convergence parameter in each case. Absolute values are used to enable the use of a log scale.

3.3 Substitution in $GaV_4S_{8-y}Se_y$

Both GaV_4S_8 and GaV_4Se_8 host magnetic skyrmions, although rather than the Bloch type skyrmions found in bulk materials such as Cu_2OSeO_3 and MnSi [50], GaV_4S_8 and GaV_4Se_8 host lattices of Néel skyrmions (see Fig. 3.1b) [152, 153, 154]. As it is uncommon to find Néel skyrmions in bulk systems, the discovery has led to significant research over the last decade [155, 156, 157, 158].

Chemical substitution has been shown to have a positive effect on the stability and lifetime of Bloch skyrmions, as well as increasing the energy barrier for their creation [159, 160, 161]. High level substitution in $\mathrm{GaV_4S_{8-y}Se_y}$ ($y = 2, 4$) has been shown to destroy the skyrmion lattice and create a spin-glass state [162, 163]. We will present calculations of lower level substitution in $\mathrm{GaV_4S_{8-y}Se_y}$ ($y = 1, 7$), examining the effects it has on the spin density around the V tetrahedra.

3.3.1 Computational methods

We performed convergence calculations on both $\mathrm{GaV_4S_8}$ and $\mathrm{GaV_4Se_8}$ to determine the cut-off energy and $\boldsymbol{k}$-point grid required to produce accurate depictions of the spin density. Figure 3.7 shows the convergence testing of both materials. From the figure we can see that to converge the calculations to better than 10 meV/atom, we require a cut-off energy of 1000 eV and a 3×3×3 $\boldsymbol{k}$-point grid, which we have used for all calculations. Calculations carried out on substituted materials are performed with the same convergence parameters.

We performed all calculations on a primitive unit cell containing one formula unit of each material. There are four symmetry inequivalent S/Se sites in $\mathrm{GaV_4S_8}$ and $\mathrm{GaV_4Se_8}$ which are available for substitution, see Fig. 3.8. Experimentally, it is found that the substituent sits on different sites in $\mathrm{GaV_4S_8}$ than in $\mathrm{GaV_4Se_8}$ [164]. We consider two different possible substitution sites in each of $\mathrm{GaV_4S_8}$ and $\mathrm{GaV_4Se_8}$, performing DFT calculations with Se substituted onto the $\mathrm{S_3}$ and $\mathrm{S_4}$ sites in $\mathrm{GaV_4S_8}$ and with S substituted onto the $\mathrm{Se_1}$ and $\mathrm{Se_2}$ sites in $\mathrm{GaV_4Se_8}$. These sites have been shown to be those realised experimentally [164].

$\mathrm{GaV_4S_8}$ and $\mathrm{GaV_4Se_8}$ are both Mott insulators [165] exhibiting strongly correlated electron behaviour [166]. Both the local spin-density approximation (LSDA) and the PBE functional are not sufficient to capture all the correlated effects. When using DFT to study correlated materials, it is common to include a Hubbard U [167]. A Hubbard U acts as a local Coulomb repulsion localised on an atomic orbital. To correctly identify a value of U to use in our calculations,

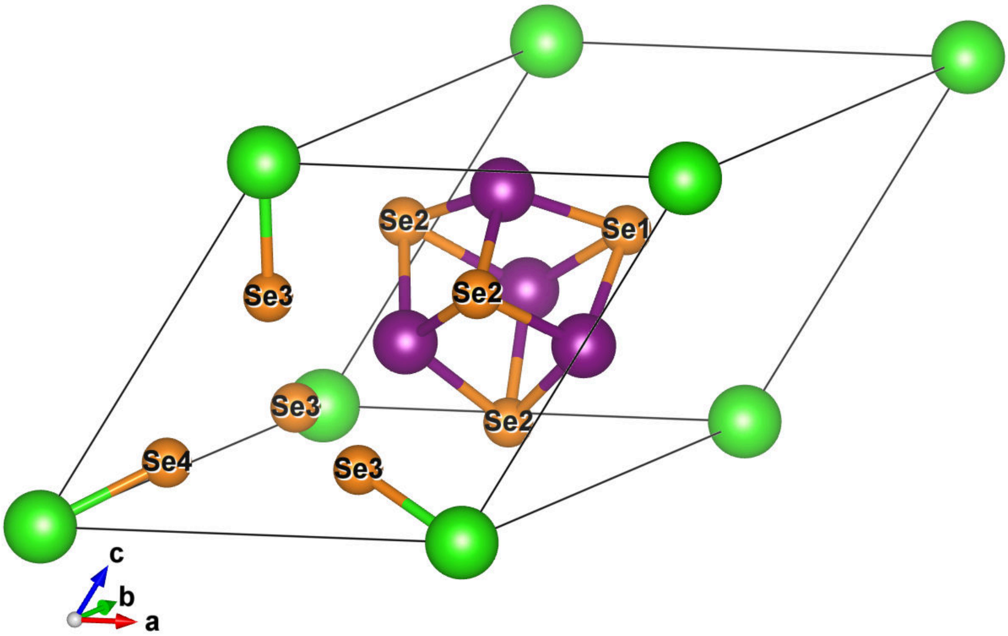

Figure 3.8: Crystal structure of GaV_4Se_8 showing the inequivalent Se sites. Ga, V and Se atoms are shown in green, purple and orange respectively.

we performed several PBE+U calculations on both GaV_4S_8 and GaV_4Se_8 over the range $U = 0.5$ to 3.0 eV on the V d-orbitals. Figure 3.9 shows the effect on the spin density per V ion in GaV_4S_8 and GaV_4Se_8 as a function of U. In both materials, the magnetisation reaches a constant value around $U = 2.5$ eV, which is the value used for all subsequent calculations. It has previously been reported that it is not possible to open the band gap using any physical value of U [168]. We have calculated the band structure of GaV_4S_8 with and without the Hubbard U to show this effect, see Fig. 3.10. With no Hubbard U, Fig. 3.10a, there is a clear metallic character to the bands with plenty of bands in both spin channels crossing the Fermi level. Including $U = 2.5$ eV, Fig. 3.10b, there is a clear change in the bands in both spin channels, opening up a gap in the spin-up channel. However, there are still bands crossing the Fermi level. We can see that by including the Hubbard U lifts the degeneracy of some of the spin-up

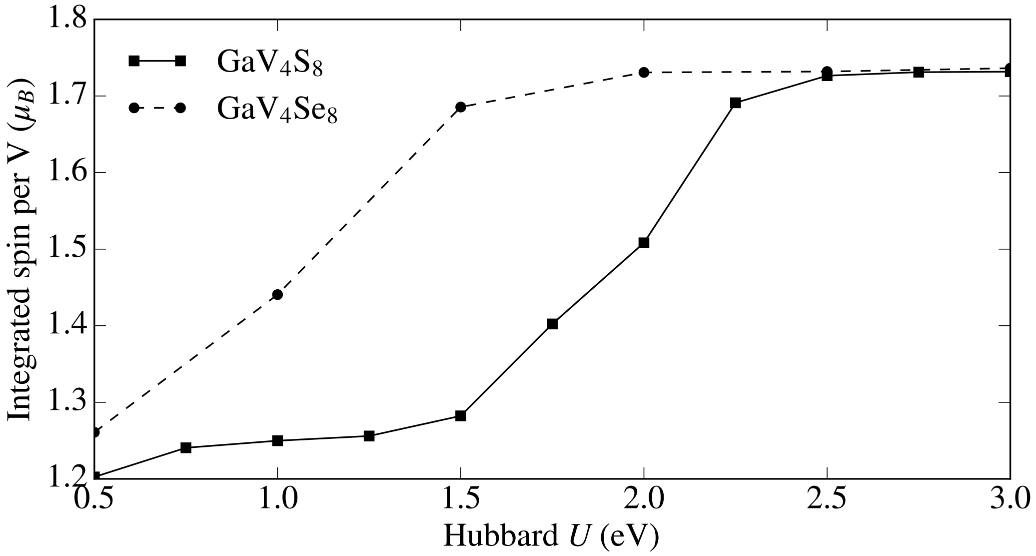

Figure 3.9: Integrated spin density per V ion as a function of Hubbard U in GaV_4S_8 and GaV_4Se_8. In each case the U has been added to the V d-orbitals.

and spin-down bands which contributes to the increase in magnetic moment.

3.3.2 Results and discussion

We wish to explain the changes in magnetism upon low-level substitution in $GaV_4S_{8-y}Se_y$ by performing spin-DFT calculations on the two materials corresponding to $y = 1$ and $y = 7$. Upon substitution we see changes in the distribution of spin density. We compare the difference in spin density in the substituted materials with the spin density in the pristine materials for both candidate substitution sites. Changes in the spin density for GaV_4S_8 and GaV_4Se_8 are shown in Fig. 3.11 and Fig. 3.12 respectively. Regardless of the choice of substitution site, we find that the changes in spin are more dramatic at the S end of the series. Changes in the spin density for $y = 1$ are spread throughout the crystal, inducing spin on the substituted Se and surrounding atoms as well as in the V tetrahedra. On the other end of the spectrum, changes in the spin density are more muted, either centring on the substituent or the V tetrahedra, but not both. We can see that in Fig. 3.11b and Fig. 3.12b that the change in spin density on the V ions retains d-orbital character. This indicates that there

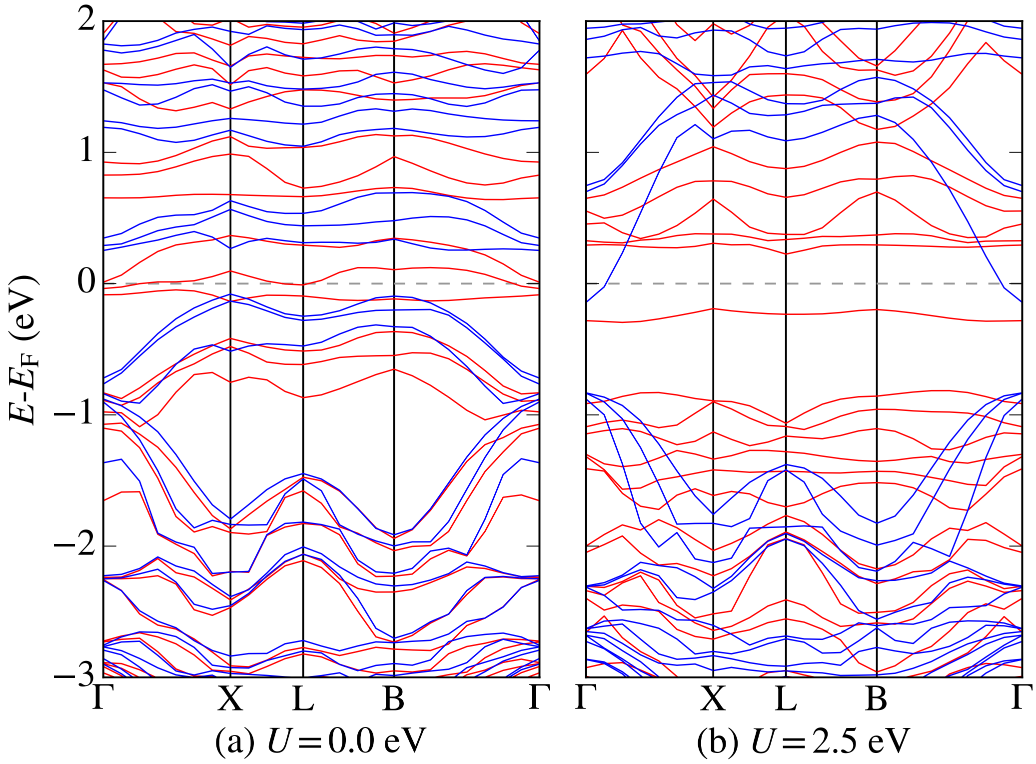

(a) $U = 0.0$ eV (b) $U = 2.5$ eV

Figure 3.10: Band structure of GaV_4S_8 (a) without inclusion of a Hubbard U and (b) with a Hubbard U of 2.5 eV on the V d-orbitals. Spip-up bands are shown in red and spin-down bands are shown in blue. Plots produced using dispersion.py [104] (See App. C).

is simply a scaling in the amount of spin on these ions, this is notable in the case of $y = 7$ (Fig. 3.12b) as this is occurs despite the substitution site being located close to the V tetrahedra. It has been reported [164] that there is a decrease in the magnetisation upon substitution which occurs faster in the S substituted material. Our calculations reflect that the changes in spin density are not uniform upon substitution at each end of the series.

Analysis of experimental measurements taken using μSR find two internal fields in GaV_4S_8 with a third field appearing upon substitution. This third field is larger than the next highest field by a factor of 3, suggesting a change in the magnetic moments or a change in spin distribution [117]. Muon stopping sites have previously been reported in this material [163]. One of the muon stopping sites lies close to the V tetrahedron, which would probe this change in spin magnitude. The changes in spin distribution calculated around

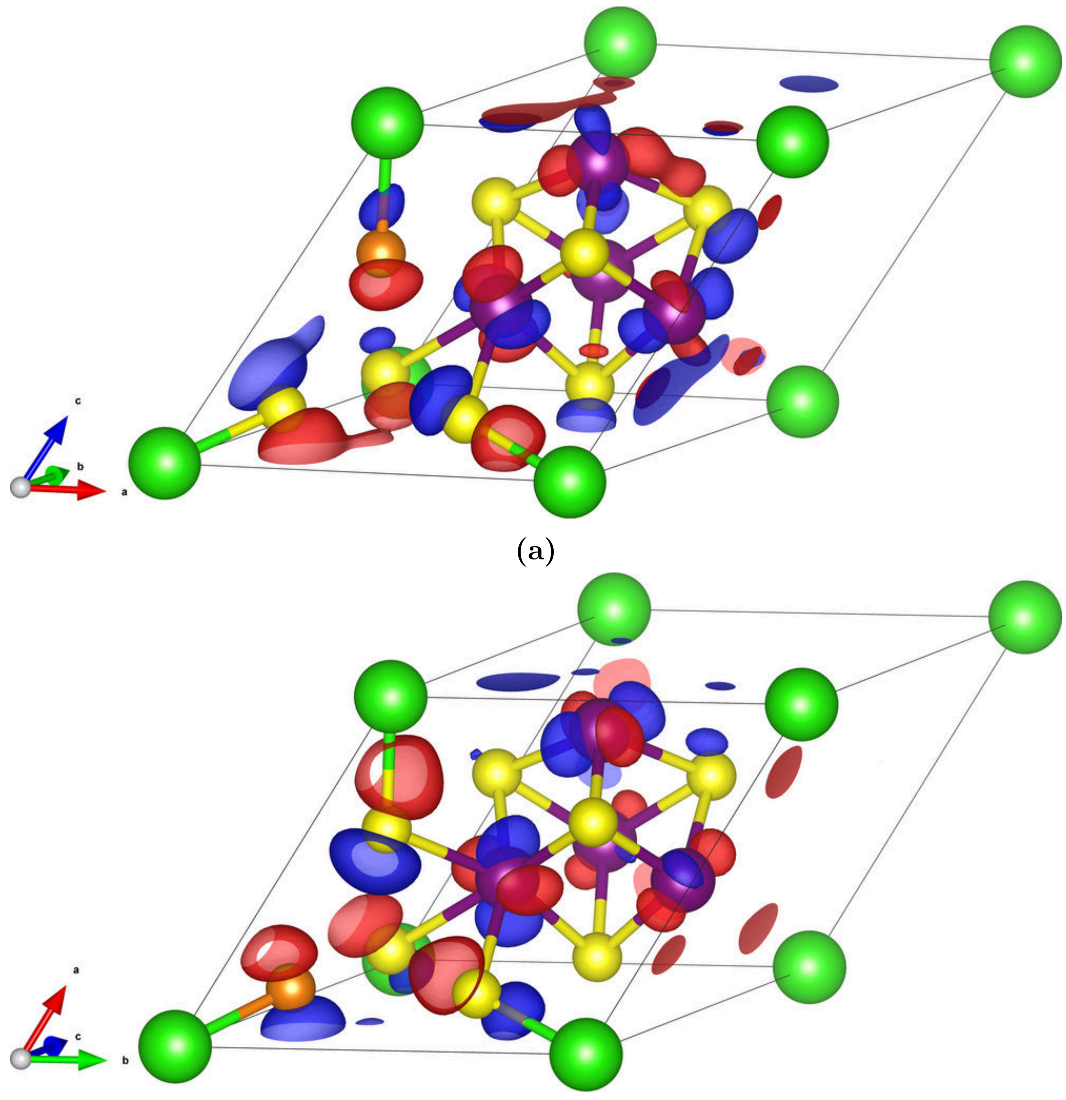

(a)

(b)

Figure 3.11: Difference in spin density between GaV_4S_8 and $GaV_4S_{8-y}Se_y$, $y = 1$ with Se substitution on the (a) S_3 and (b) S_4 sites. Ga, V, S and Se atoms are shown in green, purple, yellow and orange respectively. Images produced with VESTA [148].

the V tetrahedra in GaV_4S_8 could provide an explanation for this increase in the measured field. Further details about the experimental work can be found in Ref [117]. Additionally, by changing the spin distribution around V ions in both GaV_4S_8 and GaV_4Se_8, it is possible that this could induce changes to the exchange pathways. Skyrmions are formed by competing exchange interactions and changing these pathways could cause the glasslike magnetic ground state found in $GaV_4S_{8-y}Se_y$ for $y = 2$ and $y = 4$ [163]. In reality, the level of

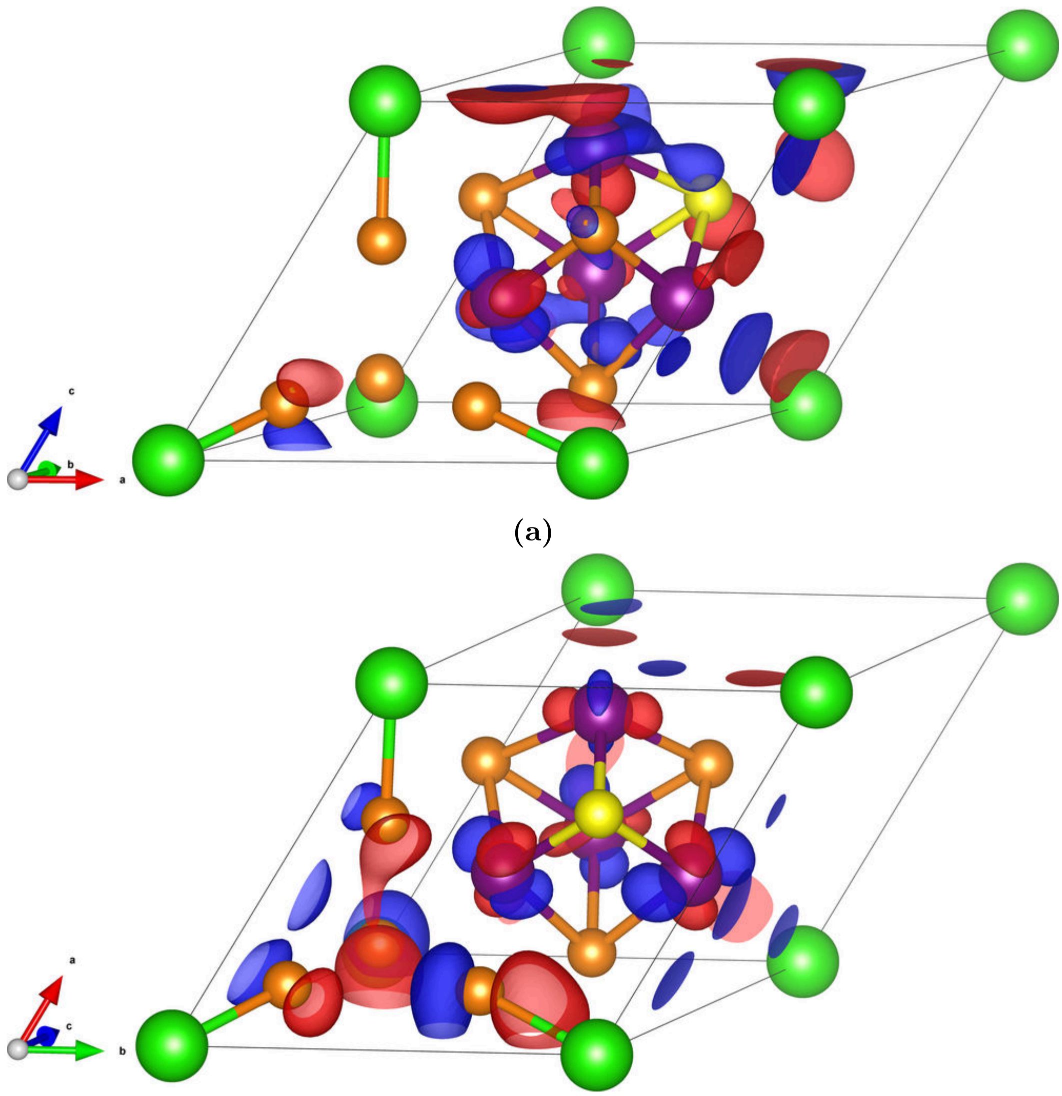

(a)

(b)

Figure 3.12: Difference in spin density between GaV_4Se_8 and $GaV_4S_{8-y}Se_y$, $y = 7$ with S substitution on the (a) Se_1 and (b) Se_2 sites. Ga, V, S and Se atoms are shown in green, purple, yellow and orange respectively. Images produced with VESTA [148].

substitution would not be necessarily uniform throughout the crystal. Different regions in the crystal could have higher levels of substitution which would exhibit the changes in spin density which we see from spin-DFT calculations, while other regions may more closely resemble the pure crystal. As skyrmions are long range topological objects, higher levels of substitution are more likely to interfere with the exchange mechanisms over a larger region of the skyrmion lattice.

3.4 Conclusions

In conclusion, we have shown how spin-DFT can be used to give a deeper understanding of experimental data, and help to explain phenomena in complex magnetic systems. Even when the magnetic structure of a material is beyond the current capabilities of spin-DFT calculations, we can examine the electronic structure to look for the physics which underpins the long range magnetism.

We have introduced the DFT+μ technique used to complement the analysis of μSR experiments, and showed how we can use standard DFT methods to locate the muon stopping site, something which is usually inaccessible experimentally. We found that there are three distinct muon stopping sites in the skyrmion host, Cu_2OSeO_3, although in reality only two of the sites are occupied, consistent with experimental findings. The third site is located within a Cu tetrahedron which would likely be inaccessible to an implanting muon.

We have also showed how spin-DFT can give us information about the distribution of the electrons and their spin density. We presented calculations on the chemical substitution of the Mott insulators GaV_4S_8 and GaV_4Se_8. We showed that changes in the spin density are greater upon substitution at the S end of the series. For $y = 1$, the changes in the spin density affect the entire crystal, both around the substituent and inside the V tetrahedra. At the other end of the series, the changes in spin density are less pronounced. Changes in the spin density surrounding the V ions could indicate an altering of the exchange pathways, explaining why substitution destroys the skyrmion lattice in these materials in favour of a glasslike state.

Chapter 4

Magnetic coupling in $[Cu(pyz)_{0.5}(gly)]ClO_4$

'Twas brillig, and the slithy toves
Did gyre and gimble in the wabe:
All mimsy were the borogoves,
And the mome raths outgrabe.
—Lewis Carroll,
The Jabberwocky

In this chapter, we will present results of density functional theory (DFT) calculations on the effects of pressure on the magnetic interactions in a molecular material, $[Cu(pyz)_{0.5}(gly)]ClO_4$ [169]. DFT gives us the ability to study the energy of different magnetic configurations, by comparing these energies, one can extract the strength of the exchange coupling between magnetic ions. In this chapter we will examine how one can calculate coupling parameters from DFT and apply the method to study the effects of pressure on the magnetic behaviour of $[Cu(pyz)_{0.5}(gly)]ClO_4$.

The work in this chapter is based on calculations performed by myself at the University of Durham and is yet to be published. Analysis of the results is my own, with useful input from collaborators at the University of Durham and Warwick University. X-ray crystallography measurements were carried out by collaborators at Warwick University.

4.1 Introduction

4.1.1 Magnetic exchange

In Chap. 2 we discuss the Schrödinger equation and the Hamiltonian which links the equation to a physical system. There is no mention of magnetism explicit in the Hamiltonian we discussed above; all magnetic behaviours arise due to Coulomb interactions between electrons. However, rather than trying to understand all of the complexities of the many-body Hamiltonian, we wish to examine only the parts which determine magnetic effects. We are often able to apply a low energy model to our Hamiltonian which approximates magnetic interactions. Starting with a two electron system, comparing the difference between a singlet $[|\uparrow\downarrow\rangle]$ and a triplet $[|\uparrow\uparrow\rangle, |\downarrow\downarrow\rangle, \frac{1}{\sqrt{2}}(|\uparrow\downarrow\rangle + |\downarrow\uparrow\rangle)]$ state, we arrive at an effective Hamiltonian for the spin part of the wavefunction [5],

$$\hat{\mathcal{H}}^{\text{spin}} = -J\boldsymbol{S}_1 \cdot \boldsymbol{S}_2, \tag{4.1}$$

where $\boldsymbol{S}_{1(2)}$ is the spin of electron 1(2) and J is a constant which describes the magnitude of the exchange between each pair of spins. This can be extended to many-body systems, known as the Heisenberg model [5],

$$\hat{\mathcal{H}}^{\text{spin}} = \sum_{i>j} J_{i,j}\boldsymbol{S}_i \cdot \boldsymbol{S}_j, \tag{4.2}$$

where $\boldsymbol{S}_i$ is the spin on the i^{th} magnetic ion and $J_{i,j}$ is the exchange interaction strength between each pair of ions. The negative sign has been absorbed by $J_{i,j}$ such that $J > 0$ corresponds to antiferromagnetic alignment [170]. This model can be used to find the interaction strengths between each magnetic ion. The nearest neighbour interactions often dominate and therefore the exchange parameters for more distant interactions can often be approximated as zero.

4.1.2 Magnetism in molecular crystals

When looking for magnetic effects in condensed matter, the traditional place to look is in inorganic materials such as Fe, Ni, Co and their alloys. However, organic materials that host long range magnetism have become a relevant class for studying magnetic behaviour [171]. To study particular effects in magnetism, such as the effects of dimensionality, using traditional inorganic magnets one needs to find a material which exhibits the desirable features [169]. Depending on the magnetic interactions in the material, the magnetic dimensionality can be different to the structural dimension [172]. In a molecular magnet, the interactions are between molecules rather than atoms, and as such tend to be weaker due to their separations. Therefore, by either growing the crystals under specific conditions, or by applying external pressures, one can change the structure and alter the magnetic interactions [171, 172]. This ability to tune the magnetic interactions allows such materials to be a testing ground for new physics and the search for new magnetic states. In particular, applying pressure can cause a transition across a quantum critical point (QCP), for example this could lead to a change in the magnetic state of the system [173, 174].

An example of a molecular crystal which displays long range magnetic ordering is $[Cu(pyz)_{0.5}(gly)]ClO_4$ (pyz = pyrazine = $C_4H_4N_2$; gly = glycine = $C_2H_5NO_2$) [169, 175]. $[Cu(pyz)_{0.5}(gly)]ClO_4$ is formed of corrugated sheets of weakly coupled antiferromagentic $S = 1/2$ Cu–pyz–Cu dimers, which are each connected to 4 other dimers through a glycine group. Each molecular sheet is connected to other layers through ClO_4 molecules. The structure is shown in Fig. 4.1.1a. Previous studies of the magnetism in $[Cu(pyz)_{0.5}(gly)]ClO_4$ show that the ground state shows no long-range magnetic order [169].

There are three dominant exchange pathways in $[Cu(pyz)_{0.5}(gly)]ClO_4$: the intradimer exchange interaction, J_{pyz}, is mediated by the pyrazine ring joining the Cu dimers; the main interdimer exchange, J'_{gly} is mediated through the glycine ligands and the second interdimer coupling mediated though the ClO_4, with coupling strength $J''_{\mathrm{ClO_4}}$. These exchange pathways are shown in Fig 4.1.1.

It has previously been shown that $J''_{\mathrm{ClO_4}}$ is much weaker than the other two couplings [175] resulting in a quasi-two-dimensional magnetic structure, where the magnetism is constrained to the plane of the corrugated sheets.

By applying pressure to a molecular system, one can reduce the energy gap between the singlet and triplet state [171, 170, 176, 174]. It may be possible to apply enough pressure to cause a flip in the singlet and triplet energy levels and thereby switch the magnetic coupling from antiferromagnetic to ferromagnetic. We present a first principles study on the effects of pressure on the magnetism and structure of the molecular magnetic material, $[\mathrm{Cu(pyz)_{0.5}(gly)}]\mathrm{ClO_4}$. We will show how pressure causes changes in the structure which alter the exchange pathways.

4.2 Computational methods

To determine the effects of pressure on the exchange couplings in $[\mathrm{Cu(pyz)_{0.5}(gly)}]\mathrm{ClO_4}$, we performed spin-density functional theory (spin-DFT) calculations treating exchange and correlation (xc) with the Perdew, Burke and Ernzerhof (PBE) functional [69]. Calculations were converged to better than 1 meV/atom using a plane wave cutoff of 1500 eV and a 5×5×3 Monkhorst and Pack (MP) $\boldsymbol{k}$-point grid [85]. This level of convergence is smaller than the energy gaps between different states, allowing us to confidently differentiate their relative energies. The experimental structure when treated under the generalised gradient approximation (GGA) resulted in unphysical pressures which prevented the stabilisation of any long-range magnetic states. To obtain a crystal structure that is consistent with DFT, we performed a geometry optimisation calculation allowing all atoms and cell parameters to relax. From the resulting DFT-relaxed cell, a further set of geometry optimisation calculations were performed with the addition of isotropic pressure applied over a range of 0 to 60 kbar [177]. As before, all unit cell parameters were allowed to relax such that we can determine changes to the structure due to the external pressure.

Using a single unit cell rather than a supercell, we are not able to describe

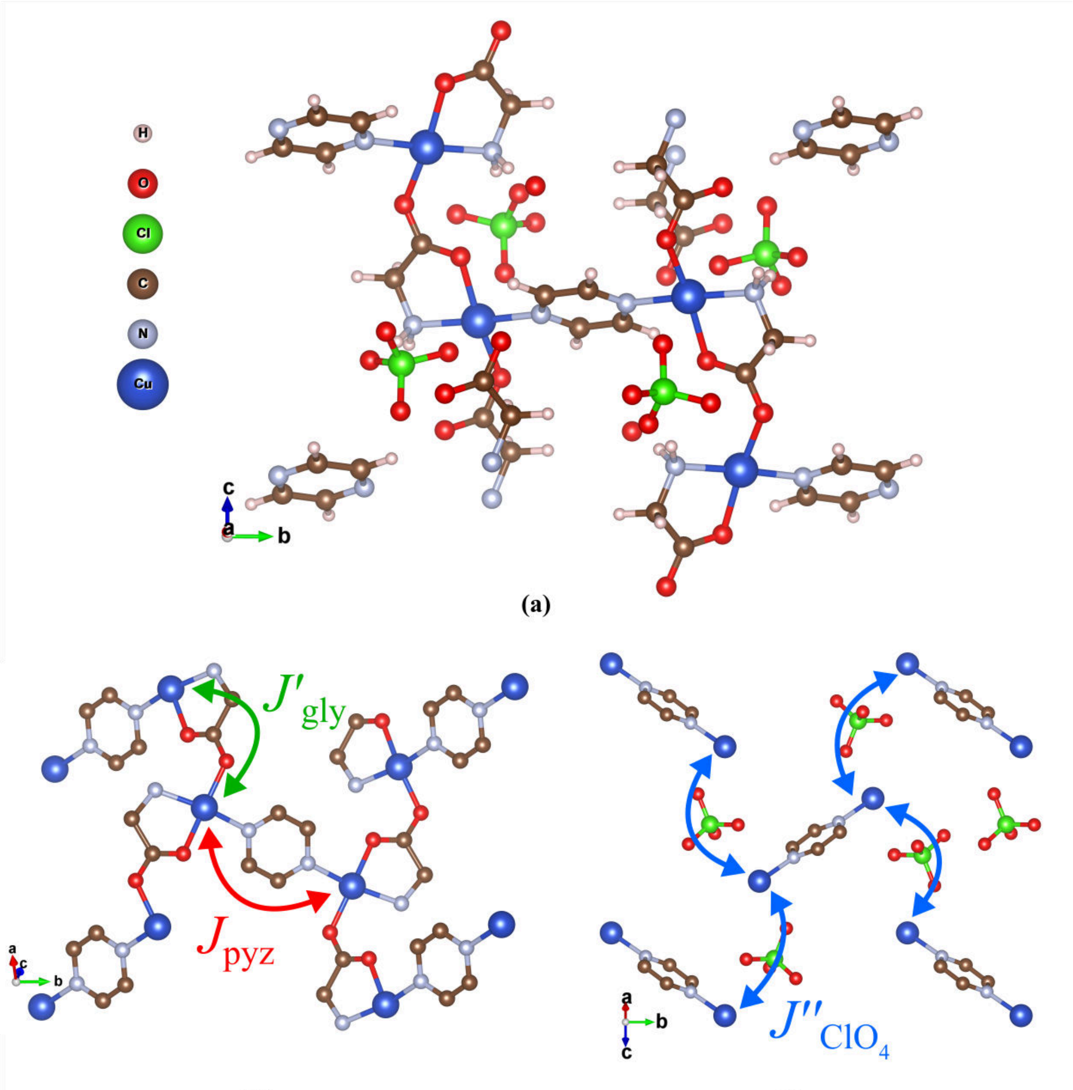

(a)

(b) (c)

Figure 4.1.1: (a) Structure of molecular magnetic material, $[\mathrm{Cu(pyz)_{0.5}(gly)]ClO_4}$. (b) Cu—pyrazine and Cu—glycine groups showing their respective exchange pathways, H and $\mathrm{ClO_4}$ groups have been removed for clarity. (c) Exchange pathways mediated by the $\mathrm{ClO_4}$ groups, H and pyrazine rings have been removed for clarity. Images produced with VESTA [148].

all three of the exchange pathways discussed above. Instead we consider two exchange coupling constants, the intradimer coupling $J_0 = J_{\mathrm{pyz}}$ and an effective interdimer coupling J_{eff}, where $J_{\mathrm{eff}} = 4(J'_{\mathrm{gly}} + J''_{\mathrm{ClO_4}})$. The four in the above equation accounts for the fact that there are four times as many interdimer pathways as intradimer pathways per unit cell. A supercell would be required to extract all three coupling constants. However, due to the large number of

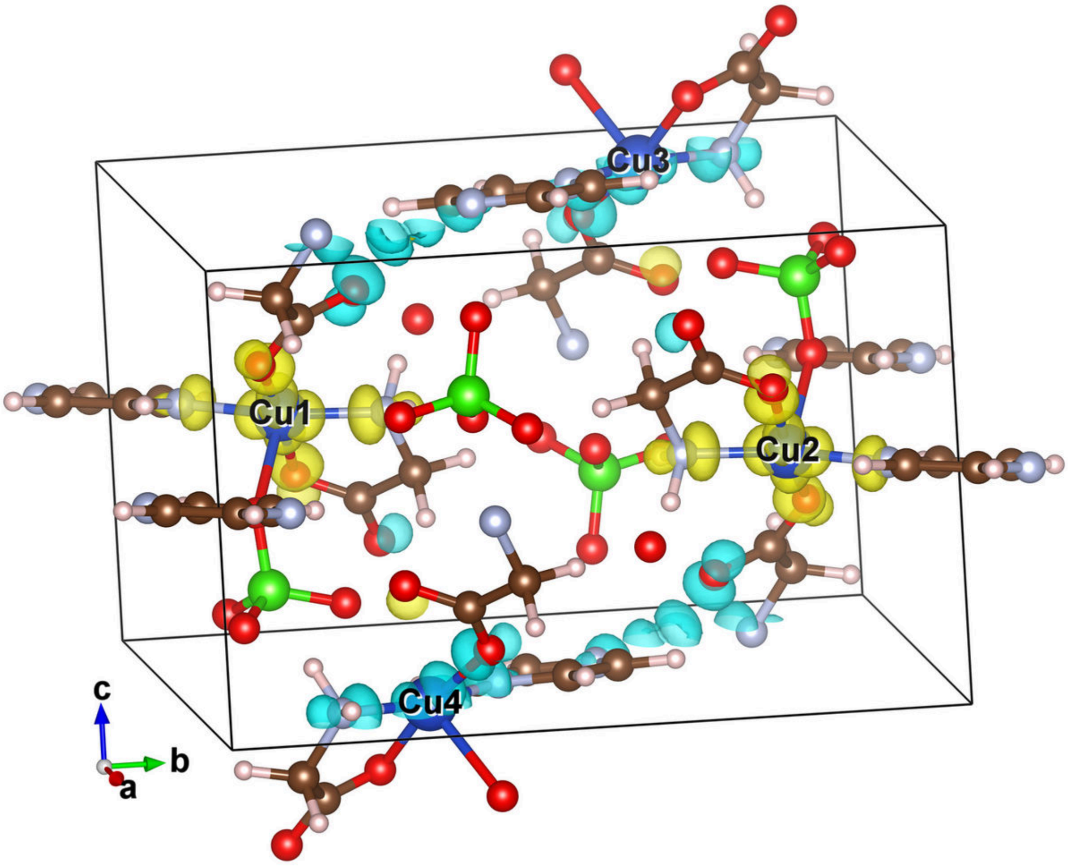

Figure 4.2.1: Spin density of the antiferromagnetic ground state of $[Cu(pyz)_{0.5}(gly)]ClO_4$. Labels on the Cu ions refer to the order of ions considered in each different spin configuration. Images produced with VESTA [148].

atoms in the single unit cell, the computational costs would be prohibitively large.

Calculating exchange constants using DFT involves comparing the total energies of different spin states. From a single pair of electrons, we can calculate the difference in energy between the singlet and the triplet state [178],

$$J = E_{\mathrm{T}} - E_{\mathrm{S}}. \tag{4.3}$$

One can then extend this to a system of multiple atoms by considering pairwise interactions [179]. We can express the total energy of any spin state in terms of J_0 and J_{eff},

$$E = J_0 \sum_i \boldsymbol{S}_{1,i} \cdot \boldsymbol{S}_{2,i} + J_{\mathrm{eff}} \sum_{m,n,i,j} \boldsymbol{S}_{m,i} \cdot \boldsymbol{S}_{n,i} + E_0, \tag{4.4}$$

where i and j label the dimers and m and n represent each magnetic state. Alongside the two exchange parameters, J_0 and J_{eff}, there is a third unknown, E_0, which describes all of the energy contributions common to each state and not related to the arrangement of spins. There is no inversion centre in $[\mathrm{Cu(pyz)_{0.5}(gly)}]\mathrm{ClO_4}$, introducing the possibility of non-zero Dzyaloshinskii–Moriya interaction (DMI) which may contribute to the spin Hamiltonian. However, we perform all calculations using collinear spin-DFT which precludes the computation of the DMI which favours canting of non-collinear spins

To calculate the coupling constants, we follow the method outlined in Ref. [180]. A single unit cell containing four Cu ions was used in all calculations of the spin configurations. This allows us to extract 16 different magnetic states. However, as the system is degenerate with respect to a global spin flip, only eight of the possible states are unique. We are able to save on the computational effort by not calculating the ferromagnetic state, as this is not necessary to calculate the two effective exchange parameters. Using the seven configurations, we can formulate a set of simultaneous equations, shown in Table 4.1. We have more equations than unknown parameters; as the calculations provide an over-complete description of the possible spin states, spin configurations that are equivalent in our model can be used to estimate the uncertainty in the couplings. Using the variance in the total energies of equivalent configurations, we are able to calculate the standard error.

For each unit cell relaxed under pressure, a full set of magnetic calculations were performed. In each case, the magnetic ions were initialised with spins corresponding to the desired spin state. Self-consistent field (SCF) calculations were performed to calculate the total energy of each configuration using the density mixing (DM) scheme to more reliably preserve the spin initialisations

Spin configuration	Energy
$\uparrow\downarrow\uparrow\uparrow$	E_0
$\uparrow\downarrow\downarrow\uparrow$	$2J_0 + J_{\text{eff}} + E_0$
$\uparrow\downarrow\downarrow\downarrow$	E_0
$\uparrow\uparrow\downarrow\uparrow$	E_0
$\uparrow\uparrow\uparrow\downarrow$	E_0
$\uparrow\downarrow\uparrow\downarrow$	$2J_0 - J_{\text{eff}} + E_0$
$\uparrow\uparrow\downarrow\downarrow$	$-2J_0 + J_{\text{eff}} + E_0$

Table 4.1: Energies of configurations of spins in $[\mathrm{Cu(pyz)_{0.5}(gly)}]\mathrm{ClO_4}$ in terms of the electronic portion of the energy E_0 and the intradimer, J_0, and interdimer, J_{eff}, couplings. The spins of each configuration correspond to the label given to each Cu ion shown in Fig. 4.2.1.

throughout the minimisation. Once each calculation had finished, the final spin state was confirmed by examining the Mulliken population analysis. An example of one of the antiferromagnetic calculations is shown in Fig. 4.2.1. The total energies can be used to form a matrix relating to the simultaneous equations in Table 4.1, which can then be solved to determine the coupling parameters.

4.3 Results and discussion

4.3.1 Structural effects

We find that by relaxing the experimental structure at ambient pressure, the unit cell volume calculated from DFT is approximately 25% larger than found experimentally. This increase is consistent with the known properties of GGAs [67]. The increase is not uniform across all unit cell directions. We find increases of 3.1%, 6.7% and 17% in the a, b and c directions respectively, which is expected due to the different bonding mechanisms present each direction. These effects may be exaggerated when compared to experiment. The covalent bonds that form the corrugated sheets of dimers are more accurately described using GGA DFT than the weaker interdimer bonds [181, 182], this has the effect of increasing the interdimer spacing. DFT does not capture Van

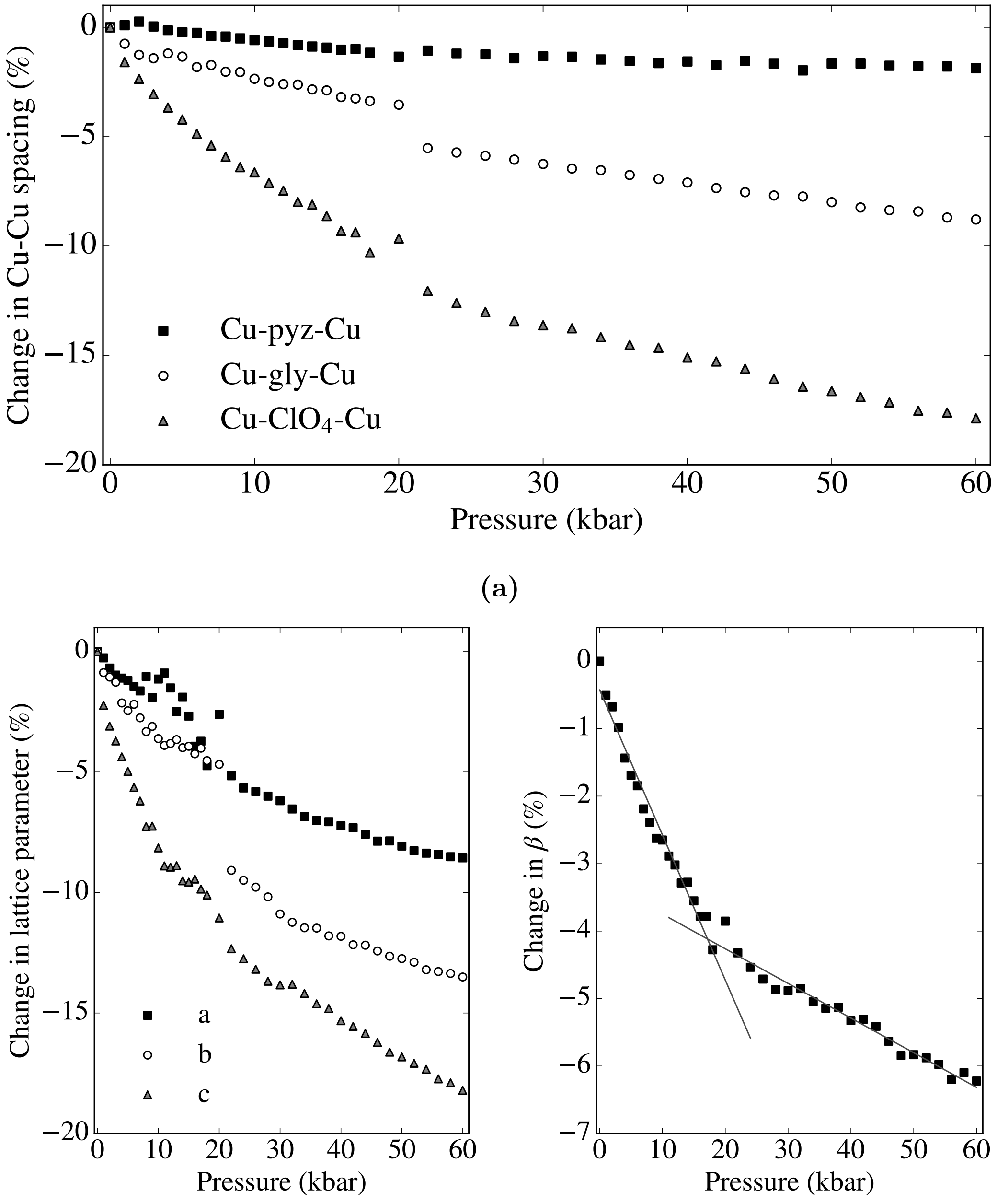

(a)

(b)

(c)

Figure 4.3.1: Effect of pressure on the structure of $[Cu(pyz)_{0.5}(gly)]ClO_4$. (a) Percentage change in distance between Cu ions along the exchange pathways as a function on pressure applied isotropically. (b) Percentage change in lattice parameters as a function of pressure. (c) Percentage change in unit cell angle β with pressure, fitting lines are added to highlight the distinct regimes.

der Waals (VDW) forces, while it may be possible to include these effects empirically, this would be unnecessary at higher pressures.

The effects of externally applied pressure on the unit cell of

$[Cu(pyz)_{0.5}(gly)]ClO_4$ are shown in Fig. 4.3.1. The distances between Cu ions along exchange pathways are shown in Fig. 4.3.1a, where it can be seen that the most dramatic changes occur between the Cu ions along the exchange pathway mediated by ClO_4 (J''_{ClO_4}). The Cu–Cu distance is decreased by approximately 1 Å with the application of 20 kbar. There is a small discontinuous change in the glycine exchange pathway, in the order of 3%. The Cu spacing along the Cu–pyz–Cu direction changes the least, less than 2% over the entire range, due to the covalent bonding. All lattice parameters decrease with applied pressure, with the decrease being continuous for a and c. However, there is a discontinuity in b at approximately 20 kbar (Fig. 4.3.1b). The discontinuity in b corresponds to a change in the unit cell angle β, and while β always decreases with increasing pressure, the rate of decrease slows at around 20 kbar, as seen in Fig. 4.3.1c.

Further changes to the structure are shown in Fig. 4.3.2 which shows changes in various angles between the molecular units. The angle between the bonds connecting the Cu ions to the pyrazine ligands, termed the pyrazine kink angle (Fig. 4.3.2a), is essentially constant across the entire range of applied pressures. The rigidity of the dimer is due to the covalent bonding. We see more dramatic changes in the other molecular angles shown in Fig. 4.3.2b-d. The largest change is observed in the interlayer dihedral angle (Fig. 4.3.2b). We calculate a sharp decrease in the dihedral angle around 20 kbar, the same pressure at which we see changes to the lattice. At high pressures, the dihedral angle becomes mostly constant around 112°, a change of approximately 15° from ambient pressure. The angle between the Cu ion and the pyrazine ligand, called the pyrazine twist angle (Fig. 4.3.2c) decreases with applied pressure, although the overall change is small at less than 2°. We see similar changes in the angle between the pyrazine and glycine ligands, Fig. 4.3.2d.

There are two main factors which contribute to the structural changes we see at around 20 kbar. Firstly, the change in the interlayer dihedral angle allows for more efficient packing along the b axis. This also accounts for the discontinuous change in the lattice parameter b. Secondly, a change in the orientation of ClO_4

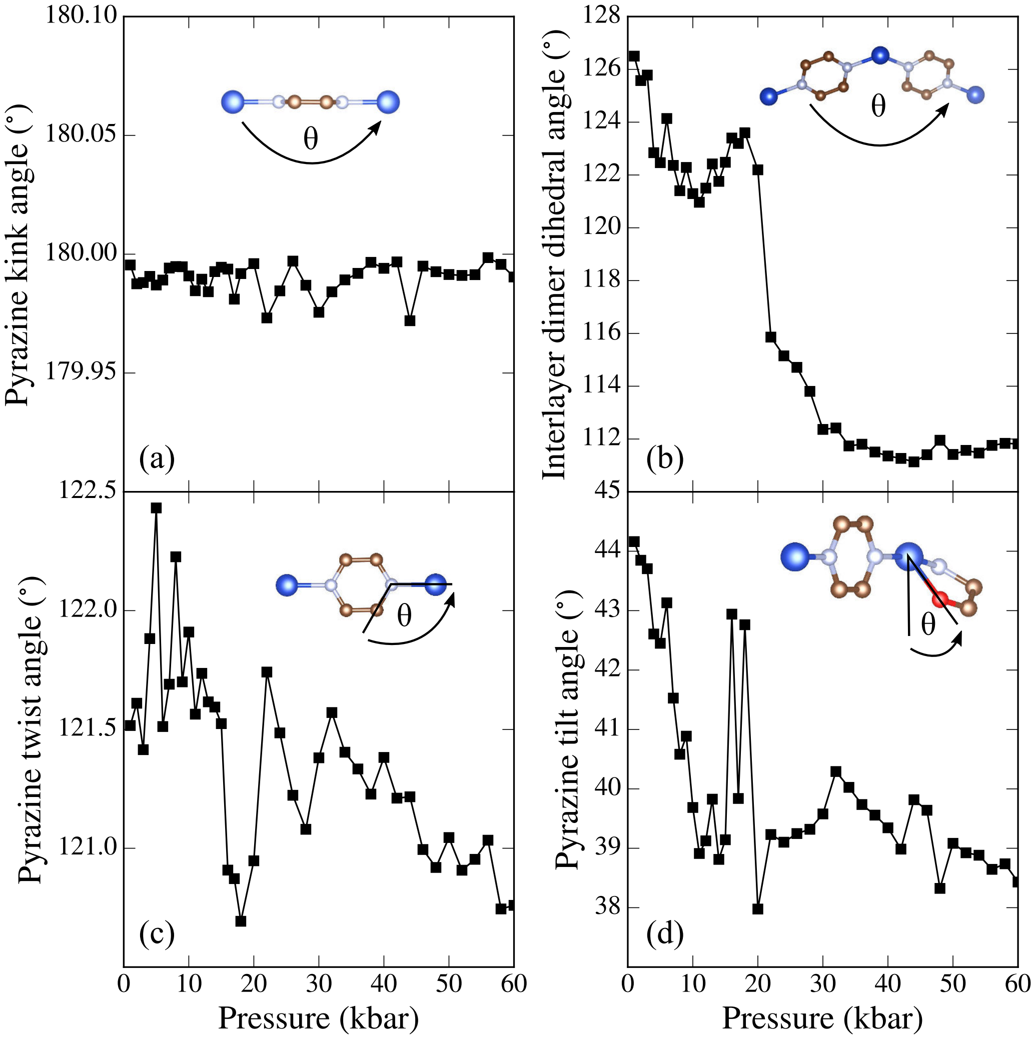

Figure 4.3.2: Dimer angles as a function of applied pressure. (a) the kink angle of the Cu dimer along the pyrazine ligand. (b) dihedral angle between the interlayer Cu dimers. (c) twist angle of the Cu dimer with respect to the pyrazine ligand. (d) tilt angle between the pyrazine and glycine ligands. Inset diagrams highlight each angle.

molecules above 20 kbar allows for closer packing. The orientation of ClO$_4$ molecules above and below the transition pressure are shown in Fig. 4.3.3a and Fig. 4.3.3b respectively. The orientation of the ClO$_4$ molecules remains mostly constant in the two pressure regimes.

DFT is known to have some systematic problems with determining geometries. Using the PBE functional, we expect that the ambient pressure cell will be larger than the true cell, which we indeed find. For similar reasons, changes

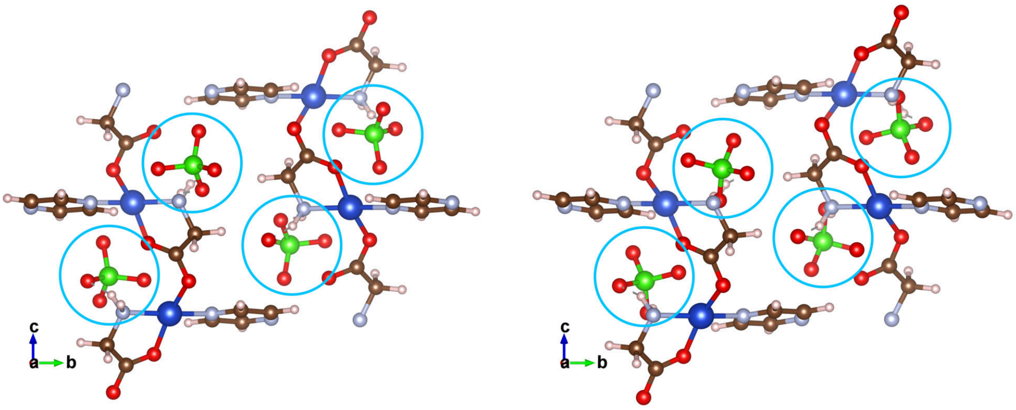

(a) 18 kbar

(b) 22 kbar

Figure 4.3.3: Structure of $[Cu(pyz)_{0.5}(gly)]ClO_4$ under pressure of (a) 18 kbar and (b) 22 kbar. There is a change in orientation of the ClO_4 molecules (highlighted in blue) in (b) which persists at higher pressure. Images produced with VESTA [148].

to the molecular components of the crystal due to the application of pressure are likely to differ from experiment in some key ways. Firstly, as PBE-DFT binds covalent bonds less tightly than reality, and under predicts the effects of intermolecular bonds, it is possible that relative changes to the positions of the dimers may be exaggerated. The under predication of the intermolecular bonds is greater than for the covalent bonding, this may account for the large change in the interlayer Cu–Cu distance. We also see evidence of this with the pyrazine kink angle, which does not change as we apply pressure, it is likely that due to the underestimation of the interlayer bonding, it is energetically favourable to alter some other part of the crystal structure rather than the strong Cu–pyz–Cu bonds. Accounting for these effects, one would expect that the structural transitions which we calculate to occur at 20 kbar to be measured at a lower applied pressure. Despite these systematic issues, we can still rely on the calculations to capture the main physical trends relevant to the magnetic exchange.

4.3.2 Magnetic effects

We find that for each structure calculated under pressure, it is possible using spin-DFT to find sufficient spin states to calculate values for J_0 and J_{eff}. An

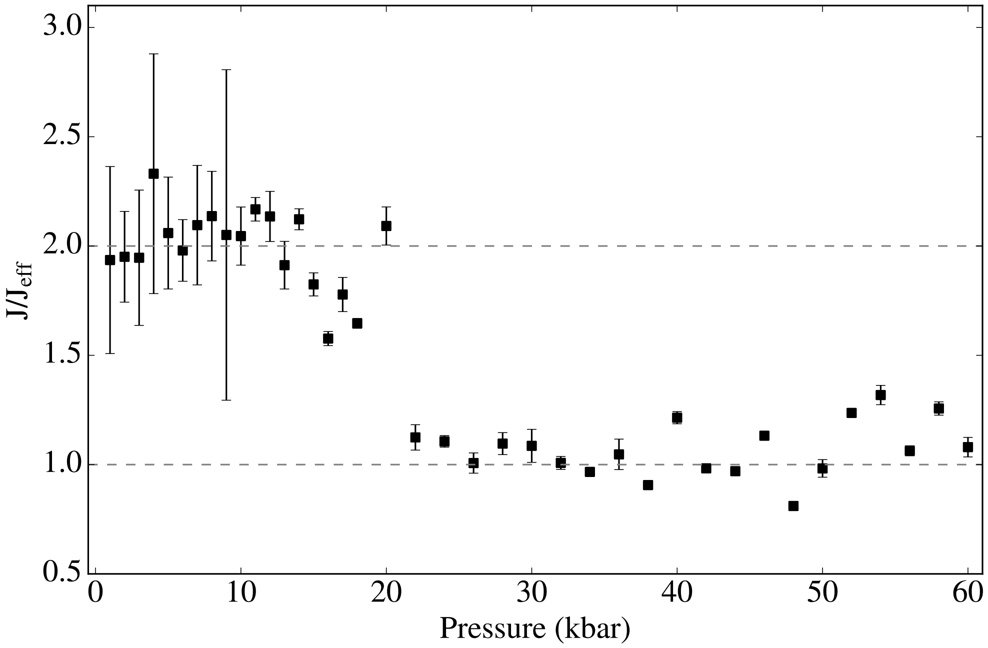

Figure 4.3.4: Ratio of calculated coupling constants J and J_{eff} as a function of isotropic pressure, dotted lines indicate the two distinct regimes.

example of the spin distribution for one of the configurations can be seen in Fig.4.2.1. We see that spin is not just localised on the Cu ions, but also on the neighbouring molecules. We find localisation of spin onto the N in the pyrazine ligands as well as on the O in the glycine ligands, Fig. 4.2.1. In both cases, these are the closest neighbours to the Cu. Notably there is insignificant spin localised on the ClO$_4$ molecules. It is likely that this localised spin on the ligands contributes to the stronger exchange interaction seen in along these pathways. At ambient pressure, the spin configuration with the lowest total energy and therefore the possible ground state magnetic structure, is antiferromagnetic both within the Cu dimers and between the dimers, this suggests that both J_0 and J_{eff} describe antiferromagnetic interactions. Projecting the spin density onto the Cu ions using Mulliken analysis reveals that there is no change in the magnetic moments as a function of pressure, it remains constant at $0.5\mu_{\mathrm{B}}$. We therefore do not have to consider variations in the magnitude of the spins in our calculation of the exchange couplings.

The effect of pressure on the exchange constants of [Cu(pyz)$_{0.5}$(gly)]ClO$_4$

can be seen in Fig. 4.3.4. At all pressures J_0 and J_{eff} are found to be positive, indicating that the magnetic interactions are antiferromagnetic, consistent with the antiferromagentic state having the lowest energy. There are two distinct regimes for the coupling constants as with the structural parameters, with the coupling strengths changing from those found at ambient pressure above 20 kbar. Across the full range of pressures the coupling constant J_0 remains quite stable around $J_0 = 8$ K, with a small increase at the highest pressures to $J_0 \approx 9$ K. For the second coupling constant, J_{eff}, the behaviour is more complex: in the region below 20 kbar the coupling is roughly half the value of J_0, and at higher pressures J_{eff} increases, such that the ratio $J_0/J_{\text{eff}} \approx 1$. In the region around the structural transition the effect on the coupling constants is less clear, but the general trend shows that J_{eff} increases with increasing pressure over a range of approximately 10 kbar to its final value above 20 kbar. Since J_{eff} included the effects of exchange along both the glycine ligand and the ClO_4 molecule, it is sensitive to changes in those pathways. From the structural data, we see that there are significant changes in the Cu–Cu accounting for the J_{eff}, including a small discontinuity in the Cu–gly–Cu distance corresponding to the change in interlayer dihedral angle. It is also possible that the reorientation of the ClO_4 molecules could cause changes in the exchange mechanism by aligning different atomic orbitals.

The change in J_{eff} at the transition pressure indicates a closing of the singlet-triplet gap in $[Cu(pyz)_{0.5}(gly)]ClO_4$. This effect has been observed previously in similar quantum magnets [176, 183, 184]. In the case of $TlCuCl_3$, this transition across the QCP leads to change in the ground state magnetic structure, going from a quantum disordered state to a long-range antiferromagnetic state. Due to the increase in the interdimer coupling, J_{eff} in $[Cu(pyz)_{0.5}(gly)]ClO_4$, it is possible that at the calculated transition pressure of 20 kbar, there is a transition from the known disordered state to an antiferromagnetic state, as in $TlCuCl_3$.

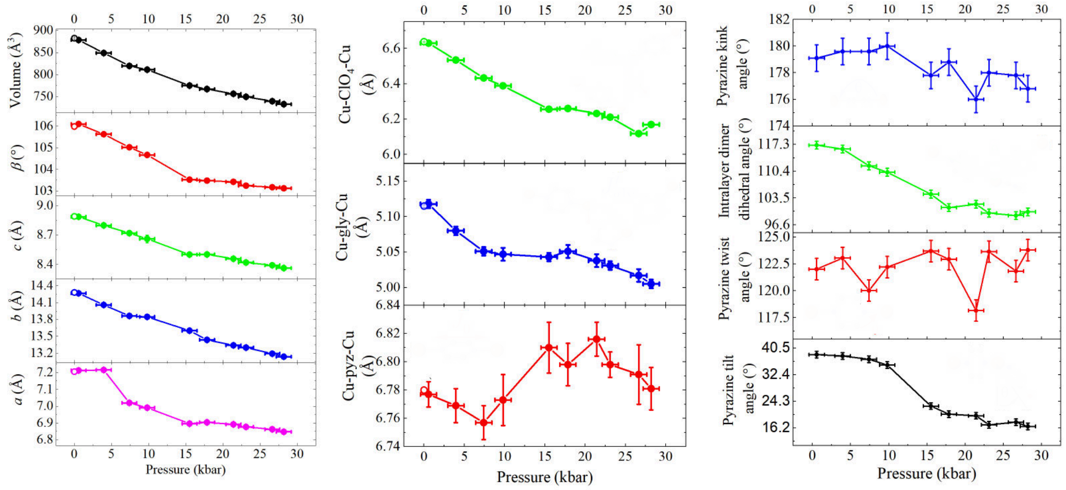

Figure 4.3.5: X-ray diffraction measurements of the structure of [Cu(pyz)$_{0.5}$(gly)]ClO$_4$ with the application of pressure. Pressure is applied by placing the crystal in a diamond anvil cell. Figure provided by experimental collaborators at Warwick University.

4.3.3 Comparison to experiment

We can compare the predictions of the effects of pressure on [Cu(pyz)$_{0.5}$(gly)]ClO$_4$ to measurements of the structural parameters made with X-ray diffraction, shown in Fig. 4.3.5. Notably, we see a second order change in the β cell angle when measured experimentally. This matches well with DFT predictions shown in Fig. 4.3.1c. The change in β occurs at lower pressure than calculated, this may due to the underestimation of bonding forces using PBE causing the transition to occur at higher pressures in the calculations. We also note that the Cu–pzy–Cu distance is seen to remain stable with applied pressure, much as predicted by our DFT calculations. The DFT calculations predict well the changes to the spacing of the Cu ions, with the largest changes occurring in the Cu–ClO$_4$–Cu distances along the secondary interdimer exchange pathway. The main deviation from theory seen in the experimental data is the lack of discontinuity in the b lattice parameter. Correspondingly, measurements show that the cell volume varies fairly continuously. However, our DFT calculations capture the main trends in the structural data and also in measurements of the exchange constants. From magnetometry measurements, the effective interdimer coupling increases upon the application of pressure as the interdimer Cu–Cu distances decrease [185]. Also, the intradimer exchange coupling remains mostly constant, as predicted by our DFT calculations.

4.4 Conclusions

We have used DFT to investigate the effects of pressure on the structure and magnetic interactions of a quantum magnet, [Cu(pyz)$_{0.5}$(gly)]ClO$_4$. We have shown that by performing structural relaxations under pressure, we find that there is a first order discontinuity in the b lattice parameter and a second order discontinuity in the β cell angle, both at 20 kbar. We also found that the Cu dimers undergo a reorientation at the same pressure. DFT predictions of the effects of pressure on the structure agree well with X-ray diffraction measurements. In addition, we calculated the pressure dependence of two exchange coupling constants, corresponding to exchange along the pyrazine ligand and an effective coupling constant combining the effects of the interdimer and the inter layer exchange pathways. We found that there is a change in the magnetic exchange indicative of a QCP at the same pressure that causes changes to the structure. The effective coupling constant J_{eff} doubles from its ambient pressure value such that the ratio of coupling parameters is nearly equal. This type of change to the interdimer coupling has been observed before in TlCuCl$_3$ and is associated with a change from a quantum disordered ground state to a long-range antiferromagnetic state. It is likely that the application of pressure drives such a transition in [Cu(pyz)$_{0.5}$(gly)]ClO$_4$.

Molecular magnet systems provide a playground for observing the building blocks of magnetism. We are unable to distinguish between changes in the glycine mediated and ClO$_4$ mediated exchange constants in our calculations. However, it is possible given the change in the Cu–ClO$_4$–Cu distance as a function of pressure that the exchange along this direction could drive the change in the ratio calculated. If that were the case, the application of pressure would induce a change in the dimensionality of the magnetism in this system, going from quasi-two-dimensional to a three-dimensional magnet. DFT proves to be an invaluable technique for understanding these types of systems and the electron interactions that determine the magnetic behaviour.

Chapter 5

Magnetism in intercalated transition-metal dichalcogenides

> *"It's a type of galvanic force" I said, then hesitated. "Which is a fancy way of saying that I've got no idea at all."*
>
> —Patrick Rothfus,
> *The Name of the Wind*

This chapter presents theoretical studies on examples of intercalated transition-metal dichalcogenides (TMDCs), of the form $N_{1/3}MX_2$ where N and M are each different transition metals, and X is a chalcogen. There are many possible combinations, some of which exhibit magnetic properties with potential technological importance. In this chapter, we will focus on the sulfides, where X = S. The main focus is on the low temperature magnetism and transport of $\mathrm{Cr_{1/3}NbS_2}$ and $\mathrm{Cr_{1/3}TaS_2}$ which have gained recent attention for the discovery of a chiral soliton lattice (CSL). This CSL has possible applications for spintronic devices. Building on the previously reported electronic structure for $\mathrm{Cr_{1/3}NbS_2}$, we present new work that leads to an explanation of the low temperature transport properties, along with new magnetometry measurements which support the findings of our density functional theory (DFT) calculations. We highlight from the calculations of the density of states (DoS) that both $Cr_{1/3}NbS_2$ and $Cr_{1/3}TaS_2$ are half-metals, and in both materials there is a small gap-like feature in one of the spin channels which we assert explains the low-temperature physics. This gap is then confirmed by magnetometry measurements and agrees with the results of the DFT calculations. Further, we present the results of electronic structure calculations of a range of materials in the same class of the form $N_{1/3}NbS_2$ where N is a transition metal in the first period. We show that the electronic structure is remarkably simple, and can be almost entirely explained by the filling of d-orbitals at the Fermi-level.

This chapter is based mostly on work found in Ref. [106]. The DFT calculations were performed by myself and the data analysed alongside collaborators at the University of Durham. Magnetometry measurements were performed by Thomas Hicken at the University of Durham on samples prepared at Warwick University.

5.1 Introduction

Research into the TMDCs goes as far back as the 1970s [186, 187, 188], however since the discovery of graphene in 2004 [189], two-dimensional materials in general have seen a resurgence with the goal of developing new low-dimensional devices. Amongst the many materials which can be exfoliated to form low dimensional solids are the TMDCs, which have the form MX_2 where M is a transition metal and X is a chalcogen [190, 191, 192, 193]. These materials display properties which are of interest across a wide range of disciplines, for example, NbS_2 exhibits low-temperature type-II superconductivity [194, 195, 196] and MoS_2 lamellae are semiconducting while the bulk is insulating [197, 198]. More recently, the metal-ion-intercalated TMDCs have attracted attention [199, 200]. The general structure of the intercalated material can be seen in Fig. 5.1.2. Of interest here are the Cr intercalated materials $Cr_{1/3}NbS_2$ and $Cr_{1/3}TaS_2$ which have long been known to host a helimagnetic ground state [201, 202]. Adding Cr ions between the TMDC layers has the effect of removing the inversion symmetry, and as a result these materials can exhibit Dzyaloshinskii–Moriya inter-

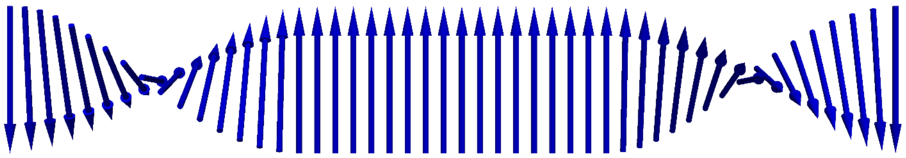

Figure 5.1.1: Schematic of a chiral soliton with the applied ***H***-field applied vertically in the plane of the figure.

action (DMI). The helices found in these materials have long periods relative to their unit cell size [202, 203], and are thought to be caused by the competition of DMI and spin-orbit coupling (SOC). $Cr_{1/3}NbS_2$ has been long known to host chiral helimagnetism, but the discovery of the CSL in $Cr_{1/3}NbS_2$ [204] and later in $Cr_{1/3}TaS_2$ [205] has renewed interest in these materials. A CSL can be described by a helix separated by regions of ferromagnetic order (see Fig. 5.1.1); it can be formed in these materials by applying a magnetic field along the c axis. Being an example of topological magnetism [51], there are hopes that such materials will have technological applications.

There have been reports of unusual low-temperature transport in $Cr_{1/3}NbS_2$, specifically a large change in the Seebeck coefficient around $T = 40$ K [203], and an increase in the Hall coefficient below $T = 50$ K [206]. There have been attempts to explain these observations, firstly a suggestion that SOC becomes important at low temperatures and induces changes in the dominant transport mechanism [203]. Also, it has been suggested that an increase in the helical length below $T = 40$ K, which is caused by a decrease in the DMI could be responsible. However, none of these explanations account for all observations. We posit that all of these phenomena can be explained by examining the electronic structure. Both the Seebeck effect, where a temperature gradient induces a potential difference across a sample, and the Hall effect, where a voltage is caused transverse to the applied current, are sensitive to the underlying electronic structure. In this chapter we will present experimental and *ab initio* results

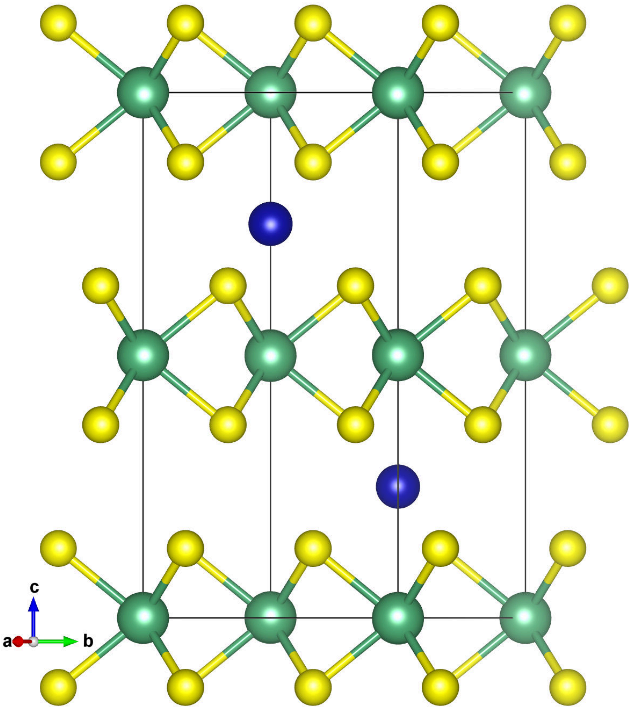

Figure 5.1.2: Structure of the intercalated TMDCs. The chemical form is $N_{1/3}MX_2$ where N are the intercalated atoms (blue), M is the transition-metal (green) and X is the chalcogen (yellow). The layers form the standard TMDCs which are held together via van der Waals interactions. Image produced with VESTA [148].

which provide a complete explanation for all observed properties. This is based on transitions which occur across a gap-like feature found in the DoS of both $\mathrm{Cr_{1/3}NbS_2}$ and $\mathrm{Cr_{1/3}TaS_2}$. We shall also report electronic structure calculations of a range of intercalated TMDCs which should allow one to make predictions about which materials would warrant further experimental investigation.

5.2 Computational details

DFT calculations of $\mathrm{Cr_{1/3}}M\mathrm{S_2}$ (M = Nb or Ta) were performed using the plane-wave, pseudopotential code, CASTEP [24]. Experimental lattice parameters were used, $a = b = 5.76$ Å, $c = 11.84$ Å and $a = b = 5.74$ Å, $c = 11.90$ Å for $\mathrm{Cr_{1/3}NbS_2}$ and $\mathrm{Cr_{1/3}TaS_2}$ respectively. Since TMDCs are Van der Waals (VDW) materials, using the experimental lattice parameters is preferable to performing a geometry optimisation since DFT is known to not capture VDW [181, 182]. Had calculations been performed on a geometry-optimised cell, the TMDC layers would likely be unphysically far apart. As a result, there are residual forces on the S and Nb atoms, however these are all less than 0.5 eV/Å per atom. Exchange and correlation (xc) interactions were treated under the generalised gradient approximation (GGA), using the Perdew, Burke and Ernzerhof (PBE) functional [69]. Ultrasoft pseudopotentials were used to approximate electrons in the atomic core. The total energy was found using a self-consistent field (SCF) calculation under the ensemble density functional theory (EDFT) scheme with a tolerance of 10^{-5} eV/atom. Calculations were performed with a plane-wave basis cut off of 1400 eV and Monkhorst and Pack (MP) SCF $\boldsymbol{k}$-point sampling of 15×15×15 [85], leading to convergence better than 10 meV per atom. $\mathrm{Cr}_{1/3}M\mathrm{S}_2$ (M = Nb or Ta) have long period helimagnetic groundstates at low temperature [203, 202] such that the local arrangement of magnetic moments is approximately ferromagnetic. We use spin-density functional theory (spin-DFT) to realise a ferromagnetic configuration with a Cr magnetic moment of approximately $3\hbar/2$.

Spectral calculations were performed to generate band structures and projected density of states (PDoS) for both $\mathrm{Cr}_{1/3}\mathrm{NbS}_2$ and $\mathrm{Cr}_{1/3}\mathrm{TaS}_2$. When calculating the DoS a 25×25×25 MP $\boldsymbol{k}$-point grid was used for $\mathrm{Cr}_{1/3}\mathrm{NbS}_2$, and 15×15×15 for $\mathrm{Cr}_{1/3}\mathrm{TaS}_2$. To calculate the PDoS, we perform a Mulliken analysis of the spectral wavefunction at every $\boldsymbol{k}$-point to project the wavefunction onto a linear combination of atomic orbitals (LCAO). We are then able to determine the relative character of each band and calculate the contribution of each LCAO state to the overall DoS. The output of the DoS calculations were used to generate Fermi surfaces by locating which bands cross the Fermi level and performing 3D interpolation to estimate the surface. Fermi surfaces were calculated using CASTEP2FS [207] with the aid of the Atomic Simulation Environment (ASE) [208] to analyse the Brillouin zone (BZ) of the materials. As the calculations require interpolation on the spectral $\boldsymbol{k}$-point grid, the Fermi surfaces of $Cr_{1/3}NbS_2$ are produced with a higher degree of reliability.

We performed further calculations of the band structures and DoS of $Cr_{1/3}NbS_2$ and $Cr_{1/3}TaS_2$ using SOC to determine the effect it has on the electronic structure around the Fermi level. Calculations were carried out using relativistic pseudopotentials with a fully non-collinear treatment of electron spins. The quantisation axis for these calculations was set along the c axis such that we returned the same ferromagnetic state as for the non-SOC calculations.

The Seebeck coefficients for $Cr_{1/3}NbS_2$ and $Cr_{1/3}TaS_2$ were calculated using the BOLTZTRAP code [209], initialised using the electronic structure calculations described above. BOLTZTRAP is an implementation of the Boltzmann transport equations which allow for the calculation of transport properties from the energy dispersion relation. While most transport properties require an estimation of the relaxation time, the Seebeck calculations presented here are independent of this parameter. Transport properties depend on the temperature of the sample and any applied potential difference, which has the effect of shifting the Fermi energy. We calculated the Seebeck coefficient in both materials over a temperature range of 1 to 300 K and chemical potential spanning 1.36 meV with 0.14 meV spacing centered around the Fermi level calculated from DFT. To reduce the effects of noise at low temperatures, we used 100 and 200 lattice points per $\boldsymbol{k}$-point for $Cr_{1/3}NbS_2$ and $Cr_{1/3}TaS_2$ respectively to account for the relative $\boldsymbol{k}$-point densities. We find that the Seebeck coefficient is highly sensitive to the choice of chemical potential. To best match the experimental Seebeck coefficient in $Cr_{1/3}NbS_2$ the value of Fermi energy was taken as approximately -18 meV with respect to the Fermi energy predicted by DFT. This is within the uncertainty of our calculations. Due to the practicalities of measuring the Seebeck coefficient, it is difficult to ensure that the measurement is taken at precisely zero bias, this is also reflected in the choice of Fermi energy. In $Cr_{1/3}TaS_2$ it is expected that the Seebeck coefficient behaves similarly to that of $Cr_{1/3}NbS_2$ so a value of approximately -6 meV with respect to the DFT Fermi energy was chosen.

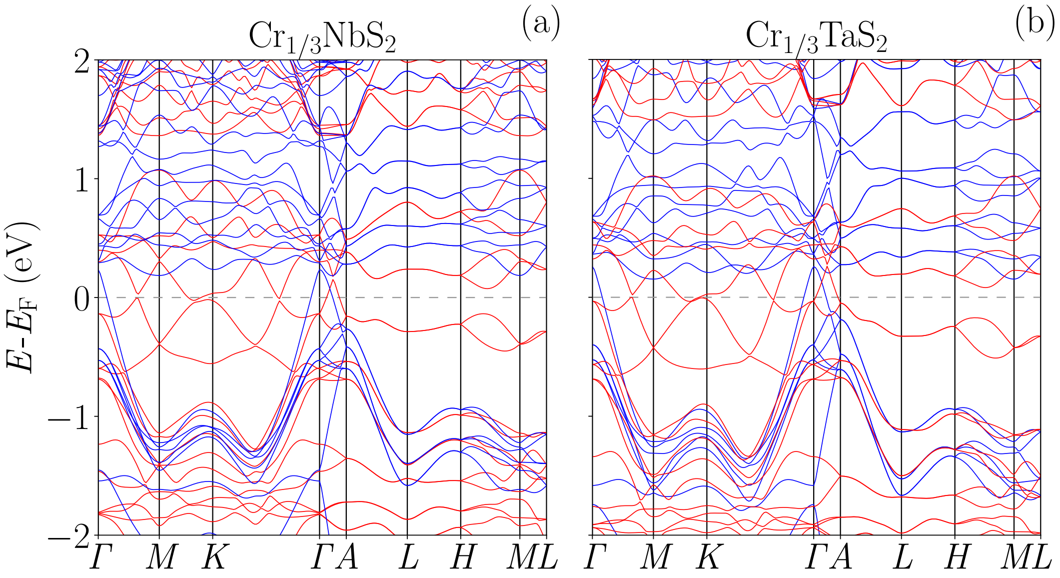

Figure 5.2.1: Band structures of (a) $\mathrm{Cr}_{1/3}\mathrm{NbS}_2$ and (b) $\mathrm{Cr}_{1/3}\mathrm{TaS}_2$ along a high symmetry path in the BZ. Spin-up and spin-down bands are coloured red and blue respectively. Plots produced using dispersion.py [104] (See App. C)

In addition, we performed calculations of the electronic structure of $N_{1/3}\mathrm{NbS}_2$ where N are the transition metals in the first period. For each material a plane-wave cut off of 1700 eV was used along with a MP $\boldsymbol{k}$-point grid of 7×7×7 for convergence better than 1 meV/atom. Xc was treated using the PBE functional. The lattice parameters of each material were held fixed at the experimental values of $\mathrm{Co}_{1/3}\mathrm{NbS}_2$, $a = b = 5.77$ Å, $c = 11.89$ Å. Because of the VDW nature of the materials the structural parameters are insensitive to the choice of intercalant [210, 211]. Therefore, it is a valid approximation to hold the lattice constants fixed across the series. Each calculation was performed using the density mixing (DM) scheme with a ferromagnetic spin initialisation of $1\hbar/2$ per ion. There have been reports on the magnetic structure of some of these materials, for example $N_{1/3}\mathrm{NbS}_2$ (N = V, Mn) have been found to be ferromagnetic at low T while $N_{1/3}\mathrm{NbS}_2$ (N = Co, Ni, Fe) are antiferromagnetic [212, 211, 213]. To capture some of the correlation effects that often contribute to long range magnetic order, we included a small Hubbard U of between 2.0 eV and 2.5 eV on the N d-orbitals. These values were chosen as the smallest value required to form a ferromagnetic state. A Hubbard U acts as a local Coulombic repulsion which is often used to address the band gap problem, but in magnetic ions can be used to localise spin. It was only possible to realise a ferromagnetic moment in some of the materials in this series, while $Sc_{1/3}NbS_2$, $Cu_{1/3}NbS_2$ and $Zn_{1/3}NbS_2$ were all found to be non-magnetic. While a ferromagnetic state is not the groundstate in some of the materials studied, these calculations still provide interesting insight into the behaviour of the series as a whole. We will limit our discussion below to only those materials where we find a ferromagnetic state in our calculations. In a collinear system any magnetic state which is realised is degenerate under a global spin flip, therefore when the total moment of these ferromagnetic calculations is negative, we apply a global flip of the spins to allow for comparison.

5.3 Results and discussion

5.3.1 Electronic structure of $Cr_{1/3}MS_2$ (M = Nb or Ta)

The band structures of $Cr_{1/3}NbS_2$ and $Cr_{1/3}TaS_2$ can be seen in Fig. 5.2.1. The band structure of $Cr_{1/3}NbS_2$ matches previous work [203] and shares many similar features with that of $Cr_{1/3}TaS_2$. The complicated structure around the Γ-point is the main contributor to the DoS at the Fermi level. In both materials the ferromagnetic moment on the Cr ions has lifted the spin degeneracy, resulting in distinct bands for the spin-up and spin-down electrons.

Figure 5.3.1 shows the PDoS for $Cr_{1/3}NbS_2$ and $Cr_{1/3}TaS_2$. The largest contribution to the DoS at the Fermi level comes from the spin-up channel, with no contribution from the spin-down channel. The bands in the spin-down channel are strongly peaked at the Γ-point suggesting delocalized electrons; those in the spin-up channel are much more flat, indicating a more localised character. It has previously been reported that $Cr_{1/3}NbS_2$ is a low-carrier-concentration metal or heavily-doped semiconductor [203]. However, in the spin-up channel there is more density around the Fermi level, which, in addition to the integer spin per unit cell [214], suggests both materials are half-metallic [215]. A

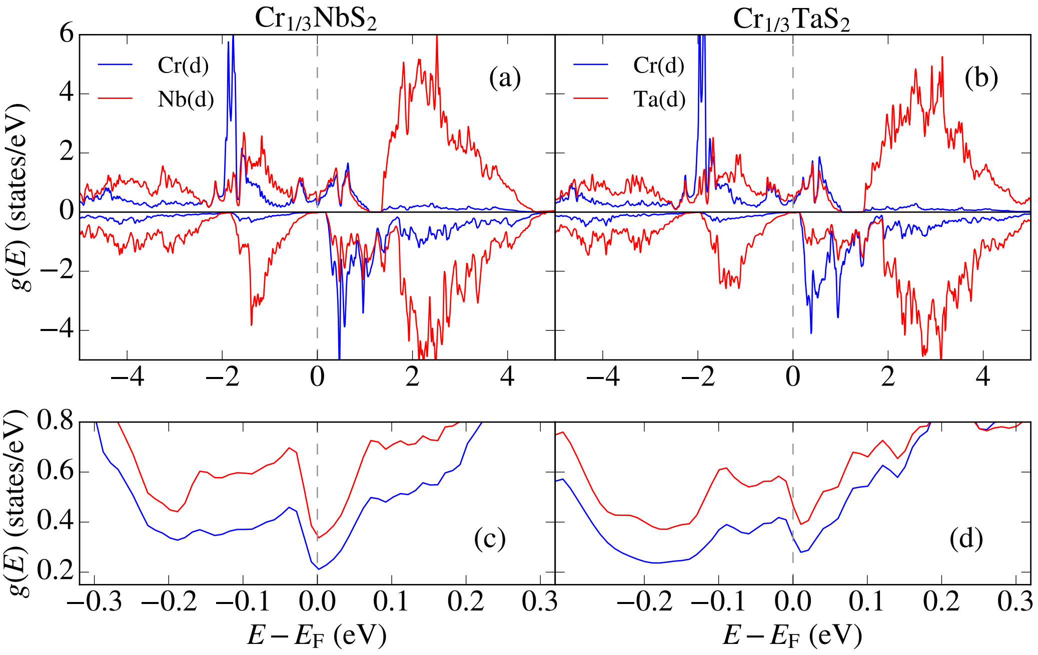

Figure 5.3.1: (a) and (b) PDoS of d-orbital contributions from transition metals in $Cr_{1/3}NbS_2$and $Cr_{1/3}TaS_2$. (c) and (d) Regions around the Fermi level showing the pseudogap feature in the spin-up channel. Spin-up densities are positive and spin-down densities are negative. The dashed line shows the location of the Fermi level. Adaptive broadening is applied tp the peaks [105] in the OPTADOS code [216, 94].

half metal is characterised by a gap at the fermi level in one channel of a spin-resolved DoS, that is to say it is conducting in one spin-channel while insulating or semi-conducting in the other. There is a small gap-like feature at the Fermi level in the spin-up channel, with a width of approximately $\Delta E = 80$–90 meV in both materials, where there is a reduction in the DoS to almost zero. This gap was first reported by Ghimire *et al.* [203] where it was called a ‘pseudogap’. However, no further mention of this feature was made by the authors and no suggestion that it is the driving force behind the low-temperature physics.

We have also performed calculations with the inclusion of SOC. A comparison of the spectral calculations with and without SOC are shown in Fig. 5.3.2. We note that there are no significant changes to the electronic structure and the pseudogap remains the same. Using a non-collinear treatment of electrons means it is no longer trivial to decompose electrons into spin-up and spin-down

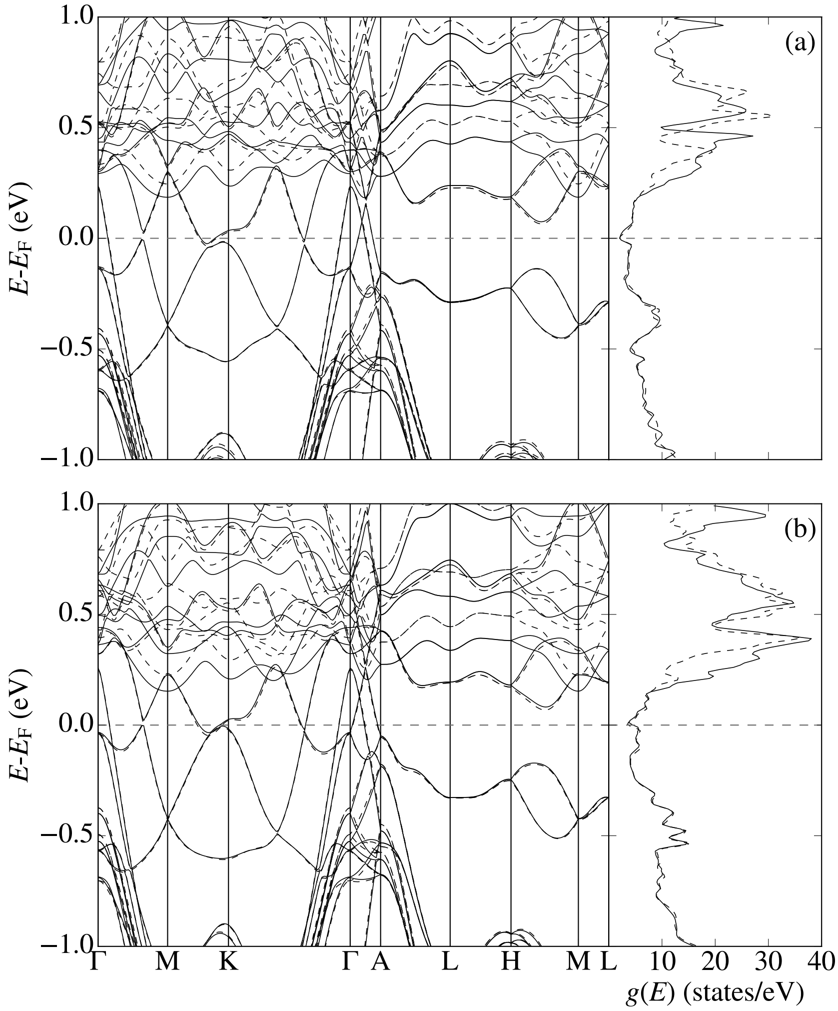

Figure 5.3.2: Band structures and DoS of (a) $Cr_{1/3}NbS_2$ and (b) $Cr_{1/3}TaS_2$ calculated with SOC (solid lines) and without (dashed lines). Plots produced using dispersion.py [104] (See App. C) and OPTADOS [216, 94].

channels, and therefore the total DoS is plotted. Despite using the total DoS the pseudogap at the Fermi level is still identifiable since there are no spin-down states due to the half-metallic nature of these materials. In the band structures, we find that around the Fermi level in $Cr_{1/3}MS_2$ (M = Nb or Ta) the energy difference is small, approximately 10 meV in $Cr_{1/3}NbS_2$ and 15 meV in $Cr_{1/3}TaS_2$. The effect of SOC in $Cr_{1/3}TaS_2$ is expectedly larger due to the increased mass of Ta.

Given the distinct spin dependence of the DoS and location of the pseudogap, we would expect spin dynamics to occur at low temperatures as spin-up electrons fluctuate across the pseudogap. We will go on to discuss other theoretical calculations as well as experimental work which also highlight the importance of the pseudogap in driving both electronic and magnetic effects in these materials.

Figure 5.3.3 shows the Fermi surfaces for $Cr_{1/3}NbS_2$ and $Cr_{1/3}TaS_2$. Both sets of Fermi surfaces are similar which reflects the similarity in the DoS at the Fermi level. In the case of $Cr_{1/3}NbS_2$ we see clear evidence of Fermi surface nesting, which has been previously reported experimentally in this material [217]. The parent material NbS_2 stands out amongst TMDCs as it does not exhibit charge density waves (CDW) while other similar materials do [218, 219]. Many TMDCs show Fermi surface nesting which drives the instability leading to the formation of CDW. The nesting in $Cr_{1/3}NbS_2$ is limited which likely accounts for its structural stability and lack of evidence of CDW. We can also see the same nesting characteristics in $Cr_{1/3}TaS_2$, however this is limited by the resolution of the calculations.

We can use individual electron orbitals to examine the effects of half-metalicity in real space. By looking at the spatial distribution of each electron we begin to see more clearly the effects of the pseudogap for spin-up electrons and the true gap for spin-down electrons. We are interested in seeing how the distribution of electrons changes as we excite electrons at the gap, therefore the distributions of the highest occupied and lowest unoccupied electron states are shown in Fig. 5.3.4. In the case of spin-up electrons [Figure. 5.3.4a] there are electron states localised around the Cr ions which have *d*-orbital character both occupied and unoccupied. Spin-up electrons in the highest occupied state would therefore be able to excite into into the lowest unoccupied state and remain localised on the Cr ions. For the spin-down electrons [Figure. 5.3.4b] we see a completely different distribution. The highest occupied electron state is localised on the Cr ions as is the case for spin-up electrons. However, looking at the lowest unoccupied electron state, we see that this is no longer localised on the Cr. This is the same effect as there being a gap in the PDoS for spin-down electrons. Excitation of the highest occupied electrons into unoccupied

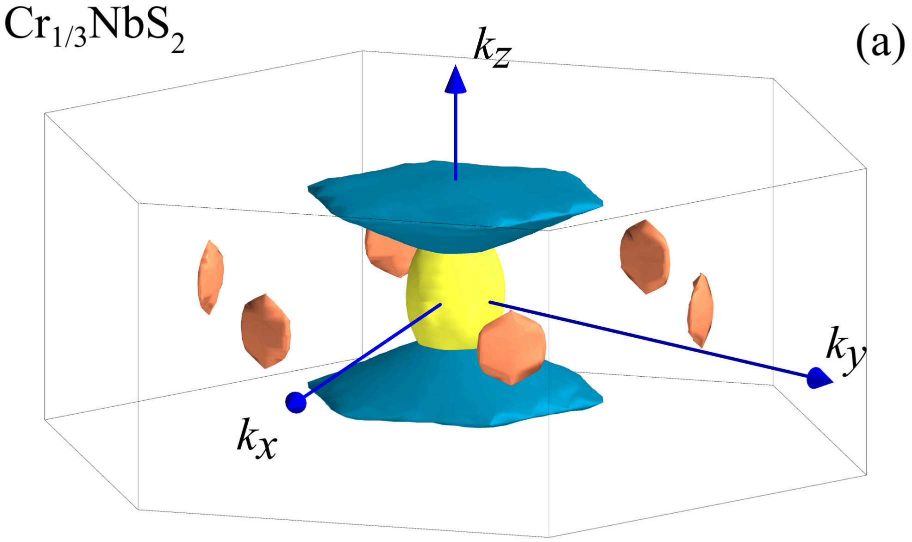

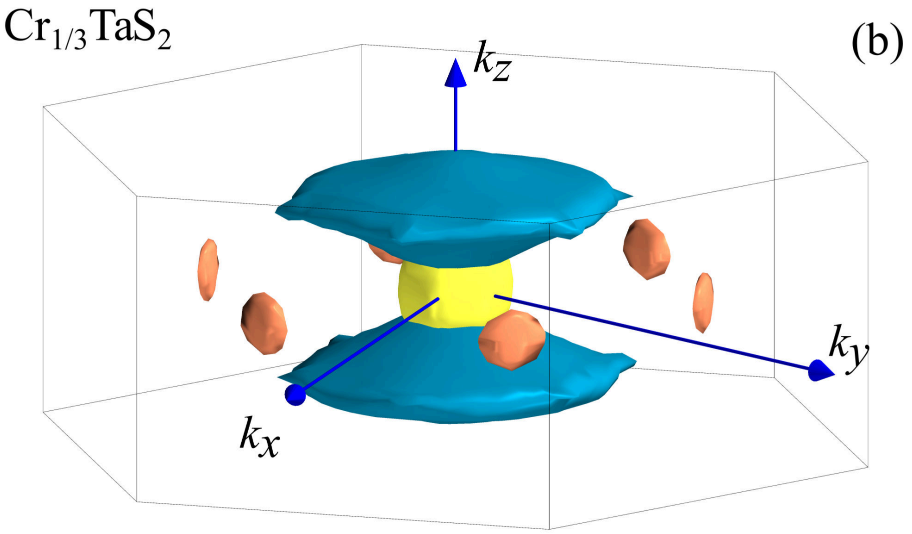

Figure 5.3.3: Fermi surfaces as calculated from DFT for (a) $Cr_{1/3}NbS_2$, and (b) $Cr_{1/3}TaS_2$. Two spin-up bands cross the Fermi energy, and are shown in blue and orange. The yellow band is spin down. Image produced using castep2fs [207] (see App. C)

states around the Cr would require significantly more energy than the spin-up electrons, certainly much more energy than available at the temperatures of interest in these materials.

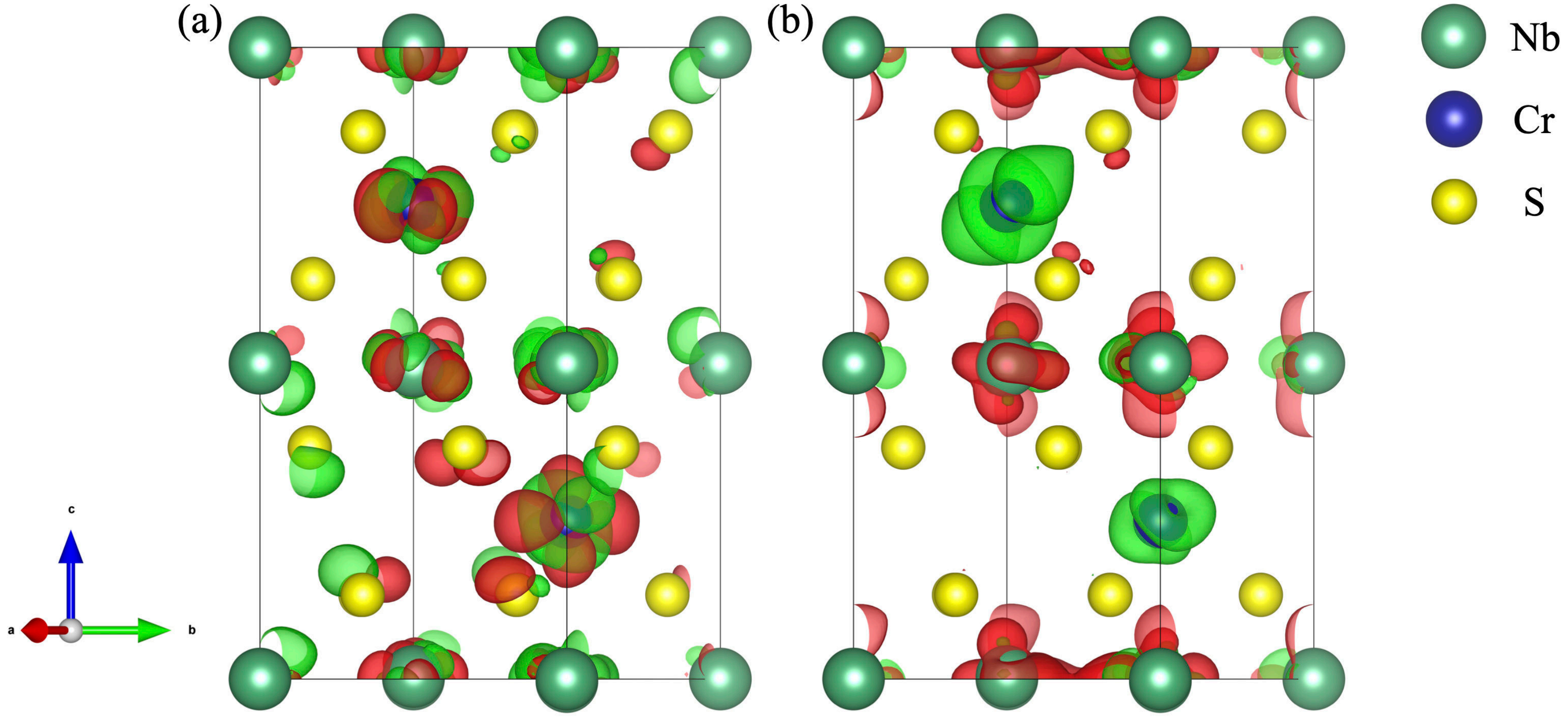

Figure 5.3.4: Highest occupied (red) and lowest unoccupied (green) orbitals of Cr1/3 NbS2. Spin-up channel shown in (a) and spin-down channel in (b). Image produced with VESTA [148].

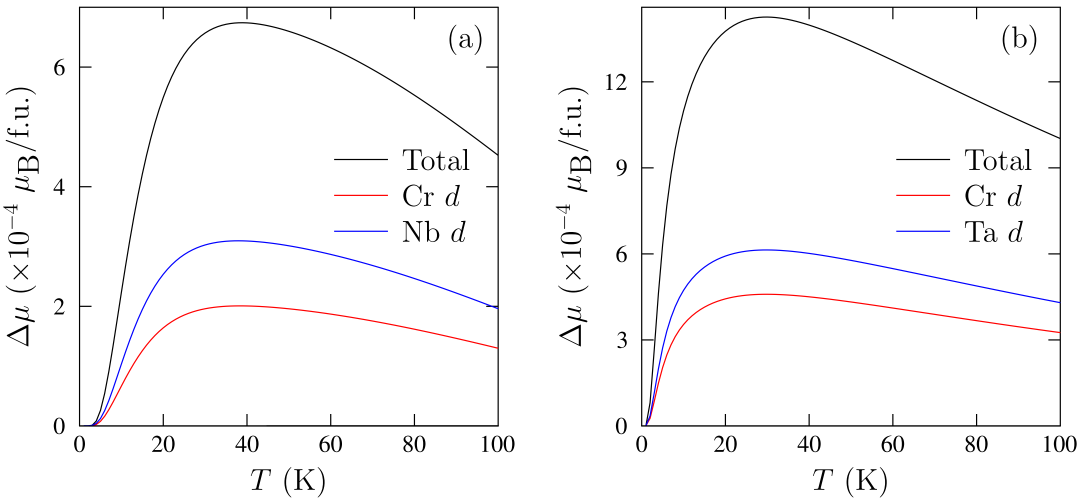

Figure 5.3.5: Predicted temperature dependence of the change in μ for (a) $Cr_{1/3}NbS_2$ and (b) $Cr_{1/3}TaS_2$ excluding critical behaviour. Total change, and change in Cr and M d orbitals are shown.

5.3.2 Transport and magnetic properties of $Cr_{1/3}MS_2$ (M = Nb or Ta)

Figure 5.3.5 shows the predicted temperature dependence of the magnetic moment in $Cr_{1/3}NbS_2$ and $Cr_{1/3}TaS_2$. This temperature dependence of the moment is calculated from the DoS using the Fermi-Dirac distribution. As DFT is a 0 K theory, we have no knowledge of how temperature would modify the magnetic state, therefore our model does not capture the critical behaviour as one approaches the magnetic transition. The moment is calculated using,

$$\mu(T) = \int_{-\infty}^{\infty} \mathrm{d}\epsilon [g^{\uparrow}(\epsilon) - g^{\downarrow}(\epsilon)] f_{\mathrm{FD}}(T; E_{\mathrm{F}}), \tag{5.1}$$

where μ is the magnetic moment, $g^{\uparrow(\downarrow)}$ are the spin up (down) DoS, f_{FD} is the Fermi-Dirac distribution and E_{F} is the Fermi energy. By multiplying the DoS of each spin channel with the Fermi-Dirac distribution one obtains the number of electrons of each spin. Taking the difference, we can approximate the total moment to first order. As we are interested only in temperatures of order 50 K which is much lower than the Curie temperature, T_{C}, for both materials, our approximation is valid. In both materials, μ peaks at approximately 40 K.

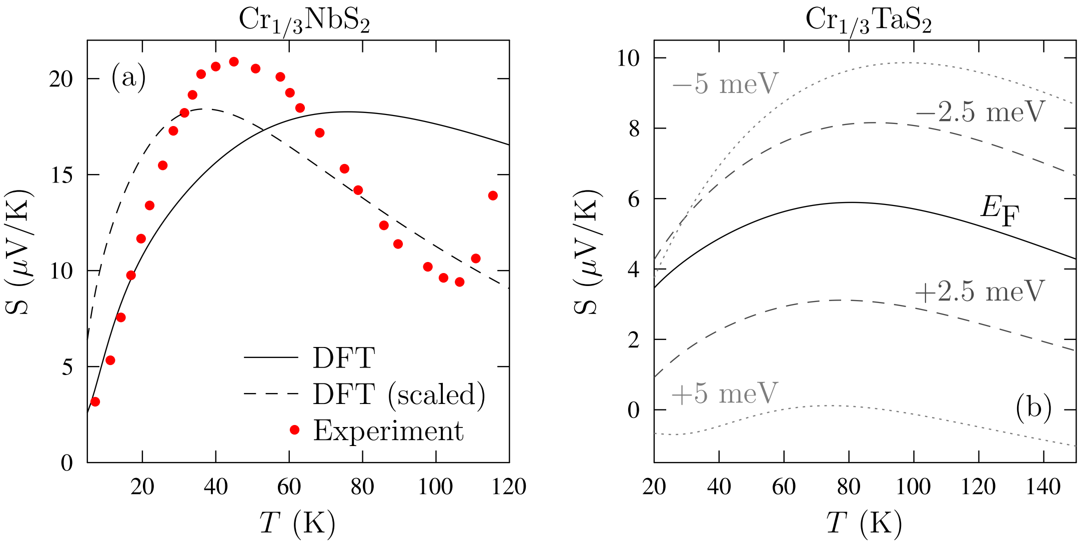

Figure 5.3.6: Seebeck coefficient $S = \mathrm{Tr}(S_{\mu\nu})/3$ for (a) Cr$_{1/3}$NbS$_2$ and (b) Cr$_{1/3}$TaS$_2$. In (a), S is compared with experiment [203] and is also shown with temperatures scaled according to the gap size, as described in the text. In (b) the range of the possible values of the Seebeck coefficient due to uncertainty in the Fermi energy is shown.

Figure 5.3.6a–b shows Tr $(S_{\mu\nu})/3$, with a maximum reflecting the presence of the pseudogap. This prediction of the Seebeck coefficient of Cr$_{1/3}$NbS$_2$ qualitatively matches the measurements in the low-temperature regime [203], although around T_C the computed behaviour deviates from experiment due to the onset of the magnetic transition. As stated above the BOLTZTRAP calculations are only valid well below T_C. The gap found in our calculations is slightly larger than the measured gap (see Sec. 5.3.3), causing the features in $S_{\mu\nu}$ to occur at higher T compared to those found experimentally. (As this is not a true gap, it is likely this is unrelated to the band gap problem highlighted in Chap. 2.) In Fig. 5.3.5a we have used the measured gap to scale the temperature to better compare to the experimental data ($T \rightarrow T\Delta E_{\mathrm{exp}}/\Delta E_{\mathrm{DFT}}$), this results in good agreement with the peak position found in the measurements.

We find similar behaviour in $S_{\mu\nu}$ for Cr$_{1/3}$TaS$_2$ [Figure. 5.3.5b], this is expected due to the level of similarities between the electronic structure of the two materials. Although it is not possible to estimate the Hall coefficient without knowledge of the relaxation time [209], it is likely that the pseudogap explains the observed features in the Hall coefficient of Cr$_{1/3}$NbS$_2$ reported by Ghimire

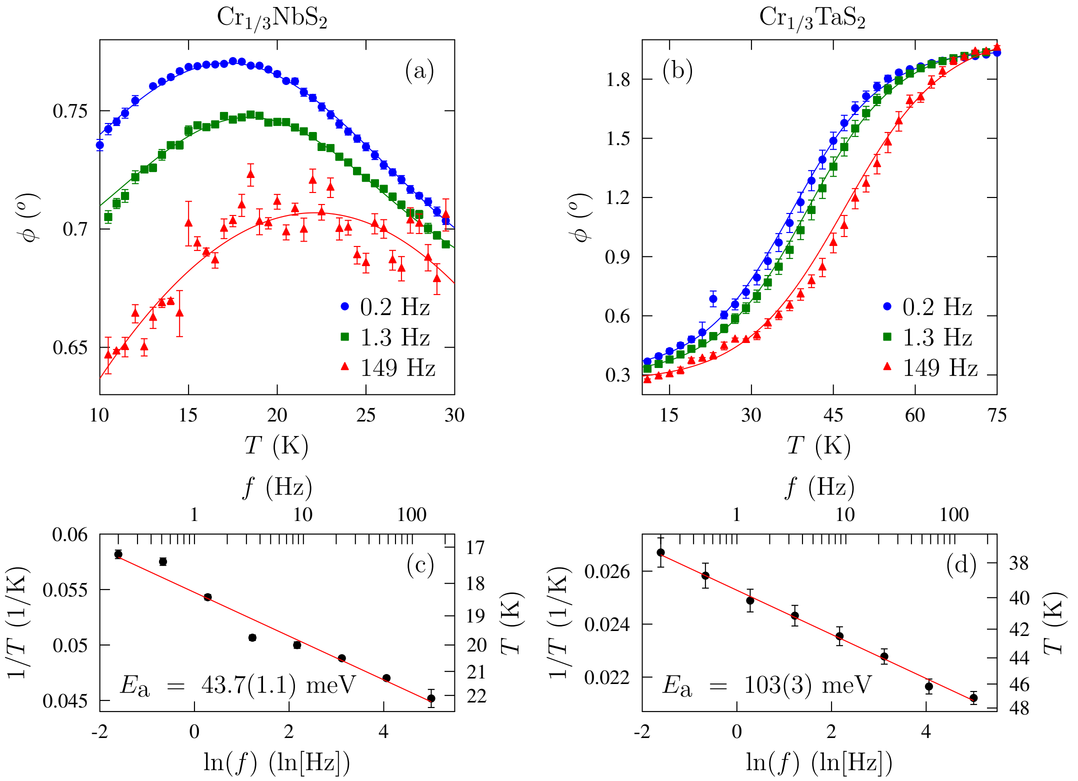

Figure 5.3.7: Example measurements of the phase lag, ϕ, of AC susceptibility measurements on $Cr_{1/3}MS_2$ (M = Nb or Ta) (a,b). Solid lines are the fits to the data, a Gaussian for $Cr_{1/3}NbS_2$ and a sigmoid for $Cr_{1/3}TaS_2$. Central temperature position of the fits are shown in (c,d), this then is used to extract activation energies, E_a.

et al. [203].

From the DoS we find a pseudogap in both $Cr_{1/3}NbS_2$ and $Cr_{1/3}TaS_2$. In each quantity calculated from our electronic structure of both materials, we see peaks in each at the same characteristic temperature, consistent also with experimental work. The pseudogap is seen as the cause of all of this low temperature behaviour, which could not otherwise be elucidated without first principles calculations. We will present below experimental evidence that directly shows that the pseudogap exists in both materials.

5.3.3 Experimental results

We performed AC susceptibility measurements on $Cr_{1/3}NbS_2$ and $Cr_{1/3}TaS_2$ to investigate the impact of the pseudogap on the magnetism. In an AC susceptibility measurement, a time varying magnetic field is applied to the sample and the resulting magnetisation is observed. The measured susceptibility is in general complex with an in-phase (real) component, χ', and an out-of-phase (imaginary) component, χ'', which relates to dissipative processes, where energy is lost from the system [220]. The complex susceptibility can be decomposed into an amplitude, $\chi = \sqrt{\chi'^2 + \chi''^2}$, (the size of the induced magnetisation) and the phase lag, $\phi = \arctan(\chi''/\chi')$, (how much the induced oscillations lag behind the applied field). We show in Fig. 5.3.7a–b the measured phase lag as a function of temperature for a selection of indicative frequencies. The temperature dependence of the phase lag can be fitted in both cases, for $\mathrm{Cr_{1/3}NbS_2}$ the data are best described using a Gaussian function, while for $\mathrm{Cr_{1/3}TaS_2}$ a sigmoid function is better. We have extracted the central locations of each fit T^* as a characteristic temperature of each fit, using the peak of the Gaussian and the inflection point of the sigmoid, to see the effects of frequency on the distributions. Given the close similarity of the electronic structure of each material, more investigation is warranted to discover why the AC susceptibility phase lag has different functional forms. The dependence of T^* on frequency is shown in Fig. 5.3.7c–d, and we find that $1/T^*$ is linear with the logarithm of frequency. This relationship follows an Arrhenius law, which are used to describe activated processes,

$$f = Ce^{-E_a/k_\mathrm{B}T^*}, \tag{5.2}$$

where f is the frequency, C is an amplitude, k_B is the Boltzmann constant and E_a is an activation energy. The gradient of the straight lines in Fig. 5.3.7c–d give the activation energy which can be interpreted as an energy gap. For $\mathrm{Cr_{1/3}TaS_2}$ we extract a value of $E_a = 103 \pm 3$ meV which is the same order of magnitude as the pseudogap found from the DFT calculations. The gap obtained for $\mathrm{Cr_{1/3}NbS_2}$ is $E_a = 43.7 \pm 1.1$ meV which is below the lower estimate of our calculations but still the correct order of magnitude, this is the value used to scale the calculated Seebeck data discussed in Sec. 5.3.2.

In addition to the AC susceptibility measurements, muon-spin spectroscopy

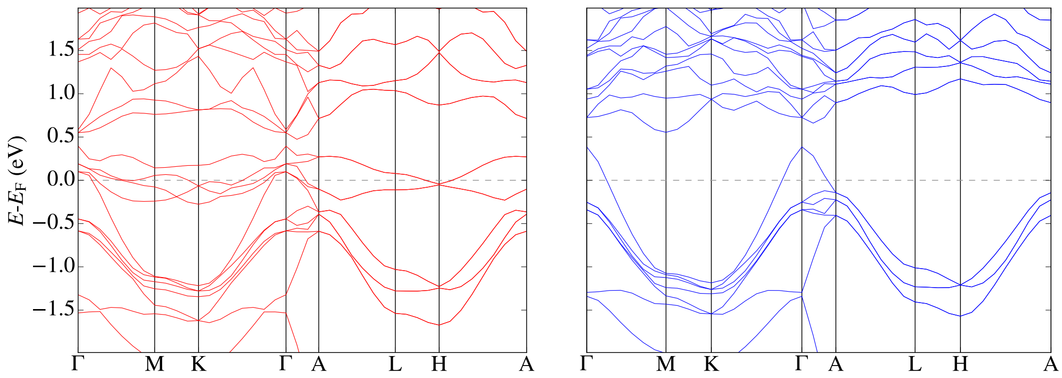

(a) $Ti_{1/3}NbS_2$

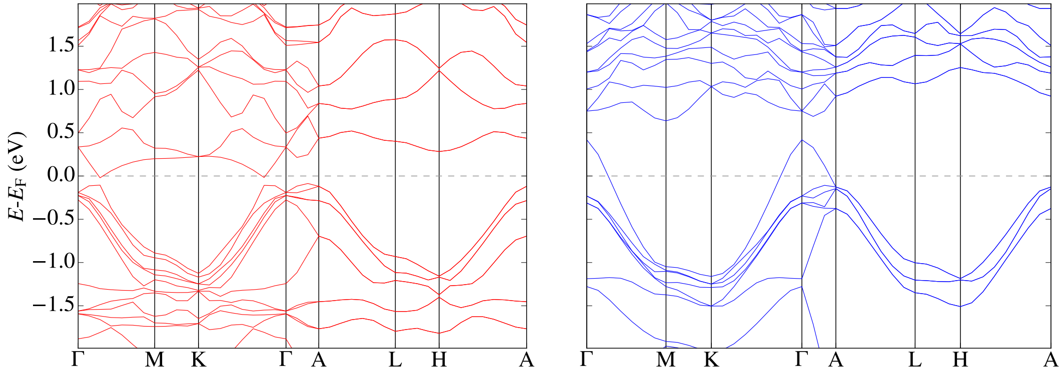

(b) $V_{1/3}NbS_2$

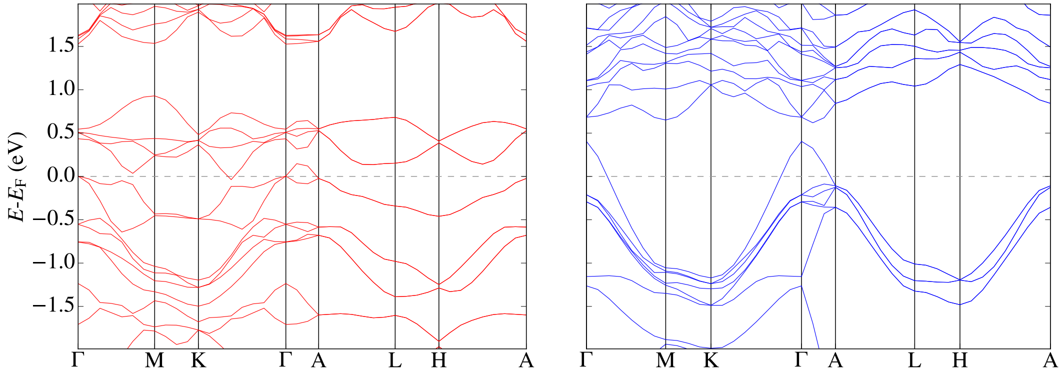

(c) $Cr_{1/3}NbS_2$

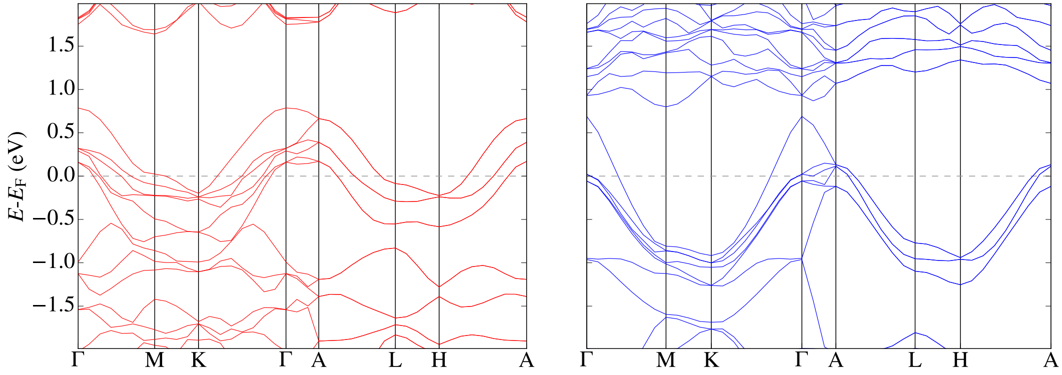

(d) $Mn_{1/3}NbS_2$

Figure 5.3.8: Spin-up (left) and spin-down (right) band structures of the intercalated TMDCs where the intercalated transition-metal has a 3d shell which is less than half filled. Plots produced using dispersion.py [104] (See App. C)

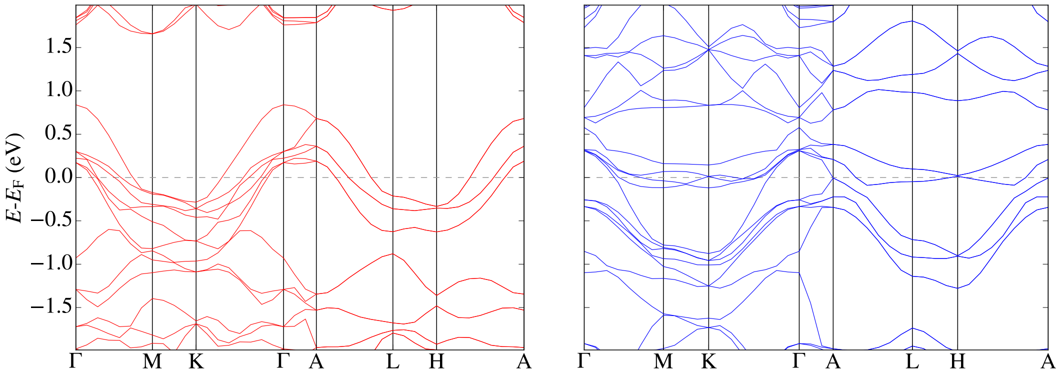

(a) $Fe_{1/3}NbS_2$

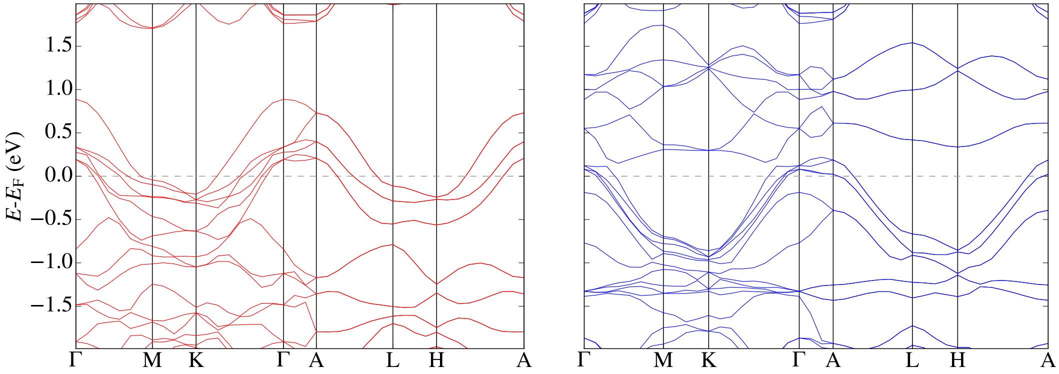

(b) $Co_{1/3}NbS_2$

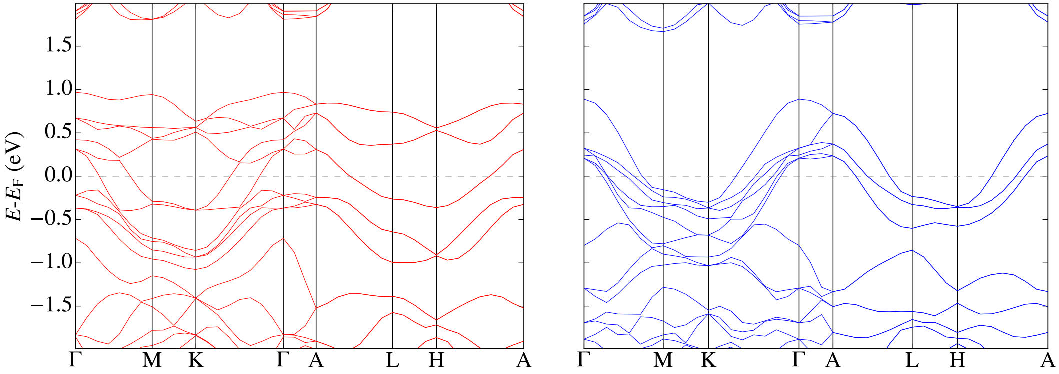

(c) $Ni_{1/3}NbS_2$

Figure 5.3.9: (Left) spin-up and (right) spin-down band structures of the intercalated TMDCs where the intercalated transition-metal has a 3*d* shell which is more than half filled. Plots produced using dispersion.py [104] (See App. C)

(μSR) measurements have been carried out. Measurements of the spin dynamics have been taken using μSR (see Ref. [106] for details) and show behaviour consistent with the pseudogap.

5.3.4 Band filling in $N_{1/3}$NbS$_2$

Across the first period, from Sc to Zn, each atom has an extra 3d-electron. For d-orbitals, $l = 2$, so there are 5 m_l states per spin for a total of ten available states. In single atoms, one would expect that each extra electron would sit in the next available atomic orbital. In real materials with many electrons and various atomic species, typically the filling of electrons is far more complicated than this simple atomic picture. We present here results from electronic structure calculations which show that this simple picture can be applied to the electron configurations in intercalated TMDCs. Figure. 5.3.8 shows the band structures of $N_{1/3}$NbS$_2$ (N = Ti, V, Cr, Mn) while Fig. 5.3.9 shows the band structures of $N_{1/3}$NbS$_2$ (N = Fe, Co, Ni). We note that as we progress from Ti$_{1/3}$NbS$_2$ through to Mn$_{1/3}$NbS$_2$, in Fig. 5.3.8, the band structure of the spin-down electrons (right) remains essentially static while changes occur in the bands of the spin-up electrons. The opposite effect can be seen in the band structures of Fe$_{1/3}$NbS$_2$–Ni$_{1/3}$NbS$_2$. In this case the spin-up bands are the ones which are mostly static, with the spin-down bands changing across the series, although this is less prominent for these materials. The static nature of a subset of the bands in the band structure has consequences for the magnetic moment found on the magnetic ions, Fig. 5.3.10. We can see that for the materials where the intercalant has a less than half-filled 3d-shell, the magnetic moment increases across the series, and then begins to drop again as we move to the materials with a more than half-filled shell. Taking Mn$_{1/3}$NbS$_2$ as an example, if we were to naively assume that the moment is simply obtained by adding electrons to the spin-up sub shells of the Mn 3d-orbital, one would expect a total moment of $5\hbar/2$, however this is not what we see. By looking more closely at the orbital populations, Fig. 5.3.11, we can see that this picture is not quite correct. In

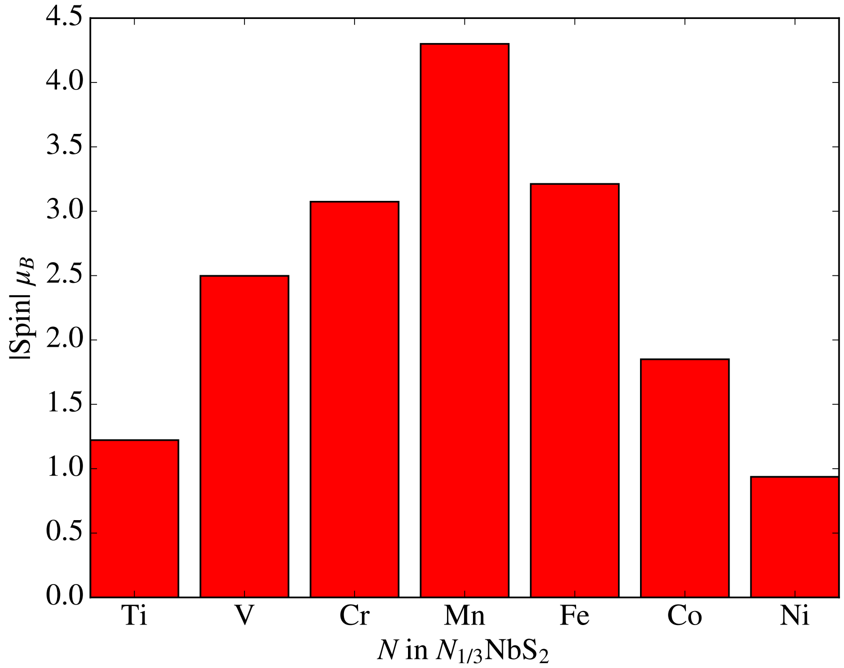

Figure 5.3.10: Bar graph showing the magnitude of total spin as a function of transition-metal, N, in $N_{1/3}\mathrm{NbS}_2$.

the first half of the period, we add approximately one electron to the spin-up subshells, once we reach Mn the spin-up shells are filled at which point we start filling the spin-down shells. This explains the decrease in moment as we approach the end of the series. We also see that there is just less than one electron populating the spin-down shells of all materials, it is this electron that accounts for the difference in Mn magnetic moment which one might naively assume to be $5\hbar/2$.

By looking at the DoS of the intercalated TMDCs we can make comparisons to the DoS of $\mathrm{Cr}_{1/3}\mathrm{NbS}_2$ and $\mathrm{Cr}_{1/3}\mathrm{TaS}_2$, particularly with regards the pseudogap which we know to produce interesting magnetic and transport effects. All of the DoS in $N_{1/3}\mathrm{NbS}_2$ can be seen in Fig. 5.3.12 with the exception of $\mathrm{Cr}_{1/3}\mathrm{NbS}_2$ which is shown in Fig. 5.3.1a. As with the band structures of these materials, the DoS show remarkable similarities in the spin-up and spin-down channels. We can identify in many of the materials the region of reduced DoS in the spin-down channel which we identify makes $\mathrm{Cr}_{1/3}\mathrm{NbS}_2$ and $\mathrm{Cr}_{1/3}\mathrm{TaS}_2$ half metals.

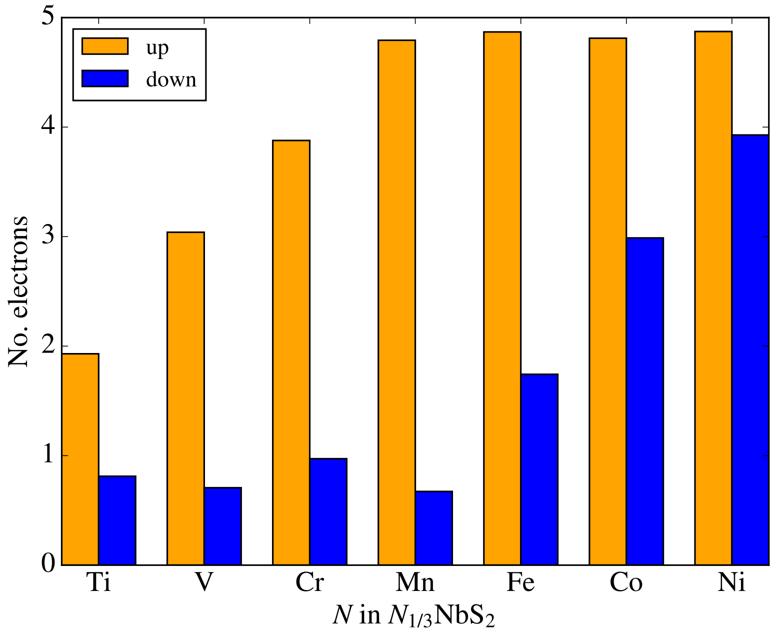

Figure 5.3.11: Bar graph showing the electron population of the spin-up (orange) and spin-down (blue) 3d-orbitals of the transition-metal, N, in $N_{1/3}$NbS$_2$.

Only for the materials where the intercalant has a less than half-filled $3d$-orbital do we find this reduction at the Fermi level. Many of the same features in the DoS are present across the series, however their relative position is shifted, for example in Fig. 5.3.12b we see the same pseudogap feature in the spin-up channel ∼0.6 eV above the Fermi level. It is interesting that the properties of these materials are determined by band-filling effects due strictly to the choice of intercalant. In the Cr intercalated materials, the pseudogap is found at the Fermi level because of the electron configuration of Cr. Rather than being a feature of the class of materials as a whole, intercalation with Cr is required to form the pseudogap.

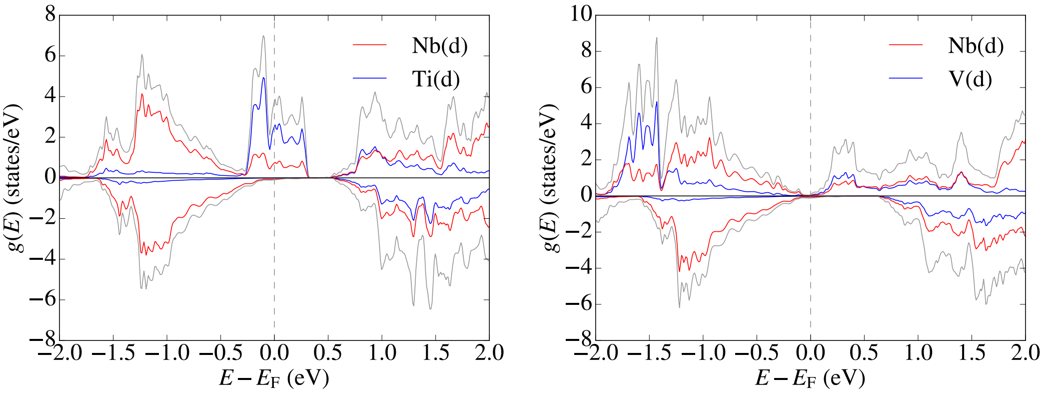

(a) $Ti_{1/3}NbS_2$ **(b)** $V_{1/3}NbS_2$

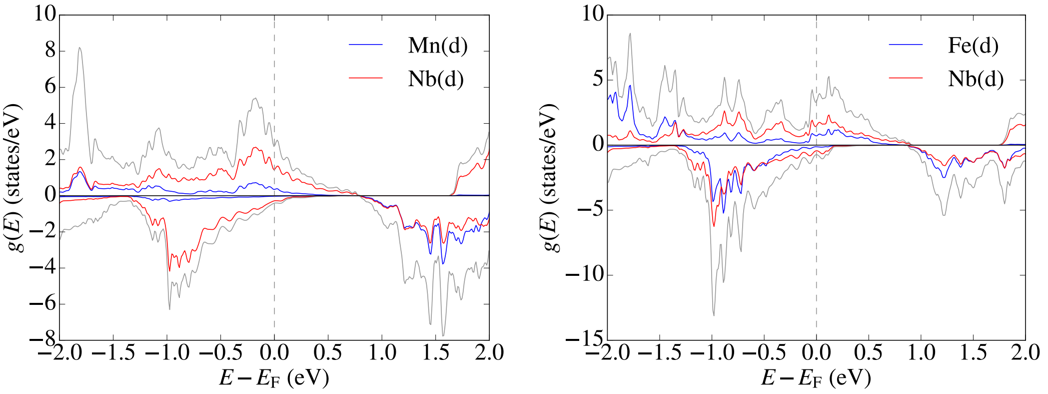

(c) $Mn_{1/3}NbS_2$ **(d)** $Fe_{1/3}NbS_2$

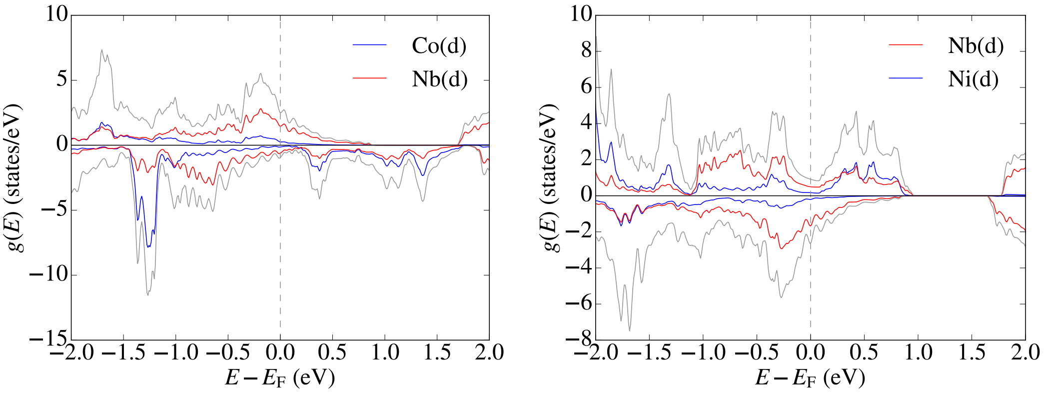

(e) $Co_{1/3}NbS_2$ **(f)** $Ni_{1/3}NbS_2$

Figure 5.3.12: DoS of transition-metal intercalated TMDCs with the intercalant coming from the first period of the transition metals. PDoS contributions for the transition-metal *d*-orbitals are shown as the main contributor to the total DoS around the Fermi level. Peaks are broadened using adaptive broadening [105] in the OPTADOS code [216, 94].

5.4 Conclusions

In conclusion, we have shown that electronic structure calculations can be used to explain all observed low temperature properties of $Cr_{1/3}NbS_2$ and $Cr_{1/3}TaS_2$, both materials we find to be half-metals contrary to previous reports. The presence of a small depression in the DoS in the spin-up channel in both materials allows dynamic fluctuation to occur at the Fermi level at low temperatures. These calculations do not require the added complication of SOC to capture the pseudogap, which in turn allows us to conclude that these low temperature effects are not driven by changes in the DMI. In addition to these first principles calculations, we have used AC susceptibility to confirm the existence of the pseudogap. We measured the gap width within good agreement of the DFT results. Throughout both the theoretical calculations and experimental results, we noted remarkable similarities between the materials $Cr_{1/3}NbS_2$ and $Cr_{1/3}TaS_2$, this is further supported by the recent discovery of the CSL in $Cr_{1/3}TaS_2$. As well as performing calculations on the Cr intercalated materials, we presented a broad study of the intercalated TMDCs. We have demonstrated that the electronic structure of the materials can be mostly predicted simply by the number of $3d$-electrons in the intercalant. A simple band filling model can be applied to these materials. To replicate the desirable properties of $Cr_{1/3}NbS_2$ and $Cr_{1/3}TaS_2$, materials with a pseudogap at the Fermi level should be sought. Our research is crucial for directing this search, as we now know that it is Cr rather than other species which leads to this feature. We might suggest investigation of materials such as $Cr_{1/3}MoS_2$ or $Cr_{1/3}WS_2$ for similar magnetic features. Overall our work shows how important it is to consider not only experimental techniques when studying materials with potential technological application, but also to include rigorous first principles studies.

Chapter 6

Source-corrected local spin density approximation

> *When you look at the book again many years later, you find yourself there, too, a slightly younger self, slightly different, as if the book had preserved you like a pressed flower.*
>
> —Cornelia Funke,
> *Inkspell*

In this chapter, we present our implementation of a correction to the local spin-density approximation (LSDA) developed by Sharma *et al.* [56] in CASTEP [24]. We will highlight the relevant physics that motivates this method and provide a mathematical description. We will show how the method can be implemented in a plane-wave pseudopotential density functional theory (DFT) code. Then, we shall present results of testing the implementation on a series of magnetic materials and the tuning of free parameters in the method. We shall then, using the new implementation, present the results of calculation on the pyrochlore material, $Dy_2Ti_2O_7$. Using this correction to an existing functional, we shall show that we are able to realise non-collinear magnetic structures in $Dy_2Ti_2O_7$ which are not possible using the standard functionals.

The implementation presented in this chapter was carried out by myself under the supervision of Stewart Clark at the University of Durham. All calculations presented in this chapter were performed by myself and the analysis is my own. A publication of these results is in preparation.

6.1 Introduction

We have discussed in Chap. 2 the difference between collinear and non-collinear systems. A system displaying collinear magnetism (CM) rather than non-collinear magnetism (NCM) can be said to have a global quantisation axis along which all the spins in the system is aligned. This is not the case for non-collinear spins, where each electron spin can have a different local direction. We often discuss spin in a system in terms of the spin density, or equivalently the magnetisation as defined in Eq. 2.39, rather than in terms of the spins of individual electrons. The magnetisation is a continuous vector field in the case of NCM, although this field becomes discretised onto a grid to perform calculations. By convention, in a spin-density functional theory (spin-DFT) calculation with collinear spin, the quantisation axis is along the z direction. However, if a system displays CM along a different axis, we can reproduce this behaviour by setting a quantisation axis along this axis and performing a calculation where the spin density is treated as non-collinear. The magnetisation will be aligned with this quantisation axis, although we retain the ability to describe the magnetisation and the potentials in three-dimensions. This allows us to describe the non-collinearity of the underlying fields, that is to say the degree to which the fields deviate from flowing along one global direction. Capturing the non-collinear behaviour of the fields is critical to reproducing realistic magnetic states using spin-DFT.

The accuracy of a DFT calculation depends heavily on the choice of exchange and correlation (xc) functional. Whenever one performs a DFT calculation, one must choose from a vast selection of xc functionals [64, 221]. Different xc functionals capture aspects of a physical system with varying accuracy, and if comparison to experimental methods is sought, the xc functional will determine how accurately the calculations describe the physical quantity in question. For example, if one wished to describe structural parameters of a material, rather than using the Perdew, Burke and Ernzerhof (PBE) [69] functional, one might consider the PBEsol functional [70] as it results in better agreement with experiment [222]. Materials which show exotic long-range and non-collinear spin textures have been a focus for researchers for many years, with *ab initio* methods for capturing this non-collinearity appearing in the 1980s [11]. Much research has gone into developing xc functionals specific to non-collinear spin [223, 224]. However, there are no functionals that consistently replicate experimental magnetic states over a wide range of materials. Most currently available xc functionals are simple extensions to functionals designed for collinear systems. We will briefly outline the process here.

For calculations of magnetic properties there are two key parameters, the charge density $n(\boldsymbol{r})$ and the magnetisation density $\boldsymbol{m}(\boldsymbol{r})$. In a non-collinear treatment, the electron potentials become 2×2 matrices and the vector magnetisation arises from the three Pauli spin matrices [55]. In standard DFT we have an xc functional $E_{\mathrm{xc}}[n(\boldsymbol{r})]$ and an associated xc-potential, $V_{\mathrm{xc}}(\boldsymbol{r})$, given by the functional derivative:

$$V_{\mathrm{xc}}(\boldsymbol{r}) = \frac{\delta E_{\mathrm{xc}}[n(\boldsymbol{r})]}{\delta n(\boldsymbol{r})}. \tag{6.1}$$

For a non-collinear potential, we can express it in terms of a scalar potential and a vector magnetic field [55, 56, 58],

$$\mathcal{V}_{\mathrm{xc}}(\boldsymbol{r}) = V_{\mathrm{xc}}(\boldsymbol{r})\mathrm{I}_{2\times 2} + \mu_{\mathrm{B}}\boldsymbol{B}_{\mathrm{xc}}(\boldsymbol{r}) \cdot \boldsymbol{\sigma}, \tag{6.2}$$

where $\boldsymbol{B}_{\mathrm{xc}}$ is the vector component of the xc potential, $\boldsymbol{\sigma}$ is the vector where each element is one of the Pauli spin matrices, μ_{B} is the Bohr magneton, and $\mathrm{I}_{2\times 2}$ is the identity matrix. Calculating the xc spin-potential for a non-collinear density is not an easy matter. We cannot use the expression in Eq. 6.1 directly as the density in a non-collinear treatment is not a scalar field. We can define each term in Eq. 6.2 separately. The scalar potential $V_{\mathrm{xc}}(\boldsymbol{r})$ can be defined as in Eq. 6.1 taking the density to be the scalar part of the non-collinear density in Eq. 2.46. The vector term, or the magnetic field, can be defined,

$$\mu_{\mathrm{B}}\boldsymbol{B}_{\mathrm{xc}}(\boldsymbol{r}) = \frac{\delta E_{\mathrm{xc}}[\boldsymbol{s}(\boldsymbol{r})]}{\delta \boldsymbol{s}(\boldsymbol{r})}, \tag{6.3}$$

where $\boldsymbol{s}(\boldsymbol{r})$ is the vector spin density. However, we do not have an approximation for $E_{\mathrm{xc}}[\boldsymbol{s}(\boldsymbol{r})]$ at present. Currently available parametrisations only exist for collinear systems where there are a well defined number of spin-up and spin-down electrons, i.e. $E_{\mathrm{xc}}[n^{\uparrow}, n^{\downarrow}]$.

To make use of the functionals we have such as LSDA, at each point in space, one must rotate the vector spin density such that it lies along the z axis, allowing us to decompose it into spin-up and spin-down densities which can be used to calculate E_{xc} [11, 59]. As the resulting energy is calculated piece-wise, it imposes a non-physical constraint that the magnetisation must be locally collinear with $\boldsymbol{B}_{\mathrm{xc}}(\boldsymbol{r})$.

Sharma *et al.* [56] highlight a further problem with standard functionals. From Gauss's law for magnetism, for any arbitrary magnetic field, $\boldsymbol{B}$, the divergence of the field should be zero, i.e. $\boldsymbol{\nabla}\cdot\boldsymbol{B} = 0$. This argument follows from the absence of magnetic sources. However, Sharma *et al.* [56] point out that this condition is not met for the most common functionals LSDA and PBE and suggest a method for improving these functionals. We outline their method here.

Starting from the Helmholtz theorem, a vector field can be decomposed into two components, one of that is divergence free and one that is curl free [225],

$$\boldsymbol{B}(\boldsymbol{r}) = \boldsymbol{\nabla}\times\boldsymbol{A} + \boldsymbol{\nabla}\phi. \tag{6.4}$$

To ensure that the magnetic field is source free we must explicitly subtract the term which contributes to the divergence of the field, $\boldsymbol{\nabla}\phi$. We have the freedom to select the gauge and chose ϕ such that it is the solution to the Poisson equation,

$$\nabla^2\phi(\boldsymbol{r}) = -4\pi\boldsymbol{\nabla}\cdot\boldsymbol{B}. \tag{6.5}$$

The source-free magnetic field can then be defined,

$$\tilde{\boldsymbol{B}}(\boldsymbol{r}) \equiv \boldsymbol{B}(\boldsymbol{r}) + \frac{1}{4\pi}\nabla\phi(\boldsymbol{r}). \tag{6.6}$$

Sharma *et al.* [56] then define the magnetic field as,

$$\boldsymbol{B}_{\mathrm{xc}}(\boldsymbol{r}) = s\tilde{\boldsymbol{B}}(\boldsymbol{r}), \tag{6.7}$$

where s is an empirical scaling parameter.

6.2 Implementation

We have implemented the above method in the plane-wave pseudopotential code CASTEP. Rather than defining a brand new xc functional, the source-free LSDA described by Sharma *et al.* [56] is an alteration of the existing functional. A user of this functional need not do anything other than they would for a calculation using LSDA. Each time the xc energy and potential is calculated, this potential is used to construct the xc magnetic field, $\boldsymbol{B}_{\mathrm{xc}}(\boldsymbol{r})$. Using the procedure described above, we can then calculate the source-free field, $\tilde{\boldsymbol{B}}_{\mathrm{xc}}(\boldsymbol{r})$, and reconstruct the spin potential. It is this potential that then used in the Hamiltonian of the system. Critically, this is not a one shot approach, the correction is calculated every time the xc potential is required and is therefore self-consistent.

We shall describe the process of calculating the correction in a plane-wave code. Starting from a general non-collinear spin potential [55],

$$\mathcal{V}_{\mathrm{xc}} = \begin{pmatrix} V^{\uparrow\uparrow}(\boldsymbol{r}) & V^{\uparrow\downarrow}(\boldsymbol{r}) \\ V^{\downarrow\uparrow}(\boldsymbol{r}) & V^{\downarrow\downarrow}(\boldsymbol{r}) \end{pmatrix}, \tag{6.8}$$

we can define the components of the magnetic field from Eq. 6.6 in terms of the matrix elements of the potential,

$$B^x_{\mathrm{xc}}(\boldsymbol{r}) = \frac{V^{\uparrow\downarrow}(\boldsymbol{r}) + V^{\downarrow\uparrow}(\boldsymbol{r})}{2}, \tag{6.9}$$

$$B^y_{\mathrm{xc}}(\boldsymbol{r}) = \frac{V^{\downarrow\uparrow}(\boldsymbol{r}) - V^{\uparrow\downarrow}(\boldsymbol{r})}{2\,\mathrm{i}}, \tag{6.10}$$

$$B^z_{\mathrm{xc}}(\boldsymbol{r}) = \frac{V^{\uparrow\uparrow}(\boldsymbol{r}) - V^{\downarrow\downarrow}(\boldsymbol{r})}{2}. \tag{6.11}$$

We can take advantage of $\mathcal{V}_{\mathrm{xc}}$ being Hermitian and only store one of the off-diagonal components, this reduces memory usage in a large computation.

Having arrived at an expression for $\boldsymbol{B}_{\mathrm{xc}}(\boldsymbol{r})$ we make use of the plane-wave basis set to efficiently solve the Poisson equation in Eq. 6.5. In a plane-wave basis, $\phi(\boldsymbol{r})$ can be expressed,

$$\phi(\boldsymbol{r}) = \sum_{\boldsymbol{G}_j} c_{\boldsymbol{G}_j} e^{\mathrm{i}\,\boldsymbol{G}_j\cdot\boldsymbol{r}}, \tag{6.12}$$

where $\boldsymbol{G}$ are the reciprocal lattice vectors and $c_{\boldsymbol{G}}$ are the Fourier expansion coefficients of $\phi(\boldsymbol{r})$. The Fourier expansion allows us to efficiently compute the Laplacian of the scalar potential ϕ,

$$\nabla^2\phi(\boldsymbol{r}) = -\sum_{\boldsymbol{G}_j} |\boldsymbol{G}_j|^2 c_{\boldsymbol{G}_j} e^{\mathrm{i}\,\boldsymbol{G}_j\cdot\boldsymbol{r}}. \tag{6.13}$$

We can also express $\boldsymbol{B}_{\mathrm{xc}}(\boldsymbol{r})$ in terms of its Fourier coefficients, $\boldsymbol{b}_{\boldsymbol{G}_j}$,

$$\boldsymbol{B}_{\mathrm{xc}}(\boldsymbol{r}) = \sum_{\boldsymbol{G}_j} \boldsymbol{b}_{\boldsymbol{G}_j} e^{\mathrm{i}\,\boldsymbol{G}_j\cdot\boldsymbol{r}}. \tag{6.14}$$

It can be shown that for a given vector $\boldsymbol{G}_j$, the Fourier coefficients of $\boldsymbol{\nabla}\cdot\boldsymbol{B}_{\mathrm{xc}}(\boldsymbol{r})$ can be given as

$$\mathscr{F}[\boldsymbol{\nabla}\cdot\boldsymbol{B}_{\mathrm{xc}}(\boldsymbol{r})](\boldsymbol{G}_j) = \mathrm{i}\,\boldsymbol{G}_j\cdot\boldsymbol{b}_{\boldsymbol{G}_j}, \tag{6.15}$$

where $\mathscr{F}$ denotes a Fourier transform (FT). By rearranging Eq. 6.5 and substituting the reciprocal space expressions in Eq. 6.13 and Eq. 6.15, we come to an expression for the Fourier coefficients of $\phi(\boldsymbol{r})$,

$$c_{\boldsymbol{G}_j} = \frac{\mathrm{i}\,\boldsymbol{G}_j \cdot \boldsymbol{b}_{\boldsymbol{G}_j}}{4\pi|\boldsymbol{G}_j|^2}. \tag{6.16}$$

Knowing these coefficients we can build the source-free magnetic field and reconstruct the spin potential using Eq. 6.2. We note that the corrected xc potential is no longer strictly local as we use knowledge of the gradient of the potential when solving the Poisson equation.

In addition to the treatment of non-collinear spin, we have implemented the correction for use when the calculation uses only collinear spin. The mathematical formalism for the collinear implementation is almost identical as presented above. The only difference is that we set the off diagonal terms in Eq. 6.8 to zero, thereby allowing us to separate subsequent expressions into spin-up and spin-down terms aligned along the z direction.

6.3 Testing on magnetic materials

To test the validity of the implementation of the source-corrected LSDA, we performed various calculations on a range of elemental magnets and magnetic compounds. The materials chosen for our testing are: Fe, Co, Ni, Ni_3Al, FeTe and $BaFe_2As_2$. These materials are ideal for testing due to their large magnetic moments and small unit cells. With the exception of $BaFe_2As_2$, calculations for each material can be performed on a laptop in a handful of minutes. The main focus of the testing is on body centred cubic (bcc), or α-Fe, where we performed magnetic calculations on a geometry optimised cell. For Fe, total energies are converged to better than 10 meV using a 7×7×7 Monkhorst and Pack (MP) $\boldsymbol{k}$-point-grid and a planewave cut off radius of 1600 eV. We used norm-conserving relativistic pseudopotentials throughout. In the interests of speed and efficiency, we performed all calculations on the other test materials using CASTEP default cut-off energy and MP $\boldsymbol{k}$-point-grids. Each of the materials tested have a ferromagnetic phase which we investigate using a quantisation axis aligned with the crystallographic c direction. We initialised spin along this direction in each material to ensure that the energy minimisation returned a state with long range magnetic order. We considered spin-orbit coupling (SOC) in all calculations for testing purposes unless otherwise stated.

6.3.1 Energy minimisation

While calculations using this functional are relatively straight forward, there are numerical issues which complicate the calculations in more complex systems. These numerical issues arise from the choice of energy minimisation scheme. The calculations performed by Sharma *et al.* [56] involve minimising the total energy through Hamiltonian diagonalisation. In the calculations presented above, the total energy is obtained using the density mixing (DM) minimisation scheme. Both of these schemes result in the correct final energy. However, using the ensemble density functional theory (EDFT) minimisation scheme [97] often results in a failure to reach the tightest convergence tolerances. The problem arises from the fact that EDFT is a fully variational minimisation technique, that is to say, at each step in the self-consistent field (SCF) calculation, the energy and the density are fully consistent. This is not the case in the DM scheme where the energy and the density are not required to be consistent until the end of the minimisation. In a normal calculation, the xc potential is calculated from the density. We calculate the xc energy for any particular functional using the density, and then calculate the xc potential from the energy functional. However, by introducing the correction to the xc potential, Eq. 6.6, the potential no longer corresponds to the xc energy,

$$\frac{\delta E_{\mathrm{xc}}[\hat{n}(\boldsymbol{r})]}{\delta \hat{n}(\boldsymbol{r})} \neq \tilde{\mathcal{V}}_{\mathrm{xc}}(\boldsymbol{r}). \tag{6.17}$$

A flow chart outlining this process can be seen in Fig. 6.3.1.

The potential calculated by applying the correction is used to construct the Hamiltonian operator for the next step in the minimisation. The Hamiltonian

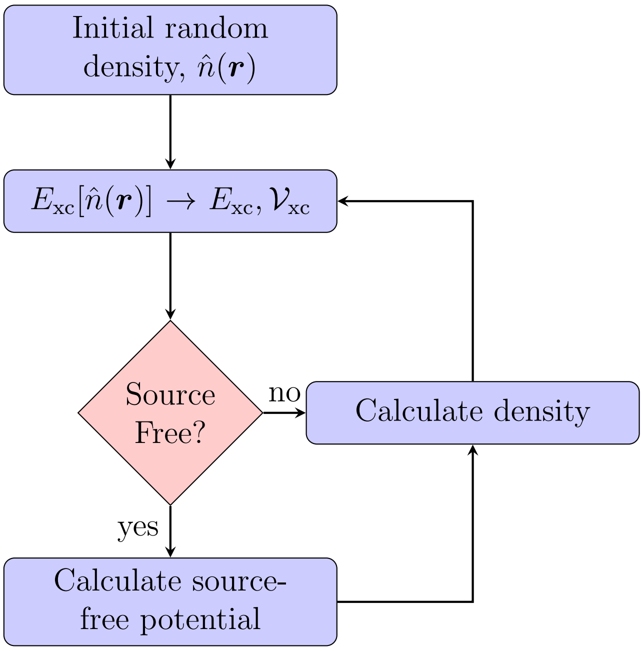

Figure 6.3.1: Flow chart for the EDFT minimisation with an extra step for calculating the source-free correction.

informs the down-hill direction for the energy minimisation, as discussed in Sec. 2.6.1 and App. A. The result of applying the correction is that the Hamiltonian is no longer guaranteed to be the steepest descent direction in the energy landscape. However, as the correction to the potential is typically small, the corrected Hamiltonian remains a down-hill direction, at least early in the calculation where changes in energy are larger between SCF steps. The numerical issues arise when the SCF calculation is coming to the end. At the end of the minimisation, one typically looks for changes in energy that are of the order 10^{-6} eV/atom, this is approaching the magnitude of the energy cost of the source-free correction. With these final SCF steps, the minimisation direction found using the source-corrected Hamiltonian leads to an energy that is higher than the previous step. At this point in the calculation, it is not possible to find a search direction which lowers the energy causing the minimisation algorithm to terminate, believing it has found the minimum energy. A schematic of this final SCF step is shown in Fig. 6.3.2.

When using the spin-DFT minimisation scheme to calculate properties with the source-corrected LSDA, the results are not strictly self consistent. However,

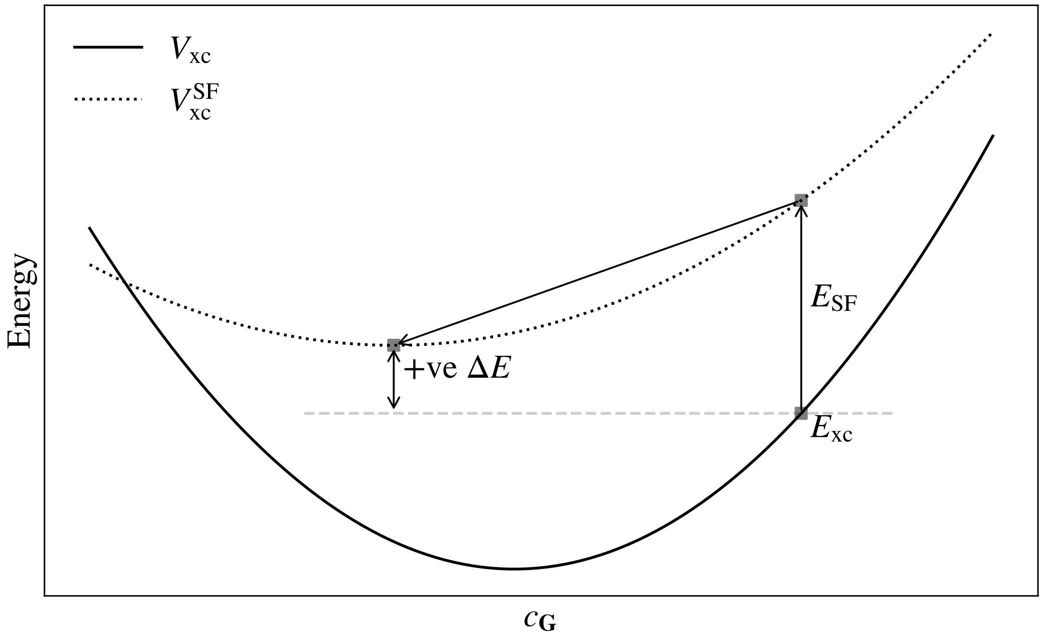

Figure 6.3.2: Schematic of a single step of an EDFT energy minimisation including source-free correction during which the minimisation fails. The solid line represents the energy calculated from the uncorrected xc functional and the dotted line represents the unknown energy due to the source-corrected function. The energies are depicted as being static while in practice due to the self-consistent nature of the calculations, the energy landscape would change as we change the expansion coefficients $c_{\boldsymbol{G}}$.

this is true of all minimisation schemes as we must always accept some numerical tolerance in the convergence of minimisation. It is not possible to know *a priori* if the corrected LSDA functional will cause the minimisation to fail or at what level of convergence. Due to the random initialisation of the Kohn-Sham (KS) orbitals, the path the minimisation takes through parameter space will change, even between different calculations performed on the same material. The inconsistency between the energy and the corrected potential is always present, even if the minimisation does not fail. It may be possible that the inconsistency happens to be smaller than the electronic convergence tolerance of the calculation. Figure 6.3.3 shows an example SCF calculation performed on Ni using the EDFT scheme where the inconsistency leads to a failure. The minimisation performs six iterations normally before it is unable to find a search direction that lowers the total energy. It then performs a further two iterations where all search directions lead to a higher energy before terminating. It is worth noting that this does not lead to any errors being produced by CASTEP as it appears to have found a legitimate energy minimum. In practice, this inconsistency between the energy and the potential causes only minor issues for most calculations tested. The energy minimisation shown for Ni in Fig. 6.3.3 represents an extreme case where the changes in energy before failure are large ($\sim 10^{-2}$ eV). For most calculations performed, the changes in energy reach a much tighter tolerance of approximately 10^{-5} eV/atom before running out of search directions. Rather than resulting in the complete failure of the correction when used in conjunction with an EDFT minimisation, the results must be considered carefully to determine if the energy convergence is suitable for the desired application. For example, if one is determining the most stable magnetic configuration in a crystal by comparing the energies of multiple non-collinear spin-DFT calculations, it is important that the convergence of each calculation is comparable as a small change in energy could change the order of the total energies.

6.3.2 Magnetic fields

A useful way to visually test the effects of the correction to $\boldsymbol{B}_{\mathrm{xc}}$ is to examine the magnetic field lines. It is easy to see from magnetic field lines if the source terms have been correctly removed from the field. Using electric fields as an analogy, electric field lines emerge radially outwards from a point charge. However, to create a system that is source-free, we may add a second point charge of opposite sign. The field lines now will emerge from one charge and flow into the second charge, forming loops. Due to Maxwell's equations ($\boldsymbol{\nabla} \cdot \boldsymbol{B} = 0$), we know that magnetic fields ought to follow this second scheme.

The magnetic field lines presented below are all calculated from the contribution to the total potential from V_{xc}. We have ignored all other contributions to the potential, and as such these do not represent physical fields. Starting from a point in the unit cell, we calculate the direction and magnitude of the

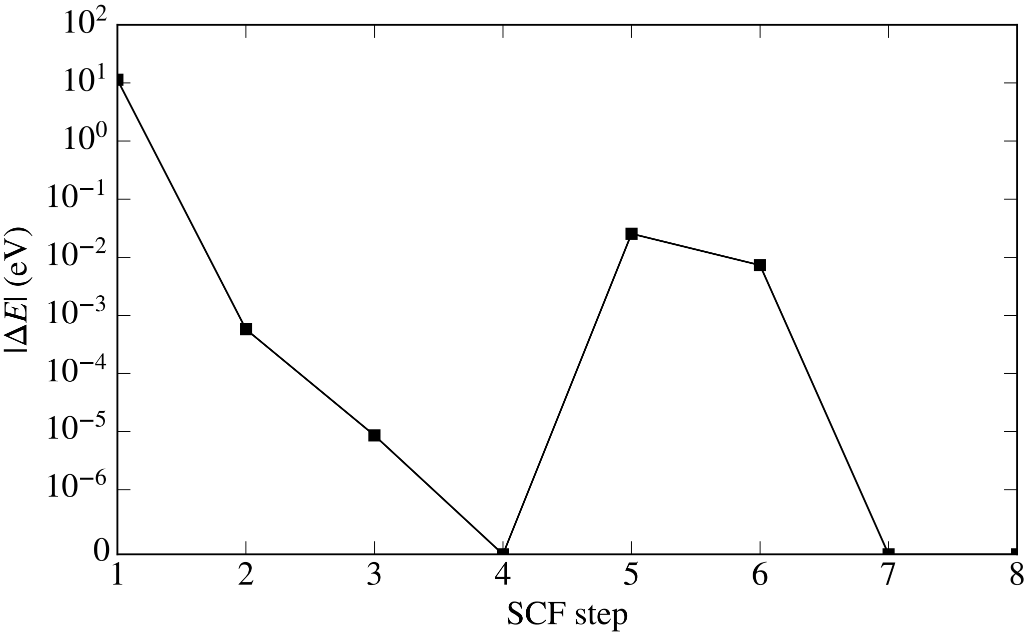

Figure 6.3.3: Minimisation of total energy of Ni using the EDFT under the source-corrected LSDA. The change in energy, ΔE is relative to the total energy at the previous step.

field from the xc potential at that point. Using a small step size we move along the direction of magnetic field at that point. We then use this new position in the unit cell to calculate the field and repeat the process. Connecting up these points produces a near-continuous path through the unit cell which approximates the field lines. As the potential is discretised onto a grid, we make use of interpolation to evaluate the field at arbitrary points between the grid points. Due to this interpolation, particularly in regions of low magnetic field strength where numerical noise dominates, we produce field lines that are not smooth. However, as the magnitude is insignificant in these regions, the field lines are less important.

In Fig. 6.3.4, we compare the field lines due to $\boldsymbol{B}_{\mathrm{xc}}$ in α-Fe. Using both the LSDA and the source-free LSDA we find magnetic moments on each atom aligned along the c axis. We can see in Fig. 6.3.4a the field lines arising from the LSDA without the source correction. These lines are all parallel and flow only in the c direction. As we have set a quantisation axis for these calculations along

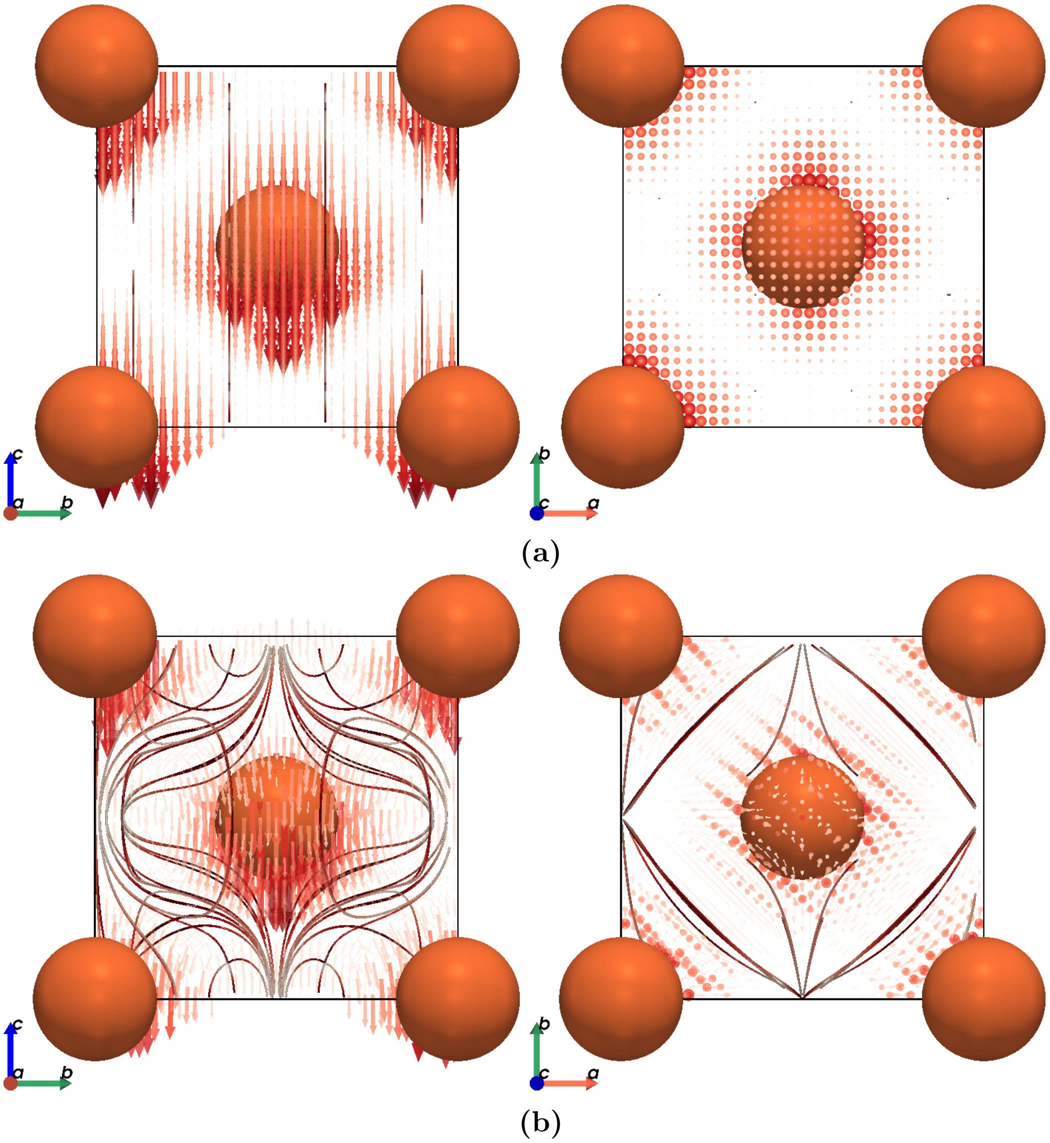

(a)

(b)

Figure 6.3.4: Xc magnetic fields of of α-Fe shown along the a (left) and c (right) crystal directions. (a) Fields calculated using standard LSDA functional and (b) fields calculated using source-free LSDA with $s = 1$. Colour of the field lines represents the magnitude of the field at that point, from white at low fields to red at high fields. Vectors show the direction of the field flow with size and colour representing magnitude. Where the field magnitude is lower than 10% of the maximum, vectors have been omitted for clarity. Magnetic moments lie in the negative c direction in both cases. Images produced using nc_cryst [226] (See App. C).

the c direction, the spin density is all aligned along this axis. It is clear that these field lines for α-Fe are globally collinear with the magnetisation, one of the main issues with the LSDA highlighted by Sharma *et al.* [56]. In a physical system, there is no requirement for the magnetic field and the magnetisation to be collinear at each point in space. This is one aspect of magnetic phenomena not captured by the LSDA. As we use periodic boundary conditions (PBC), the calculations are of infinite crystals rather than isolated unit cells. For the LSDA, the field lines are parallel throughout the entire infinite crystal, implying the presence of a magnetic source at the surface. If we instead study the field lines due to the source-corrected functional, Fig. 6.3.4b, we see that the field lines are different. The field lines form closed loops around the Fe ions, following similar patterns one sees by sprinkling Fe filings around a bar magnet. These field lines are continuous across the PBC. As we have used the same quantisation axis in both calculations, the magnetisation is also collinear with the c axis when using the source-free LSDA. It is clear then that the field lines for $\boldsymbol{B}_{\mathrm{xc}}$ are no longer constrained to be locally collinear with the magnetisation when the source terms are removed.

We see similar results when we calculate the $\boldsymbol{B}_{\mathrm{xc}}$ field lines in hexagonal close packed (hcp)-Co, Fig. 6.3.5. Using the LSDA, Fig. 6.3.5a, we again see parallel field lines aligning with the magnetisation which lies along the c axis for both Co ions. From the source-corrected LSDA, Fig. 6.3.5b, we see improved non-collinearity of the field lines. Close to the Co ions, field lines emerge from the centre of the ion and terminate again at the centre of the ion. The behaviour further from the Co in the interstitial region is more complicated due to interactions between both ions.

We see from the field line calculations of both Fe and Co that the source-corrected functional results in more physical magnetic field lines in elemental ferromagnets. An example of the effects of the source-corrected functional on the xc field lines on a non-elemental magnet, FeTe, can be seen in Fig. 6.3.9b. In this case, the field lines flow between the layers of Fe ions past the Te ions. It is

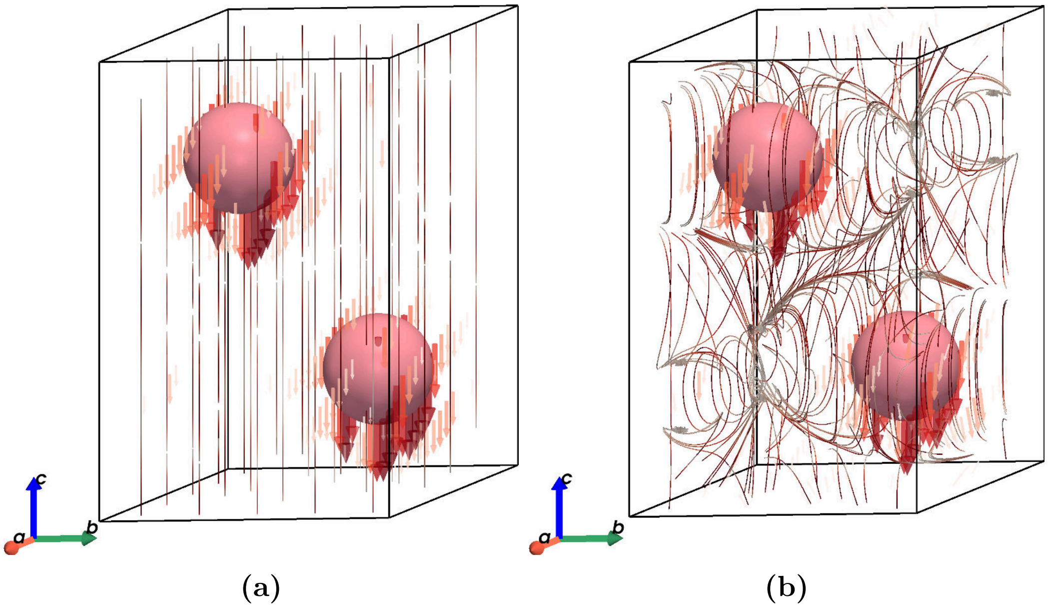

Figure 6.3.5: Magnetic field lines due to xc in hcp-Co calculated with (a) LSDA and source-free (b) LSDA calculated with $s = 1$. Colour of the field lines represents the magnitude of the field at that point, from white at low fields to red at high fields. Images produced using nc_cryst [226] (See App. C).

less obvious that the xc field lines in FeTe represent a source-free field. We lose the simplicity of the elemental magnets by including non-magnetic ions which complicate the exchange interactions. However, we still see the improved non-collinearity of the magnetic field around the ions arising from the source-free functional.

6.3.3 Free scaling parameter

The definition of the source-free LSDA, Eq. 6.7, has a free parameter, s, which scales the source-free xc magnetic field. This parameter is used to empirically alter the magnetic field to better reproduce experimental results. Sharma *et al.* [56] argue that the best value of this parameter is $s = 1.12$ as this best replicates the magnetic moments for the materials they tested. We have performed a series of calculations varying this parameter to find an appropriate value for studying magnetism in condensed matter.

We start by examining the effects of this empirical scaling parameter on α-Fe. We performed a series of calculations on Fe by varying s between 0.5

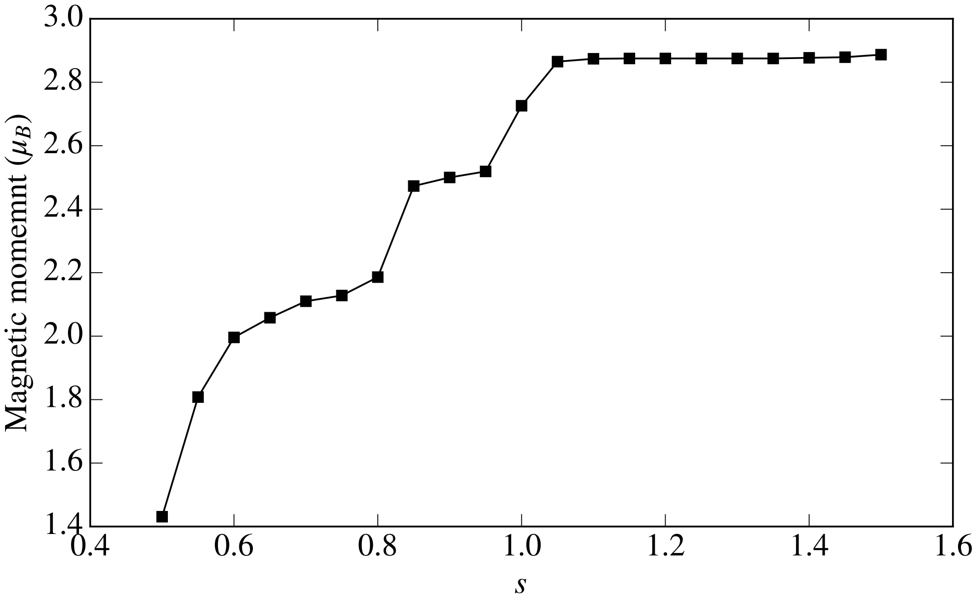

Figure 6.3.6: Magnetic moment on the Fe ions in bcc-Fe as a function of empirical scaling parameter, s, of the xc magnetic field.

and 1.4 and looking at the change in the magnetic moment on the Fe ions. The change in magnetic moment is shown in Fig. 6.3.6. For these calculations we have neglected SOC as we expect the effects to be small in this material. At low values of s, the magnetic moment is much lower than the experimental value of $2.2\mu_{\mathrm{B}}$ [56]. As s is increased, the magnetic moment increases sharply before levelling off above $s = 1.0$ to a magnetic moment of around $2.9\mu_{\mathrm{B}}$ due to saturation of the magnetic moment by the large field. The scaling parameter alters the magnitude of the internal magnetic field, hence the increase in the magnetic moment. The increase in the magnetic moment is not linear as one would expect from increasing a static external magnetic field. We see that increasing s also affects $\boldsymbol{B}_{\mathrm{xc}}$, leading to an increased magnitude and density of field lines. One would expect that scaling the internal magnetic field may cause changes to the underlying electronic structure that determine the magnetic moment. To that effect, we performed calculations of the band structure of Fe as a function of s, some example band structures can be seen in Fig. 6.3.7. If we were applying an external field to a collinear system with spin-up and spin-down bands in the band structure, we would expect to see a lifting of the degeneracy

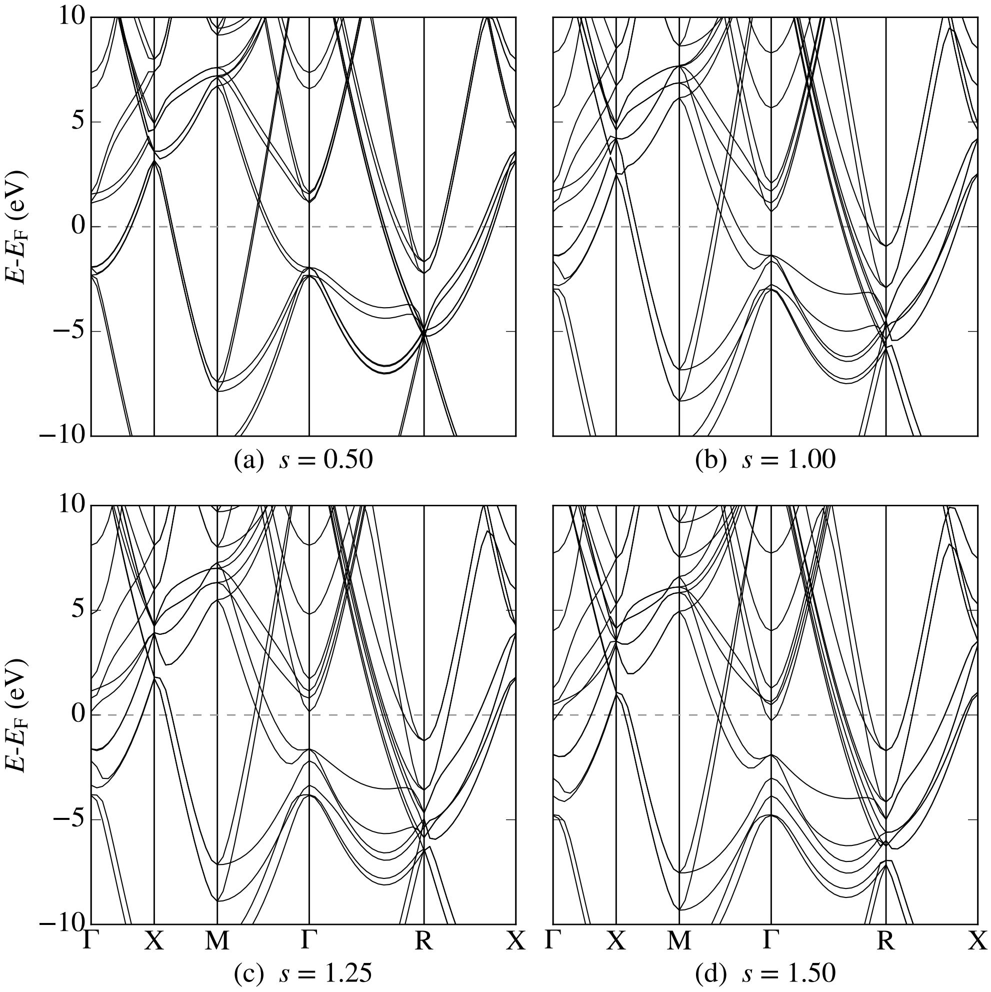

(a) $s = 0.50$ (b) $s = 1.00$

(c) $s = 1.25$ (d) $s = 1.50$

Figure 6.3.7: Band structures calculated using the source-free functional. Each band structure is calculated using different values of the scaling parameter s. Plots produced using dispersion.py [104] (See App. C).

of the bands through Zeeman splitting. Looking at Fig. 6.3.7a and Fig. 6.3.7b, we can see there are some bands that open up at the M point as we increase s. Of course with a non-collinear band structure we cannot say for certain if these bands are spin-up or spin-down even though our calculation produces a ferromagnet. As we get to higher values of s, instead of increasing the splitting of the bands, we see that the bands begin to rigidly shift downwards. This is consistent with the observations of the magnetic moments as this rigid shift would have a limited effect on the size of the moments.

Next we present results of the effects of s on a non-elemental magnet, FeTe.

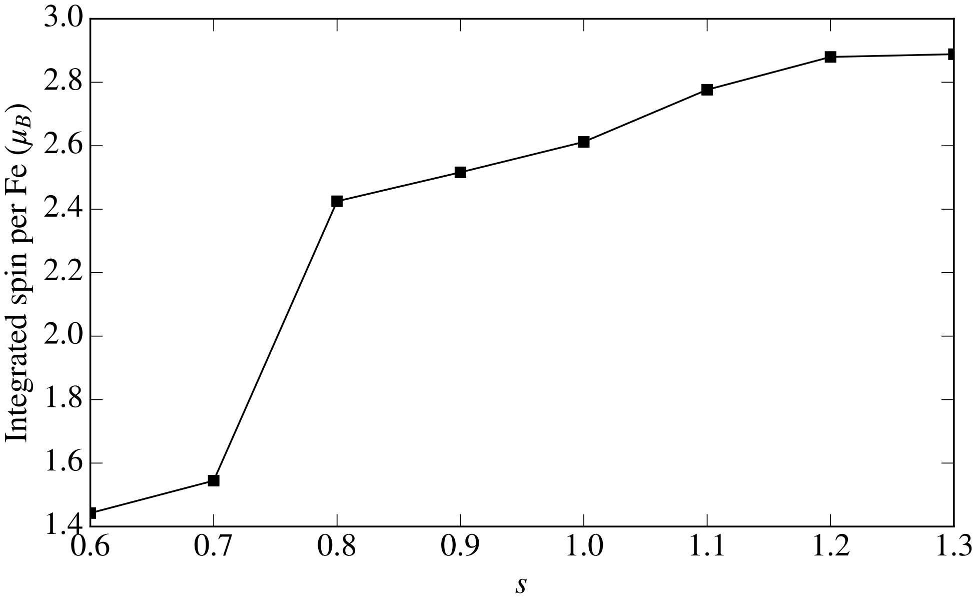

Figure 6.3.8: Magnetic moment on the Fe ions in FeTe as a function of empirical scaling parameter, s, of the xc magnetic field.

In Fig. 6.3.8 we show the integrated spin density in FeTe as a function of s. Much like the magnetic moment of α-Fe, we see a large increase in the spin density at low values of s in FeTe. Rather than a plateau in the magnetisation at higher values of s, we see a reduced rate of increase. This suggests that the values of s tested in FeTe are not sufficient to saturate the magnetisation, unlike Fe. The general trend is a constant increase in the magnetisation as s increases, as we saw in elemental Fe. As Fig. 6.3.8 shows the integrated spin density of FeTe rather than the magnetic moment as for Fe, it is possible that increasing s also increases the magnetisation in the interstitial region.

We can also investigate the effects of the scaling parameter on the magnetic field lines, allowing us to gain a better understanding of the entire field rather than reducing it to a single number. The field lines of $\boldsymbol{B}_{\text{xc}}$ calculated from the source-free LSDA using two different values of s are shown in Fig. 6.3.9. We have chosen values that represent the two distinct regimes in the magnetisation shown in Fig. 6.3.8. Using a low value of $s = 0.6$, Fig. 6.3.9a, we see that the field lines are split into two different regions. There are the field lines resulting from the field due to the bottom layer of Fe ions and the field lines resulting

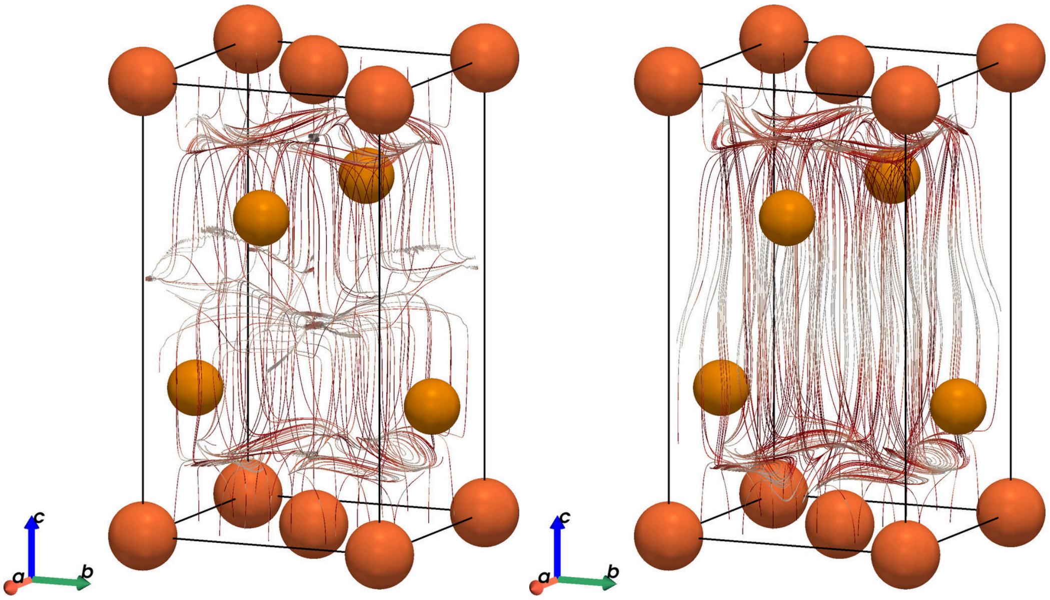

(a) $s = 0.6$ **(b)** $s = 1.0$

Figure 6.3.9: Magnetic field lines due to xc in FeTe with example empirical scaling of the magnetic field (a) $s = 0.6$ and (b) $s = 1.0$. Fe is shown in orange and Te is shown in gold. Colour of the field lines represents the magnitude of the field at that point, from white at low fields to red at high fields. Images produced using nc_cryst [226] (See App. C).

from the top layer. Between the layers at the centre of the crystal along the c axis, there is a region of low field strength. In this case the field lines flow through the Te ions and back down towards the face centred Fe ion. For the higher value of s where we see an increase in the magnetisation, we show the field lines for the case of $s = 1.0$ in Fig. 6.3.9b. We can no longer split the field into two regions; for the higher values of s, the field lines flow from the bottom layer of Fe ions to the top layer. The Te ions, despite not having any magnetic moments, influence the direction of the field lines. Rather than flowing directly upward through the crystal, the field lines flow through and around the Te ions. By increasing the field strength with the scaling parameter, the magnetic field is strong enough to flow through the entire crystal rather than splitting into two different domains. This shows that using a single parameter, we are able to dramatically change the underlying magnetic field, altering the interactions between the magnetic ions.

Given the investigations into the effects of the scaling parameter s, there is insufficient evidence to show that any particular value of s systematically results in improvements to the field and resulting magnetic properties. By scaling the internal field, it is possible to tune the resulting magnetic moment, this could be used to reproduce experimentally measured values. While a particular value may systematically improve the results of calculations of a particular class of materials, it is unlikely that this improvement would be realised for any arbitrary material. The use of this parameter is dependent on the purpose of the calculations performed. Scaling the magnetic moment to experimental values may allow for better comparison to experiment for other calculated properties by removing systematic errors from the calculations. For our purposes, we are interested in a first principles approach to studying magnetism, therefore all further calculations are performed with $s = 1$.

6.3.4 Magnetic moments

One of the main results of the source-corrected xc functional presented by Sharma *et al.* [56] is that it leads to improved magnetic moments in condensed matter when compared to the uncorrected LSDA. We have performed non-collinear spin-DFT calculations on the materials in our test set to examine the magnetisation in each using both the corrected and uncorrected LSDA. Using the DM scheme, we are able to ensure that spin initialisations are held throughout the SCF calculation to result in a ferromagnetic state. We have looked at the integrated magnetisation density normalised by the number of magnetic ions in the system. The results of these calculations are shown in Table 6.1. We see a systematic increase in the total amount of spin in each system. Interestingly, in the case of Ni_3Al, the LSDA finds no overall magnetic state. While using the source-free LSDA we realise a non-zero moment on the Ni ions. In each case except for Ni_3Al, the integrated magnetisation density per magnetic ion is higher than the experimental magnetic moment, even when using the LSDA. When using the source-free LSDA, the magnetisation is often much larger than the experimental moment. As we are using the total integrated magnetisation to

Material	Integrated spin density per magnetic ion (μ_B)		Experimental moment (μ_B)
	LSDA	Source-free LSDA	
Fe	2.15	2.71	2.2 [56]
Co	1.76	1.96	1.57 [227]
FeTe	2.41	2.78	2.25 [228]
Ni	0.95	1.00	0.65 [56]
Ni_3Al	0.00	0.15	0.077 [56]
$BaFe_2As_2$	0.91	2.86	0.87 [229]

Table 6.1: Calculated spin density per magnetic ion calculated with the source-free LSDA and uncorrected LSDA.

approximate the magnetic moment on the ions, it is possible that spin density in the regions between the atoms could be artificially increasing the estimate. Using a Mulliken projection could lead to a better approximations to experiment. As we find that the source-free LSDA implemented in CASTEP leads to magnetic moments that are too large compared with experiment, this also suggests that we should avoid using any value of the scaling parameter that would lead to yet larger moments. The increase in moment when using the source-free LSDA functional is likely due to the increased internal magnetic field we find compared to the LSDA.

6.4 Spin ice in $Dy_2Ti_2O_7$

In this section, we use the source-corrected LSDA to perform non-collinear spin-DFT calculations on the pyrochlore material, $Dy_2Ti_2O_7$, making use of the improved non-collinearity to realise its magnetic structure.

6.4.1 Introduction

In a system with antiferromagnetic exchange interactions between magnetic ions, the crystal structure plays a role in how the magnetic moments can be arranged. In a cubic crystal displaying antiferromagnetic exchange, it is possible for each ion to have the opposite spin of its neighbours [5]. An issue occurs when

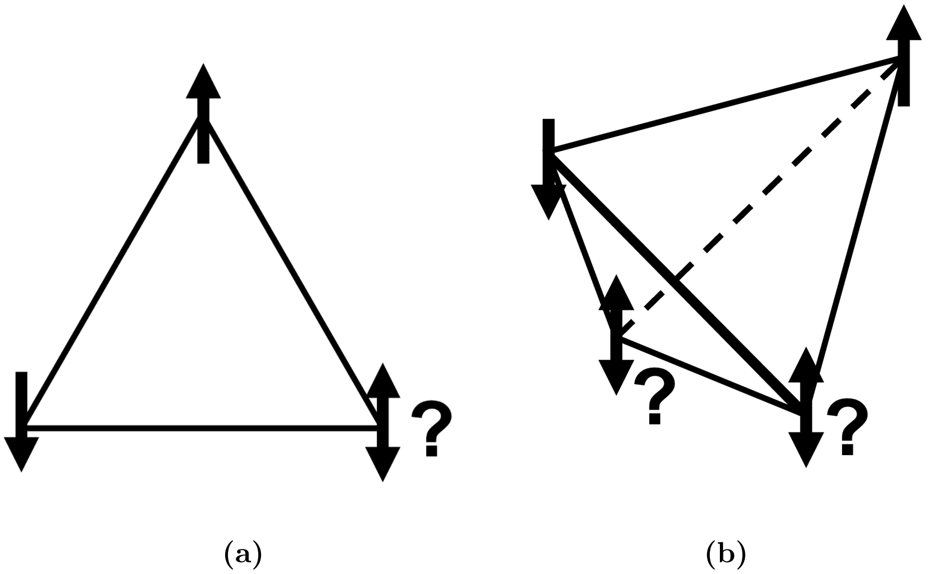

Figure 6.4.1: Geometrical frustration caused by antiferromagnetic exchange interactions in (a) a triangular lattice and (b) a tetrahedral lattice.

the arrangement of ions is a different geometry, such as a triangular lattice in two dimensions. In that case it is impossible to satisfy all of the interactions, at least two of the ions will have the same spin as one neighbour. In three dimensions, this effect is seen in tetrahedral lattices, where two of the spin site are unable to satisfy their interactions. This is known as geometric frustration in magnetism (Fig. 6.4.1) and can lead to a variety of exotic magnetic structures. Frustration is known to stabilise magnetic skyrmions [230, 231] as well as spin-ice states in pyrochlore materials [12, 14].

Spin-ices gain their name from similarities to the properties of water-ice, H_2O. Linus Pauling described the behaviour of the H atoms in single crystal samples of ice [232], showing that two H atoms are located close to an O atom while two others are located further away. This *two-in, two-out* description of H atoms can be applied exactly to the magnetic moments in some of the pyrochlore materials which comprise corner sharing tetrahedra of metal ions. In a spin-ice, two of the spins point inward to the centre of the tetrahedron while the other two point outwards from the centre [233]. Arising from frustration, there are many degenerate ways of arranging the spins on the corners of the tetrahedron. The possible combinations of spins in pyrochlore spin-ices grow exponentially with the size of the crystal, leading to a residual entropy in these systems when cooled to low temperatures [12]. The same entropy was shown experimentally by Pauling with water-ice.

One of the most famous examples of a spin-ice pyrochlore is $Dy_2Ti_2O_7$ which comprises corner sharing tetrahedra of Dy^{3+} ions. These tetrahedra are integral to the formation of the spin-ice state, whereby two spins point in and two spins point out along the local $\langle 111 \rangle$ axis. The spin-ice state in $Dy_2Ti_2O_7$ has been widely studied over the previous 30 years [233, 234, 235, 236, 237], although there have been limited first principles simulations of this state. A spin-ice is inherently non-collinear and highly degenerate, thus it provides a challenge for spin-DFT calculations, particularly with the xc functionals currently at our disposal.

Not only does the spin ice state in $Dy_2Ti_2O_7$ provide a way to investigate the residual entropy in water-ice, it is also well known for demonstrating magnetic monopoles. In 2008, quasiparticles resembling magnetic monopoles were discovered in $Dy_2Ti_2O_7$ by Castelnovo *et al.* [238]. These are formed by creating defects in the two-in, two-out structure. By inducing a flip of one of the spins in a tetrahedron, the result is a *three-in, one-out* tetrahedron. But, as these are corner sharing tetrahedra, this causes the neighbouring tetrahedron to have a *one-in, three-out* spin configuration [239, 236]. For a typical tetrahedron, the divergence of the magnetisation is zero as we have equal amounts of spin flowing into the tetrahedron as flowing out. In the defect tetrahedron, we have more spin flowing in one direction than the other. Of course globally throughout the crystal the internal magnetic field is divergence-free, but locally a spin-ice tetrahedron with a defect appears like a magnetic monopole. By flipping one spin, one creates two tetrahedra with non-typical spin configurations. However by flipping a second spin in the second tetrahedron we can move this defect along through the crystal. Therefore, the two monopoles are free to exist independently in the crystal. $Dy_2Ti_2O_7$ is an important material for testing the fundamental properties of magnetism and it is important that first-principles studies of this material are able to capture the physics underpinning the spin-structure. We shall present results of spin-DFT calculations where we make use of the source-corrected LSDA functional to stabilise the spin-ice state.

6.4.2 Computational methods

We calculated the spin structure of $Dy_2Ti_2O_7$ using a primitive crystallographic cell including 22 atoms, using lattice parameters of 7.19 Å calculated by DFT structural relaxation [240]. The primitive cell is sufficient to capture the spin-ice ground state and is preferable to performing calculations on the conventional cell which is four times larger. Calculations of the spin structure of $Dy_2Ti_2O_7$ were calculated with a 5×5×5 MP $\boldsymbol{k}$-point-grid with a plane-wave cut-off of 840 eV. The convergence testing is shown in Fig. 6.4.2. The SCF calculation was performed using the EDFT minimisation scheme. Due to the complicated electronic and spin structure of $Dy_2Ti_2O_7$, it was not possible to find an energy minimum using the DM scheme and we therefore used the EDFT scheme for our calculations. This would have been preferable to avoid the minimisation issues discussed in Sec. 6.3.1. We performed identical calculations treating xc with both LSDA and the newly implemented source-free LSDA to compare the resulting spin configurations. In the case of both LSDA and the source-corrected LSDA we initialise a non-collinear spin on each of the Dy ions along the direction of the local $\langle 111 \rangle$ direction. Based on testing of the scaling parameter, s, in Sec. 6.3.3 and on further testing done on $Dy_2Ti_2O_7$, we conclude that there is no *a priori* reason to use a any value other than $s = 1$.

6.4.3 Results and discussion

First we shall look at the magnetic field lines due to xc in $Dy_2Ti_2O_7$. The xc magnetic fields for both functionals are shown in Fig. 6.4.3. The structures of the field lines are more complicated than we see in the ferromagnetic Fe and the other simple magnets discussed above. However, it is still possible to

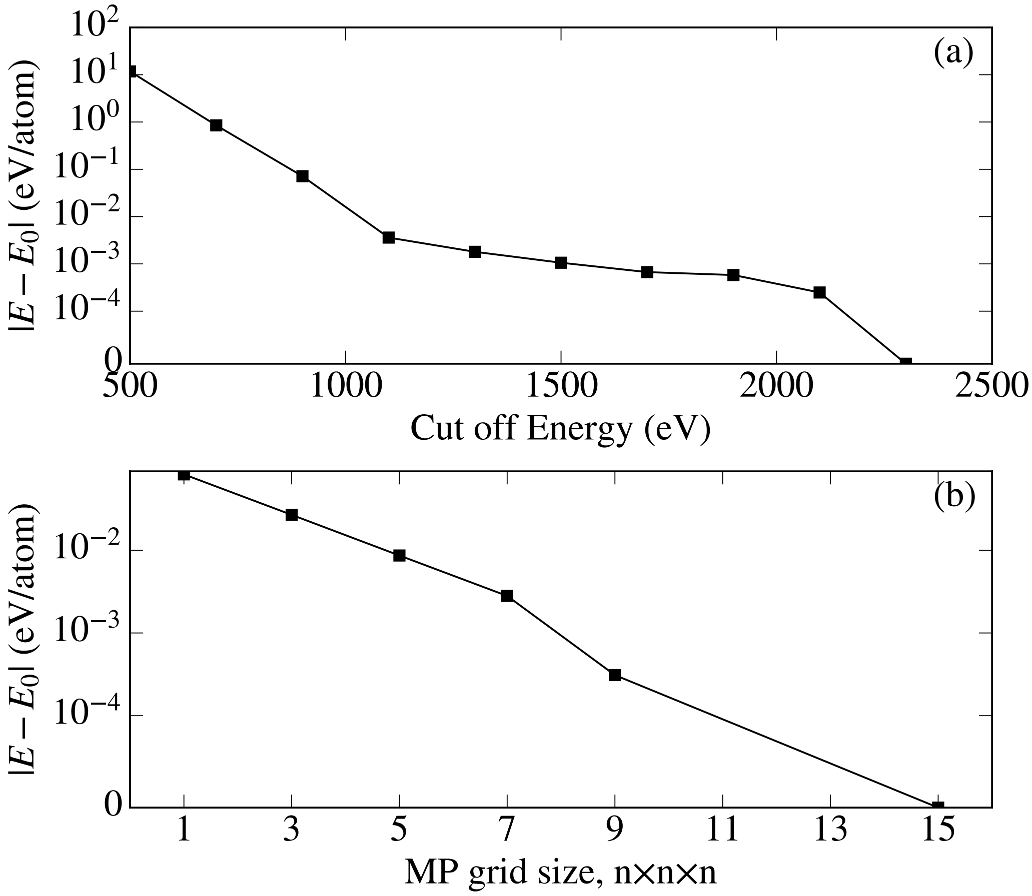

Figure 6.4.2: Convergence testing of (a) plane-wave basis set and (b) $\boldsymbol{k}$-point set for $Dy_2Ti_2O_7$. The energy E_0 is assumed to be the value obtained by using the highest convergence parameter in each case. Absolute values are used to enable the use of a log scale.

see that the field lines remain locally collinear around the Dy ions in the case of the LSDA (Fig. 6.4.3a), aligning with the magnetisation which is localised around these ions. In the interatomic regions it is less clear that the field lines are collinear, largely due to the lack of significant spin density, which is instead dominated by numerical noise. However, for the source-free functional (Fig. 6.4.3b) the field lines display more non-collinearity and no longer strictly follow the magnetisation as we have seen in the cases of simple magnets. We will show below that by better capturing the physics of the internal fields using the source-corrected LSDA, we are able to realise the experimental magnetic structure.

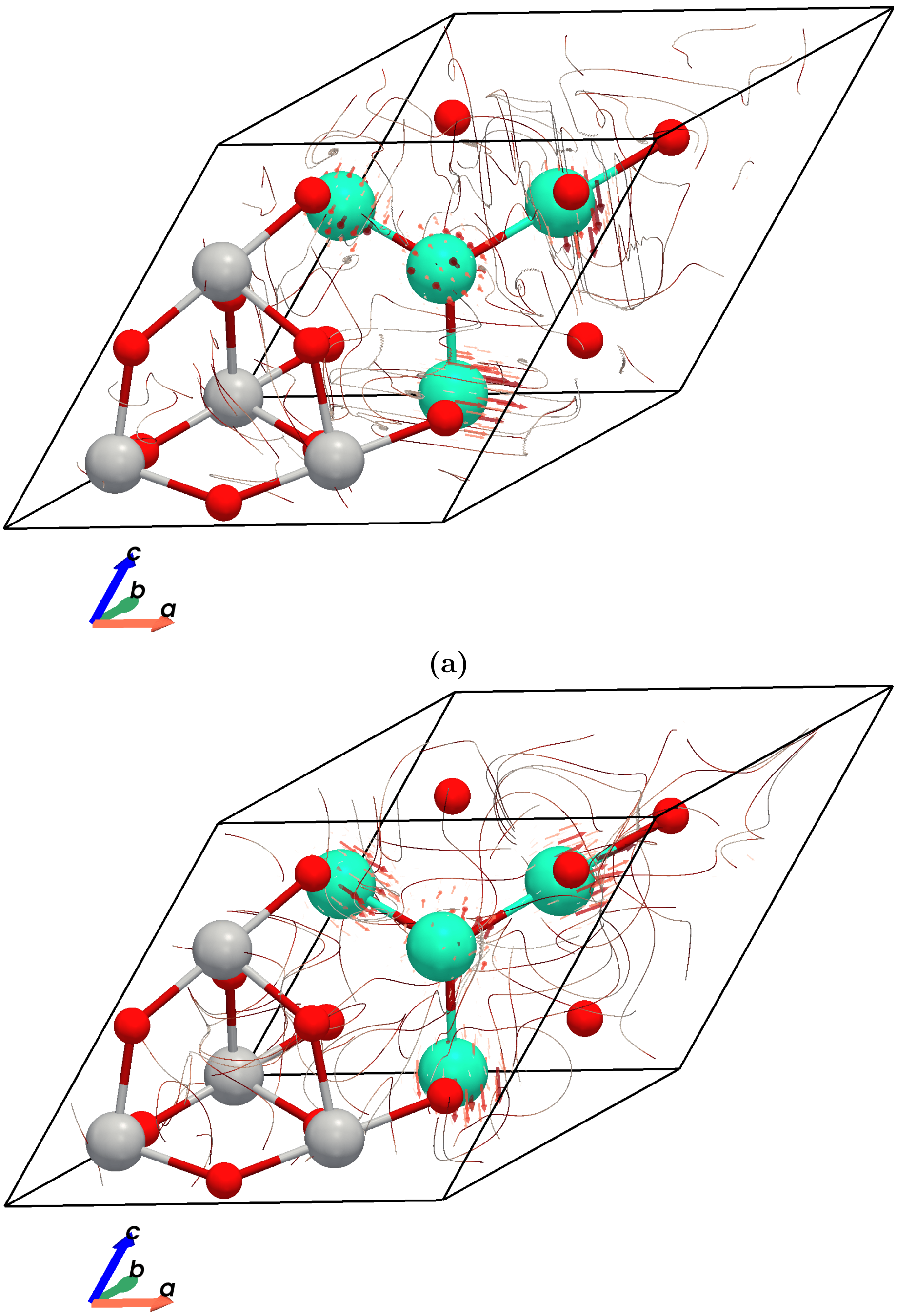

(a)

(b)

Figure 6.4.3: Magnetic field lines of B_{xc} for a primitive unit cell of $Dy_2Ti_2O_7$ calculated using the (a) LSDA and the (b) source-corrected LSDA, The opacity of the field lines represents the relative strength of the field. For the LSDA field there is a local collinearity with the spin projected onto the Dy atoms, whereas for the source-free functional B_{xc} is no longer aligned with the magnetisation. Dy, Ti and O ions are shown in green, silver and red respectively. Images produced using nc_cryst [226] (See App. C).

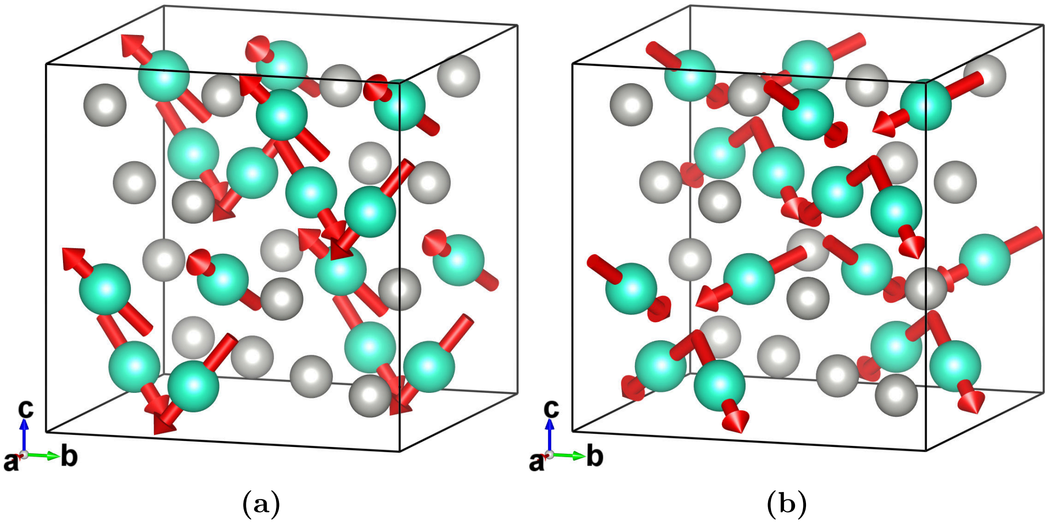

(a) (b)

Figure 6.4.4: Example magnetic configurations of $Dy_2Ti_2O_7$ calculated using (a) LSDA and source-free (b) LSDA are shown in the conventional unit cell. Dy ions and Ti ions are shown in green and silver respectively. The red arrows show the non-collinear spin density projected onto a local atomic basis for the Dy ions. Oxygen atoms are not shown for simplicity. Images produced with VESTA [148].

The improvement in non-collinearity provided by the source-free LSDA leads us to realise a spin-ice structure in $Dy_2Ti_2O_7$ which we find is not possible using LSDA despite using the same initialisation. The resulting spin structures are shown in Fig. 6.4.4 where we have taken our spin density and projected it onto the Dy ions using Mulliken analysis. We have taken our results calculated from the primitive unit cell and transformed to the conventional cell which is more commonly seen in the literature. These calculations were performed a number of times, and in each case for the given convergence parameters, we realise a spin-ice-like state using the source-free LSDA functional. It is not possible to truly describe a spin-ice using spin-DFT because a spin-ice is an inherently correlated system with many possible degenerate groundstates that exist in a quantum superposition. As spin-DFT is a variational process, we force the system to settle into one distinct groundstate rather than coexisting in all possible groundstates. Our calculations using the source free functional produce one possible groundstate of a spin-ice system, following the two-in, two-out ice rule. We therefore refer to it as a spin-ice for simplicity. Conversely, while the LSDA results in a non-collinear configuration of spins, there is no apparent structure and a different arrangement is found each time, Fig. 6.4.4a. This is indicative of the randomly-initialised orbitals falling into a different local minimum each time we perform the calculation. By removing the unphysical source terms from the B_{xc} it appears we simplify the energy landscape which aids in the minimisation. The source-free functional is able to reliably reproduce the experimental non-collinear magnetic structure of a well known and much studied spin-ice material, Fig. 6.4.4b. Including the source-free correction seems to induce an anisotropy which favours spin alignment in the two-in, two-out pattern. In addition, as we saw with the magnetic moment of our set of test materials, the magnetic moment on the Dy^{3+} is increased under the source-free functional, from 5.0 μ_{B} using LSDA to 5.2 μ_{B} with the source-free functional.

Realising the spin-ice structure in $\text{Dy}_2\text{Ti}_2\text{O}_7$ using the newly implemented source-free functional is not completely straight forward. There are some numerical considerations that must be addressed. Firstly, the convergence criteria used in these calculations are slightly below what we would typically use for magnetic calculations. The calculations are converged to approximately 50 meV/atom rather than better than 10 meV/atom which would be more accurate for the energy scales of magnetic interactions [241]. This uncertainty is dominated by the plane-wave cut-off. However, we find that increasing the size of the plane-wave cut-off complicates the energy minimisation. The energy minimisation is trying to find the optimal value of the plane-wave coefficients that form the set of KS orbitals with the minimum energy. Therefore, the dimensionality of the parameter space is that of the number of plane-wave coefficients. For even a moderate system, this can be in the order of 5000 coefficients. By increasing the plane-wave cut-off we increase the dimension of the search space, and increase the difficultly of the minimisation. The energy landscape of a non-collinear system is already challenging for variational minimisation, as there exists many shallow minima. That is to say that significant changes in the spin configuration correspond to small changes in energy. We find that the calculations performed with higher cut-off energies fail to find the spin-ice state, not because it is not a stable solution of the source-free Hamiltonian, but because the scale of parameter space prevents the minimisation reaching the desired spin configuration.

In addition to the fundamental issues with the minimisation inherent to variational approaches to non-collinear systems, we also face issues relating to the EDFT scheme. In all calculations of the spin-ice state in $Dy_2Ti_2O_7$ using EDFT, we find that the calculation terminates before reaching the full convergence criteria. However, we note that the change in energy between interactions of SCF minimisation consistently reaches $\sim 10^{-5}$ eV/atom. It is possible that this reduced SCF convergence of the spin-ice state accounts for the slight imperfections seen in the spin directions shown in Fig. 6.4.4. While the spins clearly point in the characteristic two-in, two-out structure, they do not point perfectly into the centre of the tetrahedron with an average deviation of 13°. As a result of this deviation, we find that the system is not perfectly antiferromagnetic as one would expect from a spin-ice.

6.5 Conclusions

In conclusion, we have implemented a recently developed xc functional in a plane-wave code, CASTEP. This functional is a correction to the LSDA which removes magnetic sources from the resulting xc magnetic field, with the aim of improving the ability to describe non-collinear states. We have demonstrated that our implementation of this functional is correct by performing calculations on a number of simple magnetic materials. By examining the magnetic field lines of Fe due to the LSDA and the source-corrected LSDA, we have shown that by removing source terms from the functional, the field lines behave more physically, resembling the fields of a magnetic dipole. While the magnetisation density found in these materials is effectively collinear due to the inclusion of a quantisation axis, the magnetic field exhibits non-collinear properties. This decoupling is made possible by correcting the source terms in the xc functional.

We have extensively tested the physical consequences of the scaling parameter of the corrected xc field. By examining the effects this parameter has on the magnetic moments and on the band structure, we conclude that the no scaling should be applied to the magnetic field to preserve the first principles nature of the calculations. Scaling the field causes shifting in the orbital bands and an increase in the magnetic moment. While scaling the field may improve agreement with experiment, we opt for a first principles approach using $s = 1$.

We discussed an issue that arises when performing a fully self-consistent minimisation technique using the corrected-functional. As we do not know the energy corresponding to the corrected xc potential, the energy minimisation can fail to reach the minimum within a tight tolerance. However, we show that the failure typically occurs towards the end of the minimisation near completion. In these cases, we conclude that caution must be taken to determine if the final energy is converged well enough for the users' needs.

Finally, we applied the newly implemented functional to the famous spin-ice material $Dy_2Ti_2O_7$. We find that where the LSDA is unable to capture the spin-ice state, even with spin-initialisation, the source-free functional reproducibly realises a spin-ice configuration in $Dy_2Ti_2O_7$. This is due to the enhanced non-collinearity of the underlying xc magnetic field. The availability of this functional in CASTEP should allow the calculation of exotic magnetic textures which were previously inaccessible.

Chapter 7

Conclusions

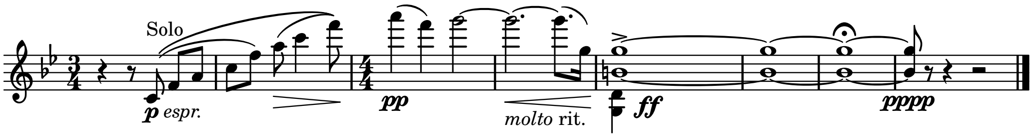

—Ralph Vaughan Williams,

Fantasia on a Theme

by Thomas Tallis

The intention of this thesis has been to showcase density functional theory (DFT) as an incredibly useful tool for understanding the behaviour of magnetic materials. DFT is remarkably versatile; we have presented results where it is used to complement experimental measurements and give support to conclusions drawn from experiment. We have also used DFT as a predictive tool, investigating particulars of the electronic structure in a material, highlighting possible avenues of experimental investigation. By providing a detailed discussion of the underlying theory of DFT and how it is adapted to work on a computer (Chap. 2), going forward we are able to critically discuss applications of DFT whilst being aware of its limitations.

We have used spin-density functional theory (spin-DFT) to investigate the properties of materials hosting exotic magnetism. Magnetic skyrmions have been one of the most hotly researched topics in condensed matter in the last decade. We have shown that DFT can be an important tool in the understanding of skyrmion materials. In Chap. 3 we probed two such materials, Cu_2OSeO_3

and $GaV_4S_{8-y}Se_y$ with a range of DFT techniques. For Cu_2OSeO_3, we are able to leverage structural relaxation, a particular strength of DFT, to locate the stopping sites of an implanted positive muon, modelled as light H ion. Known as density functional theory + μ (DFT+μ), finding the muon stopping sites allows us to simulate the spectra measured in a muon-spin spectroscopy (μSR) experiment. As μSR is a technique that probes the magnetic environment locally around the implanted muon, knowing its location is a great benefit. In Cu_2OSeO_3, we are able to locate three candidate muon stopping sites. However, by examining the local geometry and the total energy of the three sites, we are able to conclude that only two of the sites would likely be accessible to the muon. In combination with some potential magnetic structures, these sites are used to simulate the muon spectra to good agreement. In $GaV_4S_{8-y}Se_y$, we probe the effects of chemical substitution on magnetic behaviours. DFT allows us to easily alter the chemical makeup of a crystal. In this case we can swap out single atoms in the unit cell and look at the changes it induces in the spin-density. We find that swapping a S atom for a Se atom and *vice versa* in GaV_4S_8 and GaV_4Se_8 leads to dramatic changes in the spin density around the substituent and the magnetic V ions. From experimental observations, it is known that both materials in their pure form host Néel skyrmions, and that large substitutions cause a change to a spin-glass state [162, 164, 163]. We are able, with spin-DFT, to look at the distribution of spin density around each atom. We see that the changes are quite different upon substitution in the two materials, this is consistent with experimental observations of the spin-glass state which occurs at higher levels of substitution of Se in GaV_4S_8.

Furthermore, we have used spin-DFT to probe the magnetic interactions of condensed matter by calculating, from first principles, the exchange coupling in a quantum magnet, $[Cu(pyz)_{0.5}(gly)]ClO_4$ [169] (Chap. 4). By comparing the total energy of several different spin configurations, we can apply a simple model of the exchange couplings to find the strength along each pathway. Making use of geometry optimisation, we can apply pressure to the crystal and repeat the calculations to see how the exchange changes. We find that the application of pressure causes significant changes to the structure with the largest effect being in the distance between Cu ions between the dimer layers. The exchange can be described by two constants, one along the intradimer bonds and one effective constant accounting for exchange between the dimers. The effective interdimer exchange coupling constant increases as the dimers are pushed closer together and is approximately equal to the intradimer coupling at high pressure.

We have shown that the electronic structure of a material can reveal a lot about behaviours that can be observed experimentally. Using spin-DFT calculations, we can look at the details of the electron states at the Fermi energy. In particular, for the intercalated transition-metal dichalcogenides (TMDCs) materials $Cr_{1/3}NbS_2$ and $Cr_{1/3}TaS_2$, in Chap. 5 we find that there is a reduction in the density of states (DoS) at the Fermi level that we then measured using AC susceptibility. From the electronic structure we were also able to reproduce from first principles the measured transport properties of these materials [203]. From the similarities in the DoS between $Cr_{1/3}NbS_2$ and $Cr_{1/3}TaS_2$, it is reassuring that the chiral soliton lattice (CSL) known about in $Cr_{1/3}NbS_2$ for a number of years [204] was recently discovered in $Cr_{1/3}TaS_2$ [205]. We again leverage the ability of DFT to build crystals without expensive and time-consuming syntheses. We can easily change the intercalant and perform calculations of the band structure to observe how it changes with the metal ion. Interestingly, we see that the band structures reflect an electron filling effect whereby the atomic orbitals of the transition metal get filled sequentially. This allows us to predict the magnetic moment of the intercalant using only the number of electrons in the $3d$ orbital.

Finally, in Chap. 6, we implement a method for improving the results of non-collinear spin-DFT calculations. By realising that the local spin-density approximation (LSDA) results in an exchange and correlation (xc) magnetic field that contains unphysical magnetic sources, the correction described in Ref. [56] aims to systematically improve the calculations of non-collinear magnetic fields.

We detailed the process of implementing this correction in the CASTEP code and extensively test its validity using a range of magnetic materials. We then investigate how using this functional improves results of materials of active research interest by studying the spin-ice pyrochlore $Dy_2Ti_2O_7$ [15]. Using the corrected functional, we are able to repeatedly stabilise the famous *two-in, two-out* spin texture, known as a spin-ice, on the Dy ions in $Dy_2Ti_2O_7$. This is a remarkable result as similar attempts using the LSDA routinely return spins that are randomly oriented. These developments in the theory of spin-DFT are crucial to the continued normalisation of spin-DFT as a tool used by experimentalists and theorists alike.

7.1 Future outlook

The intercalated TMDCs appear to be one of the most promising classes of materials for studying chiral magnetism and work is being done to find further examples hosting exotic spin textures. Our calculations of the electronic structure of TMDCs intercalated with first period transition metals are invaluable for predicting the behaviours of these materials. To further develop our ability to predict the magnetic behaviour of these materials, calculations including variations in the unit cell size could be performed. Our calculations include a fixed cell size across the series due to the lack of experimental lattice parameters for most of the materials. Changing the lattice may lead to results which better approximate the experimental electronic structure. Since we find that the changes in the magnetism are dominated by the intercalant, varying the underlying TMDC could result in desirable electronic and transport properties while preserving the magnetism. Using DFT for these purposes is much quicker and cheaper than synthesising crystals.

The ability of DFT calculations to explain experimental data is a key strength. One of the clearest examples of this is DFT+μ, where μSR experiments are complemented so very well by calculations that it is now almost expected that muon-site calculations accompany an experiment. The development of MuFinder by Huddart *et al.* [119] is a great step in allowing experimentalists to wield the power of DFT to aid their experiments. Future work is needed to assess the nature of the *quantum muon*, examining how quantum effects of the muon in the crystal affect observations of the magnetism. It may be possible that DFT+μ could one day encompass the study of this quantum behaviour as readily as locating muon stopping sites.

A large part of the progress seen in the field of DFT calculations since its inception has been down to improvements in computing power. Studying materials with 1,000 atoms in the unit cell is very much a possibility using modern supercomputers. We cannot however brute force every problem in DFT, some of the challenges we face require improvements to underlying theory as well as computational algorithms. Magnetism in DFT is one of the frontiers of current development, we have shown in this thesis that using spin-DFT can uncover properties of magnetic materials that are difficult, if not impossible to access from any other technique. It is now almost commonplace to use spin-DFT to calculate the exchange coupling constants between atoms. Going forward, the next focus should be using spin-DFT to discover more material parameters such as Dzyaloshinskii–Moriya interaction (DMI) constants and magnetocrystalline anisotropy constants. There has been promising work in this field, but applications are limited to simple crystals. We envisage spin-DFT forming part of a *magnetic production line*, whereby magnetic parameters are determined from first principles then used in micromagnetic simulations to predict magnetic phenomena in materials which can then be studied experimentally. To reach that stage, we first need to be able to reliably form arbitrary non-collinear states in spin-DFT so as to compare the energies. Techniques that apply constraints to the energy minimisation are a good step in this direction.

In addition to the commensurate non-collinear magnetism mentioned above, lots of magnetic objects are incommensurate with primitive unit cells. The work by Müller *et al.* [242] is a promising step in this direction. By employing a generalised Bloch formalism, the authors use the ground state orbitals as Bloch functions to describe long range magnetic and electronic states such as spin-helices and charge density waves (CDW). While the theory is relatively easy to comprehend, implementing it in a plane-wave pseudopotential code like CASTEP is an involved process. We have begun the process of including this method in CASTEP and future work should focus on completing this effort and applying it to incommensurate magnetic materials. It is the hope of the author that it will soon become routine to perform spin-DFT calculations to investigate non-collinear magnetism, including large non-collinear structures such as skyrmions.

Appendix A

Energy minimisation

In many cases, a DFT code is used as a black box. Other than choosing a task and perhaps deciding upon an xc functional, many users will have little understanding of what happens *under the hood*. This does a disservice to the many talented people who have written the code that actually allows us to simply *find the groundstate*. The electronic minimisation is the most important part of any calculation, it is how we find the groundstate which is the jumping off point for all the many exciting DFT applications.

There are broadly two possible ways to the find the groundstate, direct diagonalisation and iterative minimisation [243, 242]. As stated in Sec. 2.5.3, we use a plane wave basis set with the primary drawback of immense numbers of basis functions, this means that direct minimisation via Hamiltonian diagonalisation is going to be a tremendous bottleneck to any calculation [244]. We therefore use iterative approaches, we shall further restrict our discussion to the fully variational method known as ensemble density functional theory (EDFT). Many people performing calculations would be familiar with density mixing (DM), however the process is a few steps removed from the elegance of EDFT.

In Sec. 2.6.1 we outline how one can calculate a gradient, here we shall compute the gradient from the functional derivative. We shall suppress $\boldsymbol{k}$-point indices for simplicity. Starting from the Kohn-Sham (KS) energy functional,

$$E_{\mathrm{KS}}[n] = \sum_i \left\langle \phi_i(\boldsymbol{r}) \left| -\frac{\boldsymbol{\nabla}^2}{2} \right| \phi_i(\boldsymbol{r}) \right\rangle + E_{en}[n] + E_{\mathrm{H}}[n] + E_{\mathrm{xc}}[n], \tag{A.1}$$

we wish to find how the energy changes when we vary the orbitals,

$$\frac{\delta E_{\mathrm{KS}}[n]}{\delta \left\langle \phi_i(\boldsymbol{r}) \right|} = \frac{\delta}{\delta \left\langle \phi_i(\boldsymbol{r}) \right|} \left[\sum_i \left\langle \phi_i(\boldsymbol{r}) \left| -\frac{\boldsymbol{\nabla}^2}{2} \right| \phi_i(\boldsymbol{r}) \right\rangle + E_{en}[n] + E_{\mathrm{H}}[n] + E_{\mathrm{xc}}[n] \right]. \tag{A.2}$$

We can use the chain rule to make the above slightly easier,

$$\frac{\delta E_{\mathrm{KS}}[n]}{\delta \left\langle \phi_i(\boldsymbol{r}) \right|} = \frac{\delta E_{\mathrm{KS}}[n]}{\delta n(\boldsymbol{r})} \frac{\delta n(\boldsymbol{r})}{\delta \left\langle \phi_i(\boldsymbol{r}) \right|} = 2 \frac{\delta E_{\mathrm{KS}}[n]}{\delta n(\boldsymbol{r})} \left| \phi_i(\boldsymbol{r}) \right\rangle, \tag{A.3}$$

which gives us a choice in terms of which derivative to perform for each term in the KS energy. Combining terms, such that we only consider the effective KS energy, $E_{\mathrm{eff}}[n] = E_{en}[n] + E_{\mathrm{H}}[n] + E_{\mathrm{xc}}[n]$, we get the expression,

$$\frac{\delta E_{\mathrm{KS}}[n]}{\delta \left\langle \phi_i(\boldsymbol{r}) \right|} = \frac{\delta}{\delta \left\langle \phi_i(\boldsymbol{r}) \right|} \left[\sum_i \left\langle \phi_i(\boldsymbol{r}) \left| -\frac{\boldsymbol{\nabla}^2}{2} \right| \phi_i(\boldsymbol{r}) \right\rangle \right] + 2 \frac{\delta E_{\mathrm{eff}}[n]}{\delta n(\boldsymbol{r})} \left| \phi_i(\boldsymbol{r}) \right\rangle. \tag{A.4}$$

Performing the above functional derivatives,

$$\frac{\delta E_{\mathrm{KS}}[n]}{\delta \left\langle \phi_i(\boldsymbol{r}) \right|} = -\boldsymbol{\nabla}^2 \left| \phi_i(\boldsymbol{r}) \right\rangle + V_{\mathrm{eff}}(\boldsymbol{r}) \left| \phi_i(\boldsymbol{r}) \right\rangle, \tag{A.5}$$

which we can simplify in terms of the KS Hamiltonian,

$$\frac{\delta E_{\mathrm{KS}}[n]}{\delta \left\langle \phi_i(\boldsymbol{r}) \right|} = 2\hat{\mathcal{H}} \left| \phi_i(\boldsymbol{r}) \right\rangle. \tag{A.6}$$

The simplicity of this is useful in a computational sense: rather than having to calculate the gradient using a finite difference method we have an analytical form. This gradient can then be used to perform a line search to improve the orbitals,

$$\left| \phi_i(\boldsymbol{r}) \right\rangle \rightarrow \left| \phi_i(\boldsymbol{r}) \right\rangle - \lambda(\hat{\mathcal{H}} - \epsilon_i) \left| \phi_i(\boldsymbol{r}) \right\rangle, \tag{A.7}$$

where we have absorbed the factor of 2 into the step length, λ and ϵ_i the eigenvalue of $\hat{\mathcal{H}}$ used as a Lagrange multiplier. Having updated the orbitals, we must ensure that the new set are orthonormal, this can be done using the Gram–Schmidt procedure [245].

This gives a mathematical route for finding gradients and updating one's position in phase space. These are the ingredients needed for an energy minimisation given the necessity of self-consistency. We can use these tools to find the energy minimum using any number of standard techniques such as a conjugate gradient or steepest descent algorithm [243].

Energy minimisation is used in every calculation in this thesis, and is of particular consequence for determining the ground state of the source-free potential discussed in Chap. 6. Understanding how a minimisation works is important for understanding where the method fails.

Appendix B

Hartree potential and energy in reciprocal space

It can be seen in Eq. 2.31 that we have to consider two different real space variables $\boldsymbol{r}$ and $\boldsymbol{r}'$ when calculating the Hartree potential. In addition, due to the long range nature of the Hartree potential the integral must be performed over all space, it is certainly not sufficient to truncate the integral over the unit cell. If one were to only consider real points inside the unit cell and discretised the grid into N points, calculation of the potential would require $\mathcal{O}(N^2)$ operations. By rewriting the potential in reciprocal space we can significantly improve this scaling.

The Hartree potential can be expressed in terms of the density through a Poisson equation,

$$\nabla^2 V_{\mathrm{H}}(\boldsymbol{r}) = -n(\boldsymbol{r}). \tag{B.1}$$

Noting that the potential and the density can each be represented in reciprocal space,

$$V_{\mathrm{H}}(\boldsymbol{r}) = \frac{1}{\Omega}\sum_{\boldsymbol{G}} V_{\mathrm{H}}(\boldsymbol{G}) e^{i\boldsymbol{G}\cdot\boldsymbol{r}}, \text{ and} \tag{B.2}$$

$$n(\boldsymbol{r}) = \frac{1}{\Omega}\sum_{\boldsymbol{G}} n(\boldsymbol{G}) e^{i\boldsymbol{G}\cdot\boldsymbol{r}}, \tag{B.3}$$

we can rewrite Eq. B.1 and make use of the plane wave basis for the differentiation,

$$\begin{gathered}
\frac{1}{\Omega}\sum_{\boldsymbol{G}\neq 0}\boldsymbol{G}^2 V_{\mathrm{H}}(\boldsymbol{G})e^{i\boldsymbol{G}\cdot\boldsymbol{r}} = \frac{1}{\Omega}\sum_{\boldsymbol{G}\neq 0} n(\boldsymbol{G})e^{i\boldsymbol{G}\cdot\boldsymbol{r}} \\
\Rightarrow V_{\mathrm{H}}(\boldsymbol{G}) = \sum_{\boldsymbol{G}}\frac{n(\boldsymbol{G})}{\boldsymbol{G}^2}.
\end{gathered} \tag{B.4}$$

The resuling form of V_{H} requires only computation of order $\mathcal{O}(N)$, even with the addition of the fast Fourier transform (FFT) required to transform the potential and density into reciprocal space, $\mathcal{O}(N\log(N))$, the total computation effort is greatly reduced. Similar terms as above can be found for all three electrostatic potentials, *electron–electron, electron–nuclear* and *nuclear–nuclear*, each of which has an infinite contribution when $\boldsymbol{G} = 0$ [246]. Fortunately it can be shown that these infinities cancel in a charge neutral system and can therefore do not need to be calculated.

Appendix C

Software tools

Presented here are the tools developed throughout this PhD that aid in the analysis of CASTEP output. All software is publicly available by scanning the QR code below or at this link: `https://www.github.com/zachary-hawk`.

dispersion.py

`dispersion.py` is a CASTEP post processing tool for displaying band structures and phonon dispersions. It has a number of different options which allow for customisations to the plotted spectra. Here are the options:

`seed`	The castep seed used in the calculations.
`--save`	This flag suppresses the output plot and saves it to file.
`-m/--multi`	Set the bands to be multicoloured rather than black.
`-l/--line`	Pass a floating point number to us as the linewidth of the bands.
`--lim`	This accepts two values as the energy range (band structure) or frequency (phonons) to display.
`-s/--spin`	Plot the spin-up and spin-down bands in different colours to identify magnetic features.
`--overlay`	This allows the user to plot two band structures or phonon dispersions on top of one another.
`--overlay_labels`	Change the labels of the subsequent plots which have been overlayed.
`--n_up`	Only display the specified spin up bands by the index.
`--n_down`	Only display the specified spin down bands by the index.
`--fontsize`	Set the font size of the figure labels.
`--title`	Select a title for the plot.
`--fig`	Add figure labels, for example '(a)' or '(ii)'.
`-e/--exe`	Change the file extension for a saved plot.
`--dos`	Plot a density of states (DoS) vertically alongside a band structure, read from `.dat` file.
`--path`	Generate a suggested path through the Brillouin zone (BZ) or convert labels into BZ coordinates.

`--pdos`	Read a CASTEP `.pdos` file and use information to assign orbital characters to each band.
`--species`	Change the default projected density of states (PDoS) from orbitals to species.
`--phonon`	Plot a phono dispersion from a `.phonon` file rather than a band structure.
`-b/--bandgap`	Add indicating arrows to a band structure to show the band gap.
`--no_plot`	Suppress plotting without saving. Perhaps useful if you only need band gap information
`-E/--optados`	Use castep Fermi energy if optados error persists.
`-as/--aspect_ratio`	Aspect ratio for plots, either “letter” or “square”.
`-z/--zero`	Prevent Fermi level being shifted to 0 eV
`--show`	Set choice of spin bands to be plotted, choose “up”, “down” or “both”.
`--show_axes`	Turn off axis labels, choose “x”, “y”, “both” or “none”.
`--stretch`	Stretch factor to manually alter the aspect ratio of the figure.
`--pickle`	Save the resulting figure as a Python pickle file for later use.

castep2fs

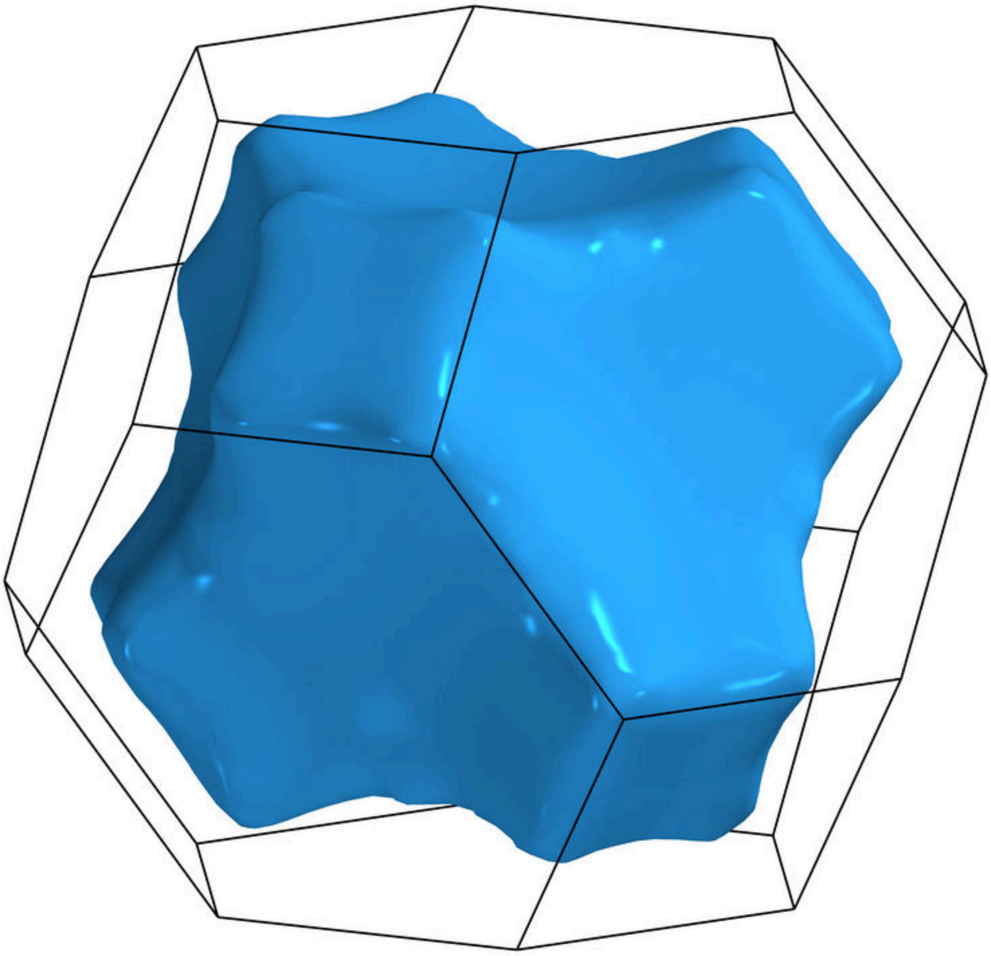

Figure C.0.1: Fermi surface of Al calculated using the CASTEP tool castep2fs [207]. The smoothness of the surface can be improved by including more $\boldsymbol{k}$-points in the DoS calculation. Alternatively if computational resources are limited, artificial smoothness can be added.

A Fermi surface is a fundamental property of a material, representing the surface of constant energy of the highest occupied states in the BZ. It is a 3D representation of the electron filling in $\boldsymbol{k}$-space. The ideal Fermi surface of a free electron metal is a sphere which has volume of a half of the BZ, meaning one electron filling a doubly valent state. In real materials with electron interactions and external potentials, the Fermi surfaces can become rather complicated, with

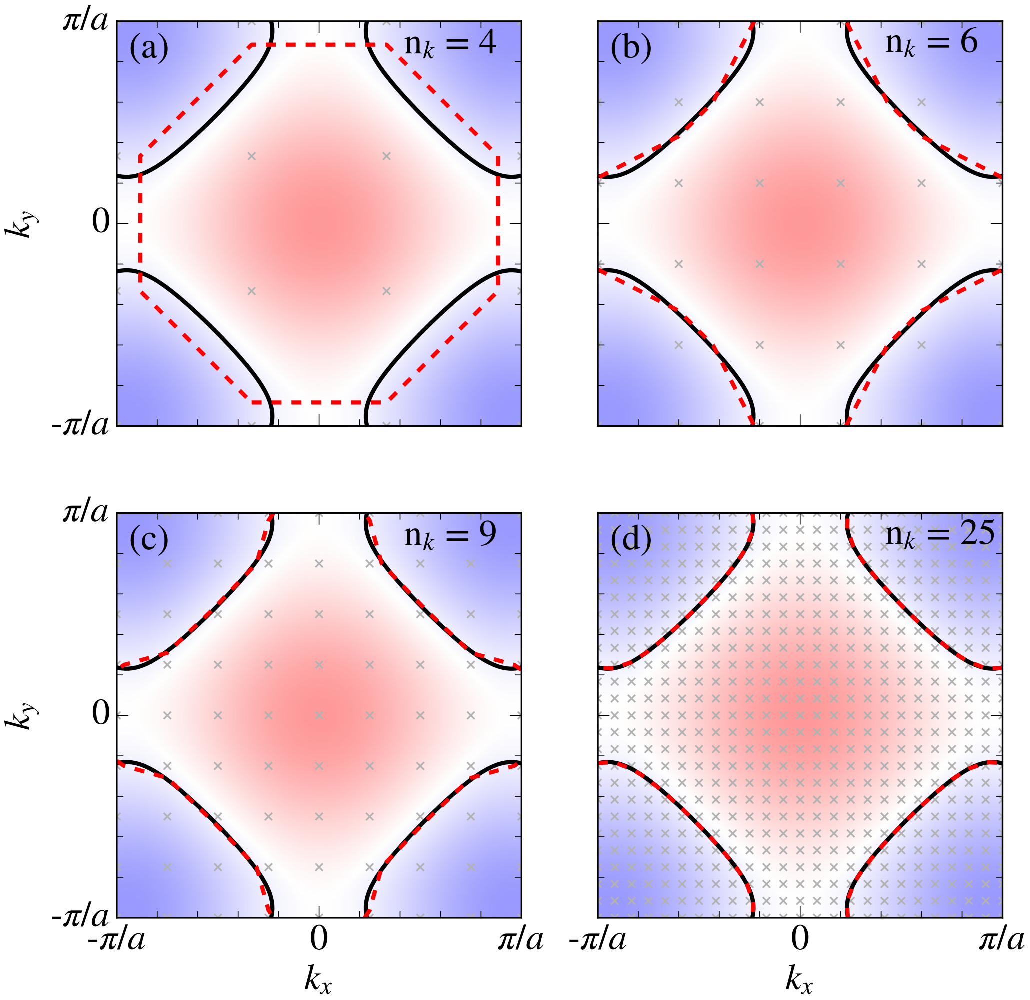

Figure C.0.2: Schematic of $\boldsymbol{k}$-point interpolation for finding the Fermi surface. Colour plots show an example energy landscape in the first Brillouin zone with the black lines representing the analytic Fermi surface (line in 2D). Red dotted lines show resulting Fermi surface from interpolation of sampled $\boldsymbol{k}$-points (grey crosses). The number of $\boldsymbol{k}$-points sampled in each direction is given by n_k.

the surface spanning multiple BZs.

`castep2fs` provides a simple tool to extract an estimate of the Fermi surface of a metal from a density functional theory (DFT) DoS. An example of the Fermi surface produced by `castep2fs` is shown in Fig. C.0.1, with CASTEP input files shown in Fig. C.0.4 and Fig. C.0.3. Note in Fig. C.0.4 the high number of spectral $\boldsymbol{k}$-points used, this is required as the points on the Fermi surface must be calculated by interpolating the $\boldsymbol{k}$-point grid. A demonstration of the principle in 2D is shown in Fig. C.0.2. The options available for `castep2fs` are:

`seed`	The castep seed used in the calculations.
`-B/--background`	Change the background colour
`--save`	Save image of the Fermi surface.
`-fs, --fermi`	Suppress plot the of Fermi surface, show only the BZ.
`-c/--colour`	Change the colouring scheme to one of the the Matplotlib colour maps.
`--show`	Select which bands to show, spin-up, spin-down or both.
`--nsurf`	Choose which surfaces to plot by band index.
`-p, --primitive`	Display the primitive cell
`-s/--smooth`	Degree of smoothing used on the surfaces to compensate for finite grids.
`-v/--velocity`	Colour Fermi Surfaces by Fermi Velocity.
`-m/--mass`	Colour Fermi Surfaces by effective mass.
`-o/--opacity`	Opacity of the Fermi surfaces.
`-z/--zoom`	Zoom in to the BZ.
`-P/--position`	The position vector of the camera used to view the Fermi surface.
`-f/--faces`	Show faces surounding the Brillouin zone.
`-B/--background`	Choose the background colour scheme, Document, ParaView, night or white.
`-O,--offset`	Offset energy for the surface, useful if the Fermi energy is not well believed.
`-a/--axes`	Toggle axes visibility.
`--axis_labels`	Toggle axes labels.

`--pdos`	Use PDoS to color fermi surface.
`--species`	Project PDoS onto species rather than orbitals
`--gif`	Option to generate an orbital `.gif`.
`-d/--dryrun`	Fermi surface analysis without displaying results.
`--slice`	Plot a slice of the energy for a band in the BZ.
`--holes`	Calculate electron and hole orbits.
`--super`	Display a supercell of the BZ.
`--path`	Plot a path through the BZ from a list of high symmetry points.

```
TASK : SPECTRAL
SPECTRAL_TASK: DOS
XC_FUNCTIONAL : LDA
SPIN_POLARISED : T
WRITE_CELL_STRUCTURE : T
PDOS_CALCULATE_WEIGHTS : T
```

Figure C.0.3: Example CASTEP .param file for Fermi surface calculation of Al.

```
%BLOCK LATTICE_CART
2.855954790000000   0.000000000000000   0.000000000000000
1.427977395000000   2.473329400199852   0.000000000000000
1.427977395000000   0.824443133399951   2.331877321319162
%ENDBLOCK LATTICE_CART

%BLOCK POSITIONS_FRAC
Al   0.000000000000000   0.000000000000000   0.000000000000000
%ENDBLOCK POSITIONS_FRAC

SPECTRAL_KPOINTS_MP_GRID : 15 15 15
SYMMETRY_GENERATE
SNAP_TO_SYMMETRY
```

Figure C.0.4: Example CASTEP .cell file for Fermi surface calculation of Al.

nc_cryst

`-i, --initmag`	Plot initial magnetic moment vectors.
`-c, --castep`	Read `<seed>.castep` file to determine moments. Only for NCM calculation.
`-f, --field`	Read formatted potential or density to produce field. Only for NCM calculation.
`-o/--orient`	Orientation of the crystal structure, takes values ‘`a, b, c, a*, b*, c*`’.
`-B/--bond`	Set maximum bond length.
`--save`	Save image.
`-d/--delete`	Delete atoms.
`-p/--position`	Camera position vector.
`-V/--volumetric`	Provide file with volumetric data: `.xsf` `.den_fmt` `.pot_fmt` accepted.
`-I/--iso`	Isosurface value for volumetric data.
`--colour`	HEX code for Isosurface colouring.
`-z/--zoom`	Zoom multiplier.
`-e/--exclude`	Exclude atoms outside first unit cell.
`-l/--lines`	Disable plotting of field lines of a provoded field lines.
`-P/--plane`	Three points in fractional coordinates to define a plane for B-field.
`-w/--widget`	Disable interactive widgets.
`-s/--saturation`	Saturation level for sections.
`-S, --spin`	Plot spin isosurfaces from `.den_fmt`.
`-C, --charge`	Plot charge isosurfaces from `.den_fmt`.

`-r/--reduction`	Factor used to reduce the size of atoms, useful for visualising volumetric data without loss of context.
`--flip`	Flip the spin indices.
`--vec_field`	Plot a vector field of the spin density
`-vc/--vec_cutoff`	Magnitude cut off for inclusion in vector field
`-tol/--vec_tol`	Tolerance for grouping vectors in vector field
`--fmag`	Turn off opacity for field lines

Bibliography

[1] E. Schrödinger, An undulatory theory of the mechanics of atoms and molecules, Phys. Rev. **28**, 1049 (1926).

[2] R. Feynman, Fun to Imagine - 2: Stretching, Pulling and Pushing (1983).

[3] N. Bohr, *Studies on the Electron Theory of Metals*, Ph.D. thesis, University of Copenhagen (1911).

[4] H. J. van Leeuwen, *Vraagstukken uit de electronentheorie van het magnetisme*, Ph.D. thesis, Delft University of Technology (1919).

[5] S. J. Blundell, *Magnetism in Condensed Matter* (Oxford University Press, Oxford, 2003).

[6] E. Fermi, Un metodo statistico per la determinazione di alcune priorieta dell'atome, Rend. Accad. Naz. Lincei **6**, 32 (1927).

[7] L. H. Thomas, The calculation of atomic fields, in *Mathematical proceedings of the Cambridge philosophical society*, Vol. 23 (Cambridge University Press, 1927) pp. 542–548.

[8] P. Hohenberg and W. Kohn, Inhomogeneous electron gas, Phys. Rev. **136**, B864–B871 (1964).

[9] W. Kohn and L. J. Sham, Self-consistent equations including exchange and correlation effects, Phys. Rev. **140**, A1133–A1138 (1965).

[10] U. Von Barth and L. Hedin, A local exchange-correlation potential for the spin polarized case. i, J. Phys. C: Solid State Physics **5**, 1629 (1972).

[11] J. Kubler, K.-H. Hock, J. Sticht, and A. Williams, Density functional theory of non-collinear magnetism, J. Phys. F **18**, 469 (1988).

[12] S. Blundell, *Magnetism: A very short introduction* (Oxford University Press, 2012).

[13] L. Néel, Propriétés magnétiques des ferrites; ferrimagnétisme et antiferromagnétisme, in *Annales de physique*, Vol. 12 (1948) pp. 137–198.

[14] M. J. Harris, S. Bramwell, D. McMorrow, T. Zeiske, and K. Godfrey, Geometrical frustration in the ferromagnetic pyrochlore $Ho_2Ti_2O_7$, Phys. Rev. Lett. **79**, 2554 (1997).

[15] S. T. Bramwell and M. J. Harris, The history of spin ice, J. Phys. Condens. Mater. **32**, 374010 (2020).

[16] Y. Guo, S. J. Clark, and J. Robertson, Electronic and magnetic properties of Ti_2O_3, Cr_2O_3, and Fe_2O_3 calculated by the screened exchange hybrid density functional, J. Phys. Condens. Mater. **24**, 325504 (2012).

[17] C. Ekuma, V. Anisimov, J. Moreno, and M. Jarrell, Electronic structure and spectra of CuO, Eur. Phys. J. B **87**, 1–6 (2014).

[18] M. Otrokov, I. P. Rusinov, M. Blanco-Rey, M. Hoffmann, A. Y. Vyazovskaya, S. Eremeev, A. Ernst, P. M. Echenique, A. Arnau, and E. V. Chulkov, Unique thickness-dependent properties of the van der Waals interlayer antiferromagnet $MnBi_2Te_4$ films, Phys. Rev. Lett. **122**, 107202 (2019).

[19] M. van Schilfgaarde, I. Abrikosov, and B. Johansson, Origin of the Invar effect in iron–nickel alloys, Nature **400**, 46–49 (1999).

[20] H. Dreyssé, *Electronic structure and physical properties of solids: The uses of the LMTO method* (Springer, 2011).

[21] J. Callaway and C. Wang, Self-consistent calculation of energy bands in ferromagnetic nickel, Phys. Rev. B **7**, 1096 (1973).

[22] C.-p. S. Wang and J. Callaway, Band structure of nickel: Spin-orbit coupling, the Fermi surface, and the optical conductivity, Phys. Rev. B **9**, 4897 (1974).

[23] M. Singh, C. Wang, and J. Callaway, Spin-orbit coupling, Fermi surface, and optical conductivity of ferromagnetic iron, Phys. Rev. B **11**, 287 (1975).

[24] S. J. Clark, M. D. Segall, C. J. Pickard, P. J. Hasnip, M. J. Probert, K. Refson, and M. Payne, First principles methods using CASTEP, Z. Kristall. **220**, 567–570 (2005).

[25] P. Kurz, F. Förster, L. Nordström, G. Bihlmayer, and S. Blügel, Ab initio treatment of noncollinear magnets with the full-potential linearized augmented plane wave method, Phys. Rev. B **69**, 024415 (2004).

[26] J. Hafner, Ab-initio simulations of materials using VASP: Density-functional theory and beyond, J. Comput. Chem. **29**, 2044–2078 (2008).

[27] P.-W. Ma and S. Dudarev, Constrained density functional for noncollinear magnetism, Phys. Rev. B. **91**, 054420 (2015).

[28] R. Cuadrado, M. Pruneda, A. García, and P. Ordejón, Implementation of non-collinear spin-constrained DFT calculations in SIESTA with a fully relativistic Hamiltonian, J. Phys. Mater. **1**, 015010 (2018).

[29] A. Edström, D. Amoroso, S. Picozzi, P. Barone, and M. Stengel, Curved Magnetism in CrI 3, Phys. Rev. Lett. **128**, 177202 (2022).

[30] P. Liu, S. Khmelevskyi, B. Kim, M. Marsman, D. Li, X.-Q. Chen, D. Sarma, G. Kresse, and C. Franchini, Anisotropic magnetic couplings and structure-driven canted to collinear transitions in Sr_2IrO_4 by magnetically constrained noncollinear DFT, Phys. Rev. B. **92**, 054428 (2015).

[31] S. Mankovsky and H. Ebert, First-principles calculation of the parameters used by atomistic magnetic simulations, EST **4**, 034004 (2022).

[32] A. Liechtenstein, M. Katsnelson, and V. Gubanov, Exchange interactions and spin-wave stiffness in ferromagnetic metals, J. Phys. F **14**, L125 (1984).

[33] A. I. Liechtenstein, M. Katsnelson, V. Antropov, and V. Gubanov, Local spin density functional approach to the theory of exchange interactions in ferromagnetic metals and alloys, J. Magn. Magn. Mater. **67**, 65–74 (1987).

[34] C. Abert, Micromagnetics and spintronics: models and numerical methods, Eur. J. Phys. B **92**, 1–45 (2019).

[35] J. Callaway and C. Wang, Transverse magnetic susceptibility in the local exchange approximation, J. Phys. F **5**, 2119 (1975).

[36] J. Callaway, C. S. Wang, and D. G. Laurent, Magnetic susceptibility and spin waves in ferromagnetic metals, Phys. Rev. B **24**, 6491–6496 (1981).

[37] O. Šipr, S. Mankovsky, and H. Ebert, Spin wave stiffness and exchange stiffness of doped permalloy via ab initio calculations, Phys. Rev. B **100**, 024435 (2019).

[38] T. Lancaster and S. J. Blundell, *Quantum field theory for the gifted amateur* (Oxford University Press, Oxford, 2014).

[39] M. Born and R. Oppenheimer, Zur quantentheorie der molekeln, Annalen der physik **389**, 457–484 (1927).

[40] S. Pisana, M. Lazzeri, C. Casiraghi, K. S. Novoselov, A. K. Geim, A. C. Ferrari, and F. Mauri, Breakdown of the adiabatic Born–Oppenheimer approximation in graphene, Nat. Mater. **6**, 198–201 (2007).

[41] T. Van Mourik, M. Bühl, and M.-P. Gaigeot, Density functional theory across chemistry, physics and biology, Philos. Trans. Royal Soc. A **372**, 20120488 (2014).

[42] R. J. Bartlett and M. Musiał, Coupled-cluster theory in quantum chemistry, Rev. Mod. Phys. **79**, 291 (2007).

[43] P. Echenique and J. L. Alonso, A mathematical and computational review of Hartree–Fock SCF methods in quantum chemistry, Mol. Phys. **105**, 3057–3098 (2007).

[44] J. C. Slater, The theory of complex spectra, Phys. Rev. **34**, 1293 (1929).

[45] R. Stowasser and R. Hoffmann, What do the Kohn- Sham orbitals and eigenvalues mean?, J. Am. Chem. Soc. **121**, 3414–3420 (1999).

[46] A. I. Krylov, From orbitals to observables and back, The J. Chem. Phys. **153**, 080901 (2020).

[47] J. P. Perdew, What do the Kohn-Sham Orbital Energies Mean? How do Atoms Dissociate?, in *Density Functional Methods In Physics* (Springer US, 1985) pp. 265–308.

[48] N. D. Woods, M. Payne, and P. Hasnip, Computing the self-consistent field in Kohn–Sham density functional theory, J. Phys. Condens. Matter. **31**, 453001 (2019).

[49] A. Bogdanov and U. Rößler, Chiral symmetry breaking in magnetic thin films and multilayers, Phys. Rev. Lett. **87**, 037203 (2001).

[50] S. Mühlbauer, B. Binz, F. Jonietz, C. Pfleiderer, A. Rosch, A. Neubauer, R. Georgii, and P. Böni, Skyrmion lattice in a chiral magnet, Science **323**, 915–919 (2009).

[51] T. Lancaster, Skyrmions in magnetic materials, Contemp. Phys. **60**, 246–261 (2019).

[52] C. A. Ullrich, (Spin-) density-functional theory for open-shell systems: Exact magnetization density functional for the half-filled Hubbard trimer, Phys. Rev. A **100**, 012516 (2019).

[53] M. Townsend, G. Longworth, C. Ross, and R. Provencher, Ferromagnetic or antiferromagnetic Fe III spin configurations in sheet silicates, Phys. Chem. Miner. **15**, 64–70 (1987).

[54] H. Al-Attar and Y. Kakehashi, Magnetic phase diagram of Fe and Ni from crystals to amorphous structures, J. Appl. Phys. **86**, 3265–3273 (1999).

[55] N. I. Gidopoulos, Potential in spin-density-functional theory of noncollinear magnetism determined by the many-electron ground state, Phys. Rev. B. **75**, 134408 (2007).

[56] S. Sharma, E. Gross, A. Sanna, and J. Dewhurst, Source-free exchange-correlation magnetic fields in density functional theory, J. Chem. Theory Comput. **14**, 1247–1253 (2018).

[57] S. Lang, *Introduction to linear algebra* (Springer New York, 1986).

[58] K. Capelle and G. Vignale, Nonuniqueness of the potentials of spin-density-functional theory, Phys. Rev. Lett. **86**, 5546 (2001).

[59] H. Eschrig and W. Pickett, Density functional theory of magnetic systems revisited, Solid State Commun. **118**, 123–127 (2001).

[60] K. Yosida, *Theory of Magnetism* (Springer, New York, 1996).

[61] I. Dzyaloshinskii, Theory of helicoidal structures in antiferromagnets. I. Nonmetals, Sov. Phys. JETP **19**, 960–971 (1964).

[62] T. Moriya, Anisotropic superexchange interaction and weak ferromagnetism, Phys. Rev. **120**, 91 (1960).

[63] M. A. Marques, M. J. Oliveira, and T. Burnus, Libxc: A library of exchange and correlation functionals for density functional theory, Comput. Phys. Commun. **183**, 2272–2281 (2012).

[64] S. Lehtola, C. Steigemann, M. J. Oliveira, and M. A. Marques, Recent developments in libxc—A comprehensive library of functionals for density functional theory, SoftwareX **7**, 1–5 (2018).

[65] J. P. Perdew and A. Zunger, Self-interaction correction to density-functional approximations for many-electron systems, Phys. Rev. B. **23**, 5048 (1981).

[66] J. Kohanoff and N. Gidopoulos, Density functional theory: basics, new trends and applications, Handbook of Mol. Phys. and quantum chemistry **2**, 532–568 (2003).

[67] G.-X. Zhang, A. M. Reilly, A. Tkatchenko, and M. Scheffler, Performance of various density-functional approximations for cohesive properties of 64 bulk solids, New J. Phys. **20**, 063020 (2018).

[68] A. D. Becke, Density-functional thermochemistry. I. The effect of the exchange-only gradient correction, J. Chem. Phys. **96**, 2155–2160 (1992).

[69] J. P. Perdew, K. Burke, and M. Ernzerhof, Generalized Gradient Approximation Made Simple, Phys. Rev. Lett. **77**, 3865–3868 (1996).

[70] J. P. Perdew, A. Ruzsinszky, G. I. Csonka, O. A. Vydrov, G. E. Scuseria, L. A. Constantin, X. Zhou, and K. Burke, Restoring the density-gradient expansion for exchange in solids and surfaces, Phys. Rev. Lett. **100**, 136406 (2008).

[71] J. P. Perdew, Density functional theory and the band gap problem, Int. J. Quantum Chem. **28**, 497–523 (1985).

[72] J. P. Perdew, W. Yang, K. Burke, Z. Yang, E. K. Gross, M. Scheffler, G. E. Scuseria, T. M. Henderson, I. Y. Zhang, A. Ruzsinszky, *et al.*, Understanding band gaps of solids in generalized Kohn–Sham theory, Proc. Natl. Acad. Sci.s **114**, 2801–2806 (2017).

[73] H. Xiao, J. Tahir-Kheli, and W. A. Goddard III, Accurate band gaps for semiconductors from density functional theory, J. Phys. Chem. Lett. **2**, 212–217 (2011).

[74] J. P. Perdew and K. Schmidt, Jacob's ladder of density functional approximations for the exchange-correlation energy, in *AIP Conference Proceedings*, Vol. 577 (American Institute of Physics, 2001) pp. 1–20.

[75] S. K. Ghosh and R. G. Parr, Phase-space approach to the exchange-energy functional of density-functional theory, Phys. Rev. A **34**, 785 (1986).

[76] A. D. Becke and M. R. Roussel, Exchange holes in inhomogeneous systems: A coordinate-space model, Phys. Rev. A **39**, 3761 (1989).

[77] J. P. Perdew, M. Ernzerhof, and K. Burke, Rationale for mixing exact exchange with density functional approximations, J. Chem. Phys. **105**, 9982–9985 (1996).

[78] P. J. Stephens, F. J. Devlin, C. F. Chabalowski, and M. J. Frisch, Ab initio calculation of vibrational absorption and circular dichroism spectra using density functional force fields, J. Phys. Chem. **98**, 11623–11627 (1994).

[79] A. D. Becke, A new mixing of Hartree–Fock and local density-functional theories, J. Chem. Phys. **98**, 1372–1377 (1993).

[80] M. G. Medvedev, I. S. Bushmarinov, J. Sun, J. P. Perdew, and K. A. Lyssenko, Density functional theory is straying from the path toward the exact functional, Science **355**, 49–52 (2017).

[81] S. Lehtola, A review on non-relativistic, fully numerical electronic structure calculations on atoms and diatomic molecules, Int. J. Quantum Chem. **119**, e25968 (2019).

[82] T. H. Dunning Jr, Gaussian basis sets for use in correlated molecular calculations. I. The atoms boron through neon and hydrogen, J. Chem. Phys. **90**, 1007–1023 (1989).

[83] M. Weinert, G. Schneider, R. Podloucky, and J. Redinger, FLAPW: applications and implementations, J. Phys. Condens. Matter. **21**, 084201 (2009).

[84] C. Kittel, *Introduction to Solid State Physics*, 8th ed. (Wiley, 2004).

[85] H. J. Monkhorst and J. D. Pack, Special points for Brillouin-zone integrations, Phys. Rev. B. **13**, 5188–5192 (1976).

[86] H. Hellmann, A new approximation method in the problem of many electrons, The J. Chem. Phys. **3**, 61–61 (1935).

[87] J. C. Phillips, Energy-band interpolation scheme based on a pseudopotential, Phys. Rev. **112**, 685 (1958).

[88] L. Kleinman and D. Bylander, Efficacious form for model pseudopotentials, Phys. Rev. Lett. **48**, 1425 (1982).

[89] D. Vanderbilt, Soft self-consistent pseudopotentials in a generalized eigenvalue formalism, Phys. Rev. B **41**, 7892 (1990).

[90] P. A. M. Dirac, The quantum theory of the electron, Proc. R. Soc. Lond. **117**, 610–624 (1928).

[91] A. Dal Corso and A. M. Conte, Spin-orbit coupling with ultrasoft pseudopotentials: Application to Au and Pt, Phys. Rev. B. **71**, 115106 (2005).

[92] P. Weinberger, All you need to know about the Dirac equation, Philosophical Magazine **88**, 2585–2601 (2008).

[93] K. Lejaeghere, G. Bihlmayer, T. Björkman, P. Blaha, S. Blügel, V. Blum, D. Caliste, I. E. Castelli, S. J. Clark, A. Dal Corso, *et al.*, Reproducibility in density functional theory calculations of solids, Science **351**, aad3000 (2016).

[94] A. J. Morris, R. J. Nicholls, C. J. Pickard, and J. R. Yates, OptaDOS: A tool for obtaining density of states, core-level and optical spectra from electronic structure codes, Comput. Phys. Commun. **185**, 1477–1485 (2014).

[95] X. Gonze, Perturbation expansion of variational principles at arbitrary order, Phys. Rev. A **52**, 1086 (1995).

[96] K. Refson, P. R. Tulip, and S. J. Clark, Variational density-functional perturbation theory for dielectrics and lattice dynamics, Phys. Rev. B. **73**, 155114 (2006).

[97] N. Marzari, D. Vanderbilt, and M. C. Payne, Ensemble density-functional theory for ab initio molecular dynamics of metals and finite-temperature insulators, Phys. Rev. Lett. **79**, 1337 (1997).

[98] M. C. Payne, M. P. Teter, D. C. Allan, T. Arias, and J. D. Joannopoulos, Iterative minimization techniques for ab initio total-energy calculations - molecular-dynamics and conjugate gradients, Rev. Mod. Phys. **64**, 1045–1097 (1992).

[99] D. Alfe, Ab initio molecular dynamics, a simple algorithm for charge extrapolation, Comput. Phys. Commun. **118**, 31–33 (1999).

[100] Y. Xia, D. Qian, L. Wray, D. Hsieh, G. Chen, J. Luo, N. Wang, and M. Hasan, Fermi surface topology and low-lying quasiparticle dynamics of parent Fe_{1+x}Te/Se superconductor, Phys. Rev. Lett. **103**, 037002 (2009).

[101] E. Kirstein, D. Yakovlev, M. Glazov, E. Zhukov, D. Kudlacik, I. Kalitukha, V. Sapega, G. Dimitriev, M. Semina, M. Nestoklon, *et al.*, The Landé factors of electrons and holes in lead halide perovskites: universal dependence on the band gap, Nat. Commun. **13**, 1–8 (2022).

[102] J. Liu, Origin of high photocatalytic efficiency in monolayer g-C_3N_4/CdS heterostructure: a hybrid DFT study, J. Phys. Chem. C **119**, 28417–28423 (2015).

[103] B. G. Streetman and S. Banerjee, *Solid State electronic Devices (5th ed.)* (Prentice Hall, New Jersey, 2000) p. 524.

[104] Z. Hawkhead, dispersion.py: A CASTEP tool for plotting bands tructures and phonon dispersions (2022).

[105] J. R. Yates, X. Wang, D. Vanderbilt, and I. Souza, Spectral and Fermi surface properties from Wannier interpolation, Phys. Rev. B. **75**, 195121 (2007).

[106] T. Hicken, Z. Hawkhead, M. Wilson, B. Huddart, A. Hall, G. Balakrishnan, C. Wang, F. Pratt, S. Clark, and T. Lancaster, Energy-gap driven low-temperature magnetic and transport properties in $\mathrm{Cr}_{1/3}M\mathrm{S}_2$ ($M=$ Nb, Ta), Phys. Rev. B. **105**, L060407 (2022).

[107] M. Katsnelson, V. Y. Irkhin, L. Chioncel, A. Lichtenstein, and R. A. de Groot, Half-metallic ferromagnets: From band structure to many-body effects, Rev. Mod. Phys. **80**, 315 (2008).

[108] J. Hellmann, *Einführung in die Quantenchemie* (Deuticke, Liepzig, 1937).

[109] R. P. Feynman, Forces in molecules, Phys. Rev. **56**, 340 (1939).

[110] R. S. Mulliken, Electronic population analysis on LCAO–MO molecular wave functions. I, J. Chem. Phys. **23**, 1833–1840 (1955).

[111] D. Sanchez-Portal, E. Artacho, and J. M. Soler, Projection of plane-wave calculations into atomic orbitals, Solid State Commun. **95**, 685–690 (1995).

[112] M. Segall, C. Pickard, R. Shah, and M. Payne, Population analysis in plane wave electronic structure calculations, Mol. Phys. **89**, 571–577 (1996).

[113] M. Segall, R. Shah, C. J. Pickard, and M. Payne, Population analysis of plane-wave electronic structure calculations of bulk materials, Phys. Rev. B. **54**, 16317 (1996).

[114] CASTEP Documentation, `http://www.tcm.phy.cam.ac.uk/castep/documentation/WebHelp/CASTEP.html`.

[115] A. Damascelli, Probing the electronic structure of complex systems by ARPES, Physica Scripta **2004**, 61 (2004).

[116] J. Hill and D. McMorrow, Resonant exchange scattering: polarization dependence and correlation function, Acta Crystallogr. A **52**, 236–244 (1996).

[117] T. Hicken, S. Holt, K. Franke, Z. Hawkhead, A. Štefančič, M. Wilson, M. Gomilšek, B. Huddart, S. Clark, M. Lees, *et al.*, Magnetism and Néel skyrmion dynamics in $\mathrm{GaV_4S_{8-y}Se_y}$, Phys. Rev. Research **2**, 032001 (2020).

[118] T. Hicken, M. Wilson, K. Franke, B. Huddart, Z. Hawkhead, M. Gomilšek, S. Clark, F. Pratt, A. Štefančič, A. Hall, *et al.*, Megahertz dynamics in skyrmion systems probed with muon-spin relaxation, Phys. Rev. B. **103**, 024428 (2021).

[119] B. Huddart, A. Hernández-Melián, T. Hicken, M. Gomilšek, Z. Hawkhead, S. Clark, F. Pratt, and T. Lancaster, MuFinder: A program to determine and analyse muon stopping sites, Computer Physics Communications **280**, 108488 (2022).

[120] X. Wang, H. Yuan, and X. Wang, A theory on skyrmion size, Commun. Phys. **1**, 1–7 (2018).

[121] S. Mühlbauer, D. Honecker, É. A. Périgo, F. Bergner, S. Disch, A. Heinemann, S. Erokhin, D. Berkov, C. Leighton, M. R. Eskildsen, *et al.*, Magnetic small-angle neutron scattering, Rev. Mod. Phys. **91**, 015004 (2019).

[122] S. Blundell, Spin-polarized muons in condensed matter physics, Contemp. Phys. **40**, 175–192 (1999).

[123] A. D. Hillier, S. J. Blundell, I. McKenzie, I. Umegaki, L. Shu, J. A. Wright, T. Prokscha, F. Bert, K. Shimomura, A. Berlie, *et al.*, Muon spin spectroscopy, Nat. Rev. Methods Primers **2**, 1–24 (2022).

[124] J. Beringer *et al.*, Review of Particle Physics, Phys. Rev. D **86**, 010001 (2012).

[125] A. J. Fisher, Theoretical studies of processes involving implanted muons, Current Opinion in Solid State and Materials Science **1**, 841–845 (1996).

[126] R. Valladares, M. Probert, and A. Fisher, Theoretical studies of implanted muons in organic magnets, in *C, H, N and O in Si and Characterization and Simulation of Materials and Processes* (Elsevier, 1996) pp. 247–250.

[127] M. Probert and A. Fisher, An ab initio study of muons in ethanal, J. Phys. Condens. Matter. **9**, 3241 (1997).

[128] J. Möller, D. Ceresoli, T. Lancaster, N. Marzari, and S. Blundell, Quantum states of muons in fluorides, Phys. Rev. B. **87**, 121108 (2013).

[129] J. Möller, P. Bonfà, D. Ceresoli, F. Bernardini, S. Blundell, T. Lancaster, R. De Renzi, N. Marzari, I. Watanabe, S. Sulaiman, *et al.*, Playing quantum hide-and-seek with the muon: localizing muon stopping sites, Phys. Scr. **88**, 068510 (2013).

[130] F. Bernardini, P. Bonfa, S. Massidda, and R. De Renzi, Ab initio strategy for muon site assignment in wide band gap fluorides, Phys. Rev. B. **87**, 115148 (2013).

[131] P. Bonfà and R. De Renzi, Toward the computational prediction of muon sites and interaction parameters, J. Phys. Soc. Jpn. **85**, 091014 (2016).

[132] C. G. Van de Walle, Hydrogen as a cause of doping in zinc oxide, Phys. Rev. Lett. **85**, 1012 (2000).

[133] J. Hong, Z. Hu, M. Probert, K. Li, D. Lv, X. Yang, L. Gu, N. Mao, Q. Feng, L. Xie, *et al.*, Exploring atomic defects in molybdenum disulphide monolayers, Nat. Commun. **6**, 1–8 (2015).

[134] S. Seki, X. Yu, S. Ishiwata, and Y. Tokura, Observation of skyrmions in a multiferroic material, Science **336**, 198–201 (2012).

[135] S. Moody, P. Nielsen, M. Wilson, D. A. Venero, A. Štefančič, G. Balakrishnan, and P. Hatton, Experimental evidence of a change of exchange anisotropy sign with temperature in Zn-substituted Cu_2OSeO_3, Phys. Rev. Research **3**, 043149 (2021).

[136] J. S. White, I. Levatić, A. Omrani, N. Egetenmeyer, K. Prša, I. Živković, J. L. Gavilano, J. Kohlbrecher, M. Bartkowiak, H. Berger, *et al.*, Electric field control of the skyrmion lattice in Cu_2OSeO_3, J. Phys. Condens. Matter. **24**, 432201 (2012).

[137] K. J. Franke, P. R. Dean, M. C. Hatnean, M. T. Birch, D. Khalyavin, P. Manuel, T. Lancaster, G. Balakrishnan, and P. D. Hatton, Investigating the magnetic ground state of the skyrmion host material Cu_2OSeO_3 using long-wavelength neutron diffraction, AIP Advances **9**, 125228 (2019).

[138] A. Štefančič, S. Moody, T. Hicken, M. Birch, G. Balakrishnan, S. Barnett, M. Crisanti, J. Evans, S. Holt, K. Franke, *et al.*, Origin of skyrmion lattice phase splitting in Zn-substituted Cu_2OSeO_3, Phys. Rev. Mater. **2**, 111402 (2018).

[139] J.-W. G. Bos, C. V. Colin, and T. T. Palstra, Magnetoelectric coupling in the cubic ferrimagnet Cu_2OSeO_3, Phys. Rev. B. **78**, 094416 (2008).

[140] T. Schwarze, J. Waizner, M. Garst, A. Bauer, I. Stasinopoulos, H. Berger, C. Pfleiderer, and D. Grundler, Universal helimagnon and skyrmion excitations in metallic, semiconducting and insulating chiral magnets, Nat. Mater. **14**, 478–483 (2015).

[141] V. Gnezdilov, K. Lamonova, Y. G. Pashkevich, P. Lemmens, H. Berger, F. Bussy, and S. Gnatchenko, Magnetoelectricity in the ferrimagnetic Cu_2OSeO_3: symmetry analysis and Raman scattering study, Low Temp. Phys. **36**, 550–557 (2010).

[142] K. Miller, X. Xu, H. Berger, E. Knowles, D. Arenas, M. W. Meisel,

and D. Tanner, Magnetodielectric coupling of infrared phonons in single-crystal Cu_2OSeO_3, Phys. Rev. B. **82**, 144107 (2010).

[143] M. Ozerov, J. Romhanyi, M. Belesi, H. Berger, J.-P. Ansermet, J. Van Den Brink, J. Wosnitza, S. Zvyagin, and I. Rousochatzakis, Establishing the fundamental magnetic interactions in the chiral skyrmionic Mott insulator Cu_2OSeO_3 by terahertz electron spin resonance, Phys. Rev. Lett. **113**, 157205 (2014).

[144] J. Romhányi, J. Van Den Brink, and I. Rousochatzakis, Entangled tetrahedron ground state and excitations of the magnetoelectric skyrmion material Cu_2OSeO_3, Phys. Rev. B. **90**, 140404 (2014).

[145] T. Hicken, M. Wilson, S. Holt, R. Khassanov, M. Lees, R. Gupta, D. Das, G. Balakrishnan, and T. Lancaster, Magnetism in the Néel-skyrmion host GaV_4S_8 under pressure, Phys. Rev. B. **105**, 134414 (2022).

[146] H. Effenberger and F. Pertlik, Die Kristallstrukturen der Kupfer(II)-oxo-selenite $Cu_2O(SeO_3)$ (kubisch und monoklin) und $Cu_4O(SeO_3)_3$ (monoklin und triklin), Monatshefte fuer Chemie **117**, 887–896 (1986).

[147] A. Maisuradze, Z. Guguchia, B. Graneli, H. Rønnow, H. Berger, and H. Keller, μ SR investigation of magnetism and magnetoelectric coupling in Cu_2OSeO_3, Phys. Rev. B. **84**, 064433 (2011).

[148] K. Momma and F. Izumi, VESTA 3 for three-dimensional visualization of crystal, volumetric and morphology data, J. Appl. Crystallogr. **44**, 1272–1276 (2011).

[149] A. D. Pant, Y. Sugawara, H. Nakanishi, E. Torikai, W. Higemoto, K. Shimomura, and K. Nagamine, Theoretical calculations of charge states and stopping sites of muons in glycine and triglycine, in *Proceedings of the 14th International Conference on Muon Spin Rotation, Relaxation and Resonance (μSR2017)* (2018) p. 011038.

[150] P. Bonfà, I. J. Onuorah, and R. De Renzi, Introduction and a quick look at MUESR, the Magnetic structure and mUon Embedding Site Refinement suite, in *Proceedings of the 14th International Conference on Muon Spin Rotation, Relaxation and Resonance (μSR2017)* (2018) p. 011052.

[151] T. Lancaster, F. Xiao, B. Huddart, R. Williams, F. Pratt, S. Blundell, S. Clark, R. Scheuermann, T. Goko, S. Ward, *et al.*, Quantum magnetism in molecular spin ladders probed with muon-spin spectroscopy, New J. Phys. **20**, 103002 (2018).

[152] I. Kézsmárki, S. Bordács, P. Milde, E. Neuber, L. Eng, J. White, H. M. Rønnow, C. Dewhurst, M. Mochizuki, K. Yanai, *et al.*, Néel-type skyrmion lattice with confined orientation in the polar magnetic semiconductor GaV_4S_8, Nat. Mater. **14**, 1116–1122 (2015).

[153] J. S. White, A. Butykai, R. Cubitt, D. Honecker, C. D. Dewhurst, L. Kiss, V. Tsurkan, and S. Bordács, Direct evidence for cycloidal modulations in the thermal-fluctuation-stabilized spin spiral and skyrmion states of GaV_4S_8, Phys. Rev. B. **97**, 020401 (2018).

[154] S. Bordács, A. Butykai, B. G. Szigeti, J. S. White, R. Cubitt, A. O. Leonov, S. Widmann, D. Ehlers, H.-A. K. von Nidda, V. Tsurkan, *et al.*, Equilibrium skyrmion lattice ground state in a polar easy-plane magnet, Sci. Rep. **7**, 1–11 (2017).

[155] Y. Fujima, N. Abe, Y. Tokunaga, and T. Arima, Thermodynamically stable skyrmion lattice at low temperatures in a bulk crystal of lacunar spinel GaV_4Se_8, Phys. Rev. B. **95**, 180410 (2017).

[156] S. Widmann, E. Ruff, A. Günther, H.-A. Krug von Nidda, P. Lunkenheimer, V. Tsurkan, S. Bordács, I. Kézsmárki, and A. Loidl, On the multiferroic skyrmion-host GaV_4S_8, Philos. Mag. **97**, 3428–3445 (2017).

[157] P. Padmanabhan, F. Sekiguchi, R. B. Versteeg, E. Slivina, V. Tsurkan, S. Bordács, I. Kézsmárki, and P. Van Loosdrecht, Optically driven col-

lective spin excitations and magnetization dynamics in the Néel-type skyrmion host GaV_4S_8, Phys. Rev. Lett. **122**, 107203 (2019).

[158] J. L. Zuo, D. Kitchaev, E. C. Schueller, J. D. Bocarsly, R. Seshadri, A. Van der Ven, and S. D. Wilson, Magnetoentropic mapping and computational modeling of cycloids and skyrmions in the lacunar spinels GaV_4S_8 and GaV_4Se_8, Phys. Rev. Mater. **5**, 054410 (2021).

[159] M. Birch, R. Takagi, S. Seki, M. Wilson, F. Kagawa, A. Štefančič, G. Balakrishnan, R. Fan, P. Steadman, C. Ottley, *et al.*, Increased lifetime of metastable skyrmions by controlled doping, Phys. Rev. B. **100**, 014425 (2019).

[160] M. Crisanti, M. Birch, M. Wilson, S. Moody, A. Štefančič, B. Huddart, S. Cabeza, G. Balakrishnan, P. Hatton, and R. Cubitt, Position-dependent stability and lifetime of the skyrmion state in nickel-substituted Cu_2OSeO_3, Phys. Rev. B. **102**, 224407 (2020).

[161] M. Wilson, M. Crisanti, C. Barker, A. Štefančič, J. White, M. Birch, G. Balakrishnan, R. Cubitt, and P. Hatton, Measuring the formation energy barrier of skyrmions in zinc-substituted Cu_2OSeO_3, Phys. Rev. B. **99**, 174421 (2019).

[162] A. Štefančič, S. J. Holt, M. R. Lees, C. Ritter, M. J. Gutmann, T. Lancaster, and G. Balakrishnan, Establishing magneto-structural relationships in the solid solutions of the skyrmion hosting family of materials: $GaV_4S_{8-y}Se_y$, Sci. Rep. **10**, 1–12 (2020).

[163] K. J. Franke, B. M. Huddart, T. J. Hicken, F. Xiao, S. J. Blundell, F. L. Pratt, M. Crisanti, J. A. Barker, S. J. Clark, A. Štefančič, *et al.*, Magnetic phases of skyrmion-hosting $GaV_4S_{8-y}Se_y (y = 0, 2, 4, 8)$ probed with muon spectroscopy, Phys. Rev. B. **98**, 054428 (2018).

[164] S. Holt, A. Štefančič, C. Ritter, A. Hall, M. Lees, and G. Balakrishnan, Structure and magnetism of the skyrmion hosting family $GaV_4S_{8-y}Se_y$

with low levels of substitutions between $0 \leq y \leq 0.5$ and $7.5 \leq y \leq 8$, Phys. Rev. Materials **4**, 114413 (2020).

[165] B. Brandow, Electronic structure of Mott insulators, Adv. Phys. **26**, 651–808 (1977).

[166] H. Müller, W. Kockelmann, and D. Johrendt, The magnetic structure and electronic ground states of Mott insulators GeV_4S_8 and GaV_4S_8, Chem. Mater. **18**, 2174–2180 (2006).

[167] B. Himmetoglu, A. Floris, S. De Gironcoli, and M. Cococcioni, Hubbard-corrected DFT energy functionals: The LDA+ U description of correlated systems, Int. J. Quantum Chem. **114**, 14–49 (2014).

[168] H.-S. Kim, K. Haule, and D. Vanderbilt, Molecular Mott state in the deficient spinel GaV_4S_8, Phys. Rev. B. **102**, 081105 (2020).

[169] T. Lancaster, P. Goddard, S. Blundell, F. Foronda, S. Ghannadzadeh, J. Möller, P. Baker, F. Pratt, C. Baines, L. Huang, *et al.*, Controlling magnetic order and quantum disorder in molecule-based magnets, Phys. Rev. Lett. **112**, 207201 (2014).

[170] T. Giamarchi, C. Rüegg, and O. Tchernyshyov, Bose–Einstein condensation in magnetic insulators, Nat. Phys. **4**, 198–204 (2008).

[171] S. J. Blundell and F. L. Pratt, Organic and molecular magnets, J. Phys. Condens. Mater. **16**, R771 (2004).

[172] P. A. Goddard, J. L. Manson, J. Singleton, I. Franke, T. Lancaster, A. J. Steele, S. J. Blundell, C. Baines, F. L. Pratt, R. D. McDonald, *et al.*, Dimensionality selection in a molecule-based magnet, Phys. Rev. Lett. **108**, 077208 (2012).

[173] S. Sebastian, N. Harrison, C. Batista, L. Balicas, M. Jaime, P. Sharma, N. Kawashima, and I. Fisher, Dimensional reduction at a quantum critical point, Nature **441**, 617–620 (2006).

[174] S. Bettler, G. Simutis, G. Perren, D. Blosser, S. Gvasaliya, and A. Zheludev, High-pressure Raman study of the quantum magnet $(C_4H_{12}N_2)Cu_2Cl_6$, Phys. Rev. B. **96**, 174431 (2017).

[175] J. Brambleby, P. Goddard, J. Singleton, M. Jaime, T. Lancaster, L. Huang, J. Wosnitza, C. Topping, K. Carreiro, H. Tran, *et al.*, Adiabatic physics of an exchange-coupled spin-dimer system: Magnetocaloric effect, zero-point fluctuations, and possible two-dimensional universal behavior, Phys. Rev. B. **95**, 024404 (2017).

[176] C. Rüegg, A. Furrer, D. Sheptyakov, T. Strässle, K. Krämer, H.-U. Güdel, and L. Mélési, Pressure-Induced Quantum Phase Transition in the Spin-Liquid $TlCuCl_3$, Phys. Rev. Lett. **93**, 257201 (2004).

[177] L. J. Bartolotti and R. G. Parr, The concept of pressure in density functional theory, J. Chem. Phys. **72**, 1593–1596 (1980).

[178] E. Ruiz, J. Cano, S. Alvarez, and P. Alemany, Broken symmetry approach to calculation of exchange coupling constants for homobinuclear and heterobinuclear transition metal complexes, J. Comput. Chem. **20**, 1391–1400 (1999).

[179] E. Ruiz, A. Rodríguez-Fortea, J. Cano, S. Alvarez, and P. Alemany, About the calculation of exchange coupling constants in polynuclear transition metal complexes, J. Comput. Chem. **24**, 982–989 (2003).

[180] I. O. Thomas, S. J. Clark, and T. Lancaster, Exchange constants in molecule-based magnets derived from density functional methods, Phys. Rev. B. **96**, 094403 (2017).

[181] T. Bucko, J. Hafner, S. Lebegue, and J. G. Angyán, Improved description of the structure of molecular and layered crystals: ab initio DFT calculations with van der Waals corrections, J. Phys. Chem. A **114**, 11814–11824 (2010).

[182] J. F. Dobson, K. McLennan, A. Rubio, J. Wang, T. Gould, H. M. Le, and B. P. Dinte, Prediction of dispersion forces: is there a problem?, Aust. J. Chem. **54**, 513–527 (2001).

[183] T. Hong, V. O. Garlea, A. Zheludev, J. A. Fernandez-Baca, H. Manaka, S. Chang, J. Leao, and S. Poulton, Effect of pressure on the quantum spin ladder material IPA-CuCl 3, Phys. Rev. B. **78**, 224409 (2008).

[184] T. Hong, C. Stock, I. Cabrera, C. Broholm, Y. Qiu, J. Leao, S. Poulton, and J. Copley, Neutron scattering study of a quasi-two-dimensional spin-1 2 dimer system: Piperazinium hexachlorodicuprate under hydrostatic pressure, Phys. Rev. B. **82**, 184424 (2010).

[185] M. Coake, Untitled Manuscript, unpublished.

[186] D. Moncton, J. Axe, and F. DiSalvo, Study of superlattice formation in 2H-$NbSe_2$ and 2H-$TaSe_2$ by neutron scattering, Phys. Rev. Lett. **34**, 734 (1975).

[187] O. Rajora and A. Curzon, The preparation and X-ray diffraction study of the layer materials NbS_xSe_{2-x} for $0 \leq x \leq 2$, Physica Status Solidi (a) **99**, 65–72 (1987).

[188] M. Naito and S. Tanaka, Electrical transport properties in 2H-NbS_2,-$NbSe_2$,-TaS_2 and-$TaSe_2$, J. Phys. Soc. Jpn. **51**, 219–227 (1982).

[189] K. S. Novoselov, A. K. Geim, S. V. Morozov, D.-e. Jiang, Y. Zhang, S. V. Dubonos, I. V. Grigorieva, and A. A. Firsov, Electric field effect in atomically thin carbon films, Science **306**, 666–669 (2004).

[190] S. Manzeli, D. Ovchinnikov, D. Pasquier, O. V. Yazyev, and A. Kis, 2D transition metal dichalcogenides, Nat. Rev. Mater. **2**, 1–15 (2017).

[191] Z. Wei, B. Li, C. Xia, Y. Cui, J. He, J.-B. Xia, and J. Li, Various structures of 2D transition-metal dichalcogenides and their applications, Small Methods **2**, 1800094 (2018).

[192] Q. H. Wang, K. Kalantar-Zadeh, A. Kis, J. N. Coleman, and M. S. Strano, Electronics and optoelectronics of two-dimensional transition metal dichalcogenides, Nat. Nanotechnol. **7**, 699–712 (2012).

[193] K. F. Mak, C. Lee, J. Hone, J. Shan, and T. F. Heinz, Atomically thin MoS_2: a new direct-gap semiconductor, Phys. Rev. Lett. **105**, 136805 (2010).

[194] C. Heil, S. Poncé, H. Lambert, M. Schlipf, E. R. Margine, and F. Giustino, Origin of superconductivity and latent charge density wave in NbS_2, Phys. Rev. Lett. **119**, 087003 (2017).

[195] C. Witteveen, K. Górnicka, J. Chang, M. Månsson, T. Klimczuk, and F. O. von Rohr, Polytypism and superconductivity in the NbS_2 system, Dalton Trans. **50**, 3216–3223 (2021).

[196] V. Tissen, M. Osorio, J.-P. Brison, N. Nemes, M. García-Hernández, L. Cario, P. Rodiere, S. Vieira, and H. Suderow, Pressure dependence of superconducting critical temperature and upper critical field of $2H$-NbS_2, Phys. Rev. B. **87**, 134502 (2013).

[197] R. Ganatra and Q. Zhang, Few-layer MoS_2: a promising layered semiconductor, ACS Nano **8**, 4074–4099 (2014).

[198] A. Castellanos-Gomez, M. Barkelid, A. Goossens, V. E. Calado, H. S. van der Zant, and G. A. Steele, Laser-thinning of MoS_2: on demand generation of a single-layer semiconductor, Nano Letters **12**, 3187–3192 (2012).

[199] S. Parkin and R. Friend, $3d$ transition-metal intercalates of the niobium and tantalum dichalcogenides. I. Magnetic properties, Philosophical Magazine B **41**, 65–93 (1980).

[200] S. Parkin and R. Friend, $3d$ transition-metal intercalates of the niobium and tantalum dichalcogenides. II. Transport properties, Philosophical Magazine B **41**, 95–112 (1980).

[201] T. Moriya and T. Miyadai, Evidence for the helical spin structure due to antisymmetric exchange interaction in $Cr_{1/3}NbS_2$, Solid State Commun. **42**, 209–212 (1982).

[202] Y. Kousaka, T. Ogura, J. Zhang, P. Miao, S. Lee, S. Torii, T. Kamiyama, J. Campo, K. Inoue, and J. Akimitsu, Long periodic helimagnetic ordering in CrM_3S_6 ($M=$ Nb and Ta), in *J. Phys.: Conference Series*, Vol. 746 (IOP Publishing, 2016) p. 012061.

[203] N. Ghimire, M. A. McGuire, D. S. Parker, B. Sipos, S. Tang, J.-Q. Yan, B. C. Sales, and D. Mandrus, Magnetic phase transition in single crystals of the chiral helimagnet $Cr_{1/3}NbS_2$, Phys. Rev. B. **87**, 104403 (2013).

[204] Y. Togawa, T. Koyama, K. Takayanagi, S. Mori, Y. Kousaka, J. Akimitsu, S. Nishihara, K. Inoue, A. Ovchinnikov, and J.-i. Kishine, Chiral magnetic soliton lattice on a chiral helimagnet, Phys. Rev. Lett. **108**, 107202 (2012).

[205] C. Zhang, J. Zhang, C. Liu, S. Zhang, Y. Yuan, P. Li, Y. Wen, Z. Jiang, B. Zhou, Y. Lei, *et al.*, Chiral Helimagnetism and One-Dimensional Magnetic Solitons in a Cr-Intercalated Transition Metal Dichalcogenide, Adv. Mater. **33**, 2101131 (2021).

[206] A. C. Bornstein, B. J. Chapman, N. J. Ghimire, D. G. Mandrus, D. S. Parker, and M. Lee, Out-of-plane spin-orientation dependent magnetotransport properties in the anisotropic helimagnet $Cr_{1/3}NbS_2$, Phys. Rev. B. **91**, 184401 (2015).

[207] Z. Hawkhead, castep2fs: A CASTEP tool for calculating Fermi surfaces (2022).

[208] A. H. Larsen, J. J. Mortensen, J. Blomqvist, I. E. Castelli, R. Christensen, M. Dułak, J. Friis, M. N. Groves, B. Hammer, C. Hargus, *et al.*, The atomic simulation environment—a Python library for working with atoms, J. Phys. Condens. Matter. **29**, 273002 (2017).

[209] G. K. Madsen and D. J. Singh, BoltzTraP. A code for calculating band-structure dependent quantities, Comput. Phys. Commun. **175**, 67–71 (2006).

[210] A. Hall, J. Loudon, P. Midgley, A. Twitchett-Harrison, S. Holt, D. Mayoh, J. Tidey, Y. Han, M. Lees, and G. Balakrishnan, Comparative study of the structural and magnetic properties of $Mn_{1/3}NbS_2$ and $Cr_{1/3}NbS_2$, Phys. Rev. Materials **6**, 024407 (2022).

[211] A. Hall, D. Khalyavin, P. Manuel, D. Mayoh, F. Orlandi, O. Petrenko, M. Lees, and G. Balakrishnan, Magnetic structure investigation of the intercalated transition metal dichalcogenide $V_{1/3}NbS_2$, Phys. Rev. B. **103**, 174431 (2021).

[212] Y. Kousaka, Y. Nakao, H. Furukawa, and J. Akimitsu, Chiral Helimagnetic Order in $T_{1/3}NbS_2$ (T= Cr, Mn), Activity Report on Neutron Scattering Research: Experimental Reports **16**, 814 (2009).

[213] L. S. Xie, S. Husremović, O. Gonzalez, I. M. Craig, and D. K. Bediako, Structure and Magnetism of Iron- and Chromium-Intercalated Niobium and Tantalum Disulfides, J. Am. Chem. Soc. **144**, 9525–9542 (2022).

[214] J. Coey and S. Sanvito, Magnetic semiconductors and half-metals, J. Phys. D **37**, 988 (2004).

[215] J. Coey and M. Venkatesan, Half-metallic ferromagnetism: Example of CrO_2, J. Appl. Phys. **91**, 8345–8350 (2002).

[216] R. Nicholls, A. Morris, C. Pickard, and J. Yates, OptaDOS-a new tool for EELS calculations, in *J. Phys. Conf. Ser.*, Vol. 371 (IOP Publishing, 2012) p. 012062.

[217] N. Sirica, P. Vilmercati, F. Bondino, I. Pis, S. Nappini, S.-K. Mo, A. V. Fedorov, P. K. Das, I. Vobornik, J. Fujii, *et al.*, The nature of ferromagnetism in the chiral helimagnet $Cr_{1/3}NbS_2$, Commun. Phys. **3**, 1–8 (2020).

[218] M. Leroux, L. Cario, A. Bosak, and P. Rodiere, Traces of charge density waves in NbS_2, Phys. Rev. B. **97**, 195140 (2018).

[219] W. McMillan, Landau theory of charge-density waves in transition-metal dichalcogenides, Phys. Rev. B. **12**, 1187 (1975).

[220] C. Topping and S. Blundell, AC susceptibility as a probe of low-frequency magnetic dynamics, J. Phys. Condens. Matter. **31**, 013001 (2018).

[221] S. F. Sousa, P. A. Fernandes, and M. J. Ramos, General performance of density functionals, J. Phys. Chem. A **111**, 10439–10452 (2007).

[222] G. Dongho Nguimdo and D. P. Joubert, A density functional (PBE, PBEsol, HSE06) study of the structural, electronic and optical properties of the ternary compounds $AgAlX_2$ (X= S, Se, Te), Eur. Phys. J. B **88**, 1–10 (2015).

[223] S. Sharma, J. K. Dewhurst, C. Ambrosch-Draxl, S. Kurth, N. Helbig, S. Pittalis, S. Shallcross, L. Nordström, and E. Gross, First-principles approach to noncollinear magnetism: Towards spin dynamics, Phys. Rev. Lett. **98**, 196405 (2007).

[224] F. Eich and E. Gross, Transverse spin-gradient functional for noncollinear spin-density-functional theory, Phys. Rev. Lett. **111**, 156401 (2013).

[225] K. F. Riley, S. J. Bence, and M. P. Hobson, *Mathematical methods for physics and engineering: a comprehensive guide* (Cambridge Univ. Press, Cambridge, 1997).

[226] Z. Hawkhead, nc_cryst: A tool for visualising non-collinear magnetism in crystals (2022).

[227] C. Li, A. Freeman, and C. Fu, Electronic structure and magnetic properties of the hcp Co (0001) surface, J. Magn. Magn. Mater. **94**, 134–140 (1991).

[228] S. Li, C. de La Cruz, Q. Huang, Y. Chen, J. Lynn, J. Hu, Y.-L. Huang, F.-C. Hsu, K.-W. Yeh, M.-K. Wu, *et al.*, First-order magnetic and structural phase transitions in $Fe_{1+y}Se_xTe_{1-x}$, Phys. Rev. B. **79**, 054503 (2009).

[229] Q. Huang, Y. Qiu, W. Bao, M. Green, J. Lynn, Y. Gasparovic, T. Wu, G. Wu, and X. Chen, Neutron-diffraction measurements of magnetic order and a structural transition in the parent $BaFe_2As_2$ compound of FeAs-based high-temperature superconductors, Phys. Rev. Lett. **101**, 257003 (2008).

[230] V. Lohani, C. Hickey, J. Masell, and A. Rosch, Quantum skyrmions in frustrated ferromagnets, Phys. Rev. X **9**, 041063 (2019).

[231] T. Kurumaji, T. Nakajima, M. Hirschberger, A. Kikkawa, Y. Yamasaki, H. Sagayama, H. Nakao, Y. Taguchi, T.-h. Arima, and Y. Tokura, Skyrmion lattice with a giant topological Hall effect in a frustrated triangular-lattice magnet, Science **365**, 914–918 (2019).

[232] L. Pauling, The structure and entropy of ice and of other crystals with some randomness of atomic arrangement, J. Am. Chem. Soc. **57**, 2680–2684 (1935).

[233] S. T. Bramwell and M. J. Gingras, Spin ice state in frustrated magnetic pyrochlore materials, Science **294**, 1495–1501 (2001).

[234] J. Lago, S. J. Blundell, and C. Baines, μSR investigation of spin dynamics in the spin-ice material $Dy_2Ti_2O_7$, J. Phys. Condens. Mater. **19**, 326210 (2007).

[235] K. Matsuhira, Y. Hinatsu, and T. Sakakibara, Novel dynamical magnetic properties in the spin ice compound $Dy_2Ti_2O_7$, J. Phys. Condens. Matter. **13**, L737 (2001).

[236] D. J. P. Morris, D. Tennant, S. Grigera, B. Klemke, C. Castelnovo, R. Moessner, C. Czternasty, M. Meissner, K. Rule, J.-U. Hoffmann, *et al.*,

Dirac strings and magnetic monopoles in the spin ice $Dy_2Ti_2O_7$, Science **326**, 411–414 (2009).

[237] S. Dunsiger, A. A. Aczel, C. Arguello, H. Dabkowska, A. Dabkowski, M.-H. Du, T. Goko, B. Javanparast, T. Lin, F. Ning, *et al.*, Spin ice: magnetic excitations without monopole signatures using muon spin rotation, Phys. Rev. Lett. **107**, 207207 (2011).

[238] C. Castelnovo, R. Moessner, and S. L. Sondhi, Magnetic monopoles in spin ice, Nature **451**, 42–45 (2008).

[239] M. J. Gingras, Observing monopoles in a magnetic analog of ice, Science **326**, 375–376 (2009).

[240] K. Persson, Materials Data on $Dy_2Ti_2O_7$ (SG:227) by Materials Project (2014).

[241] M. Van Schilfgaarde and V. Antropov, First-principles exchange interactions in Fe, Ni, and Co, J. Appl. Phys. **85**, 4827–4829 (1999).

[242] T. Müller, S. Sharma, E. Gross, and J. Dewhurst, Extending solid-state calculations to ultra-long-range length scales, Phys. Rev. Lett. **125**, 256402 (2020).

[243] M. C. Payne, M. P. Teter, D. C. Allan, T. Arias, and J. D. Joannopoulos, Iterative minimization techniques for ab initio total-energy calculations - molecular-dynamics and conjugate gradients, Rev. Mod. Phys. **64**, 1045–1097 (1992).

[244] T. W. Hollins, *Local Exchange Potentials in Density Functional Theory*, Ph.D. thesis, University of Durham (2014).

[245] S. J. Leon, Å. Björck, and W. Gander, Gram-Schmidt orthogonalization: 100 years and more, Numerical Linear Algebra with Applications **20**, 492–532 (2013).

[246] M. C. Gibson, *Implementation and application of advanced density functionals*, Ph.D. thesis, University of Durham (2006).